DISSERTATION

submitted to the

COMBINED FACULTY OF MATHEMATICS, ENGINEERING AND NATURAL SCIENCES

of

HEIDELBERG UNIVERSITY, GERMANY

for the degree of
Doctor of Natural Sciences

put forward by

Benedikt Alexander Löw

né Hemmer

born in Jugenheim, Germany

Oral examination: 19.06.2024

Toward Urban Greenhouse Gas Mapping with a Portable Reflected Sunlight Spectrometer

by

BENEDIKT A. LÖW

Referees: Prof. Dr. André Butz
Prof. Dr. Werner Aeschbach

Abstract

Urban regions are major sources of CO_2 and CH_4. Although their emissions are substantial, the quantification is challenged by the complex spatial distribution of sources. Ground-based remote sensing using reflected sunlight can address this challenge. For this purpose, a spectrometer is positioned above a source region, pointing towards ground targets at a shallow angle. It records solar absorption spectra containing information on CO_2 and CH_4 abundances integrated along the light path. Because of the extended quasi-horizontal light path component, the measurements are sensitive to near-ground concentrations and representative of urban enhancements. By repeatedly scanning through multiple targets, the method enables the mapping of temporal and spatial source patterns. This work presents the EM27/SCA, the first portable ground-based Fourier-transform spectrometer (FTS) designed for urban greenhouse gas mapping using near-infrared spectra of ground-scattered sunlight.

The performance of the remote sensing setup is demonstrated through an instrument deployment on Mt. Wilson looking into the Los Angeles basin, USA. The precision of the retrieved CO_2, CH_4 and O_2 slant column densities is in the range of 0.4 % to 0.5 %. The comparison to a more precise but stationary reflected-sun viewing FTS shows overall good agreement but also limited systematic deviations. The measurements reveal atmospheric scattering to be the major error source. A retrieval algorithm is implemented, which explicitly accounts for aerosol scattering and mitigates the scattering-induced bias. This allows the detection of urban enhancement patterns in the EM27/SCA measurements of the Los Angeles basin.

Zusammenfassung

Städtische Regionen sind bedeutende Quellen von CO_2 und CH_4. Obwohl ihre Emissionen beträchtlich sind, wird deren Quantifizierung durch die komplexe räumliche Verteilung der Quellen erschwert. Bodengestützte Fernerkundung von an der Erdoberfläche reflektiertem Sonnenlicht kann diese Herausforderung angehen. Dafür wird ein Spektrometer oberhalb einer Quellregion positioniert und unter einem flachen Winkel auf Bodenziele gerichtet. Es nimmt Absorptionsspektren des reflektierten Sonnenlichtes auf, die Informationen über die integrierte Menge von CO_2 und CH_4 entlang des Lichtweges enthalten. Dank der langen quasi-horizontalen Lichtwegkomponente sind die Messungen sensitiv auf die bodennahen Konzentrationen und repräsentativ für städtische Konzentrationserhöhungen. Durch wiederholtes Rastern über mehrere Ziele ermöglicht die Methode die Kartierung von zeitlichen und räumlichen Quellsignalen. Die vorliegende Arbeit präsentiert das EM27/SCA, das erste portable bodengestützte Fourier-Transformations-Spektrometer (FTS), das für die Kartierung von städtischen Treibhausgasen mit Hilfe von Nahinfrarotspektren von am Boden gestreutem Sonnenlicht entwickelt wurde.

Die Leistungfähigkeit des Fernerkundungsaufbaus wird durch einen Einsatz auf Mt. Wilson mit Blick in das Los-Angeles-Becken, USA, demonstriert. Die Präzision der abgeleiteten schrägen CO_2-, CH_4- und O_2-Säulendichten ist im Bereich von 0.4 % bis 0.5 %. Der Vergleich mit einem präziseren, aber stationären FTS für am Boden reflektiertes Sonnenlicht zeigt insgesamt eine gute Übereinstimmung, aber auch begrenzte systematische Abweichungen. Die Messungen weisen atmosphärische Streuung als Hauptfehlerquelle auf. Daher wird ein Inversionsprogramm implementiert, welches die Aerosolstreuung explizit berücksichtigt und die streuungsinduzierten systematischen Abweichungen vermindert. Dies ermöglicht die Detektion von städtischen Konzentrationserhöhungen in den EM27/SCA Messungen des Los-Angeles-Beckens.

Disclaimer

Parts of the content of this thesis have been published in the following article:

Löw, B. A., R. Kleinschek, V. Enders, S. P. Sander, T. J. Pongetti, T. D. Schmitt, F. Hase, J. Kostinek, and A. Butz (2023). "A Portable Reflected-Sunlight Spectrometer for CO_2 and CH_4". *Atmos. Meas. Tech.* 16:21, pp. 5125–5144. DOI: 10.5194/amt-16-5125-2023.

Author Contributions: BAL developed the instrument configuration and carried out the formal data analysis. BAL, RK and VE together with TJP conducted the field-deployment at Mt. Wilson. RK, TDS and FH supported the instrument development. JK built an early prototype of the instrument. TJP and SPS provided CLARS-FTS measurements and supported data analysis and field deployment. BAL and AB wrote the article with comments from all co-authors. AB conceptualized the project.

Contents

1 Introduction

Carbon dioxide (CO_2) and methane (CH_4) are the most important anthropogenic greenhouse gases (GHGs) (Forster et al. 2021). The emission of large amounts of GHGs through, e.g., production and burning of fossil fuels, global deforestation, livestock farming, rice cultivation, the use of nitrogen-containing fertilizers in agricultural activities and waste disposal (Friedlingstein et al. 2023; Saunois et al. 2020) has globally led to significant changes in the natural climatic processes (Gulev et al. 2021). By now, the global mean temperature has already risen by 1.1 °C compared to the pre-industrial era (Gulev et al. 2021). Further increase in temperature is expected and leads to drastic environmental changes impacting water availability, human health, biodiversity and food security (Jägermeyr et al. 2021; Schewe et al. 2014; Warren et al. 2018; Watts et al. 2018; Wheeler and von Braun 2013). In the context of these risks, the parties to the United Nations Framework Convention on Climate Change (UNFCCC) have agreed in the *Paris Agreement* to limit "the increase in the global average temperature to well below 2 °C" (UNFCCC 2015). Reaching this goal requires substantial additional mitigation efforts to reduce GHG emissions (Riahi et al. 2022).

Urban areas are responsible for a substantial portion of the global GHG emissions. They cause a significant portion of the energy-related CO_2 emissions (71% in 2006, IEA (2008)) and, based on consumption-based accounting, the total urban GHG emissions amount to 67–72% of the global emissions (Lwasa et al. 2022). Although not all emissions originate within city boundaries, a strong gradient between urban and rural areas exists (Marcotullio et al. 2013). Due to the increasing urban area, population and per capita emissions, urban emissions are expected to increase further (Luqman et al. 2023). The primary anthropogenic sources for GHGs within urban areas are energy production, transportation, heating, industry emissions, natural gas (NG) leakages and waste disposal (Foy et al. 2023; Gurney et al. 2019; Hopkins et al. 2016; Maasakkers et al. 2022; Sargent et al. 2021). At the same time, urban areas are vulnerable to climate changes, among others, through heat stress, water scarcity and urban flooding (Flörke et al. 2018; Kulp and Strauss 2019; Masson et al. 2020). Many urban authorities have become important actors in emission mitigation efforts and committed to ambitious goals to reduce urban GHG emissions in their jurisdictions (C40 2024; Global Covenant of Mayors 2024). Accurate and local emission information can help to inform political decision makers, indicate smart mitigation strategies and verify their effectiveness (Jungmann et al. 2022; Mueller et al. 2021; Wei et al. 2021).

The UNFCCC requires yearly GHG inventory reports, which are calculated based on consumption statistics following strict guidelines. Additionally, many scientific efforts exist to compile *bottom-up* emission estimations (Gurney et al. 2020; Gurney et al. 2019; Gurney et al. 2012; Kuenen et al. 2022; Oda 2015), disaggregating governmental statistics in space and time via activity indicators such as population, infrastructure, traffic and nighttime light data. Atmospheric measurements can complement these bottom-up estimates since atmo-

spheric inversion of such measurements provides independent *top-down* emission estimates. Spatiotemporally resolved bottom-up estimates are required as prior information for the atmospheric inversions. At the same time, such top-down estimates allow for verification of the bottom-up estimates and can reveal unaccounted emissions (Johnson et al. 2023; Moore et al. 2023; Petrescu et al. 2023; Sargent et al. 2021; Stagakis et al. 2023; Turnbull et al. 2019; Wang et al. 2024).

While emission estimates through direct flux measurements are possible, e.g., through eddy-covariance measurements (Matthews and Schume 2022; Rebmann et al. 2018; Stagakis et al. 2023; Wu et al. 2022), most top-down emission estimates are inferred from measurements of atmospheric CO_2 and CH_4 concentrations. Using either mass balance approaches or explicit atmospheric transport modeling, fluxes are computed from gradients in the measured concentrations (Christen 2014). The numerous measurement methods for atmospheric CO_2 and CH_4 concentrations can be classified into *in situ* and *remote sensing* methods. In situ measurements provide highly accurate concentration measurements at fast sampling rates (Hazan et al. 2016; Verhulst et al. 2017). However, their local sampling limits them, making them sensitive to local sources and transport patterns (McKain et al. 2012). To compensate for the locality, multiple stations are combined into networks. Prominent examples are the networks set up in Indianapolis (Davis et al. 2017; Turnbull et al. 2019), San Francisco bay area (Kim et al. 2018; Shusterman et al. 2016), Los Angeles (Verhulst et al. 2017), Boston (McKain et al. 2015; Sargent et al. 2018) and Paris (Lian et al. 2022). They are used to determine emission estimates in their respective urban regions.

Remote sensing methods analyze the spectrum of light transmitted through the atmosphere to deduce the abundance of GHGs from their spectral absorption features. This approach inherently measures column-averaged concentrations, making them less prone to local sources and more representative of urban enhancements. At the same time, the enhancement signals are much smaller. The most common GHG remote sensing techniques use absorption features in solar radiation. Solar radiation is observed either directly from the ground (Frey et al. 2019; Wunch et al. 2011) or from space by observing the ground-reflected sunlight (Butz et al. 2011; Eldering et al. 2017; Hu et al. 2018; Kiel et al. 2021; Kuze et al. 2009). Satellite-based remote sensing measurements provide global coverage, but their temporal coverage is typically limited by the revisiting time of the satellite. Ground-based direct-sun observing spectrometers operate in small networks around urban areas leveraging the GHG gradients between downwind and upwind measurements to estimate source fluxes (Dietrich et al. 2021; Hase et al. 2015; Luther et al. 2022; Ohyama et al. 2023; Vogel et al. 2019). Since these methods measure total column concentrations, the enhancements due to urban sources are typically rather small, between 0.1 % to 1.0 % for CO_2 (Hase et al. 2015; Kort et al. 2012; Vogel et al. 2019) and CH_4 (Forstmaier et al. 2023; Foy et al. 2023).

The Los Angeles (LA) basin is the second largest urban source region of GHG emissions in the US (Moran et al. 2018). Its CH_4 emissions are caused by a variety of sources, including fossil fuel production, NG storage and distribution, dairies, landfills and wastewater treatment (Carranza et al. 2018). Its CO_2 emissions are mainly caused by on-road transport, energy production, residential and industrial emissions (Gurney et al. 2019). The urban biosphere has a significant seasonal contribution to the CO_2 fluxes (Miller et al. 2020). At the same time, LA is a focus region for atmospheric measurements with the goal of quantifying urban emissions (Mitchell et al. 2022). Many top-down studies used in situ, aircraft,

total column and satellite measurements to determine the GHG emissions. Basin-wide CH_4 emissions have been estimated by, e.g., Cui et al. (2015), Hsu et al. (2010), Jeong et al. (2016), Wecht et al. (2014), Wunch et al. (2009), Wunch et al. (2016), and Yadav et al. (2019). Overall, the emissions are estimated to be $0.38\,\mathrm{TgCH_4/yr}$ with a declining trend (Yadav et al. 2023) and are heterogeneously distributed (Hopkins et al. 2016). For CO_2, Gurney et al. (2019) provides a highly resolved emission inventory. The related enhancements in the CO_2 concentrations show spatial and temporal patterns (e.g. Kiel et al. 2021; Newman et al. 2013; Verhulst et al. 2017; Wunch et al. 2009). Brioude et al. (2013) estimates CO_2 emissions of $183\,\mathrm{TgCO_2/yr}$ from aircraft data. Hedelius et al. (2018) uses total column and satellite data to quantify the basin-wide CO_2 emissions to $(104 \pm 26)\,\mathrm{TgCO_2/yr}$ and $(120 \pm 30)\,\mathrm{TgCO_2/yr}$ respectively.

Reflected-sun measurements offer an alternative measurement technique to those mentioned above. By recording spectra of ground-reflected sunlight with a ground-based instrument, the technique combines aspects of direct-sun and satellite measurements. The spectrometer points from an elevated position downwards at a shallow viewing angle into the urban source region. As it remains stationary, it can continuously monitor the source region, providing dense temporal sampling, given cloud-free weather conditions. Additionally, a significant portion of the light path is close to the surface and, therefore, influenced by the urban emission signals. This observation geometry combines a high sensitivity to urban GHG enhancements with horizontal averaging on the kilometer length scale, making the measurements representative of the urban enhancements. Similar to satellite measurements, the viewing geometry is not entirely determined by the position of the sun. Therefore, given a clear line of sight, a single instrument can scan through the entire source region. Addressing the specific challenges related to this viewing geometry is necessary to capitalize on these advantages. Compared to direct-sun observations, the radiance of surface-reflected sunlight is significantly lower, resulting in lower measurement precision. In addition, the long optical path through the boundary layer leads to a significant influence of aerosol scattering on the GHG retrievals.

The California Laboratory for Atmospheric Remote Sensing (CLARS) – Fourier-transform spectrometer (FTS) (CLARS-FTS) (Fu et al. 2014) pioneered the reflected-sun measurement geometry. The custom-built instrument is stationary and located at 1670 m a.s.l. on top of Mt. Wilson, with a direct line of sight to most of the LA basin. Since 2010, the FTS routinely records spectra pointing at 33 ground targets across the LA basin. Despite the aforementioned challenges, the CLARS-FTS measurements provide valuable insights into spatial and temporal patterns of LA basin CH_4 emissions (He et al. 2019; Wong et al. 2015; Zeng et al. 2023). They compensate for the effects of aerosol scattering by rationing between the similarly influenced CH_4 and CO_2 columns, which cancels the error. Combining these ratios with accurate CO_2 emission inventories enables the top-down estimation of CH_4 emissions. Several studies use this to infer spatial and temporal patterns of LA basin CH_4 emissions from CLARS-FTS measurements. Wong et al. (2015) derive basin-wide emission estimates of $(0.39 \pm 0.06)\,\mathrm{TgCH_4/yr}$ during 2011 to 2013 and show significant spatial variation in the CH_4/CO_2 ratios. Wong et al. (2016) derive monthly emission estimates for 2011 to 2015 which reveal a seasonal pattern in the CH_4 emissions. Later, the pattern could be linked to the seasonal pattern of NG consumption (He et al. 2019). Zeng et al. (2023) show that the LA CH_4 emission decreased by (-1.57 ± 0.41) % during 2011 to 2020. This is a significantly lower reduction than indicated by NG utility calculations. At the same time, several

approaches were developed to tackle the challenging scattering impact on the CLARS-FTS measurements. Zhang et al. (2015) show that rationing CO_2 by O_2 to XCO_2 results in a high bias due to the wavelength dependency of aerosol scattering. Based on radiative transfer modeling, they develop a scaling factor that corrects the bias in XCO_2 based on the apparent reduction in the O_2 column. Zeng et al. (2017) show that aerosol scattering effects can be derived from multiple water absorption signals across a broad wavelength range. Zeng et al. (2020b) and Zeng et al. (2018) develop a method to infer aerosol information from the $O_2\Delta$ band. Both studies aim to reduce the scattering bias in GHG retrievals. Finally, Zeng et al. (2021) develop a full-physics retrieval that accounts for aerosol scattering effects to retrieve XGHGs.

This work presents the EM27/SCA, a prototype for a portable FTS measuring in the reflected-sun geometry. The instrument can be transported without specialized equipment and requires minimal infrastructure, making it deployable to any suitable location with a clear view into a source region. This expands the application opportunities substantially and allows for temporary deployments. The instrument is derived from the robust and widely used direct-sun observing EM27/SUN (Gisi et al. 2012), with modifications made to accommodate the much lower radiances of surface reflected sunlight. It has a nominal resolution of $0.5\,\mathrm{cm}^{-1}$, which is lower than CLARS-FTS but sufficient to resolve the absorption features of CO_2, CH_4 and, for light path information, O_2. This work assesses the performance of the EM27/SCA through laboratory and field measurements. The EM27/SCA is deployed to Mt. Wilson and is compared to the CLARS-FTS in simultaneous measurements of the LA basin. These measurements are used to evaluate the measurement precision and accuracy. The key challenge of aerosol scattering-induced errors on the reflected-sun measurements is addressed by implementing a retrieval algorithm that explicitly accounts for aerosol scattering. The resulting XCO_2 and XCH_4 time series are evaluated for the detectability of urban emission patterns.

The thesis is structured as follows. Chapter 2 introduces the theoretical background necessary for evaluating near infrared (NIR) absorption spectra for atmospheric GHG abundances. Chapter 3 presents and characterizes the EM27/SCA FTS mainly through laboratory measurements. Chapter 4 presents the retrieval method used to determine GHG column densities from the measured spectra. Chapter 5 evaluates the instrument performance based on atmospheric measurements. This includes comparisons of simultaneous measurements by the EM27/SCA and the CLARS-FTS. The impact of aerosol scattering on the measurements is subsequently evaluated and a method to mitigate its influence is presented. Finally, the time series of the CO_2 and CH_4 measurements are examined for spatiotemporal urban emission patterns. Chapter 6 summarizes the findings and provides an outlook on the further prospects.

2 Radiative Transfer for Atmospheric Near Infrared Remote Sensing

The task of atmospheric remote sensing is to infer information on the state of the atmosphere from measurements of electromagnetic (EM) radiation. This requires an understanding of how radiation interacts with a medium, in our case air, while propagating through it. Radiative transfer theory provides this description, allowing us to link observations of EM radiation to the atmospheric state through knowledge of the underlying physical processes. We will limit the radiative transfer considerations to processes which are relevant in the Earth's atmosphere and to the NIR range. I present information from the textbooks by Bransden and Joachain (2003), Liou (2002), Petty (2006), and Stamnes et al. (2017), which I also recommend for further reading beyond the basic introduction provided here. Petty (2006) offers a good overview of the topic, Bransden and Joachain (2003) explains the quantum mechanical background of molecular absorption in depth and Hansen and Travis (1974) and Wendisch and Yang (2012) offer good insight into the theory on scattering by particles.

2.1 Radiative Transfer Equation

In general, radiation is described by the Stokes vector, which allows the treatment of polarized radiation. We neglect polarization effects here, focusing on the first component of the Stokes vector, the radiance. The spectral radiance I_λ is defined as the energy dE propagating in the direction $\hat{\Omega}$ through the area dA, per time dt and per solid angle $d\Omega$, in the wavelength interval from λ to $\lambda + d\lambda$

$$I_\lambda = \frac{dE}{\cos\theta \, dA \, dt \, d\lambda \, d\Omega}, \tag{2.1}$$

where θ is the angle between the surface normal vector of dA and $\hat{\Omega}$. Since we exclusively consider the spectral radiance, the wavelength index is omitted hereinafter. Additionally, the wavenumber $\tilde{\nu}$ replaces the wavelength λ as spectral coordinate. The wavenumber is the inverse of the wavelength $\tilde{\nu} = 1/\lambda$. While propagating through the atmosphere, the radiance changes through absorption, emission and scattering. The change in radiance dI along the path ds through the atmosphere is described by the radiative transfer equation (RTE)

$$\frac{dI}{ds}(\hat{\Omega}) = -(\beta_\mathrm{a} + \beta_\mathrm{s}) I + \beta_\mathrm{a} B(T) + \frac{\beta_\mathrm{s}}{4\pi} \int_{4\pi} p(\hat{\Omega}', \hat{\Omega}) I(\hat{\Omega}') d\hat{\Omega}', \tag{2.2}$$

with the absorption and scattering coefficients β_a and β_s, the Planck law $B(T)$ depending on the atmospheric temperature T, and the scattering phase function $p(\Omega', \Omega)$, all of which are described in the following sections. The first term corresponds to the extinction caused

by absorption (β_a) and out-of-beam scattering (β_s). The second term describes the thermal emission of the atmosphere, which we can safely neglect in the NIR spectral range due to minuscule radiance emitted at atmospheric temperatures. The third term describes the into-beam scattering, which acts as a source term accounting for redirection of radiance from all other directions into the considered direction. Neglecting the thermal emission term for the NIR spectral range, the relevant equation here is

$$\frac{dI}{ds}(\hat{\Omega}) = -(\beta_a + \beta_s) I + \frac{\beta_s}{4\pi} \int_{4\pi} p(\hat{\Omega}', \hat{\Omega}) I(\hat{\Omega}') d\hat{\Omega}' . \tag{2.3}$$

Absorption is specific for each molecule species and highly structured in wavenumber. Quantitatively analyzing this molecular fingerprint is the basis for the retrieval of absorber abundance in the atmosphere. Contrary, scattering has only a broadband wavenumber dependency. However, it changes the direction of the radiation, modifying the effective path photons travel through the atmosphere. Since the absorption signal depends on this path, it indirectly but importantly influences the absorption signal measured by remote sensing instruments.

The following sections discuss the molecular absorption (Section 2.2) and scattering (Section 2.3), as well as the boundary conditions (Section 2.4), i.e. solar radiation and surface reflection in more detail.

2.2 Absorption

Absorption is the process where a molecule absorbs the energy of a photon, exciting an internal energy state while simultaneously reducing the radiance. This section explains the absorption term in the RTE and describes the origin of the absorption coefficient.

Molecules have discrete energy states. These energy levels are the eigenvalues to the eigenstates of the Hamiltonian in the time-independent Schrödinger equation. In molecular absorption, a photon excites a transition between these energy states. The Hamiltonian describes the kinetic energy of electrons and nuclei as well as their interactions. Since the electron mass is orders of magnitudes lower than the nucleus mass, both can be treated separately (Born-Oppenheimer approximation). The electronic state adapts instantly to the potential formed by the nuclei. In the following, we consider only the remaining rotational and vibrational terms of the Hamiltonian and its corresponding energy.

We discuss the rotational state in the rigid rotator approximation, assuming no relative movement between the individual atoms of the molecule. In this approximation, the energy levels can be described by the molecule's principal moments of inertia which follow from its mass distribution. Symmetries in the molecule may restrict the number of independent principal moments of inertia. For a given moment of inertia I, the rotational states are discrete and can be described with the rotational quantum number J by

$$E_J = BJ(J+1), \tag{2.4}$$

with the rotational constant $B = \frac{h^2}{8\pi^2 I}$, where h is the Planck constant.

The vibrational states describe the oscillations of the nucleus inside the molecular potential. In a diatomic molecule, the covalent bond between the two atoms results from their

electrostatic interaction. Attractive and repulsive forces form a potential, which can be approximated by a harmonic potential. This yields the discrete vibrational energy states

$$E_v = h\nu_0 \left(v + \frac{1}{2} \right), \tag{2.5}$$

with the vibrational frequency ν_0 and the vibrational quantum number v. The asymmetric Morse potential provides a more accurate description of the potential for higher vibrational states, making the vibrational energy levels non-equidistant. In polyatomic molecules, we can decompose the vibrational states into normal modes which are associated with their own vibrational frequencies and quantum numbers. The energy levels are then given by the sum of the energies of the normal modes.

We combine the rotational and vibrational states to understand the absorption features observed in NIR spectra. We typically observe transitions with $\Delta v = 1$ and $\Delta J = 0, \pm 1$. The excitation energy ΔE for these transitions with an initial rotational state J_i is thus given by

$$\Delta E = (E_{v=1} + E_{J=J_i+\Delta J}) - (E_{v=0} + E_{J=J_i}). \tag{2.6}$$

Substituting the Equations (2.4) and (2.5), we obtain the energy for the corresponding transitions.

$$\Delta E = h\nu_0 + B\Delta J(\Delta J + (2J_i + 1)) = h\nu_0 + \begin{cases} -2BJ_i & \text{for } \Delta J = -1 \\ 0 & \text{for } \Delta J = 0 \\ 2B(J_i + 1) & \text{for } \Delta J = +1 \end{cases} \tag{2.7}$$

Figure 2.1 schematically shows the transitions between rotational vibrational states and the corresponding frequency of photons for their excitation. Absorption lines occur in three structured bands P, Q and R corresponding to $\Delta J = -1, 0, +1$. In this simple model, all (purely vibrational) transitions of the Q-branch correspond to the same energy. Due to the increasing energy spacing of the rotational states with J, the lines of the P- and R-branch are shifted with increasing initial rotational state towards lower and higher frequency respectively.

Equation (2.7) leads to equally spaced P- and R-branches. However, with increasing J, the nucleus distance increases. In the classical picture, this can be interpreted as a centrifugal correction to the rigid rotator assumption. This leads to the reduction of ΔE for higher J_i, decreasing the spacing of the transition energies in the P- and R-branches with increasing energy.

The previous paragraphs discussed the different energy states and the transitions between them. However, not every transition is allowed by quantum mechanical selection rules. The molecule needs an electric dipole moment for efficient coupling between the photon and the molecular state. This is not the case for some symmetrical molecules. However, the transition still occurs with lower probability in these cases, if a magnetic dipole moment or a higher order multipole moment is present (e.g. for O_2), or an excited vibrational state has an electric dipole moment (e.g. for CO_2). In some cases, conservation of the angular momentum can only be satisfied for $\Delta J \neq 0$, which leads to the absence of the Q-branch.

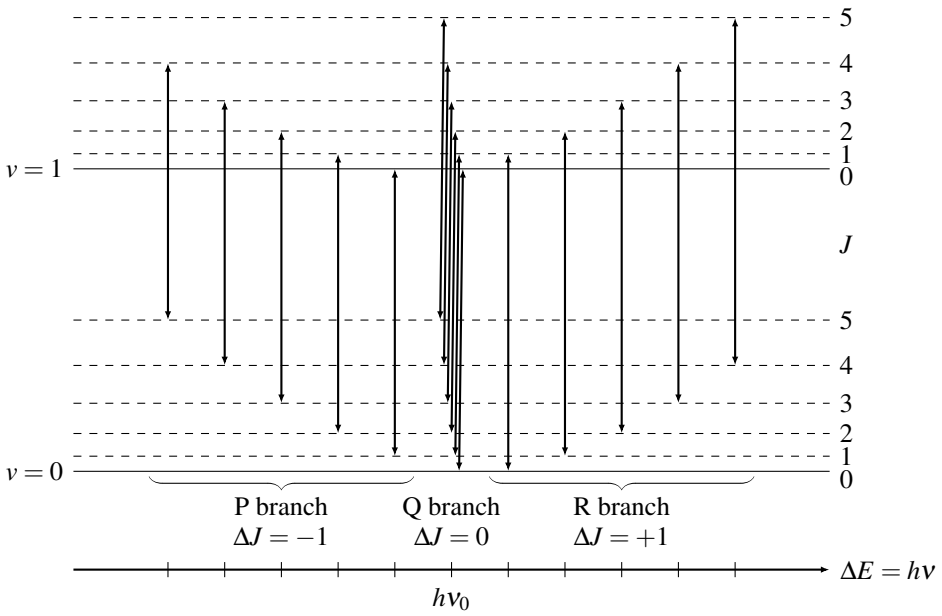

Figure 2.1: Vibrational-rotational transitions for $\Delta v = 1$ and $\Delta J = -1, 0, +1$ resulting in three branches (P, Q, R) of absorption lines, centered around the frequency ν_0 for the purely vibrational transition. Figure inspired by Petty (2006).

To describe absorption in the RTE, we need to relate the transition between molecular states to the absorption coefficient β_a. To this end, we first decompose β_a into its contribution by the column density n_i of the absorbing species i and the absorption cross section $\sigma_{\mathrm{a},i}$, which quantifies the strength of the absorption at a given wavenumber $\tilde{\nu}$. The total absorption coefficient is then the sum of all absorbing species.

$$\beta_\mathrm{a} = \sum_i n_i \sigma_{\mathrm{a},i}(\tilde{\nu}) \tag{2.8}$$

We describe the absorption cross section of a single transition by its line strength S and its lineshape f centered around the transition wavenumber $\tilde{\nu}_0$.

$$\sigma_\mathrm{a}(\tilde{\nu}) = S \cdot f(\tilde{\nu} - \tilde{\nu}_0) \tag{2.9}$$

In a first approximation, the overall absorption cross section for an absorber is the sum of all transitions. The line strength S quantifies the probability for the transition to occur. It depends on the Einstein coefficient of the specific transition and the population of the initial state. Assuming local thermal equilibrium, the population follows a Boltzmann distribution and, therefore, depends on temperature. The lineshape f specifies the distribution around the transition wavenumber. Its integral over all frequencies is normalized to one. Equation (2.7) specifies a discrete energy for a given transition, leading to a discrete photon wavenumber $\tilde{\nu}_0 = hc/\Delta E$, where c is the speed of light. However, the transition is also excited by close-by wavenumbers resulting in an absorption line of finite width. The lineshape is never a δ peak, because the finite lifetime of the excited state translates through the uncer-

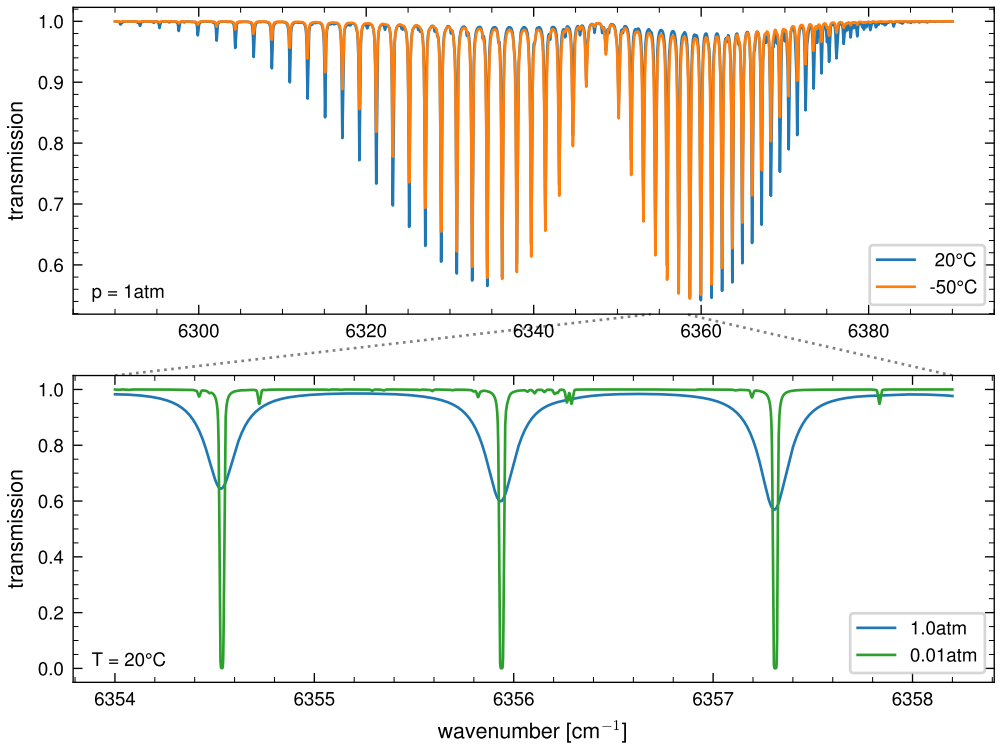

Figure 2.2: Simulated transmission spectrum of CO_2 close to 1.6 µm for two temperatures. The spectrum (top) shows a clear P and R branch structure. The spacing becomes narrower with increasing wavenumber. The line strength varies with temperature according to the ground state population, shifting outwards with increasing temperature. The lower panel shows a zoom on three absorption lines for different pressures. Pressure broadening substantially broadens the lines at surface pressure. The spectrum was simulated with a typical CO_2 column density of 8.0×10^{21} molec/cm^2. This corresponds to 400 ppm CO_2 in an isothermal (T =20 °C) atmosphere with a scale height of 8 km. Absorption cross sections were calculated by the software provided in Kochanov et al. (2016).

tainty principle to the natural linewidth. In the atmosphere however, additional broadening effects dominate. The most prominent broadening effects are (1) the Doppler broadening and (2) the pressure broadening. Doppler broadening is caused by relative motion of the absorber relative to the photon, resulting in a Doppler-shifted absorption frequency. Therefore, the lineshape is determined by the velocity distribution of the molecules (Maxwell-Boltzmann distribution), resulting in a Gaussian line broadening, the half-width of which increases with rising temperature. Pressure broadening results from the reduced lifetime of the excited state due to collisions with other molecules. Like the natural linewidth it has a Lorentzian shape but depends on pressure and temperature. The effective lineshape is the convolution of both contributions. It is referred to as Voigt profile. More sophisticated lineshape models exist, which include other higher-order effects (see e.g. Hartmann et al. (2008)).

After considering the origin of the absorption coefficient, we now turn towards its application in the RTE. When only considering the absorption term, Equation (2.2) simplifies to

$$\frac{dI}{ds} = -\beta_\mathrm{a} I\,, \tag{2.10}$$

which is easily integrated along the direction of propagation. This yields Beer-Lambert's law

$$I(s) = I_0 e^{-\int_0^s \beta_\mathrm{a}(s')ds'} = I_0 e^{-\hat{\tau}_\mathrm{a}}\,, \tag{2.11}$$

where the absorption optical path $\hat{\tau}_\mathrm{a}$ is defined as the integral over the absorption coefficient along the light path. Since we do not consider direction-changing terms, this is just an integral along the geometric light path s.

Figure 2.2 shows a simulated transmission spectrum of CO_2 close to 1.6 µm using Equation (2.11). There, we can observe the characteristics of the absorption cross sections described above. The figure shows the P- and the R-branch of the rotation vibrational spectrum. The temperature dependence of the line strengths is visible. For higher temperatures, the branches shift outward. Additionally, the reduced spacing with increasing wavenumber is apparent. When zooming in on individual lines, we observe the impact of pressure broadening dominating the lineshape at high pressure.

2.3 Scattering

The second important interaction between light and the atmosphere is the scattering by particles. To discuss the scattering terms in the RTE, we need to discuss the scattering coefficient β_s, which specifies the magnitude of the scattering, and the scattering phase function $p(\hat{\Omega}', \hat{\Omega})$, which quantifies the directional redistribution of the scattered light. Here, we only consider spherical particles. Analogue to the absorption coefficient, we decompose the scattering coefficient into the number density n_s of the scattering particles and the scattering cross section. For scattering however, it is useful to separate the scattering cross section again into the geometrical cross section πr^2 and the dimensionless scattering efficiency Q_s

$$\beta_\mathrm{s} = n_\mathrm{s}(r)\, Q_\mathrm{s}(r)\, \pi r^2\,, \tag{2.12}$$

where r is the radius of the spherical particle. The scattering coefficient specifies how much radiance is scattered, while the phase function gives a probability distribution of directions into which the radiance is redistributed in a scattering event. In this context, we express the change in direction in terms of the scattering angle Θ, which is the angle between the direction vectors of the incoming and outgoing light

$$\Theta = \hat{\Omega} \cdot \hat{\Omega}' = \cos\theta \cos\theta' + \sin\theta \sin\theta' \cos(\phi - \phi')\,, \tag{2.13}$$

where we represent the direction in polar coordinate specifying the zenith angle θ and the azimuth angle ϕ. The scattering angle determines the value of the scattering phase function $p(\Theta)$ for a given particle type. The scattering interaction between light and particle

strongly depends on the size of the particle relative to the wavelength λ of the light. This relation is quantified by the size parameter $x = \frac{2\pi r}{\lambda}$. For very small size parameter $x \lesssim 0.002$, λ is much larger then r in which case we can neglect scattering altogether. For very large $x \gtrsim 2000$, scattering can be described by geometric optics. We are interested in the scattering regimes with intermediate size parameter, where we can describe the scattering process by Rayleigh or Mie scattering. Scattering depends on the polarization of the incoming light, and can also polarize the scattered light. To treat polarized scattering fully, the scattering phase matrix (the normalized Müller matrix) has to be applied to the Stokes vector, but we neglect polarization effects here.

For small size parameter $x \lesssim 0.2$, in the Rayleigh regime, the wavelength is large compared to the scattering particle. This is typically the case for the NIR spectral range and air molecules. We can approach this case by looking at a single particle exposed to a plane wave. The incoming radiation partially polarizes the particle. This results in an oscillating dipole moment, driven by the electric field of radiation. This oscillating dipole in turn emits EM radiation, the scattered light. From this approximation, the scattering phase function can be calculated to

$$p_{\text{Rayleigh}}(\Theta) = \frac{3}{4}(1+\cos^2\Theta) \tag{2.14}$$

and the scattering efficiency is proportional to x^4 leading to a r^6/λ^4 proportionality of the $\beta_{\text{s,Rayleigh}}$. The strong antiproportionality to wavelength causes Rayleigh scattering to be comparably weak in the NIR spectral range.

For larger size parameter, we can no longer assume the particle to be in a homogeneous oscillating EM field. Now, the response of the particle to the EM radiation needs to be calculated explicitly. Mie theory treats this case for a given complex refractive index $n = n_\text{r} + i\,n_\text{i}$ of the particle. Here, the imaginary part of the refractive index introduces absorption by the scattering particle, which we will neglect for the discussion here. Figure 2.3 shows the scattering efficiency for different real refractive indices and the scattering phase function for different size parameters. For low x, the scattering efficiency is equal to Rayleigh scattering with its x^4 dependency. In the limit of large x, Q_s tends towards 2 which means that the scattering cross section of a non-absorbing particle is twice its geometric cross section. For intermediate x, we see oscillations in Q_s with superimposed ripples. The ripples quickly average out when particles of different sizes are present. Figure 2.3 shows that the phase function produces preferential forward scattering. With increasing size parameter this peak becomes more pronounced. Additionally, side lobes occur which become more and more structured with higher x, but are of small magnitude compared to the forward peak.

Scattering particles of many sizes are present in the atmosphere. Their composition is described by the particle size distribution $n_\text{s}(r)$ as a function of the particle radius. We calculate the overall scattering coefficient by integrating over all sizes

$$\beta_\text{s} = \int_0^\infty n_\text{s}(r)\, Q_\text{s}(r)\, \pi r^2 dr\,, \tag{2.15}$$

$$p(\Theta) = \int_0^\infty n_\text{s}(r)\, p(\Theta, r) dr\,, \tag{2.16}$$

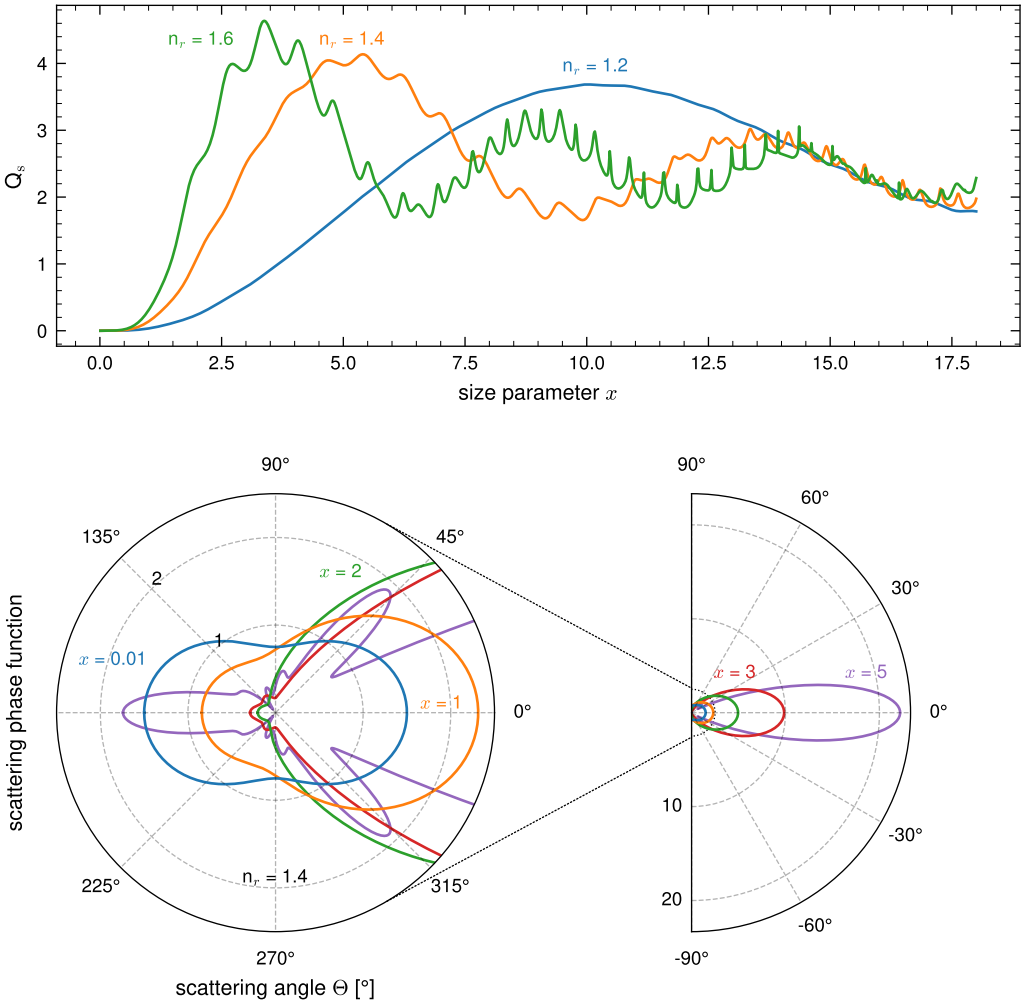

Figure 2.3: Scattering efficiency Q_s (top) and scattering phase function $p(\Theta)$ (bottom). Q_s is shown for different real refractive indexes n_r. $p(\Theta)$ different size parameters. Mie calculations are computed by software provided in Prahl 2023.

where the particle size distributions are commonly parameterized as a power law $n_\mathrm{s}(r) \propto r^{-m}$ or log normal distributions $n_\mathrm{s}(r) \propto \mathcal{N}(\ln(r), \sigma)$. To calculate the scattering properties of aerosols, we thus have to combine Mie calculation with assumptions on the particle size distribution. We typically find a weak wavelength dependence, which can be empirically parameterized with the Ångström exponent α as

$$\beta_\mathrm{s} = \beta_{\mathrm{s},0} \left(\frac{\lambda}{\lambda_0} \right)^{-\alpha}, \tag{2.17}$$

with the reference wavelength λ_0 and the corresponding scattering coefficient $\beta_{s,0}$. Typical values for α are between 1 and 1.5, but need to be measured since particle properties are spatially and temporally highly variable.

2.4 Boundary Condition

To apply the RTE to the scenario relevant to this thesis, we first have to consider the boundary conditions in the Earth's atmosphere. At the upper boundary, the radiance is given by the solar radiation. The lower boundary is given by the Earth's surface. The following paragraphs briefly discuss both boundary conditions.

The Sun In a first approximation, the sun can be described as a black body with an effective temperature of around 5800K. The solar spectrum then follows the Planck law for black body radiation. An important deviation from this poses the fact that the sun has no distinct surface, but rather becomes opaque at a certain depth (the photosphere). We only observe photons emitted in or above this layer. The temperature of this layer, determines the effective black body temperature of the sun. The depth at which the sun becomes opaque depends on the viewing angle at which the suns surface is observed. Observing the solar limb, it becomes opaque at a shallower depth, corresponding to a lower temperature. This leads to a darkening of the limb relative to the center of the sun. In addition to the smooth black body spectrum, the solar spectrum has discrete absorption lines, the Fraunhofer lines. They are caused by absorption in the solar atmosphere above the photosphere. The rotation of the sun introduces a motion relative to the viewing direction. This causes a Doppler shift in the solar spectrum depending on the viewing angle. When considering the solar spectrum integrated over the solid angle, this leads to a broadening of the Fraunhofer lines.

To characterize solar radiation for solving the radiative transport in the Earth's atmosphere, we usually consider the sun as collimated light source with the irradiance F_s from the direction $\hat{\Omega}_s$

$$I_s = F_s \delta(\hat{\Omega} - \hat{\Omega}_s)\,, \tag{2.18}$$

where we specify the direction of solar illumination in terms of the solar zenith and solar azimuth angle $\hat{\Omega}_s = (\theta_s, \phi_s)$. Here $\delta(\hat{\Omega} - \hat{\Omega}_s) = \delta(\cos\theta_s - \cos\theta)\delta(\phi_s - \phi)$, with the Dirac delta function δ. The irradiance is typically inferred from measurements, e.g. from space.

The Earth's Surface In general, the lower boundary condition is given by two contributions. The thermal emission by the Earth's surface and the reflection of radiance coming from above. For the NIR spectral range, we neglect thermal emission so that only the reflection contribution remains. The reflection strongly depends on the properties of the Earth's surface. In general, the surface reflectivity is described by the bidirectional reflectance distribution function (BDRF) $\rho(\hat{\Omega}', \hat{\Omega})$ which redistributes the radiance from above ($\hat{\Omega}'$) into the upward directions ($\hat{\Omega}$). The upward radiance is then given by the integral over all downward radiances. Two simple but common models for the BDRF are specular and Lambertian reflection.

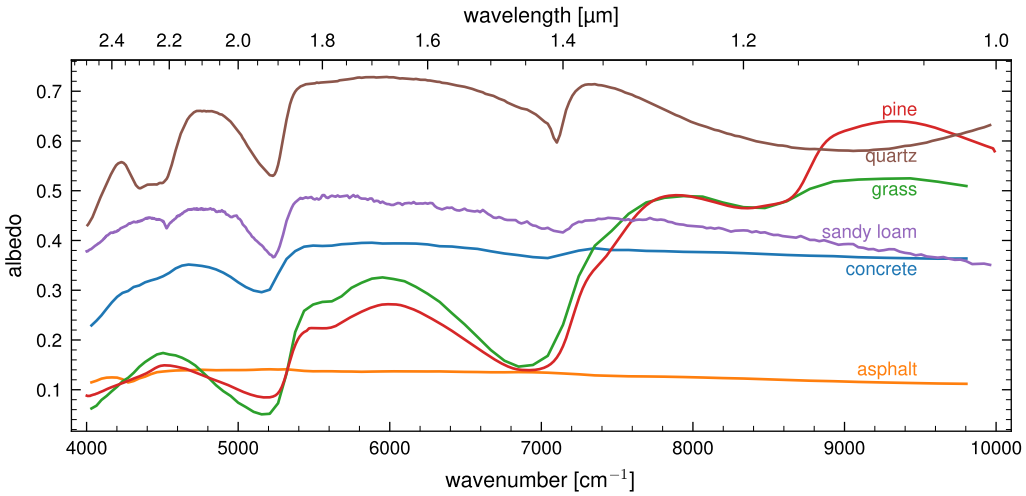

Figure 2.4: Albedo for different exemplary surface materials (data from Baldridge et al. (2009) and Meerdink et al. (2019)).

Specular reflection occurs for dielectric flat surfaces. The radiance is reflected into only one direction, where the angle of incidence equals the angle of reflection. In many cases, this is a reasonably good approximation for observing water bodies, where the angle of reflection is broadened due to waves roughening the water surface.

Lambertian reflection is a simple model for diffuse reflection. It assumes isotropic scattering, removing all angular dependence. This allows us to define a single parameter, the albedo r as the ratio between incident ($\downarrow$) and reflected ($\uparrow$) irradiance. For isotropic reflection, the irradiance is then distributed equally for all directions.

$$I^{\uparrow} = \frac{r}{\pi} F^{\downarrow} \tag{2.19}$$

The albedo depends on the surface material and is wavenumber dependent. However, it typically only varies slowly with wavenumber compared to the molecular absorption features. Figure 2.4 shows the albedo for exemplary surface materials in the NIR spectral range used here. Vegetation shows a strong decrease at higher wavenumber, while construction materials are at rather low but constant levels. However, the specific albedo clearly depends on the specific vegetation species and natural or construction material.

2.5 Solutions to the RTE in the Plane-Parallel Atmosphere

This section discusses a simplified example of how to calculate radiances recorded by a hypothetical observer in the atmosphere using the differential RTE presented in Equation (2.3). In the plane-parallel approximation, we assume that the atmosphere is homogeneous in the horizontal direction and only varies with altitude z. This is motivated by the fact that gradients in atmospheric properties, such as pressure and temperature, are usually much larger in the vertical than in the horizontal direction, especially since we only analyze cloud free

conditions. Additionally, we neglect the curvature of the Earth, since we do not consider solar zenith angles (SZAs) close to 90° and only moderate horizontal distances (tens of kilometers). These assumptions let us reparametrize the RTE from the slant path s into the vertical coordinate $z = \mu s$

$$\mu \frac{dI}{dz}(\hat{\Omega}) = -(\beta_a + \beta_s) I + \frac{\beta_s}{4\pi} \int_{4\pi} p(\hat{\Omega}', \hat{\Omega}) I(\hat{\Omega}') d\hat{\Omega}', \tag{2.20}$$

where $\mu = \cos\theta$ is the cosine of the zenith angle θ[1]. To simplify the calculations, it is useful to introduce the optical depth τ as vertical coordinate

$$\tau(z) = \int_z^\infty \beta_e(z') dz', \tag{2.21}$$

for which we combine the absorption and scattering coefficients into the extinction coefficient $\beta_e = \beta_a + \beta_s$. With this definition, the optical depth is zero at the top of the atmosphere ($\tau_\infty = 0$) and increases with decreasing altitude, reaching the maximum value τ_g at the surface. Additionally, we specify the relative importance of absorption and scattering by the single scattering albedo $\tilde{\omega} = \beta_s / \beta_e$, ranging from zero (no scattering) to one (purely scattering). With these definitions Equation (2.20) simplifies to

$$\mu \frac{dI}{d\tau} = -I + \frac{\tilde{\omega}}{4\pi} \int_{4\pi} p(\hat{\Omega}', \hat{\Omega}) I(\hat{\Omega}') d\hat{\Omega}'. \tag{2.22}$$

The upper boundary condition is the radiance coming from the sun (Equation (2.18)) propagating at SZA θ_s, corresponding to $\mu_s = \cos\theta_s$. The lower boundary condition is the reflection at the Earth's surface, for which we assume a Lambertian reflection (Equation (2.19)). For illustration purposes, we can solve Equation (2.22) for the radiance $I(\tau_{obs})$ recorded by a observer at τ_{obs} inside the atmosphere $0 < \tau_{obs} < \tau_g$, for the no scattering and single scattering cases. Neglecting scattering is a good approximation for observing direct solar radiation in a moderatly optically thin atmosphere, i.e. when no clouds are present. For very low scattering optical depth, the no-scattering approximation may also be reasonable for observing ground-reflected direct sunlight. The single scattering approximation is the first order approximation for the treatment of diffuse sunlight. It is a good approximation for either low optical depth and/or a low single scattering albedo, since in this case the photon is more likely absorbed than scattered a second time. We consider the upward looking ($\mu > 0$) and downward looking ($\mu < 0$) cases separateley. Figure 2.5 illustrates the three viewing geometries we consider here.

No Scattering: Direct Sun In the non-scattering case we neglect the second term of Equation (2.22), which lets us easily integrate from τ_∞ to τ_{obs} to obtain the observed radiance.

$$I(\tau_{obs}) = F_s \delta(\hat{\Omega} - \hat{\Omega}_s) e^{-\frac{\tau_{obs}}{\mu}} \tag{2.23}$$

[1] Contrary to some textbooks, the zenith angle is calculated between the zenith and viewing direction (instead of the propagating direction). This has the advantage that no distinction between upward and downward viewing direction is needed and at the same time the SZA is between 0° and 90°.

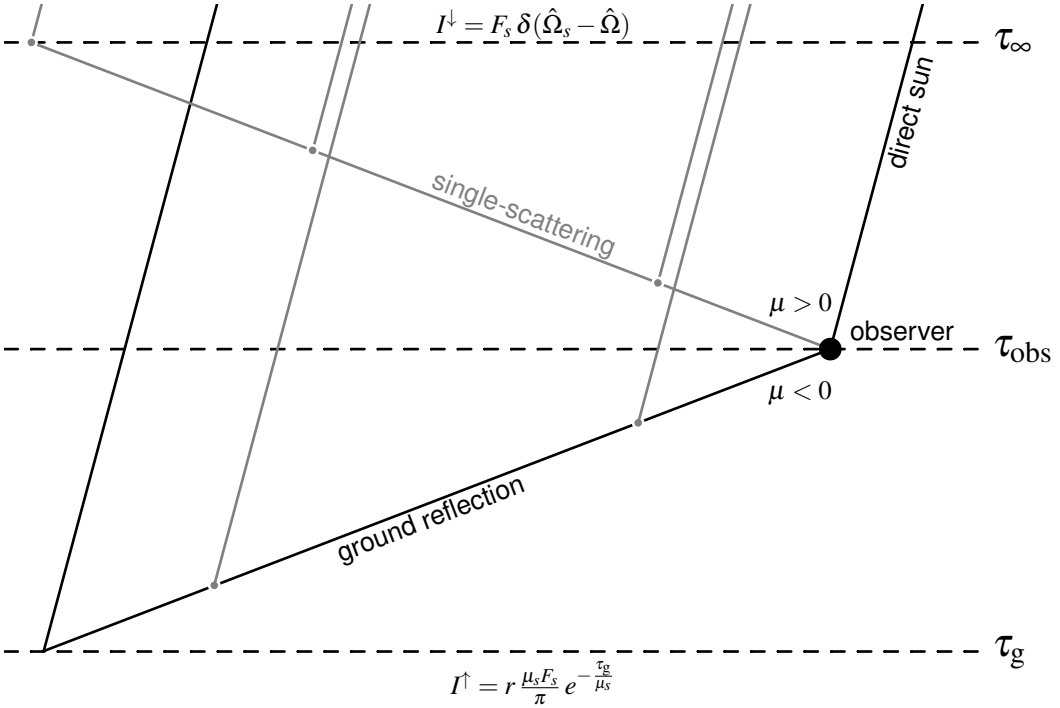

Figure 2.5: Schematic of light path in the no scattering and single scattering approximation. Four different light paths are possible. When upward looking ($\mu > 0$) direct sunlight or atmospheric scattered light can be observed. When downward looking ($\mu < 0$) ground-scattered light or a combination of ground and atmospheric scattered light can reach the observer.

We only observe any radiance if we look directly into the sun $\hat{\Omega} = \hat{\Omega}_{\text{s}}$, i.e., the zenith angle matches the SZA $\mu = \mu_{\text{s}}$. In this case, the radiance is attenuated according to Beer-Lambert's law.

No Scattering: Ground Reflection In the no-scattering downward looking case, we observe ground reflected radiance. The radiance is attenuated from the top of the atmosphere to the ground according to Beer-Lambert's law and then reduced according to the Lambertian reflection at the ground. We calculate the radiance reflected off the ground from Equations (2.19) and (2.23)

$$I^{\uparrow} = r\,\frac{\mu_{\text{s}} F_{\text{s}}}{\pi}\,e^{-\frac{\tau_{\text{g}}}{\mu_{\text{s}}}}\,, \tag{2.24}$$

where the factor μ_{s} results from incident angle of the downward radiance. The radiance is then further attenuated according to the optical depth between ground and observer.

$$I(\tau_{\text{obs}}) = r\frac{\mu_{\text{s}} F_{\text{s}}}{\pi} e^{-\left(\frac{\tau_{\text{g}}}{\mu_{\text{s}}} + \frac{\tau_{\text{obs}} - \tau_{\text{g}}}{\mu}\right)} \tag{2.25}$$

Note that the albedo r is a simple scaling factor for the reflected radiance in this case.

Single Scattering When including scattering in the RTE, radiance from other directions gets scattered into the observing direction $\hat{\Omega}$. For illustration purposes, we solve Equation (2.22) for the single scattering case. Here, only direct solar radiance contributes to the scattering integral in the second term. Using this, we can rearrange Equation (2.22) to

$$\frac{d}{d\tau}\left[Ie^{-\frac{\tau}{\mu}}\right] = \frac{F_s\tilde{\omega}}{4\pi\mu}p(\Theta)e^{\tau\left(\frac{1}{\mu_s}-\frac{1}{\mu}\right)}. \tag{2.26}$$

The scattering angle Θ follows directly from the solar and viewing directions (Equation (2.13)). In a first step, we consider the radiative transfer from any position inside the atmosphere $0 < \tau_0 < \tau_g$ to the observer. Assuming $\tilde{\omega}$ and $p(\Theta)$ to be independent of altitude, we can integrate from the initial optical thickness τ_0 to the observer optical thickness. The full calculation is written down in Appendix A.1.

$$I(\tau_{obs}) = \underbrace{I(\tau_0)e^{-\frac{\tau_{obs}-\tau_0}{\mu}}}_{I_{dir}} + \underbrace{\frac{F_s\tilde{\omega}}{4\pi\mu}p(\Theta)\frac{1}{\frac{1}{\mu}-\frac{1}{\mu_s}}\left(e^{-\frac{\tau_{obs}}{\mu_s}} - e^{-\frac{\tau_0}{\mu_s}-\frac{\tau_0-\tau_{obs}}{\mu}}\right)}_{I_{sca}} \tag{2.27}$$

We can directly identify the first term with the direct radiance contribution. The second term quantifies the solar radiance scattered into the observing viewing direction. In the following we briefly discuss the implications for upward ($\mu > 0$) and downward ($\mu < 0$) viewing directions.

Single Scattering: Diffuse Radiation For upward looking direction the integration boundary is the top of the atmosphere $\tau_0 = \tau_\infty = 0$. We get a direct contribution when looking directly into the sun, otherwise we observe only the scattered diffuse radiance.

$$I(\tau_{obs}) = F_s\delta(\hat{\Omega}_s - \hat{\Omega})e^{-\frac{\tau_{obs}}{\mu}} + \frac{F_s\tilde{\omega}}{4\pi\mu}p(\Theta)\frac{1}{\frac{1}{\mu}-\frac{1}{\mu_s}}\left(e^{-\frac{\tau_{obs}}{\mu_s}} - e^{\frac{\tau_{obs}}{\mu}}\right) \tag{2.28}$$

Single Scattering: Ground Reflection For the downward looking direction, we use the ground as the integration limit $\tau_0 = \tau_g$. We consider only non-scattered radiance for the ground reflection, which poses the lower boundary condition. We insert Equation (2.24) as lower boundary $I(\tau_0)$ into Equation (2.27) to obtain

$$I(\tau_{obs}) = r\frac{\mu_s F_s}{\pi}e^{-\frac{\tau_g}{\mu_s}}e^{-\frac{\tau_{obs}-\tau_g}{\mu}} + \frac{F_s\tilde{\omega}}{4\pi\mu}p(\Theta)\frac{1}{\left(\frac{1}{\mu}-\frac{1}{\mu_s}\right)}\left(e^{-\frac{\tau_{obs}}{\mu_s}} - e^{-\frac{\tau_g}{\mu_s}-\frac{\tau_{obs}-\tau_g}{\mu}}\right). \tag{2.29}$$

We identify the first term with Equation (2.25) contributing as pseudo-direct term. The second term quantifies scattering of direct sunlight on the path between ground and observer into the direction of the observer. We can see, that the ratio between surface albedo and $\tilde{\omega}\,p(\Theta)$ determines the relative contributions to the overall radiance.

To illustrate the interpretation of the formula, we assume the optical paths to be small ($\tau_g/\mu_s \ll 1$ and $(\tau_{obs}-\tau_g)/\mu \ll 1$). In this case, we can approximate $e^x = 1+x$. Note that this linearization is only useful for a conceptual understanding, since this approximation

only holds for negligible absorption. For the scattered radiance term (see Appendix A.2), we obtain

$$I_{\mathrm{sca}}(\tau_{\mathrm{obs}}) = \frac{F_{\mathrm{s}}}{4\pi}\,\tilde{\omega}\,p(\Theta)\,\frac{\tau_{\mathrm{obs}}-\tau_{\mathrm{g}}}{\mu}\,. \tag{2.30}$$

We find that the amount of scattered light depends on three factors, the single scattering albedo, the scattering phase function (and with it the scattering angle), as well as the optical path between ground and observer. Increasing the value of any of the three, leads to a stronger contribution of scattered light compared to pseudo-direct sunlight reflected off the ground. Since the reflected light linearly depends on the albedo, low albedo also increases the importance of scattered light. This is important, since the scattered sunlight has a shorter light path and therefore reduced molecular absorption features. This can be seen if we linearize Equation (2.29) fully with direct and scattered contributions. The linearized direct contribution is given by

$$I_{\mathrm{dir}}(\tau_{\mathrm{obs}}) = r\frac{\mu_{\mathrm{s}}F_{\mathrm{s}}}{\pi}\left(1-\frac{\tau_{\mathrm{g}}}{\mu_{\mathrm{s}}}-\frac{\tau_{\mathrm{obs}}-\tau_{\mathrm{g}}}{\mu}\right). \tag{2.31}$$

Combining this with the scattered radiance contribution from Equation (2.30), we find

$$I(\tau_{\mathrm{obs}}) = r\frac{\mu_{\mathrm{s}}F_{\mathrm{s}}}{\pi}\left(1-\frac{\tau_{\mathrm{g}}}{\mu_{\mathrm{s}}}-\left(1-\frac{\tilde{\omega}\,p(\Theta)}{4\mu_{\mathrm{s}}r}\right)\frac{\tau_{\mathrm{obs}}-\tau_{\mathrm{g}}}{\mu}\right), \tag{2.32}$$

where the scattered radiance contribution introduces the term $1-\frac{\tilde{\omega}\,p(\Theta)}{4\mu_{\mathrm{s}}r}$. Since this term is smaller than one, it reduces the attenuation between ground and observer compared to Equation (2.31), resulting in shallower absorption features.

3 Instrumentation

This chapter presents the EM27/SCA instrument and the characterization work conducted previous to the field measurements presented in Chapter 5. Section 3.1 starts with an introduction to the theory behind Fourier-transform spectrometers (FTSs). Subsequently, Section 3.2 describes the EM27/SCA instrument, layout and its components. Section 3.3 describes the computation of the spectra necessary for spectral analysis from the interferograms recorded by the EM27/SCA. Section 3.4 introduces the instrument line shape, its recording and the related uncertainty. The following sections present the laboratory characterization of the EM27/SCA's detector linearity (Section 3.5), radiometric calibration (Section 3.6), polarization characteristics (Section 3.7) and field of view (Section 3.8). Section 3.9 concludes with a discussion of the effects of scene heterogeneity on the EM27/SCA measurements. The signal to noise and precision of retrieved column density is assessed later in the Chapter 5 based on field measurements.

Previous work has significantly contributed building and characterizing the EM27/SCA instrument (Hemmer 2019; Kostinek 2015). The instrument, its performance and the comparison to the CLARS-FTS measurements were in part published in Löw et al. (2023). The work presented in this chapter significantly extends previous characterization and calibration work.

3.1 Fourier Transform Spectrometer

This section provides an introduction to the measurement principle used in this work, the Fourier transform spectrometry. The measurement concept is described and how the spectrum is inferred from the measurement data. Subsequently, the main characteristic of an ideal real FTS, the instrument lineshape (ILS), is discussed. An empirical ILS model and the introduction of numerical apodization conclude the description. An extensive background on Fourier transform spectrometry is described in Griffiths and de Haseth (2007) and I follow their notation where possible.

3.1.1 Measurement Principle

Contrary to dispersive measurement techniques, e.g. grating spectrometers, an FTS does not spatially separate different wavelengths. Instead, an FTS splits the light, applies a relative phase through a variable optical path difference (OPD) and subsequently records the interference signal in dependence of the OPD δ.

Figure 3.1 shows a generic schematic of an FTS. The light is split into two equal beams at a beam splitter. Each beam is reflected by a mirror and they recombine again at the beam splitter before being focused on the detector. The OPD δ is introduced by moving one of the

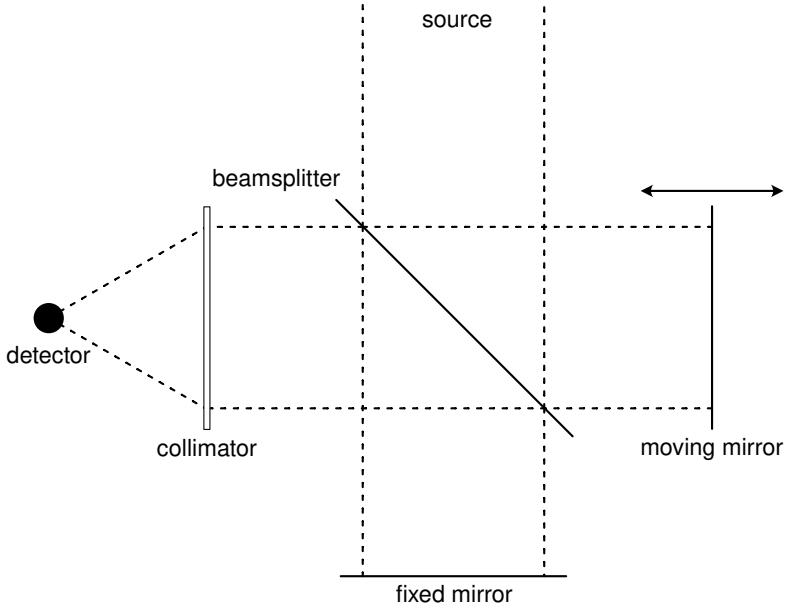

Figure 3.1: Schematic of a Fourier transform spectrometer. Light from a source is divided by a beamsplitter and reflected by a moving and a fixed mirror. This introduces a relative phase shift depending on the position of the moving mirror. The beams are recombined and focused onto a detector, which records the interference pattern.

mirrors back and forth. Assuming a monochromatic light source with wavenumber $\tilde{\nu}_0$ and intensity $I(\tilde{\nu}_0)$, the relative phase between both beams is $2\pi\tilde{\nu}_0\delta$. The interference pattern $I(\delta)$ at the detector in dependence on the OPD is given by

$$I(\delta) = \frac{1}{2} I(\tilde{\nu}_0)(1+\cos(2\pi\tilde{\nu}_0\delta)). \tag{3.1}$$

The interference signal consists of two terms, one independent and one dependent on the OPD. The constant term is commonly referred to as DC component, the varying term as AC component. While the DC component carries information on the overall intensity, the AC component carries the full spectral information. Because of this, we omit the DC term for the following consideration. The signal S recorded by the detector in dependence on the OPD depends on additional factors such as the optical throughput, efficiency of the beamsplitter, detector sensitivity and amplifier characteristics. We multiply them to the source intensity to obtain the spectral intensity $B(\tilde{\nu})$ which shares the units of S.

$$S(\delta) = B(\tilde{\nu}_0)\cos(2\pi\tilde{\nu}_0\delta) \tag{3.2}$$

$S(\delta)$ is referred to as interferogram (IFG). Since the factor between $I(\tilde{\nu})$ and $B(\tilde{\nu})$ is constant for all measurements with the same instrument and varies only slowly with wavenumber, it can be determined once through an absolute calibration of the instrument. It is otherwise not relevant for the spectral analysis here.

Until now, we only considered a monochromatic light source. For a thermal source, we integrate over all wavenumbers.

$$S(\delta) = \int_{-\infty}^{\infty} B(\tilde{\nu}) \cos(2\pi\tilde{\nu}\delta)\, d\tilde{\nu} \tag{3.3}$$

The interferogram $S(\delta)$ is thus given by the cosine Fourier transform of the spectral intensity $B(\tilde{\nu})$. The spectrum can thus be retrieved by applying the inverse Fourier transform to the interferogram.

$$B(\tilde{\nu}) = \int_{-\infty}^{\infty} S(\delta) \cos(2\pi\tilde{\nu}\delta)\, d\delta \tag{3.4}$$

In Equation (3.3), we assumed that the phase shift between both beams is equal for all wavenumbers. However, phase errors arise from the detector electronics, i.e. through electronic filters, or optical elements, i.e. dispersion in the beamsplitter, or through sampling errors. This adds an potentially wavenumber dependent phase term $\phi_{\tilde{\nu}}$, called phase error, to the interferogram.

$$S(\delta) = \int_{-\infty}^{\infty} B(\tilde{\nu}) \cos(2\pi\tilde{\nu}\delta - \phi_{\tilde{\nu}})\, d\tilde{\nu} \tag{3.5}$$

This additional phase term causes asymmetric contributions in the interferogram, as can be seen via the trigonometric identity $\cos(\alpha-\beta) = \cos\alpha\cos\beta + \sin\alpha\sin\beta$. Therefore, the interferogram is no longer the cosine Fourier transform of the spectrum, but comprises sine Fourier transform components. We define a complex spectrum $B'(\tilde{\nu})$ from $B(\tilde{\nu})$ and the phase error $\phi_{\tilde{\nu}}$.

$$B'(\tilde{\nu}) = B(\tilde{\nu}) e^{i\phi_{\tilde{\nu}}} = B(\tilde{\nu})\cos\phi_{\tilde{\nu}} + iB(\tilde{\nu})\sin\phi_{\tilde{\nu}} \tag{3.6}$$

With this, Equation (3.5) can be expressed by the complex Fourier transform

$$S(\delta) = \int_{-\infty}^{\infty} B'(\tilde{\nu}) \exp(-2\pi i\tilde{\nu}\delta)\, d\tilde{\nu}\,, \tag{3.7}$$

where the $B(\tilde{\nu})$ is the magnitude of $B'(\tilde{\nu})$. We reverse this to

$$B'(\tilde{\nu}) = \int_{-\infty}^{\infty} S(\delta) \exp(2\pi i\tilde{\nu}\delta)\, d\delta\,, \tag{3.8}$$

which implies that we can obtain $B(\tilde{\nu})$ from the interferogram $S(\delta)$ by applying the inverse complex Fourier transform. This is the foundation of Fourier transform spectroscopy. We measure the interference pattern in the OPD domain and infer the spectrum through a Fourier transformation.

3.1.2 Instrument Lineshape

Any real instrument can not measure the true source spectrum, since even an ideal instrument can not fulfill all assumptions we made in the previous section. Firstly, it can not measure the interferogram to infinite OPD. The integral in Equation (3.8) must therefore

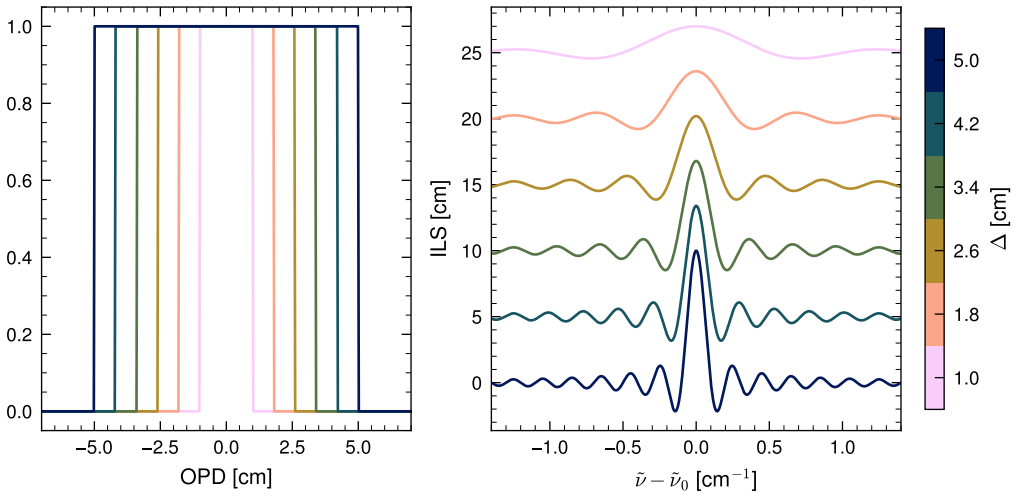

Figure 3.2: Effect of finite OPD on the spectrum measured by an ideal FTS. The left panel shows the rect function limiting the OPD. The right panel shows the resulting sinc function ILS. The ILS have been offset by 5 cm each for better visibility of the side lobes.

be finite, which leads to finite spectral resolution. Secondly, observed light must originate from a finite solid angle to obtain any signal. This also limits the achievable resolution.

The instrumental impact on the true spectrum is quantified by the instrument lineshape (ILS). The ILS describes the instrument response to a monochromatic light source. For any real measurement, the measured spectrum $B(\tilde{\nu})$ is the convolution $(*)$ of the true spectrum $\hat{B}(\tilde{\nu})$ and the ILS.

$$B(\tilde{\nu}) = \hat{B}(\tilde{\nu}) * \mathrm{ILS}(\tilde{\nu}) \tag{3.9}$$

In the following, I first discuss the main contributions to the ILS of an ideal instrument, the finite resolution and the self apodization. Since real instruments have additional shortcomings impacting their ILS, an empirical model is introduced which can be used to retrieve the ILS experimentally from controlled laboratory measurements.

Finite Resolution

The most important deviation from the theoretical instrument, is the finite maximum OPD Δ, limiting the measured interferogram $S(\delta)$ to the range $\delta \in [-\Delta, \Delta]$. This has the profound effect that the Fourier transformation integral no longer extends to infinite OPD. We can describe this by multiplying a rectangular window function $\mathrm{rect}(\delta/2\Delta)$ to the interferogram $S(\delta)$. The spectrum is thus given by

$$B(\tilde{\nu}) = \int_{-\Delta}^{\Delta} S(\delta) \exp(2\pi i \tilde{\nu} \delta)\, d\delta = \mathscr{F}\left(S(\delta) \cdot \mathrm{rect}\left(\frac{\delta}{2\Delta} \right) \right), \tag{3.10}$$

with

$$\mathrm{rect}(x) = \begin{cases} 1 & \text{if } -\frac{1}{2} \leq x \leq \frac{1}{2} \\ 0 & \text{else} \end{cases}. \tag{3.11}$$

We use the fact that the Fourier transform of the product of two functions is equal to the convolution of the Fourier transforms of each function. With this Equation (3.10) can be rewritten as

$$B(\tilde{\nu}) = \mathscr{F}(S(\delta)) * \mathscr{F}\left(\mathrm{rect}\left(\frac{\delta}{2\Delta}\right)\right). \tag{3.12}$$

We identify the first term as the true spectrum and conclude that the ILS is given by the second term, which evaluates to the sinc function.

$$\mathrm{sinc}(x) = \frac{\sin(x)}{x} \tag{3.13}$$

$$\mathrm{ILS} = \mathscr{F}\left(\mathrm{rect}\left(\frac{\delta}{2\Delta}\right)\right) = 2\Delta \cdot \mathrm{sinc}(2\pi\Delta\tilde{\nu}) \tag{3.14}$$

The ILS of an ideal instrument is therefore a sinc function. Figure 3.2 shows the ILS for different OPD. We see that the ILS is more narrow for higher maximum OPD and more smoothed out for lower values. This allows us to define the nominal resolution of the FTS to $1/\Delta$, the distance between the two first zero crossings. Two spectral lines are fully resolved if they are separated by at least this distance. Note that other definitions of the nominal resolution exists.

Self Apodization

The second limitation, even for an ideal instrument, is the finite size of the instrument FOV. Observing perfectly collimated light would mean observing a solid angle of zero. Consequently, no signal would be recorded by the detector. Observing a finite solid angle, implies light reaches the detector, which propagates inclined with respect to the interferometers optical axis. The maximum inclination angle determines the semi FOV α. For inclined beams, the optical path difference is decreased by a factor of the cosine of the inclination angle. Therefore, it is up to $\cos\alpha$ times lower for the extreme beams. Light with wavenumber $\tilde{\nu}_0$ propagating aligned with the optical axis and light with wavenumber $\tilde{\nu}_0 \cos\alpha$ propagating under the angle α undergo the same phase shift in the interferometer and can therefore not be distinguished. This effect is named *self apodization* and leads to a broadening of the ILS. Considering the inclination for the OPD in Equation (3.3), we have to integrate over all angles up to α as shown by (Schmitt 2024). Equivalently, the self apodization can be described by convolving the spectrum with a rect function spanning from $\tilde{\nu}_0 \cos\alpha$ to $\tilde{\nu}_0$ (Griffiths and de Haseth 2007; Hase 2000). Following the definition of the rect function in Equation (3.11) and applying the small angle approximation $\cos\alpha = 1 - \frac{\alpha^2}{2}$, the self apodization contribution to the ILS is given by

$$\frac{2}{\tilde{\nu}_0\alpha^2}\,\mathrm{rect}\left(\frac{\tilde{\nu} - \tilde{\nu}_0}{\frac{\tilde{\nu}_0\alpha^2}{2}} + \frac{1}{2}\right). \tag{3.15}$$

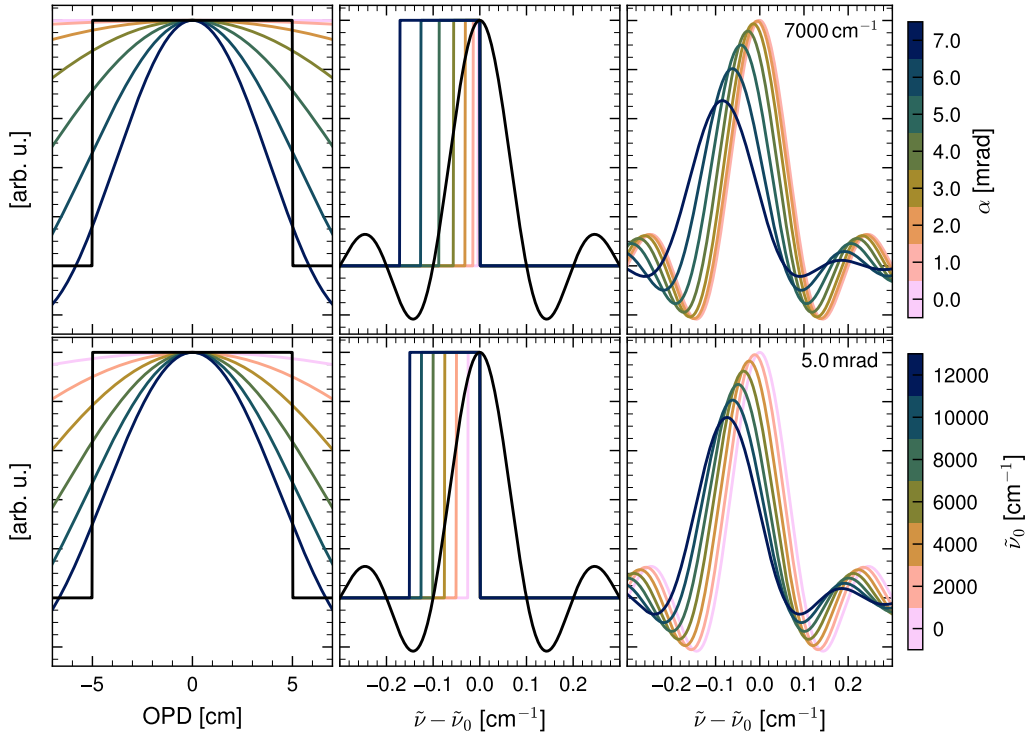

Figure 3.3: Effect of self apodization for an ideal FTS with maximum OPD of 5 cm and variable field of view (FOV). The finite OPD and FOV contributions are shown in OPD space (first column) and wavenumber space (second column). The third column shows the resulting ILS considering both contributions simultaneously. The upper panel shows the ILS broadening with increasing FOV at 7000 cm^{-1}, the lower panel shows the wavenumber dependency at semi-angle FOV of 5 mrad. For clarity, the magnitude of the finite FOV contribution is scaled to match the finite OPD contribution in the first and second column.

The theoretical ILS for an ideal FTS considering finite OPD and FOV is therefore given as the convolution of the sinc and rect contributions. The convolution of both in wavenumber space can be calculated as a multiplication in OPD space. The Fourier transformation of the rect contribution results in a sinc function in OPD space.

$$\mathrm{ILS} = 2\Delta\,\mathrm{sinc}(2\pi\Delta\tilde{\nu}) * \frac{2}{\tilde{\nu}_0\alpha^2}\,\mathrm{rect}\left(\frac{\tilde{\nu}-\tilde{\nu}_0}{\frac{\tilde{\nu}_0\alpha^2}{2}} + \frac{1}{2}\right) \tag{3.16}$$

$$\mathrm{ILS} = \mathscr{F}\left(\mathrm{rect}\left(\frac{\delta}{2\Delta}\right)\cdot\mathrm{sinc}\left(\pi\frac{\tilde{\nu}_0\alpha^2}{2}\delta\right)\right) \tag{3.17}$$

This shows that the finite FOV in fact acts as an inherent apodization (see Section 3.1.3). Figure 3.3 shows both contributions in OPD and wavenumber space, as well as resulting ILS for a range of different wavenumbers and FOVs. Since the FOV contribution is not

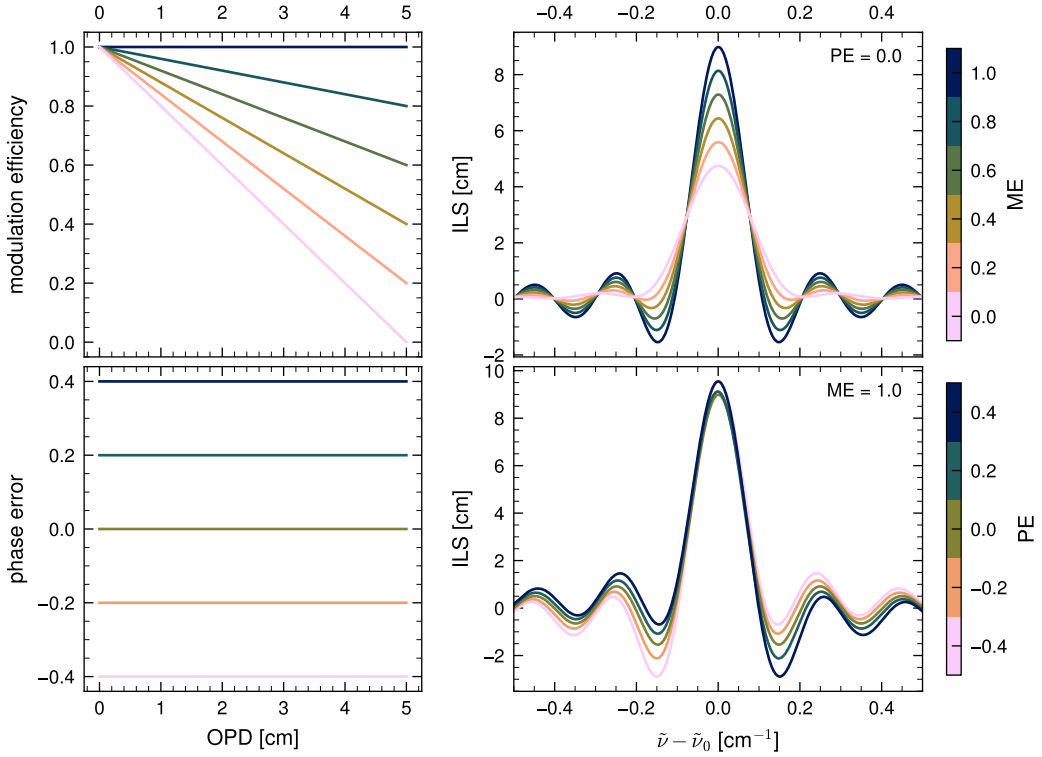

Figure 3.4: ILS of an FTS with maximum OPD of 1.8 cm and a FOV of 9 mrad based on modulation efficiency and phase error. Top row shows modulation efficiency with OPD (right) and its effect on the ILS. The bottom row shows the same for the phase error.

centered around zero, but around $\frac{\tilde{\nu}_0 \alpha^2}{4}$, the theoretical ILS is also shifted. This leads to a spectral shift of absorption lines towards lower wavenumbers in FTS spectra.

Increasing the instrument FOV increases the amount of light which reaches the detector, besides reducing the spectral resolution of the FTS. Since the ILS is a convolution of finite OPD and FOV contribution, at some point the ILS is dominated by the maximum OPD and the effect on the ILS through changes in FOV becomes negligible. Increasing the FOV as far as possible without significantly deteriorating the resolution is therefore a possibility to increase the signal.

ILS Model

So far we considered the limitations of an ideal FTS. In many cases, these considerations provide a good representation for the ILS of real FTS. Depending on context however, it may be required to consider additional instrumental imperfections by experimentally determining an empirical representation of the ILS. To this end a parameterized model for the ILS is required. Such a model was developed by Hase et al. (1999), representing the main effects, broadening and asymmetry, of an imperfect ILS. It introduces an OPD dependent

modulation efficiency (ME) and phase error (PE), which then are parameterized and varied to fit the ILS model to laboratory measurements.

Modulation efficiency describes the attenuation of the interferogram with increasing OPD. For a monochromatic interferogram, the modulation efficiency is the envelope of the cosine interferogram. In this sense, a loss in modulation efficiency acts as an apodization, broadening the ILS. When determining the ME from laboratory measurements, the ME is retrieved with finite OPD resolution. In the most simple model, we assume the ME to vary linearly with OPD. The modulation efficiency is normalized such that modulation efficiency is always one at zero OPD. This means that we can describe ME with a single parameter in this case, the modulation efficiency at maximum OPD. This also implies that the ME in principle can be greater than one. However, this is only rarely the case in real instruments. Note that the modulation efficiency is determined after considering the instruments self apodization.

While the ME parameterizes the broadening of the ILS, the PE parameterizes the degree of asymmetry. While considering the phase shift for an ideal instrument before, we only assumed a wavenumber dependent phase shift without any OPD dependence. The PE parameterizes the OPD dependent phase shift with respect to the ideal interferogram. Since a constant phase shift is already considered for an ideal instrument, the PE parameterizes the linear phase shift with OPD. As for the ME, in the simplest model a single linear phase shift parameter is retrieved across all OPD.

Figure 3.4 shows the effect of ME and PE on the ILS for the simplest model. The reduction in ME causes a broader ILS and the PE increases the asymmetry. Hase et al. (1999) introduces an extended model where ME and PE are defined on 20 OPD intervals. This allows more flexibility in the shapes the model can represent.

3.1.3 Numerical Apodization

For cases where the self apodization is not very strong, which is a typical case, the ILS exhibits strong sidelobes, due to the slow $1/x$ decay of the sinc maxima. This causes an influence of spectrally distant absorption features in the retrieval window. To reduce this effect, an additional artificial apodization is introduced by multiplying the interferogram with an apodization function. The apodization function suppresses contributions at large OPD to the interferogram. This results in reduced sidelobes, but also in a reduction of the resolution. The choice of apodization function allows a trade-off between those two quantities. Norton and Beer (1977) published a set of popular apodization functions, from which I use the Norton-Beer medium (NBM) apodization within this thesis. Figure 3.5 shows this and its effect on the ILS: The ringing is greatly suppressed at the expense of increased ILS width.

3.2 EM27/SCA

The EM27/SCA is an FTS designed to record near infrared absorption spectra of surface reflected sunlight. It collects ground-scattered sunlight with an alt-azimuthal pointing system and records one minute interferograms with a maximum OPD of 1.8 cm, corresponding to a spectral resolution of $0.56\,\mathrm{cm}^{-1}$. Figure 3.6 shows the EM27/SCA during measurements of the northern LA basin.

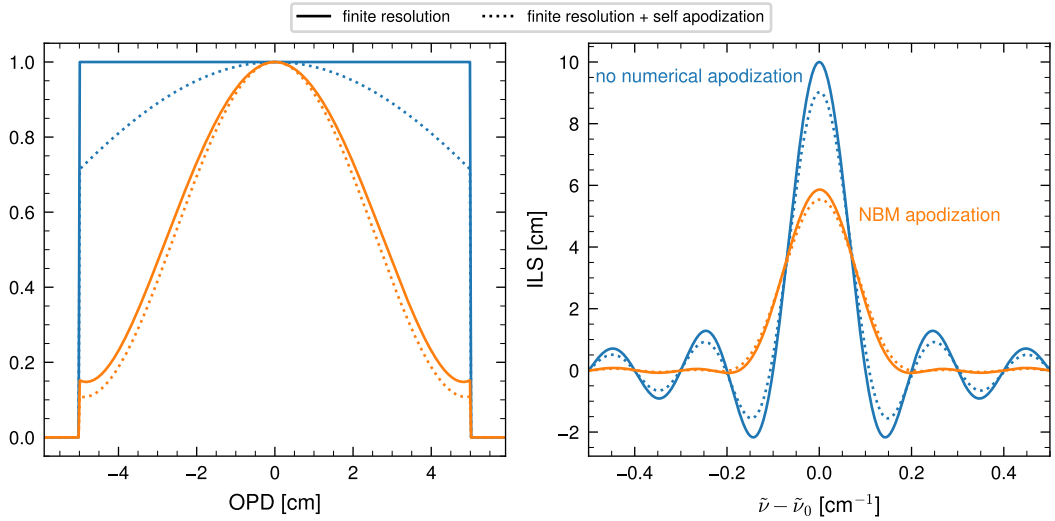

Figure 3.5: Effect of numerical apodization shown for maximum OPD of 5 cm and FOV of 10 mrad at 7000 cm^{-1}. The right panels displays the theoretical ILS resulting from finite resolution (solid) and finite resolution plus self apodization (dotted) once without numerical apodization (blue) and with a NBM apodization (orange).The left panel shows its corresponding Fourier transform in OPD space. The orange solid line in the left panel visualizes the NBM apodization function.

The EM27/SCA is a modification of the EM27/SUN FTS, which was designed for recording absorption spectra of direct sunlight. The EM27/SUN was developed by Gisi et al. (2012) in cooperation with Bruker Optics. Hase et al. (2016) later added a second detector increasing the wavenumber range to include CO absorption features. It is now commercially available from Bruker Optics and routinely used in various field campaigns (Butz et al. 2017; Hase et al. 2015; Klappenbach et al. 2015; Knapp et al. 2021; Luther et al. 2019; Vogel et al. 2019) and the COllaborative Carbon Column Observing Network (COCCON) (Alberti et al. 2022; Frey et al. 2019).

The radiance of surface reflected sunlight is several magnitudes lower compared to direct sunlight. Assuming a Lambertian surface reflection, the radiance of solar I_{sun} and reflected light I_{sca} are given by

$$I_{sca} = \frac{r}{\pi} \Omega_s \cos(\theta_s) \cdot I_{sun}\,, \tag{3.18}$$

with the surface albedo r, the SZA θ_s and the solid angle spanned by the sun Ω_s. Therefore, the surface scattered radiance is a factor $10^5 \sim 10^6$ lower than direct solar radiance, depending on surface albedo r and SZA θ_s. Kostinek (2015) made modifications to adapt the EM27/SUN for the significantly lower radiances during measurements in the reflected-sun geometry. This is achieved by (1) a new detector element with reduced noise, (2) an increased FOV and (3) enhanced light throughput by removing all internal apertures. The main modification is the new detector module, featuring a thermoelectrically cooled photodiode and a larger FOV. The thoughput is enhanced by a factor of 70, leading to an overall increase in gain of a factor 10^5 (calculation see Appendix A.3).

Figure 3.6: The EM27/SCA FTS placed on Mt. Wilson observing the northern Los Angeles basin. The components are annotated in Figure 3.8 and Figure 3.7 shows a schematic of the light path through the instrument.

Subsequently, further modifications added auxiliary equipment needed for campaign measurements (Hemmer 2019; Löw et al. 2023), most notably the modification of the pointing system and the addition of a Lambertian reflector plate. The following paragraphs describe the instrument. Figure 3.7 shows the optical setup of the EM27/SCA, Figure 3.8 shows the instrument with all components, and Table 3.1 summarizes the instrument properties.

Optical Layout The surface reflected sunlight is guided by the two 50 mm mirrors of the alt-azimuthal pointing system into the instrument. Some light is coupled out from the rim of the beam by a 10 mm prism towards the FOV camera. The remaining light is guided by a plain mirror through a 26 mm diameter iris aperture towards the entrance window. The entrance window is a Schott RG 695 longpass filter with a cut-off wavelength of 695nm (14 400 cm^{-1}). From there, it passes the interferometer, a RockSolid™pendulum interferometer with CaF_2 beamsplitter. The 633nm HeNe metrology laser, which is used for the interferogram sampling, passes the interferometer coaligned with the optical axis at the rim of the beam. Both portions of the beam are reflected by gold coated cube-corner mirrors, which are attached to the pendulum continuously modifying the optical path difference.

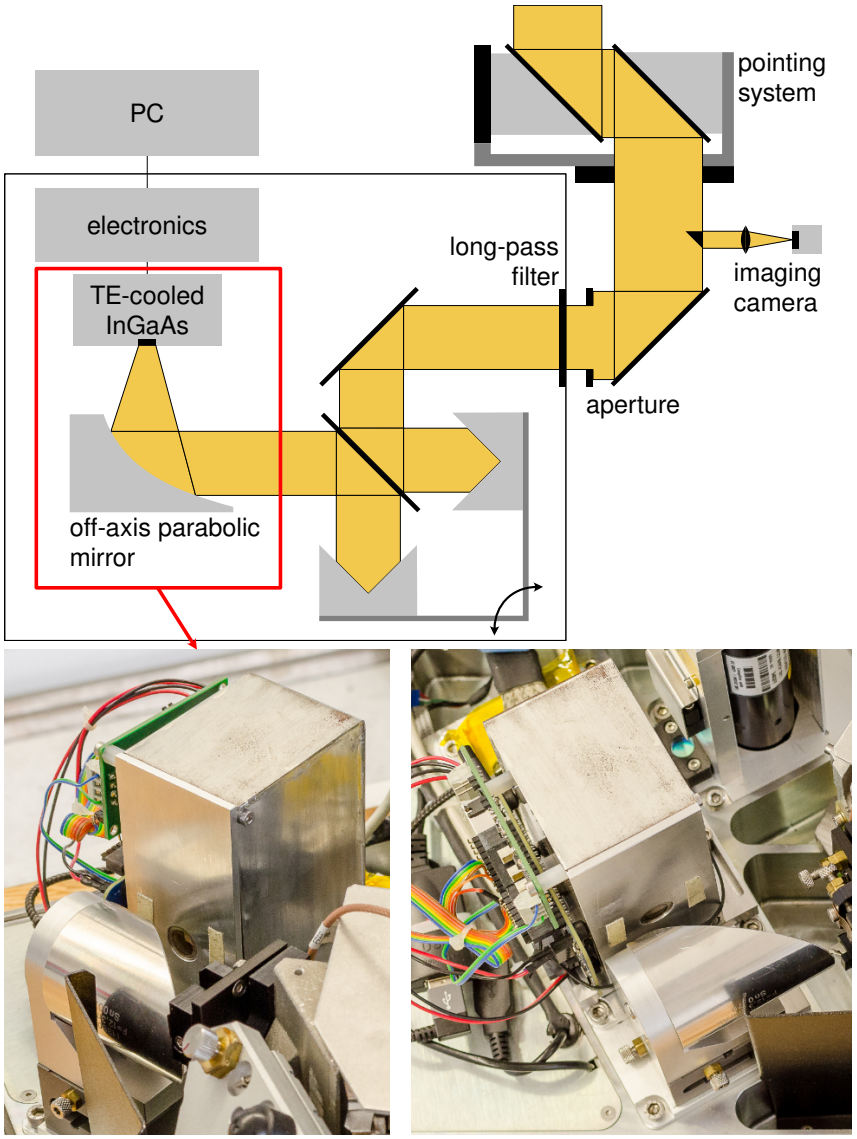

Figure 3.7: Schematic of the light path through the EM27/SCA (top, adapted from (Gisi et al. 2012)). The pointing system guides light into the instrument. A small portion is coupled out for imaging the target. After passing the interferometer, the light is focused on the InGaAs photodiode. The detector module is shown in the bottom images.

Table 3.1: EM27/SCA specifications in standard configuration.

Photodiode	InGaAs (Hamamatsu G12183-203K)
TE-cooling	$-20\,^{\circ}\mathrm{C}$
Spectral range	$4200\,\mathrm{cm}^{-1}$ to $12\,000\,\mathrm{cm}^{-1}$
Maximum OPD	1.8 cm
Nominal Resolution	$0.56\,\mathrm{cm}^{-1}$
Beamsplitter	CaF_2
Longpass	Schott RG 695
Limiting Aperture	0.3 mm (Photodiode)
Effective focal length	33 mm
Field of view	9.09 mrad
Clear aperture	2.6 cm
Lambertian reflector	SphereOptics ZenithLite r =50 %
Dimensions (h × w × l)	53 cm × 40 cm × 60 cm
Total weight	31kg

The maximum optical path difference is 1.8 cm and thus the instrument has a nominal resolution of $0.56\,\mathrm{cm}^{-1}$. After recombining at the beamsplitter the beam, a off-axis parabolic mirror (OAP) focuses the light onto the detector.

Detector The detector module comprises a OAP and in its focus a thermoelectrically cooled indium gallium arsenide (InGaAs) photodiode with the appropriate amplifier and analog-digital converter. It is displayed in the images in Figure 3.7. The photodiode (Hamamatsu G12183-203K) is cooled to an operating temperature of $-20\,^{\circ}\mathrm{C}$. As there is no other field stop installed, the circular active area of the photodiode (diameter $d = 0.3\mathrm{mm}$) and the effective focal length $f_{\mathrm{eff}} = 33\mathrm{mm}$ of the OAP determine the instruments nominal full field of view to 9.09 mrad (cf. Equation (3.30)). The spectral range is limited to above $4000\,\mathrm{cm}^{-1}$ by the cut-off of the InGaAs detector and to below $12\,000\,\mathrm{cm}^{-1}$ by a foil filter, which blocks impairing light of the metrology laser. Note that this (extended) InGaAs photodiode includes the CO spectral range. The design of the detector module is in depth described by Kostinek 2015. The improvement of the signal-to-noise ratio (SNR) with cooling was described by Hemmer (2019). The cooling performance was monitored during multiple days during field measurements where the detector temperature showed no significant variations.

Pointing system The pointing system uses an alt-azimuthal mirror pair, similar to the EM27/SUN solar tracker. It consists of two motorized 50 mm mirrors (GSO AD007), one rotating in altitude and one rotating in azimuth direction. The mirrors are driven by rotational stages (Standa 8MR190-2-28 (azimuth) and 8MR151-1 (zenith)) controlled via a dual stepper motor controller (Trinamic TMC5072). The light is reflected by the second mirror down through the central hole in the azimuth rotational stage and coupled into the instrument via a third mirror. An FOV camera, which is co-aligned with the instrument viewing direction, complements the pointing system. This allows the identification and pointing to-

Figure 3.8: The EM27/SCA and its components.

wards ground reflection targets of interest. A small portion of the light is coupled out of the rim of the downward beam by a 10 mm prism after the second rotating mirror into a camera (IDS UI-3140CP-M-GL R2) with a f=100 mm lens (Kowa LM100JC) focused to infinity. The camera features a $1/2$ inch CMOS sensor (1280 px $\times$ 1024 px). The camera is mounted on a kinematic platform mount (Thorlabs KM200B/M). It is equipped with a 900nm (MidOpt LP900-25.4) longpass filter (Hemmer 2019). The Pointing system is encased with a metal sun cover to avoid stray light (e.g. from sun reflections on the pointing systems mirror mounts) entering the instrument. Under certain sun positions relative to the instrument, light reflected from the front of the sun cover onto the reflector can impact the reflector measurements. These reflections are eliminated by laminating the front of the tracker with felt. To monitor the sky scene in addition to the target scene, an additional camera with a $f = 1.4$ wide angle lens (Fujifilm FE185C046HA-1) with a 185° FOV is attached to the side of the instrument. To increase the contrast between sky and clouds, a 1 µm (MidOpt LP1000-25.4) longpass filter is inserted. The motor controller and both cameras are attached to an encased Raspberry Pi controlling them.

Lambertian Reflector To measure spectra excluding any horizontal light path contribution we install a Lambertian reflector plate on top of the instrument main body (Müller 2019). The reflector is a ZenithLite™ reflection target with a reflectivity of 50 %, monotonously increasing from 49 % at 4000 cm^{-1} to 52 % at 12 000 cm^{-1}.

Foil Filter To prevent malicious influences of the metrology helium neon (HeNe) laser on the photodiode, a foil filter was added in front of the photodiode. The filter successfully removes the influences of the HeNe laser but has broadband effects on the spectrum. Figure 3.9 compares spectra recorded before and after installation of the foil filter on 14 August 2019. Both spectra were recorded for ILS measurements (see Section 3.4.1) but in different setups. Especially differences in positioning of the light source prevent the comparison of

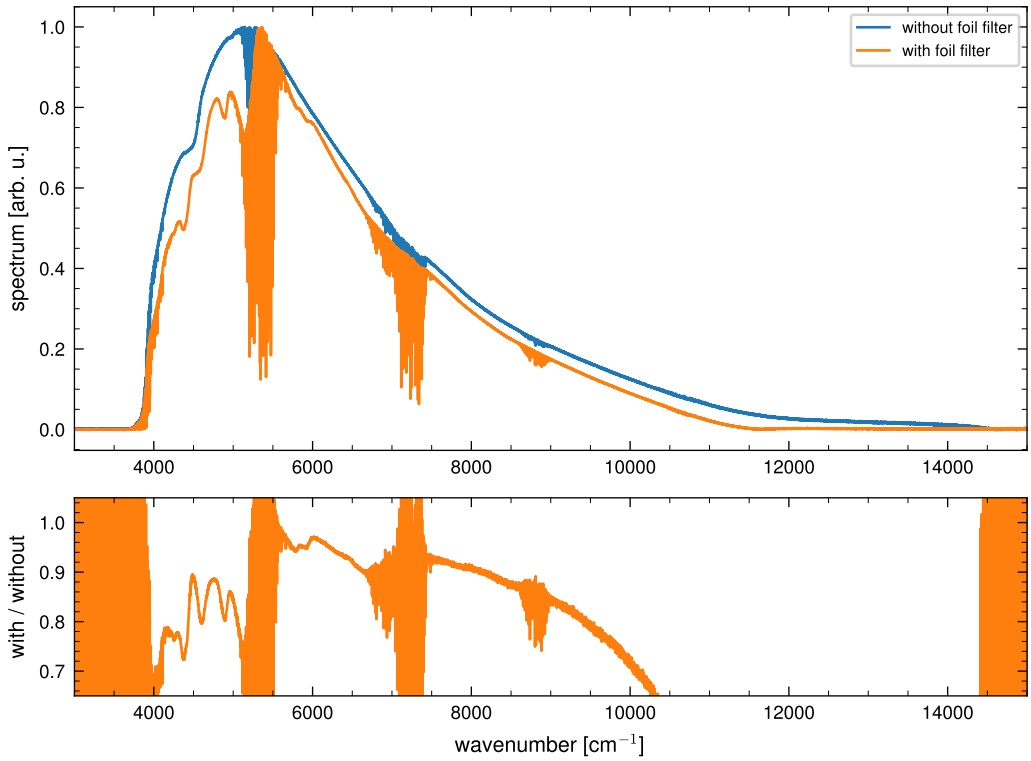

Figure 3.9: The change in spectrum through installation of the foil filter in front of the photodetector. The upper panel shows spectra before (blue) and after (orange) installation. Both spectra are normalized to its maximum, as they were recorded under differing illumination. The lower panel shows the ratio of both spectra, making the broadband variation impact of the foil filter apparent. Note, that this is not the transmittance of the foil filter, because the spectra are recorded under different illumination.

the absolute magnitude of both spectra. Nevertheless, the spectral structure imposed by the filter on the spectrum can be determined from the ratio of both spectra. The influence is especially apparent in the low wavenumber range, where it produces broadband variations in the spectrum continuum on the order of 10 %.

Aperture To improve the width and symmetry of the ILS, a 3 inch iris diaphragm (Thorlabs SM3D50D) is installed in front of and centered on the entrance aperture. The effect of the aperture on the ILS is discussed in Section 3.4.5. It is typically set to a diameter of 2.6 cm, limiting the beam diameter, which would otherwise be around 3.6 cm.

Operation Settings The EM27/SCA measurements are operated through the OPUS software, delivered by Bruker with each EM27/SUN instrument. For a single interferogram, 10 double sided forward-backward scans at maximum OPD Δ of 1.8 cm are averaged. Note that Bruker calculates resolution as $0.9/\Delta$ and references the resolution as 0.5 cm^{-1} for 1.8 cm maximum OPD. The sampling rate is set to 10 kHz, which leads to a total integration time

of roughly 1 min for all 10 scans. Since a few seconds overhead are added to each measurement, reducing the number of scans would reduce the effective total integration time over multiple measurements. For higher amount of scans, filtering one measurement in the further analysis pipeline would potentially lead to disproportional data loss and for very long integration times, the assumption of constant conditions during the measurement will break down. The 10 scans are choosen as a compromise. The signal gain is manually set to a value of one (*x1*). Note that the 'automatic' gain setting increases the overhead time significantly (Hemmer 2019). For low albedo targets, a signal gain of two (*x2*) may be used, however only marginal improvements in SNR could be detected, which usually do not justify the risk of oversaturating the detector analog-to-digital converter (ADC) (cf. Section 3.5). Measurement settings are provided through a settings file. The standard OPUS settings used within this work are provided for reference in Table A.1. During field campaigns, the overall measurement control is managed by custom python software. The software triggers the Raspberry Pi controlling the pointing and the cameras via ssh over a direct ethernet connection. Coordinated with the pointing, it triggers the recording of individual interferograms by the OPUS software through an API provided by Bruker.

3.3 From Interferogram to Spectrum

The raw EM27/SCA measurements are interferograms. Figure 3.10 shows interferograms from laboratory and field measurements of the reflector plate. Laboratory measurements are recorded using an incandescent light source (cf. Section 3.4.1). Since every interferogram consists of forward and backward scans, every measurements consists of a mirrored interferogram pair. Each part exhibits a large spike, the center-burst (CB), where at zero OPD all wavenumbers interfere constructively. Since the interferograms are recorded in DC coupling, the CB and the overall interference pattern are recorded around a continuous offset baseline. While for laboratory measurement this is smooth, in field measurements source brightness fluctuations make it variable. Recording in DC coupling has the advantage that the absolute signal can be assessed from the measurement. However, since the baseline varies with OPD, the AC component has to be extracted before performing the Fourier transformation. The instrument internally records signals at negative voltage, leading to a negative interferogram and to higher signals appearing as more negative. To avoid confusion, absolute values of the interferogram are shown in this thesis.

The interferograms need processing to obtain spectra, from which the absorption features can be evaluated in the GHG retrieval. The Fourier transform is performed with the preprocessor of the PROFFAST retrieval suite (KIT IMK-ASF 2024). It is developed at KIT for the use in the COCCON. It applies a fast Fourier transformation after correcting for variations in the DC component and numerically apodizing the interferogram. The complex spectrum is corrected for smooth variations in the phase. The resulting real spectrum is resampled before output. Forward and backward scans are processed independently and averaged only after resampling. Figure 3.11 shows the steps of computing the spectrum from the interferogram. The following paragraphs elaborate on the DC correction and phase correction, before presenting exemplary spectra.

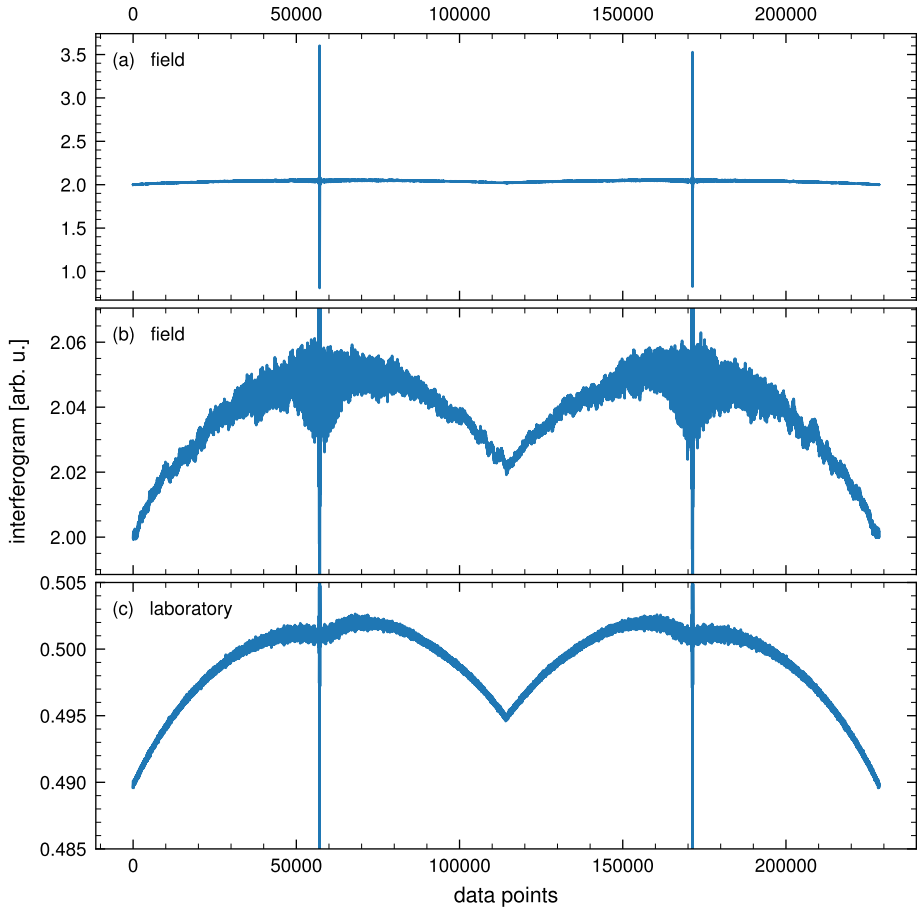

Figure 3.10: Interferograms measured with the EM27/SCA FTS. Panel (a) shows a full interferogram, panels (b) and (c) show a zoom on the interferogram baseline for measurements of the reflector in the field (b) and in the laboratory (c).

DC correction There are two contributions to the variability of the DC component of the EM27/SCA interferograms visible in Figure 3.10. The first is the static curvature, clearly visible in all interferograms including the laboratory measurements. The throughput of the interferometer is not independent from OPD, causing less light to be transmitted at large OPD. This causes the characteristic shape. The second contribution results from radiance variations caused by the atmosphere, e.g. thin clouds. This causes small and fast variations which are absent in laboratory measurements with a stable light source. Note that averaging multiple scans reduces the variability. Keppel-Aleks et al. 2007 showed that source brightness fluctuations can be corrected by reweighting the interferogram by its DC component obtained by low pass filtering the interferogram. A similar correction is applied, where the DC component is obtained by repeatedly applying a smoothing through 400 times con-

volving the interferogram with a 3 point wide triangular function, equal to a rolling 3 point average where neighbours are weighted half (0.25, 0.5, 0.25). The output DC component calculated this way is shown for one example in in the top panel of Figure 3.11. The AC interferogram $S(\delta)$ is calculated by ratioing the original interferogram $S_{\mathrm{m}}(\delta)$ with the DC component $S_{\mathrm{DC}}(\delta)$.

$$S(\delta) = \overline{S_{\mathrm{DC}}} \cdot \left(\frac{S_{\mathrm{m}}(\delta)}{S_{\mathrm{DC}}(\delta)} - 1 \right) \tag{3.19}$$

Multiplying with the mean DC component $\overline{S_{\mathrm{DC}}}$ ensures that the AC interferogram retains information on the absolute signal.

Phase Correction After DC correction, the interferogram is Fourier transformed to the complex spectrum B'.

$$B'(\tilde{\nu}) = \mathscr{F}(S_{AC}(\delta)) \tag{3.20}$$

The complex spectrum contains information on both, the true spectrum $B(\tilde{\nu})$ and the phase $\phi_{\tilde{\nu}}$ (cf. Equation (3.6)). In principle, the true spectrum can be calculated as the magnitude of the complex spectrum. However, in this case, the noise in the zero-signal regions of the spectrum, will no longer be Gaussian. Instead, the phase information is used to recover $B(\tilde{\nu})$. Since the instrument records symmetric interferograms, the information on the phase ϕ can be deduced from the full interferogram.

$$\phi_{\tilde{\nu}} = \arctan\left(\frac{\mathrm{Im}(B')}{\mathrm{Re}(B')} \right) \tag{3.21}$$

Therefore, the true spectrum is related to the complex spectrum by

$$B(\tilde{\nu}) = B'(\tilde{\nu}) e^{-i\phi_{\tilde{\nu}}} = Re(B')\cos(\phi_{\tilde{\nu}}) + \mathrm{Im}(B')\sin(\phi_{\tilde{\nu}}). \tag{3.22}$$

The phase typically varies slowly with wavenumber. Therefore, the impact of noise in the phase is reduced by only using broadband phase information. This avoids distortions in zero signal regions of the spectrum. Polynomials $P_{\cos\phi}$ and $P_{\sin\phi}$ are determined from the cosine and sine phase functions.

$$\cos(\phi) = \frac{\mathrm{Re}(B')}{|B'|}, \quad \sin(\phi) = \frac{\mathrm{Im}(B')}{|B'|} \tag{3.23}$$

The cosine and sine of the phase are averaged in the four spectral regions, where the phase is not impacted by low signal due to water absorption. The regions are specified in Table 3.2. The average values provide the support points to calculate the third order polynomials $P_{\cos\phi}$ and $P_{\sin\phi}$. The third panel of Figure 3.11 shows an exemplary phase and phase polynomials. Subsequently, the true spectrum is calculated from the complex spectrum and the polynomials by

$$B(\tilde{\nu}) = \frac{P_{\cos\phi} \cdot \mathrm{Re}(S_c) + P_{\sin\phi} \cdot \mathrm{Im}(S_c)}{\sqrt{P_{\cos\phi}^2 + P_{\sin\phi}^2}}. \tag{3.24}$$

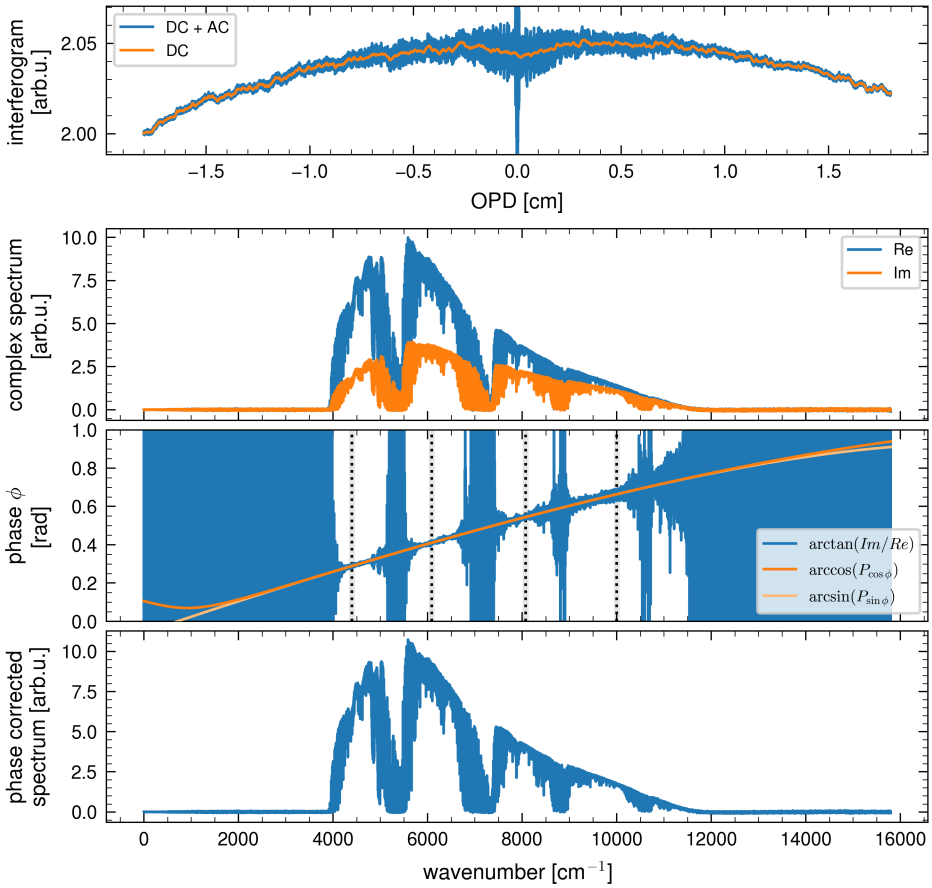

Figure 3.11: Processing from interferogram to spectrum. The interferogram (top, blue) is corrected by its DC component (orange) and Fourier transformed to the complex spectrum (second panel). The phase (third panel, blue) is approximated by 3rd order polynomials of sine and cosine of the phase functions (orange). The output spectrum (bottom panel) is calculated from the complex spectrum and the phase function polynomials.

This method for phase correction was developed by Mertz 1967 and is referenced to as Mertz method accordingly. It is typically also employed in cases where only a small part of the interferogram is double sided. This reduces the resolution of the phase spectrum but the method works nonetheless. Note that the normalization is necessary here, since the polynomials are determined independently and it can no longer be assumed that their sum squares are one.

Spectrum Figure 3.12 shows two EM27/SCA spectra, processed as described above. One observing the reflector and one from a ground target. The characteristic shape of

Table 3.2: Spectral regions used to calculate the polynomial approximation for the cosine and sine phase functions.

center [cm-1]	interval [cm-1]	
4399.074	4339.045	4459.574
6086.391	6026.451	6146.980
8075.013	8015.180	8135.709
10003.375	9943.644	10064.173

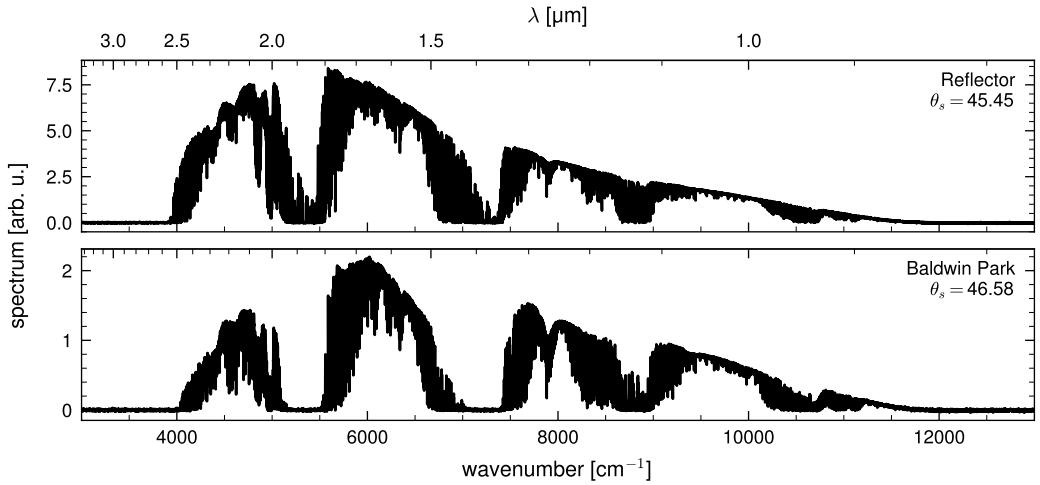

Figure 3.12: EM27/SCA spectrum of the reflector (top) and a target (bottom). The absorption features in the target spectrum are deeper due to the longer light path. The relative signal varies with wavenumber due to surface albedo.

the overall spectrum is mainly determined by the detector sensitivity. The solar spectrum and transmission properties of the optical elements also play a role. For target spectra, the ground albedo additionally changes the overall shape of the spectrum significantly, i.e. the relative signal in the different absorption bands. The contributions of the Earth atmosphere are visible as absorption bands. In addition to individual absorption lines used for the retrieval of GHGs (cf. Section 4.5), the strong water absorption bands at 5000 cm^{-1} to 5500 cm^{-1}, 7000 cm^{-1} to 7500 cm^{-1} and 8500 cm^{-1} to 9000 cm^{-1} are apparent. Absorption features are much stronger in the target spectrum due the significantly longer light path. The detector has no sensitivity past its cut-off wavenumber at around 4000 cm^{-1}. Therefore, the off-band region is used to quantify the measurement noise.

3.4 Instrument Lineshape

Section 3.1.2 described how the ideal ILS of any FTS follows from its maximum OPD and FOV. For the EM27/SCA, the ideal ILS is given by its maximum OPD of 1.8 cm and the nominal semi-angle FOV of 4.545 mrad. Note that the numerical NBM apodization used to generate the spectra is reflected in the ILS. However, the real ILS deviates significantly from this ideal ILS. For GHG retrievals, it is critical to include an accurate representation of the ILS in the forward model. The following sections present the retrieval of the EM27/SCA ILS from H_2O absorption lines measured in controlled open-path measurements, employing the ILS model presented in Section 3.1.2. Subsequently, its uncertainty and long-term stability are discussed.

Prior to the determination of the real ILS, it should be noted that the effect of self apodization on the EM27/SCA ILS is small. As displayed in Figures 3.3 and 3.5, the self apodization can be represented by a sinc in OPD space. The relative width of the maximum OPD rect function and the self apodization sinc function in OPD space determines the impact of the self apodization. For the EM27/SCA, the self apodization sinc has its first minimum at an OPD of 13.53 cm, and is thus much wider than the maximum OPD of 1.8 cm. The self apodization reduces the boxcar at maximum OPD only by 2.7 %. The peak height of the ideal ILS is only reduced by 0.5 % compared to one neglecting the FOV altogether. Because of the low impact of self apodization, the wavenumber dependence of the ideal ILS is also negligible. The peak height of an ideal ILS at 7000 cm^{-1} and 4500 cm^{-1} only differ by 0.3 %. Thus, the ILS can be assumed constant throughout the whole spectrum.

3.4.1 ILS Measurement

A reliable method to determine the ILS was introduced by Frey et al. 2015 and is routinely used for EM27/SUN instruments (Alberti et al. 2022; Frey et al. 2019). It is applied with some modifications to the EM27/SCA, mainly accommodating the larger FOV and beam diameter (Hemmer 2019). The method uses information from water absorption features in low noise spectra measured under well defined conditions to infer the ILS. An ILS model (Section 3.1.2) is fitted to the absorption spectrum, assuming a known partial water column, pressure and temperature.

Figure 3.13 shows the setup for ILS measurements. The ILS measurement procedure is as follows. The EM27/SCA is placed in a dark laboratory. The instrument sealing is

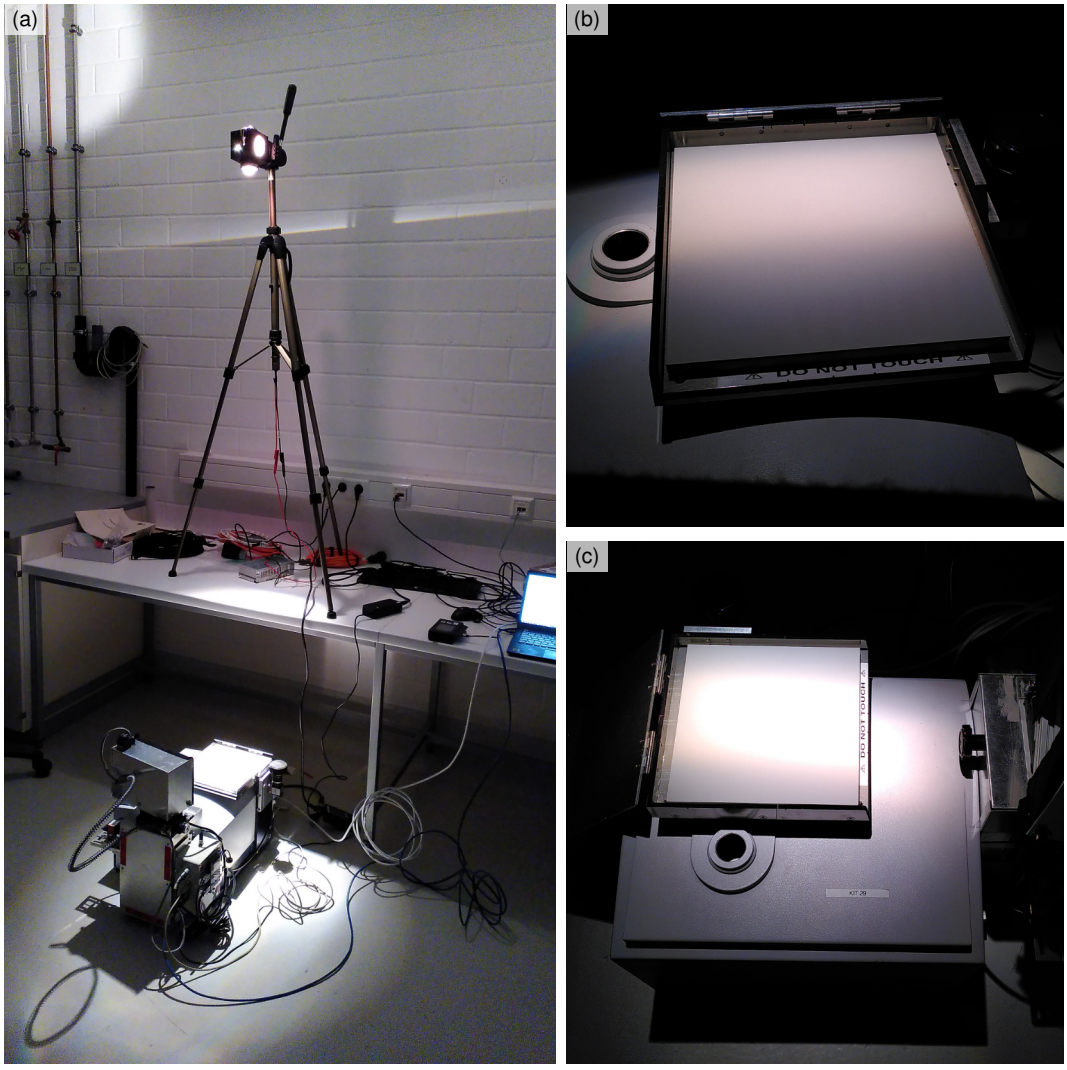

Figure 3.13: (a) The setup for recording open path ILS measurements. The instrument FOV on the reflector plate is homogeneously illuminated by a halogen light source. The instrument is vented to ensure a homogenous air column. The ILS is retrieved from water absorption lines between 7000 cm^{-1} to 7400 cm^{-1} from 30 min averaged spectra. The ILS retrieved from subsequent measurements under variation of the illumination setup ((b) and (c)) are nearly identical (cf. Figure 3.16 panel b).

Table 3.3: Parameter used for Fourier transform of ILS measurement interferograms in OPUS.

	parameter	value
Store	First	$100\,\mathrm{cm}^{-1}$
	Last	$15\,000\,\mathrm{cm}^{-1}$
Apodization	Function	NBM
	Zerofilling	8
Limit Data	Limit resolution	off
	Limit phase resolution	$4\,\mathrm{cm}^{-1}$
	Direction	Both
	Datapoints	Both
Phase correction	Mode	Mertz
Non linearity	Non linearity correction	off
Peak Search	Peak (ZPD) search mode	Absolut largest Value
	optimize position	symmetry of interferogram: automatic

removed to allow for homogeneous air column along the light path outside and inside the instrument. The instrument FOV is pointed onto the Lambertian reflector plate. The corresponding area on the reflector is homogenously illuminated from a distance of 170 cm to 180 cm with a sanded 50 W halogen light source, which is collimated by an aspheric condenser lens (Thorlabs ACL50832U). Ambient pressure, temperature and relative humidity are logged throughout the experiment with a sensor (PCE Instruments, PCE-THB 40). After completing the experimental setup, the start of the measurements is delayed for two hours to allow (1) the metrology laser to stabilize, (2) the temperature of the ILS lamp to stabilize and (3) let the air outside and inside the instrument equilibrate. Then, 30 10-scan double-sided interferograms are recorded.

For the ILS measurements, the Fourier transformation is performed with the OPUS software, since the preprocessor can not handle multiple interferograms simultaneously. I verified for one ILS measurement, that processing a spectrum generated from a manually averaged interferogram as specified in Section 3.3 yields only negligible differences in the final ILS (3 ‰ difference in ILS peak height). The interferograms are averaged and manually DC corrected by dividing the average interferogram by a smoothed version of itself. The Fourier transform is performed on the interferogram in OPUS with settings displayed in Table 3.3. To obtain a transmittance spectrum in OPUS, the spectrum is divided such that the region $7000\,\mathrm{cm}^{-1}$ to $7400\,\mathrm{cm}^{-1}$ is approximately one. The spectrum is input into the LINEFIT software (Hase et al. 1999) to retrieve the ILS. Along with the spectrum, ambient pressure p, temperature T, as well as the water column $\mathrm{SCD}_{\mathrm{H_2O}}$ between light source and detector and the partial water pressure p_p are input parameters. The partial water pressure is calculated from the relative humidity h using the Magnus formula for the saturation vapour pressure (Roedel and Wagner 2017)

$$p_p = h \cdot 611.2\,\mathrm{Pa} \cdot \exp\left(\frac{17.62 \cdot T_C}{243.12\,^{\circ}\mathrm{C} + T_C}\right), \tag{3.25}$$

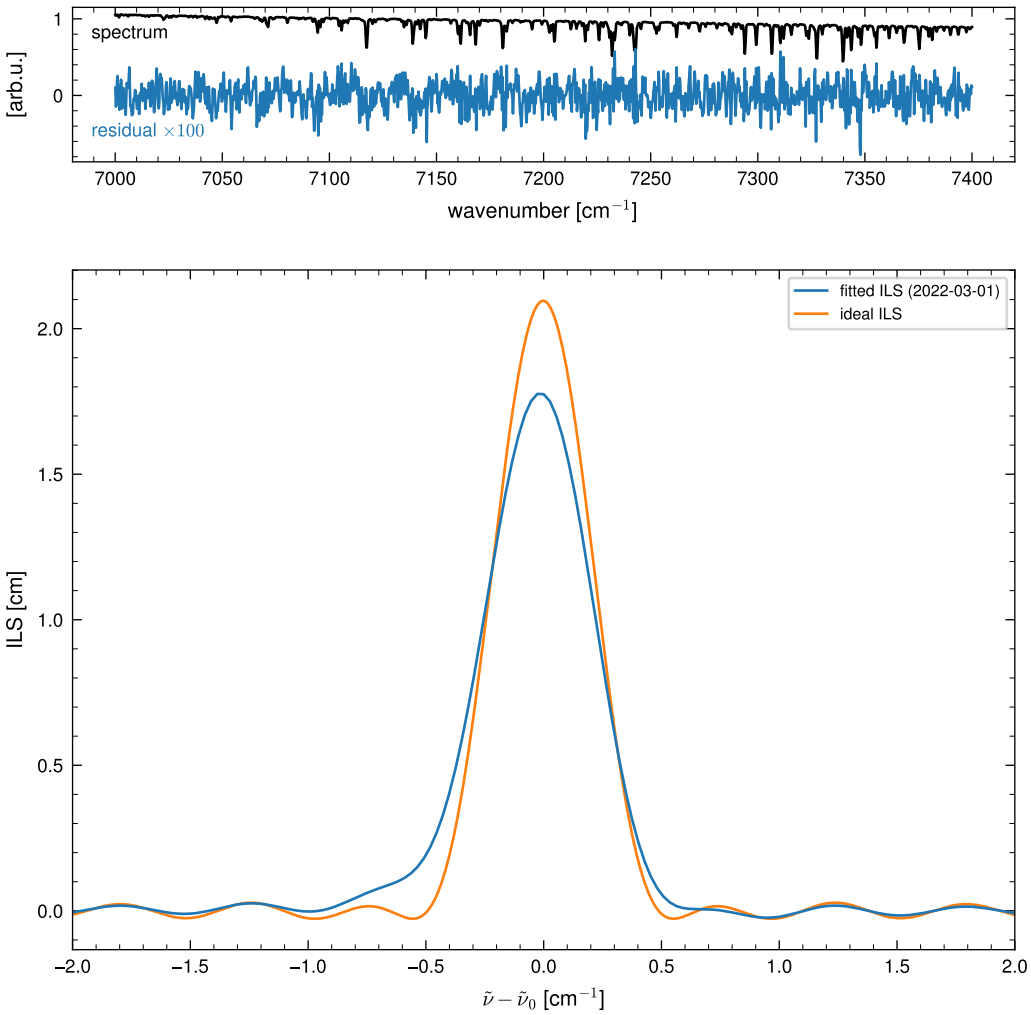

Figure 3.14: ILS fitted to laboratory open path H_2O absorption spectrum. The top panel shows the spectrum (black) and the fit residual. The lower panel shows the EM27/SCA ILS (blue) in comparison to the ILS of an ideal FTS (orange) with same maximum OPD and FOV.

which uses the temperature T_C in °C. Together with the length of the light path L, the water column is obtained with the ideal gas law

$$\mathrm{SCD}_{H_2O} = \frac{p_p L}{k_B T}. \tag{3.26}$$

The light path comprises of the distance from the light source to the reflector (typically 170 cm to 180 cm) to the pointing system (40 cm) to the detector (92 cm). The distances deviate from the standard EM27/SUN specified by Alberti et al. (2022) due to modifications of the pointing system and the lower focal distance of the OAP. LINEFIT fits an ILS model to the spectra. A correction to the calculated H_2O column is simultaneously deduced, usually on the order of a few percent. This is necessary due to the uncertainty in light path measure-

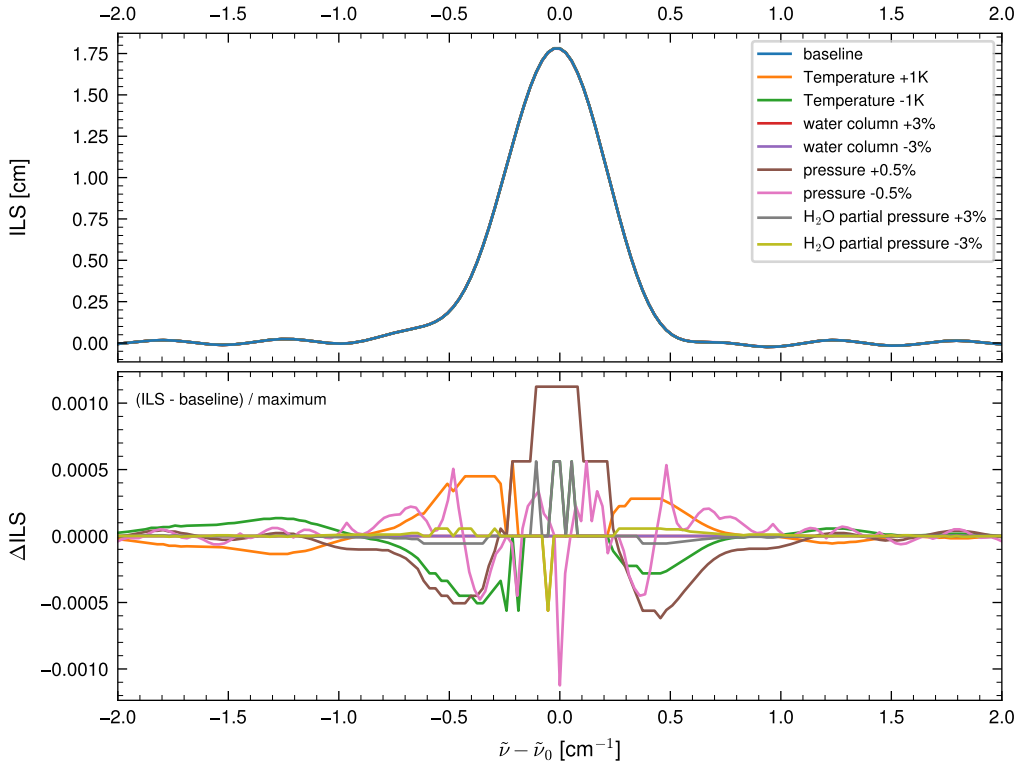

Figure 3.15: Differences in ILS retrieved with LINEFIT from the same spectrum but with varying input parameters for the ambient conditions.

ment and measurements of ambient conditions with an uncalibrated sensor. LINEFIT is run a second time with the updated water column, as recommended by F. Hase (private comm.). Usually one repetition is enough to reach a negligible correction on the water column, otherwise additional iterations are performed. The extended ILS model (cf. Section 3.4.4) is chosen, which determines the ME and PE over 20 OPD intervals. Figure 3.14 shows an exemplary fit and the resulting ILS used within this thesis. The ILS deviates considerably from the ideal ILS calculated purely from maximum OPD and FOV. It is wider and more asymmetric, resulting from a decrease in ME down to 60 % at high OPD, and a PE on the order of 0.1 rad (cf. Figure 3.17). This could be caused by vignetting of and recesses in the throughput, as well as by the imperfect focus on the photodiode. The latter component is facilitated by the short focal length of the 90° OAP focusing mirror. However, the non-ideal ILS is not a fundamental problem, because it can be accounted for in the retrieval process, as long as it is accurately known.

Two analyses determine the reliability of the ILS retrievals. First, the ILS retrieved from the same measurement with variable input parameters are compared (Section 3.4.2). Second, the ILSs retrieved from different ILS measurements are compared (Section 3.4.3).

3.4.2 Sensitivity on Input Parameters

In a first step, LINEFIT is run after varying the input parameters by a realistic offset. The immediate input parameters to LINEFIT are the water column, temperature, total pressure and partial water pressure. I vary the water column by 3 %, temperature by 1 K, total pressure by 0.5 % translating to approximately 5 mbar and the partial water pressure also by 3 %. The resulting ILS and its differences are shown in Figure 3.15. The retrieved ILS is up to 1 ‰ different, with the largest impact from change in pressure. This agrees well with the fact that pressure broadening is the dominant broadening effect on the water absorption lines at ambient conditions. Note that the ILS retrieved with reduced total pressure has a different wavenumber grid and is therefore linearly interpolated. Note that changes in temperature have more impact towards lower wavenumbers, where the ILS is asymmetric towards. Changes in water column do not affect the results of the retrieval, as the fitted correction negates changes in input parameters. Overall, the sensitivity is limited to 1 ‰ under realistic parameter variations.

3.4.3 Repeatability

To determine the repeatability of the ILS, multiple measurements are compared. Figure 3.16 shows the differences in the retrieved ILS throughout multiple measurements, quantifying short-term and long-term repeatability.

To determine the short-term repeatability, three ILS measurements are recorded back to back (second panel in Figure 3.16). In between, the instrument is rotated by 90° to check whether an illumination pattern on the reflector has an influence on the ILS measurement (cf. Figure 3.13 (b) and (c)). Afterwards, the instrument orientation is reverted to the initial positioning and the distance of the light source is reduced, reducing the absorption path length in the process. The variations are well below 1 % of the ILS peak height.

To assess the long-term repeatability, ILS measurements spanning multiple months are compared (third panel in Figure 3.16). The measurements span a time period where instrument modifications were undertaken. Modifications include the replacement of the azimuth rotation stage of the pointing system (2021-06-07), removal of the full pointing system (2021-07-13, 2021-09-20), replacement of the metrology laser (2021-07-29) and installing a spacer on the cooling controller (2022-02-17). These modifications could in principle have collateral effects on the ILS, but did not include any alignment efforts of interferometer or detector. I evaluate the differences of the ILS measurements to a reference ILS recorded on 2021-04-03. During the period, the ILS changes by up to 2 % of the reference ILS peak height.

The time period of the measurement campaign on Mt. Wilson is a period without any instrumental modifications. Multiple ILS were recorded during this period. One before shipping (2022-03-01), one after arrival on Mt. Wilson (2022-04-08) and at the end of the campaign (2022-05-06). These three measurements show low variation of 0.5 %. However, the two measurements on 2022-05-04 and 2022-05-05 show deviations of 2 %. The only obvious difference is that those two measurements were recorded with the largest H_2O column densities, 5.1 and 5.6×10^{23} molec/m^2 instead of 3.1, 3.5 and 4.0×10^{23} molec/m^2, mainly due to higher absolute humidity. However, it is unclear why such a bimodal behaviour

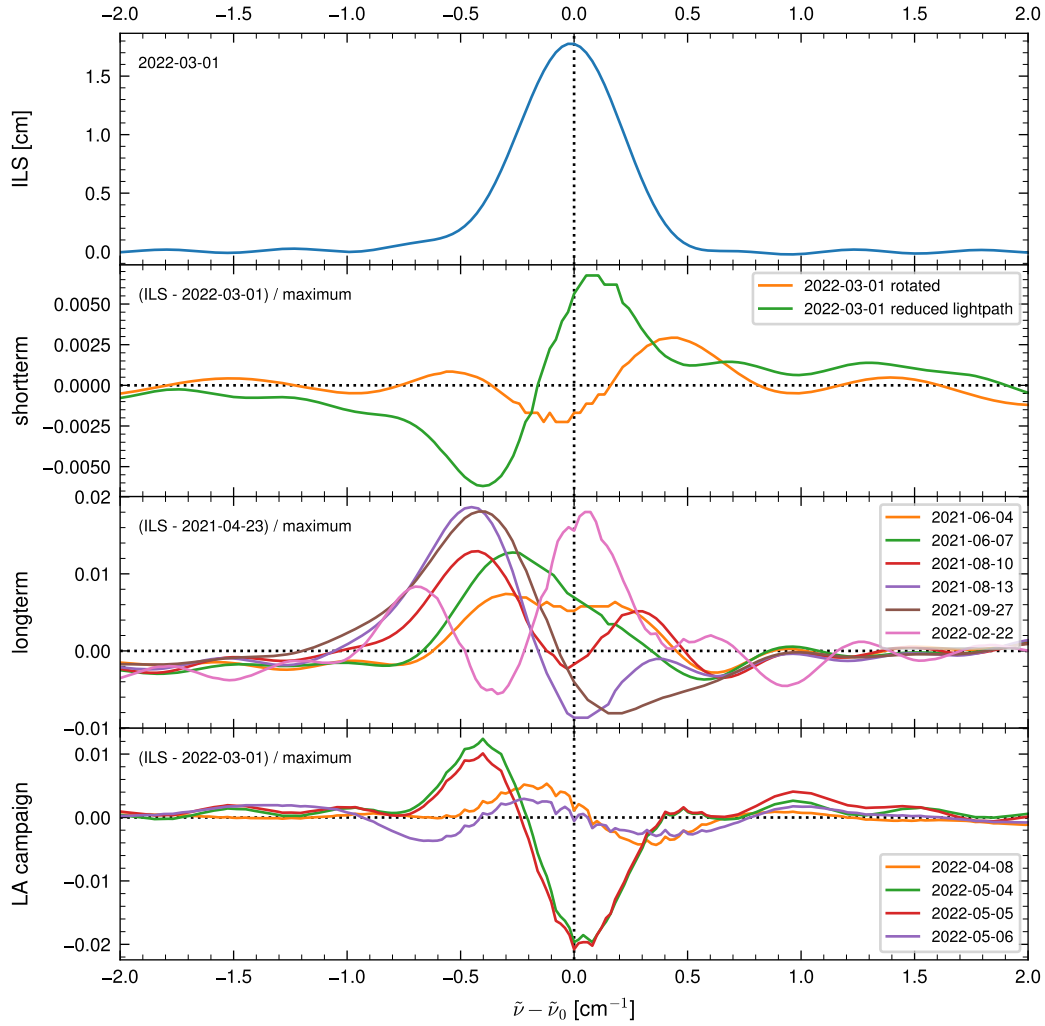

Figure 3.16: Repeatability of the EM27/SCA ILS. The top panel shows the ILS as reference to the variations in the three lower panels. All differences are normalized to the maximum of the reference ILS. The second panel displays the difference between ILS measurements from three consecutive measurements, giving a measure of short-term repeatability. The third panel shows the differences of ILS over the course of several month. Note that the instrument was modified in the timeframe, however modifications should not strongly influence the ILS. The lowest panel shows ILS differences over the course of the campaign on Mt. Wilson. The first ILS was recorded before shipping in Heidelberg.

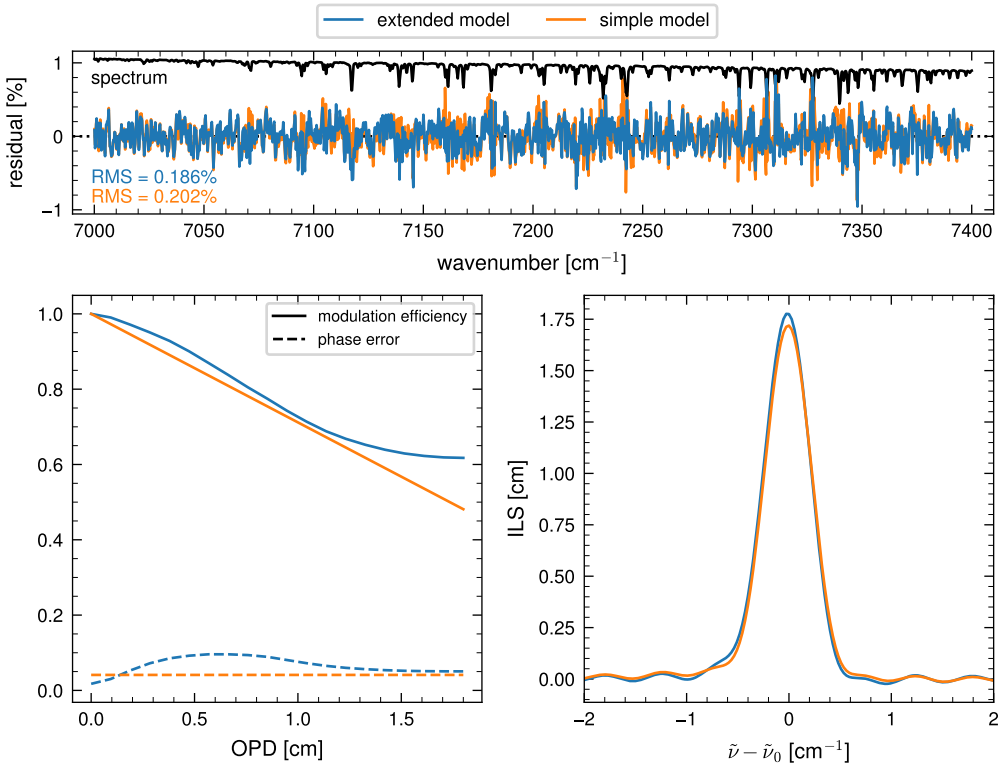

Figure 3.17: Comparison of LINEFIT ILS retrievals with simple and extended model, performed on the same spectrum. The top panel shows the fitting residuals. The bottom left panel shows the resulting modulation efficiency and phase error with OPD. The bottom right panel shows the fitted ILS.

should be observed when the differences in water columns are approximately equally spaced. In conclusion, the ILS uncertainty is on the order of 2 %.

3.4.4 ILS Parameterization

LINEFIT offers the choice to fit either a simple or an extended model. The simple model has a single parameter for each modulation efficiency and phase error, the extended model parameterizes ME and PE along the OPD with 20 parameters (cf. Section 3.1.2). To determine whether using the extended model is beneficial, LINEFIT is run on the same spectrum once with each model. Figure 3.17 shows fitting residuals resulting modulation efficiency and phase error, as well as the resulting ILS for both retrievals. The simple model shows overall lower ME. While the ME for the extended model has a similar decline at OPDs below 1.2 cm, it flattens out to 0.6 at maximum OPD. The fit residual with both models is generally quite good, with RMS of around 0.2 %. While the RMS of the fit residual is lower for the extended model, both residuals show systematic spikes around water absorption lines, but those stay below 1 %. Despite the marginally lower residual RMS, from fit quality alone it is not obvious whether the extended model is more accurate. Therefore, I

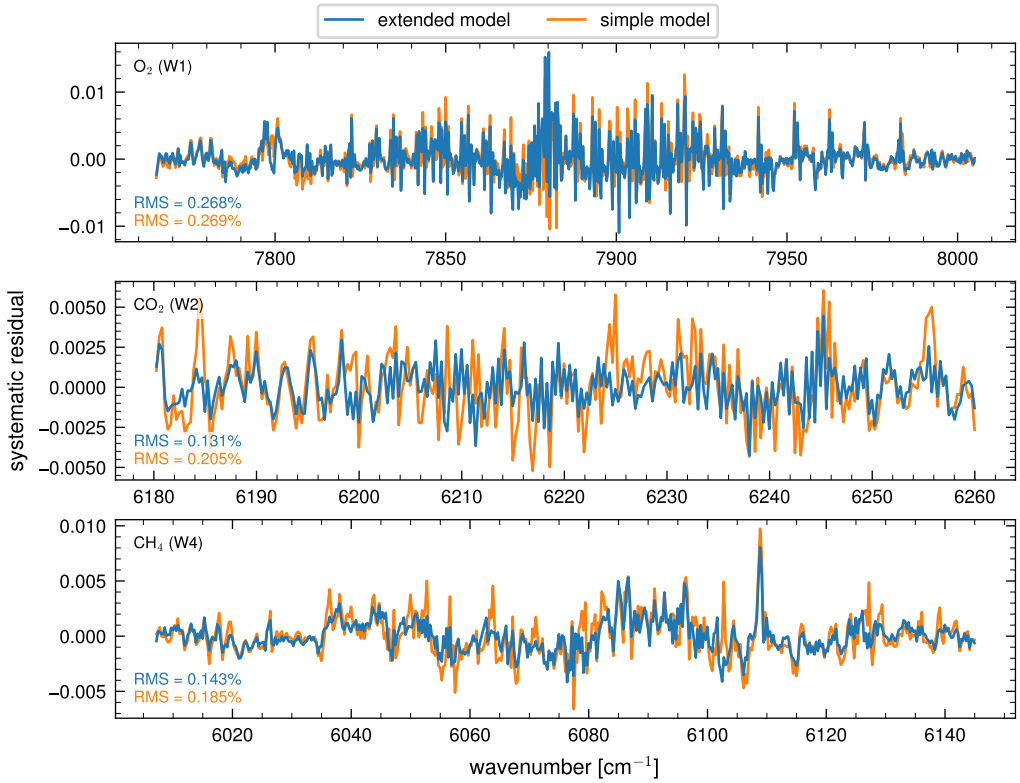

Figure 3.18: Systematic residuals of reflector measurements averaged over 13 April 2022. The systematic residuals in the CO_2 and CH_4 windows (W2–W5) are significantly lower when using the extended model ILS. For O_2 (W1) the effect is less pronounced.

evaluate the systematic residual of reflector measurements. Figure 3.18 shows the averaged residual of reflector measurements recorded on 13 April 2022. Retrieval and averaging was performed as described in Chapter 4 and Section 5.3. Using the extended model yields considerably lower and less spiked systematic residuals showing that the extended model more accurately represents the ILS.

3.4.5 Aperture

The aperture installed in front of the entrance window of the spectrometer limits the beam diameter entering the interferometer and thus has an impact on both the light thoughput as well as the ILS. To determine the optimal aperture diameter, a series of ILS is recorded at different aperture diameters. Figure 3.19 shows the resulting ILS in relation to the SNR. The SNR depends approximately linear on diameter up to 3.1 cm. This is expected for the case that the noise increases with the square root of the signal because the thoughput increases with the square of the beam diameter. For a diameter of 5.0 cm, the SNR is only marginally better than for 3.1 cm. Observing the signal in direct relation to the diameter, the signal only reduces when the aperture is closed further than 3.6 cm. This represents the maximum beam diameter through the interferometer. I chose an aperture diameter of 2.6 cm

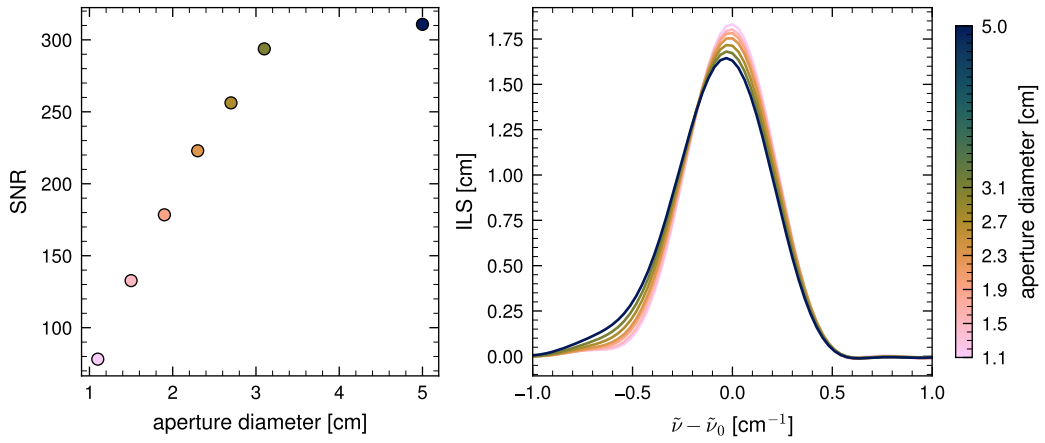

Figure 3.19: The ILS measured at different aperture diameters. The right panel shows the ILS with the respective aperture diameter color coded. The ILS narrows and SNR decreases with decreasing aperture diameter.

for further measurements, as this setting exhibits a good trade-off between a reduction in the left shoulder of the ILS and only approximately 20 % lower SNR.

Measurements on the roof of the Institute of Environmental Physics (IUP) are conducted to determine the impact of closed (2.6 cm diameter) and open (3.6 cm diameter) aperture settings. During two days, the aperture is switched between the open and the closed aperture setting at around noon. It is switched from the closed to the open setting on the first day and in inverted order on the second day. The respective ILS measured at each aperture setting is used to retrieve the measurements with the non-scattering retrieval (see Section 4.3.1). The precision is worse with closed aperture due to lower signal, but reflector XCO_2 and XCH_4 retrievals exhibit a lower bias compared to simultaneous direct-sun EM27/SUN measurements. I decide to use the closed aperture setting for the reduced systematic issues. However, in hindsight the reduced bias is mainly due to the bias in the O_2 retrieval, which have systematic problems (see Section 5.3.2). Aside from reducing the impact of scene heterogeneity (see Figure 3.26), there is no evidence for systematic improvements by utilizing the closed aperture setting, which justify the loss in signal and subsequently in precision.

3.5 Detector Linearity

To investigate the possibility of detector non-linearities, I inspect interferogram properties from multiple days. Both the DC component and the CB height reflect the total signal in the measurement. However, the CB is the absolute maximum of the interferogram and may therefore by subject to non-linearity. Thus, inspecting the dependency between the mean DC over the interferogram and the height of the CB gives a measure of detector linearity. At low values the CB height increases linearly with the DC mean. However, the CB height is capped at around 5.1. This corresponds to approximately 32000 counts in the instruments *check signal* mode. This limit is caused by the upper bound of the ADC, not by detector non-linearity, as lowering the digital gain resolves this issue. The data show no

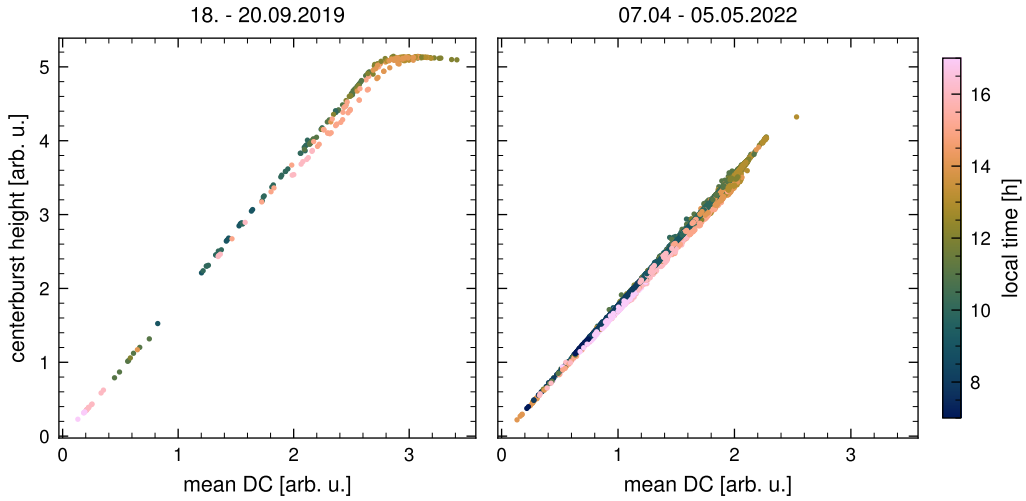

Figure 3.20: Interferogram CB height plotted against the mean value of the interferogram DC component. The CB height is impacted by non-linearities in the interferogram recording while the mean DC is a measure of overall signal.

indications for detector non-linearity. To prevent impacts from digitalization non-linearity, interferograms with CB height exceeding 4.8 are discarded. Additionally, the DC mean to CB height relationship features two branches, depending on the time of day. This is most likely due to a shift in the sampling of the CB.

3.6 Radiometric Calibration

To retrieve aerosol scattering from EM27/SCA spectra, a radiometric calibration is necessary. For lack of calibration instruments, I attain an approximative calibration by comparing EM27/SCA reflector spectra to simultaneous calibrated CLARS-FTS Spectralon observations.

For a given measurement, the spectrum $B(\tilde{\nu})$ should be related to the spectral radiance I via a spectrally dependent calibration factor $c(\tilde{\nu})$.

$$I(\tilde{\nu}) = c(\tilde{\nu}) \cdot B(\tilde{\nu}) \tag{3.27}$$

$c(\tilde{\nu})$ is determined by comparing $B(\tilde{\nu})$ to a simultaneous CLARS-FTS measurement $I_C(\tilde{\nu})$.

$$c(\tilde{\nu}) = \frac{I_C(\tilde{\nu})}{B(\tilde{\nu})} \cdot \frac{r}{r_C} \tag{3.28}$$

r and r_C account for the reflectivity of reflector and CLARS-FTS Spectralon respectively. The radiometric calibration for CLARS-FTS was provided by the CLARS team (Pongetti 2022, private comm.). It is determined from simultaneous observations with a co-located

Table 3.4: Spectral regions used the for radiometric calibration. In the gaps the ratio between EM27/SCA and CLARS-FTS spectra exhibits high variability due to low signal caused by water absorption bands.

spectral region [cm-1]
4200 – 4900
5800 – 6650
7700 – 8600
9200 – 10300

ASD spectroradiometer. The calibration was originally recorded in 2013 and confirmed in 2015.

Reflector and Spectralon spectra from EM27/SCA and CLARS-FTS are used for which the integration time fully overlaps, when accounting for the different integration time of both instruments (EM27/SCA 1 min, CLARS-FTS 3 min). Figure 3.21 shows one example pair of spectra. The higher resolution CLARS-FTS spectrum is interpolated to the EM27/SCA spectral sampling and convolved with the EM27/SCA ILS to match the resolution between both spectra. Following Equation (3.28), the CLARS-FTS spectrum is divided by the EM27/SCA spectrum and corrected for the difference in Spectralon and reflector reflectivity by multiplying with the ratio of both reflectivities. For the Spectralon, a wavenumber-independent reflectivity of 0.95 is assumed. For the reflector, a smoothed version of the reflectivity calibration data provided by the manufacturer is used. A low pass filter is applied to the result of Equation (3.28). A 4th-order butterworth filter with a critical frequency of 0.005 is used. Additionally, the water dominated spectral regions are discarded where the ratio strongly varies because of the near zero signal. Table 3.4 lists the spectral regions used to determine the radiometric calibration. In between these spectral regions, the ratio is linearly interpolated. Note that the interpolated regions are not used for further analysis. To keep information on spectral noise, the mean calibration factor in the segment 5900 cm^{-1} to 6300 cm^{-1} is used for the out-of-band region $<$3700 cm^{-1}, from which the noise is determined from during the retrieval. Note that this causes a small inconsistency in the SNR for spectral windows outside this segment. SNR will be overestimated for higher and underestimated for lower wavenumbers. To obtain the calibration, the ratios calculated from 40 spectra pairs are averaged, which were recorded at low SZA ($\theta_s < 32°$) during clear sky conditions between 8 and 14 April 2022. The final calibration is shown in the middle panel of Figure 3.21. The two lower panels in Figure 3.21 show the application of the calibration to sample spectra of the reflector and one target.

The reliability of the radiometric calibration is evaluated by comparing a calibrated spectrum to the top of the atmosphere solar spectrum and looking at the variation with SZA.

For transparent spectral regions, the irradiance measured by the EM27/SCA theoretically can be determined directly from the solar irradiance F_s, SZA θ_s and the reflector reflectivity r (cf. Equation (2.19)).

$$I = \frac{r}{\pi} \cos\theta_s F_s \tag{3.29}$$

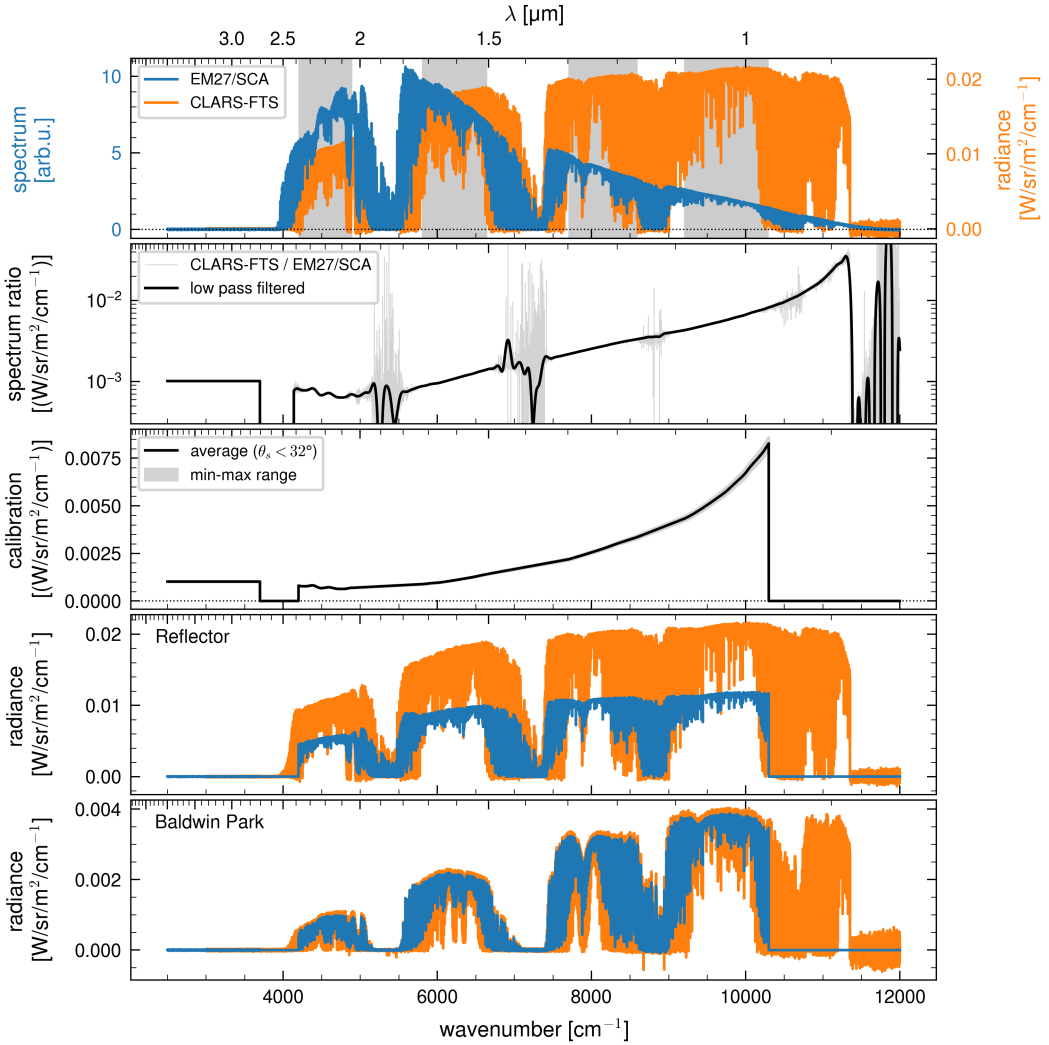

Figure 3.21: Radiometric calibration of the EM27/SCA spectra on the basis of simultaneous calibrated CLARS-FTS measurements. Top panel shows simultaneous spectra of both instruments. The CLARS-FTS spectrum in orange is in radiance units, while the EM27/SCA spectrum is in arbitrary units. The spectral regions marked in gray are used to determine the radiometric calibration. The second panel shows the ratio of both spectra after interpolating and convolving the CLARS-FTS spectrum to EM27/SCA sampling and resolution in grey, and after long pass filtering in black. The third panel shows the average of 40 coadded ratios in black and the min-max range in grey behind it. The two lower panels show simultaneous spectra of the reflector and Spectralon and one target respectively from both instruments. The difference for the reflector spectra originates from the difference in reflectivity between reflector and Spectralon.

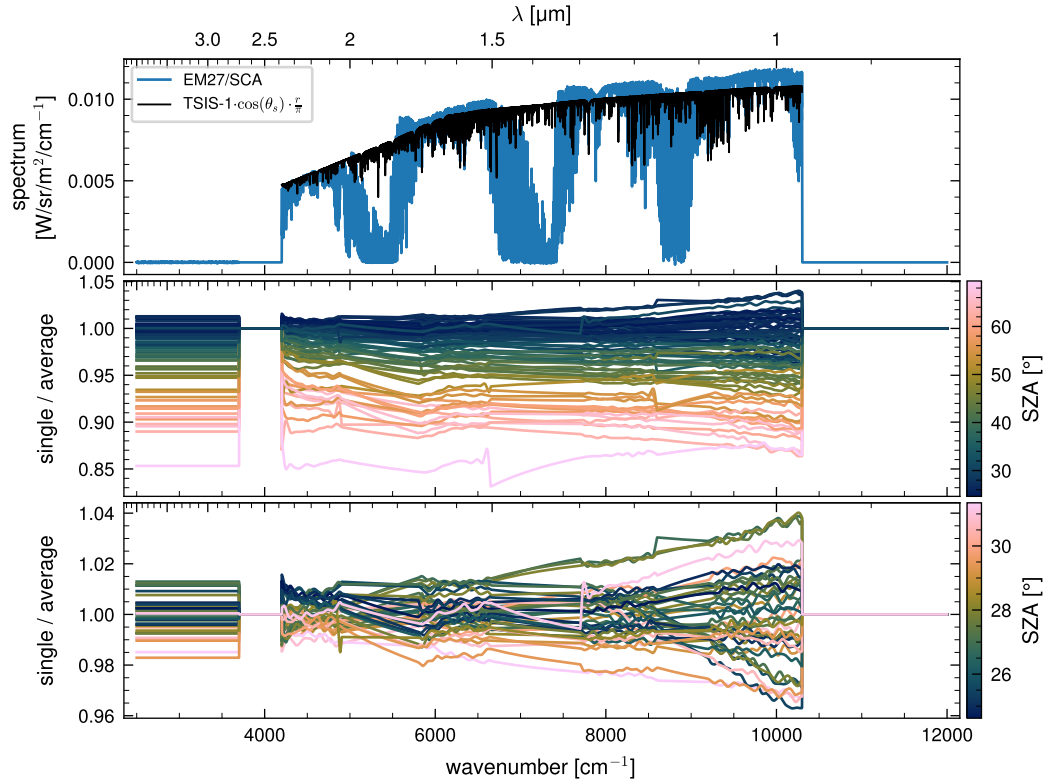

Figure 3.22: Uncertainty indications for the radiometric calibration. The top panel shows a reflector spectrum compared to the correspnding theoretical spectrum, i.e. without any atmospheric influence, but considering SZA and reflector reflectivity. The middle panel shows the ratio between calibration derived from individual spectra pairs and the operational calibration, which is the average of spectra pairs at SZA below 32°. The lowest panels shows the same but only for spectra at low SZA.

Figure 3.22 shows both a measured spectrum as well as an accordingly scaled top of the atmosphere spectrum. Both spectra agree very well in the longwave end of the spectrum. Towards higher wavenumber the measured spectrum exceeds the theoretical one by up to 10 %. Note that atmospheric scattering and unleveled reflector can distort this comparison. The main uncertainty here is the uncertain reflectivity of the aged spectralon plate.

The lower two panels of Figure 3.22 show the SZA dependency of the ratio between the final calibration and calibrations determined from individual spectra pairs. From the middle panel, it is obvious that there is a systematic low bias towards high SZA of up to 10 % to 15 %. The most likely cause is a non-negligible SZA dependency of the spectralon or reflector reflectivity. This seems possible, as the spectralon is exposed to the environment on Mt. Wilson for multiple years and from time to time manually cleaned. Additionally, the inclination of both reflectors could influence this through variations in SZA relative to the reflector surface. The lowest panel gives a estimation of the repeatability, as only SZA $< 32°$ are considered. Here, no clear SZA dependency is visible. Therefore, the repeatability is on the order of a few percent, while the absolute uncertainty is on the order of 10 %. The

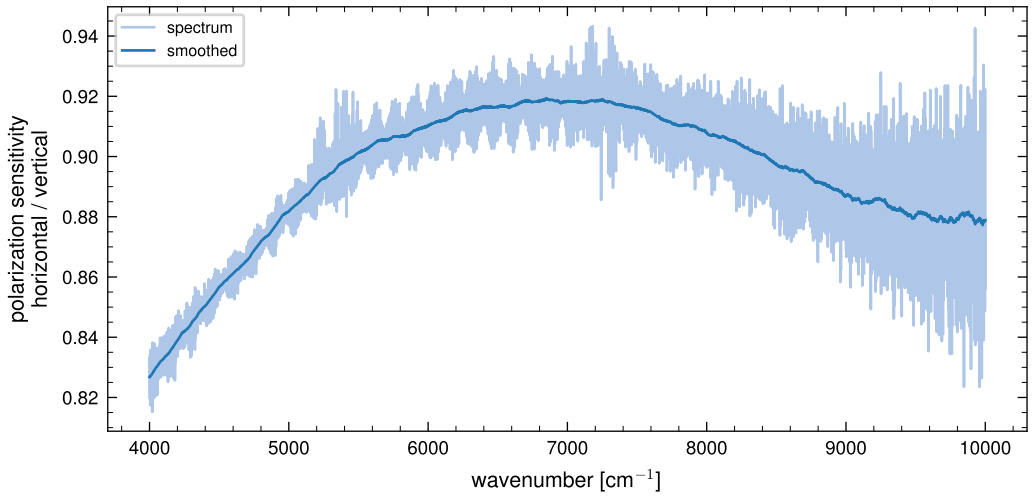

Figure 3.23: Ratio of measurements of light polarized horizontally and vertically with respect to the interferometer plane. This shows that the EM27/SCA shows only a minor sensitivity to the direction of linear polarization. It is 10 % to 15 % less sensitive to horizontally polarized light.

uncertainty in the relative radiances between absorption bands is given by the repeatability and thus approximately 2 %.

3.7 Polarization

Polarization effects can become relevant in the retrieval once atmospheric scattering is considered. Therefore, I evaluate the polarization sensitivity of the EM27/SCA. The component of any FTS influencing the polarization most is typically the beamsplitter due to the difference in reflectivity parallel and orthogonal to the beam splitter plane, as described by the Fresnel equations (Griffiths and de Haseth 2007). The largest difference in polarization should therefore occur horizontally and vertically to the interferometer plane. I test this by replacing the iris aperture with a 25 mm wire grid linear polarizer (Thorlabs WP25L-UB) in a circular mount (Thorlabs SM1FH) with 24 mm clear aperture. Two positions are marked with 90° difference on the mount and the filter is oriented such that one position is horizontal and the other is vertical to the interferometer plane. Spectra are recorded observing the illuminated reflector, with the same procedure as during ILS measurements (cf. Section 3.4.1). First, spectra are recorded with the mount but without polarizer, then I switch twice between the polarizer in vertical and horizontal orientation. 30 10-scan interferograms are averaged per position. The spectra show an etalon structure with a period of 3.35 cm^{-1}, which corresponds to the 1 mm thickness of the linear polarizer glass cover plates. The spectra are averaged over 100 cm^{-1} to smooth the etalon effect before ratioing vertical and horizontal polarized spectra.

Figure 3.23 shows the ratio of the orthogonally oriented spectra. The EM27/SCA is 10 % less sensitive to horizontally polarized light in the 1.6 µm and 1.27 µm spectral region and

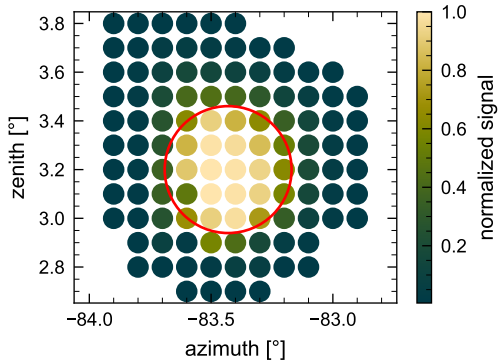

Figure 3.24: Experimental determination the EM27/SCA's FOV. The circle represents the size of the nominal FOV of 9.09 mrad.

15 % less sensitive in the 2 µm region. Additionally, spectra with about 45° polarization lie in between the horizontal and vertical spectra, verifying the assumption that horizontal and vertical axis are the major axes of polarization sensitivity. Note that horizontal and vertical polarization directions are relative to the interferometer plane. However, the pointing system rotates the FOV and thus also the direction of polarization changes depending on pointing azimuth. This means that the pointing direction needs to be accounted for when considering the polarization sensitivity in a retrieval.

ILS retrieved from measurements with both polarizations show a difference in ILS peak height of 1 % to 2 %. The ILS with horizontal polarization is slightly more peaked. This is a systematic difference, considering the short-term repeatability of ILS measurements. However, this difference is within the overall uncertainty of the ILS measurement, especially considering the spectra are recorded with only half the signal, due to the linear polarizer.

3.8 Field of View

The EM27/SCA collects ground-reflected sunlight not from a single point, but from an area defined by its FOV. The nominal FOV is determined by the most slanted light beams that still reach the detector, according to field stop and focal length of the limiting optics. For the EM27/SCA the detector itself acts as field stop. The half opening angle α of the nominal FOV is determined by the focal length of the off-axis parabolic mirror f_{eff} and the detector diameter d.

$$\alpha = \arctan\left(\frac{d}{2f_{\text{eff}}}\right) \tag{3.30}$$

$d = 0.3\,\text{mm}$ and $f_{\text{eff}} = 33\,\text{mm}$ result in a half-angle FOV of 4.545 mrad (full-angle 9.09 mrad).

Besides the nominal FOV, I additionally determine the field of view experimentally. To this end, the signal is recorded while pointing in a grid pattern to a point-like light source. For the point-like source, an iris aperture is added in front of the ILS light source and the light at the sides is blocked with a shielding plate around the aperture. The EM27/SCA

is set up 18 m away from the light source and the iris aperture is closed to 5 mm. In this configuration the light source covers a full opening angle of 0.28 mrad, approximately 3 % of the nominal FOV. Figure 3.24 shows the FOV with the nominal FOV overlayed. The measured FOV agrees broadly with the nominal one, however it is more peaked, but also expands beyond the nominal FOV. Previous measurements without the iris aperture in front of the instrument showed both effects more strongly. While this means that light from further out reaches the detector, the majority of signal comes from a more confined area. The FOV is overall relatively symmetric, with a slight elongation along one direction, which here is the zenith direction. Note that the orientation of the field of view rotates with pointing azimuth angle.

To identify specific ground targets during field measurements, knowledge of the pointing direction of the EM27/SCA is required. To this end, the instrument FOV is identified in pictures of the co-aligned FOV camera. The same light source as for the FOV screening is used. In a first step, the EM27/SCA is pointed to the light source, which is typically placed 18 m from the instrument, and the pointing direction is optimized for maximum signal. After the initial setup of the FOV camera, the camera is coaligned with the EM27/SCA by adjusting the kinematic platform mount such that the light source is roughly in the center of the camera image. Afterwards, the counter screws of the platform are fixed to prevent further movement. The following fine-tuning procedure determines the FOV center pixel in the image. After initially pointing towards maximum signal, the light source aperture is opened such that the signal lays approximately at one third of the available range (10000-12000 counts in *check signal* mode). This denotes a good trade-off between a smaller light source and enough signal for accurate pointing. From the direction of maximum signal, the pointing direction is modified in zenith and azimuth respectively. The pointing directions where the signal drops to half maximum is noted. Finally, the pointing direction is set to the center between these half intensity directions. The FOV center is then determined as the center pixel from an ellipse fit to the light source in the image at the final position. The light source aperture is closed further for this if needed. This procedure is repeated from time to time to detect changes. Differences to previous FOV calibrations are typically only a few pixels, even after transport the FOV only changed by 9px in x and 13px in y direction. In Heidelberg, this procedure was executed in a hallway without light. However, the light source is bright enought so that the procedure also works outside. Before the start of the measurements on Mt. Wilsons, the FOV calibration is performed with a larger distance to the light source of 33 m.

The main uncertainty of the pointing direction is given by the parallax error introduced by the off-center placement of the FOV camera in the beam together with the finite distance of the light source. The camera is located in the vertical beam after the pointing mirrors such that the prism couples light out of the rim of the beam. This means that the distance to the beam axis is given by the arctan of the beam radius, which is approximately 25 mm, divided by the distance to the light source, which is 18 m for measurements in Heidelberg and 33 m for the measurement on Mt. Wilson. The systematic parallax error is therefore 1.4 mrad (0.08°) and 0.76 mrad (0.043°) respectively which accounts for 20 and 10 % of the FOV radius. During operations, FOV drifts of below 0.1° are observed over the course of the day. This is most likely caused by thermal expansion in the pointing system and does

therefore not affect the coalignment of the FOV camera, however it adds to the uncertainty of the pointing itself.

3.9 Scene Heterogeneity

Real world ground scattering targets are not perfectly homogeneous. This can impact the ILS of the FTS. Radiance variations across the FOV change the relative contributions of specific directions to the overall signal. Even in an ideal instrument, this leads to a change in the ILS, since the effective FOV and therefore the self apodization changes. Additionally, shifting the central direction of the effective FOV leads to an inclination with respect to the optical axis of the FOV and accordingly to a spectral shift. A spectral shift in the EM27/SCA spectra can be observed in severely heterogeneous scenes. However, as discussed in Section 3.4, the self apodization contribution to the EM27/SCA ILS is only minor and would therefore only have a minor impact on the retrievals. However, in a real instrument the modulation efficiency might depend on the direction, mainly because of distortions in the focus of the focusing OAP or in its alignment. When the FOV is heterogeneously illuminated, the ILS measurement may no longer be representative for the scene.

Considerable reduction in ILS width are observed for some heterogeneous illumination conditions. These deviations most likely occur as a result from the extended beam diameter of the EM27/SCAs, which is well beyond its regular operation diameter of 0.6 mm. Beam guides and blocks for the metrology laser cut into the parallel beam and there is a section of different material at the side of the beamsplitter where the laser beam is guided through. Additionally, the OAP of the EM27/SCA has a particularly short focal length, which may cause imaging errors whose effect may depend on the direction of the incoming light.

The following sections demonstrate the effect of a heterogenous scene on the ILS through laboratory experiments. Subsequently, the impact in a real-world experiment with a severely heterogeneous scene is present.

3.9.1 ILS under Heterogeneous Illumination

To assess an upper limit for the effect of heterogeneous illuminatio, I investigate how a quadrant based illumination pattern affects the ILS. A 50 cm $\times$ 50 cm reflector plate with reflectivity of 95 % is set up at approximately 7 m distance to the instrument. It is homogenously illuminated with the light source for the ILS measurements. Then, parts of the reflector plate are iteratively shaded, such that only half and later a quarter of the reflector is illuminated. Figure 3.25 shows the illumination pattern. The appropriate shadow positioning is determined by moving inwards from the outside until the signal drops to half. For the quarter reflector observations, the process is repeated with a 90° rotated shadow until the signal is halved again. For each illumination pattern, 30 interferograms are recorded and an ILS is retrieved. First, the experiment is conducted without entrance aperture. Subsequently, it is repeated with the aperture set to a diameter of 2.5 cm to investigate whether the aperture reduces the impact of scene heterogeneity.

Figure 3.26 depicts the ILSs retrieved from measurements with illumination patterns according to Figure 3.25. The ILSs substantially differ from the homogeneously illuminated ILS. Since all ILS are normalized to have an integral of one, the changes in ILS peak height

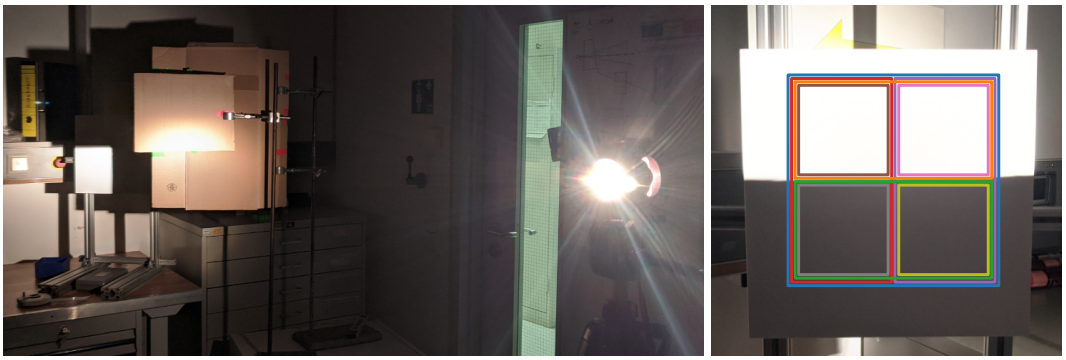

Figure 3.25: The experimental setup to determine a upper limit on the effect of scene heterogeneity on the ILS. The left panel show the setup with light source on the right and the partially illuminated reflector on the left. The shading is achieved by positioning cardboard in between light source and reflector. The right panel shows the reflector illumination patterns.

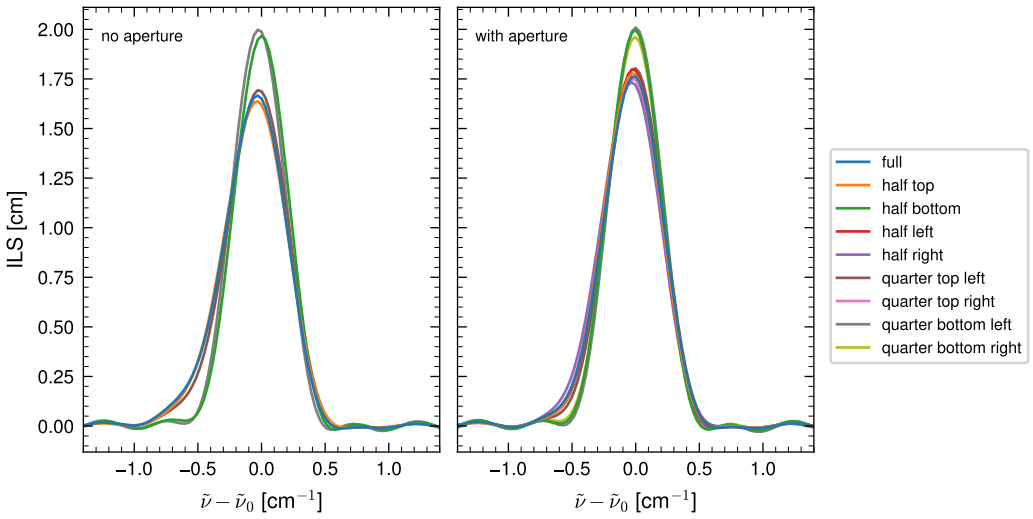

Figure 3.26: ILS retrieved from spectra recorded with different illumination patterns. The colours match the markings in Figure 3.25. Measurements without (left) and with (right) aperture are shown.

are used as a measure for changes in the ILS. In measurements where one or both *bottom* quadrants are illuminated, the ILS peak is 20 % higher. In comparison, for other quadrants the change in peak height is limited to below 4 %. There, cases with more or less peaked ILS occur. A similar pattern with a lower magnitude is present for measurements including the aperture with a diameter of 2.5 cm. The peak height increase for bottom quadrant measurements is now reduced to 14 % but still substantial. The ILSs where the other quadrants are illuminated still differ by about 2 % in peak height. In the measurements, increases in ILS peak height go along with a more narrow and more symmetric shape, as can be seen from the stronger influence on the left shoulder compared to the right shoulder. Overall, the experiment shows that in addition to reducing systematic biases (cf. Section 3.4.5) the reduced sensitivity to scene heterogeneity is a benefit of using the entrance aperture. However, the effect is still prominent making a careful choice of the ground-scattering target inevitable.

To analyze the causes for the change in ILS, I investigate the ME and PE underlying the ILS model. Figure 3.28 shows both parameters for the ILS retrieval from measurements utilizing the entrance aperture. The more sharply peaked ILS results from limited degradation of ME with OPD compared to homogeneous ILS measurements. The ME at maximum OPD is still around 0.8 for the bottom illumination patterns, while ME degrades to 0.4 to 0.5 for all other illumination patterns, including homogeneous illumination. Additionally, the lower phase error leads to a more symmetric ILS shape in these cases. Both effects lead to a more ideal ILS.

3.9.2 Real World Effect of Scene Heterogeneity

The experiment shown in the previous section is certainly an extreme case. I expect that measurements of real heterogeneous targets are less impacted. However, to determine an upper limit for the impact of scene heterogeneity on the retrieval results, a cluster of three targets close to each other is observed. One of the targets is homogeneous (Forest) and two are severely heterogeneous (Molkenkur and Hotel). Figure 3.27 shows all three targets for morning and afternoon illumination situation. Besides the differences in scene heterogeneity between the different targets, the scene changes for each target individually throughout the day. While mainly the overall scene brightness changes for the homogenous Forest target, the walls of the buildings in the other two targets change the brightness within specific regions of the FOV. The brightness variation with sun position are much stronger due to the flat surfaces compared to the vegetation portions of the FOV. Note that scene brightness changes with both solar zenith and azimuth angle when observing non-horizontal surfaces, as the incident angle relative to the surface normal depends on both.

Light paths to all targets sample similar air masses. The target distances are 3.7 km to Forest and 3.1 and 4.1 km to Molkenkur and Hotel respectively. Pointing directions to all target are within 3° in azimuth and zenith direction. The surface between the targets is covered exclusively by forest. The difference in pathlength is mainly caused by the difference in zenith combined with the slope of the hillside. Altitudes vary between 294 m (Molkenkur) and 550 m (Hotel). I expect the atmosphere to be rather homogeneous in the 400 m thick height layer between the instrument and the highest target. Thus, the retrieved CO_2 concentration can be assumed similar between all targets.

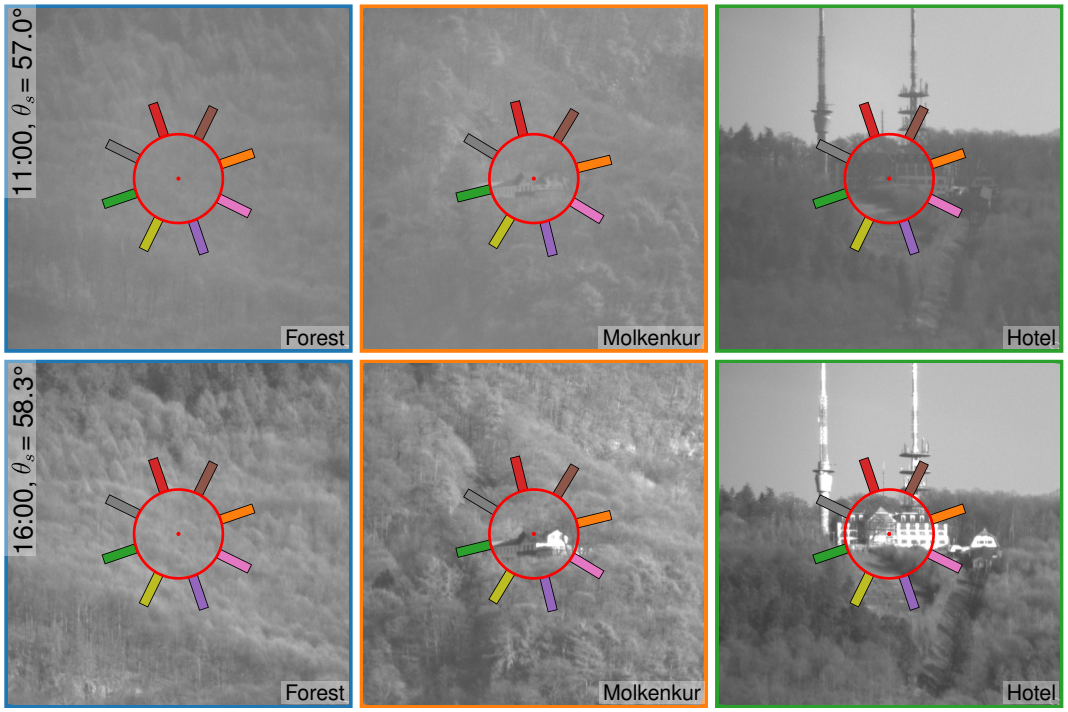

Figure 3.27: Targets selected for the heterogeneity experiment on 2021-03-02. While the forest target is rather homogeneous, the Molkenkur and Hotel targets are two heterogeneous cases. The targets are shown during different illumination conditions influencing scene homogeneity at 11:00 UTC (SZA = 57.0°, top panel) and 16:00 UTC (SZA = 58.3°, bottom panel). The red circle marks the nominal FOV and the outgoing colored bars mark the corresponding direction of the illumination patterns in the heterogeneous illumination ILS experiment (cf. Figures 3.25 and 3.26)

Figure 3.29 displays the XCO_2 values retrieved from measurements of all three targets. Initially, the ILS measured under homogeneous illumination is used. For the Hotel target, the XCO_2 continuously increases, while for the other two targets only a minor decreasing trend is visible. The increasing excess of Hotel over Forest measurements is in agreement with the hypothesis that an increasingly heterogeneous scene for the Hotel target influences the retrievals. A mismatch between the ILS used in the retrieval and the real ILS results from the heterogeneous scene. Assuming a wider ILS in EM27/SUN retrievals leads to a overestimation in XCO_2 (Alberti et al. 2022; Tu 2019). To retrieve the correct XCO_2, an ILS representative of the scene must be used. The previous laboratory measurements provide the possibility to derive a representative ILS. The Hotel scene is extreme, but still less extreme than the laboratory illumination patterns. Thus, the representative ILS is exptected to lie in between the laboratory ILS. Intermediate ILSs are generated from ME and PE parameters which are weighted between the homogeneously measured ME_{hom}, PE_{hom} (*full*, blue) and the extreme measurement ME_{het}, PE_{het} (*quarter bottom left*, grey).

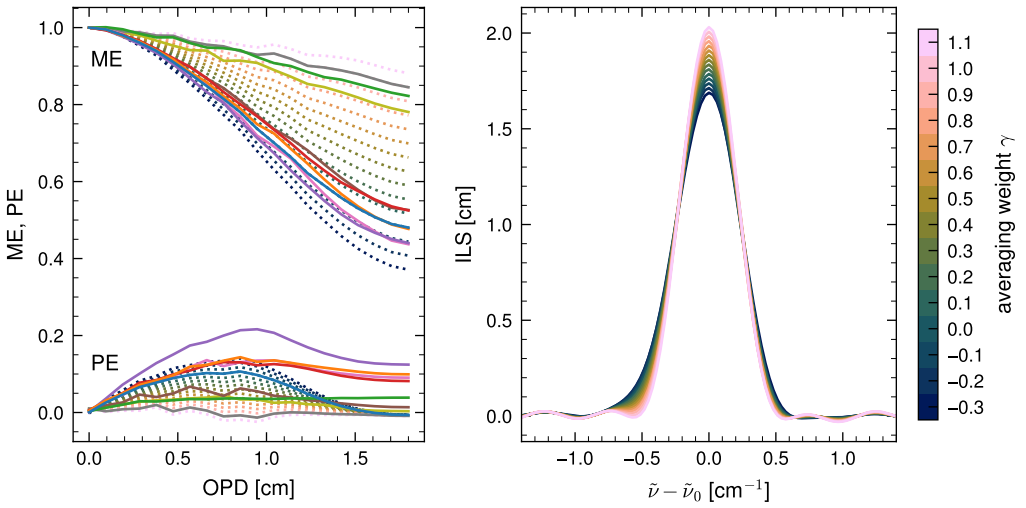

Figure 3.28: The left panel shows ME and PE for the ILS (with aperture) shown in Figure 3.26 (lines). Colours of the lines match the ILS presented there. ILS deviating from the homogeneous scene ILS by a variable degree (dotted) are used to investigate the effect of scene heterogeneity on real measurements. The right panel shows the ILS generated from the parameters on the left.

$$\mathrm{ME} = (1-\gamma)\cdot \mathrm{ME}_{\mathrm{hom}} + \gamma \cdot \mathrm{ME}_{\mathrm{het}} \tag{3.31}$$

$$\mathrm{PE} = (1-\gamma)\cdot \mathrm{PE}_{\mathrm{hom}} + \gamma \cdot \mathrm{PE}_{\mathrm{het}} \tag{3.32}$$

Here, γ is the weight between both ILS. The ILS and its ME and PE parameters are shown in Figure 3.28. This parameterization represents all laboratory measurements fairly well. For the ME, this is straight forward to identify. For the PE, this representation is also fairly good, since adding a straight line through the origin to the PE does not change the resulting ILS. This means that the PE of blue, orange, red and pink measurements generate nearly identical ILS. Even blue and purple PE show only minor differences.

I repeat the retrieval of the Hotel target scene with each of these ILS. The reduced χ^2 for the retrievals is shown in the lower panel of Figure 3.29. The χ^2 in the morning is lowest for $\gamma = 0$, which corresponds to the ILS measured under homogeneous illumination. χ^2 for this ILS substantially increases throughout the day. For afternoon measurements, retrievals with higher γ ILS fit significantly better. At the end of the time series χ^2 is lowest for $\gamma = 0.4$. Observing the Hotel target XCO_2 values resulting from the retrieval with the $\gamma = 0.4$ ILS, the XCO_2 values agree well with the other targets in the afternoon.

Turning the attention towards the Molkenkur target, the XCO_2 values agree well with the homogeneous Forest target, despite the clearly heterogeneous scene. Additionally, the χ^2 for this target is consistently lowest for retrievals using ILS with γ close to zero. χ^2 for retrievals using $\gamma = 0.1$ or 0.2 ILS is only marginally different from retrievals using the $\gamma = 0$ ILS, reflecting the measurement uncertainty. This shows that not all heterogeneous scenes suffer from systematic errors. This is plausible, considering that also in the

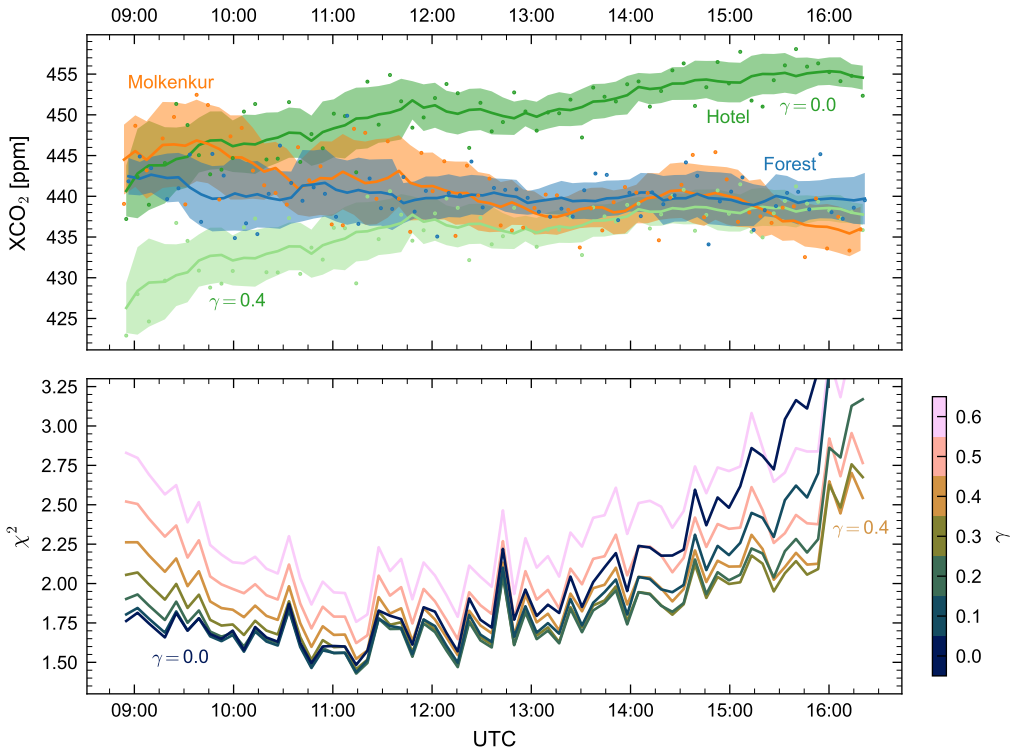

Figure 3.29: Effect of a heterogeneous scene on the retrieved column-averaged dry-air mole fraction (cf. Equation (5.11)). The upper panel shows XCO_2 retrieved from the targets Forest (blue), Molkenkur (orange) and Hotel (green, dark shade) using the homogeneous scene ILS. The lower panel shows the χ^2 of retrievals of the Hotel target with different ILS (cf. Figure 3.28). XCO_2 retrieved from the Hotel target using the $\gamma = 0.4$ ILS is shown in light shade green in the top panel.

laboratory measurements not all illumination patterns impacted the ILS retrievals equally. Patterns where *bottom* quadrants were illuminated showed significantly more peaked ILS. The colored markers in Figure 3.27 show the orientation of the laboratory illumination patterns after accounting for viewing direction during the measurements. Here, the *bottom* quadrants correspond to the left side of the FOV. The Molkenkur target scene does not exhibit increased illumination in this area, while the Hotel building extends to this region of the FOV, making the different impact of both heterogeneous scenes plausible.

In conclusion, considerable systematic errors of up to 15 ppm in XCO_2 can be introduced by real-world heterogeneous scenes. Severely impacted scenes can be diagnosed by comparing the χ^2 of retrievals using parameterized ILS. However, a correction by using the minimal χ^2 ILS for retrievals can not avoid the systematic error, as the χ^2 is similar for γ in a range of ± 0.1, which corresponds to a XCO_2 offset of close to ± 5 ppm. Additionally, the impact of scene heterogeneity depends on the specific contrast distribution across the FOV. Overall these findings emphasize the need for careful selection of the ground scattering targets.

4 Retrieval

The previous chapter presented a spectrometer which measures atmospheric absorption spectra. These measurements provide the foundation to infer information on the absorbing gases in the atmosphere. The information is encoded in the telluric absorption lines in the spectra and has to be extracted by means of an inverse retrieval method. This chapter first introduces the fundamental concepts of such an inverse method (Section 4.1). Subsequently, Section 4.2 describes the observational geometry of the measurements within this thesis. Based on this, the retrieval is presented in Chapter 4, focusing on two forward models (with and without scattering) used for the evaluation in Chapter 5. Section 4.4 names the data sources for the auxiliary data used. Section 4.5 describes the configuration of the spectral retrieval windows. Section 4.6 concludes by describing the data filtering criteria.

4.1 Inversion Theory

This section introduces the basic concepts of inverse theory, which is used to infer GHG column densities from the measured spectra. The theory presented relies on the textbooks by Aster et al. (2013) and Rodgers (2000).

The absorption processes modify the spectrum of solar light as it traverses the atmosphere. Modeling the final spectrum based on a given atmospheric state constitutes the forward problem. The problem is represented mathematically via the atmospheric state vector $\mathbf{x}$ and the measurement vector $\mathbf{y}$, which in this case is the measured spectrum. The physical processes, the absorption and the radiative transfer, are approximated by the forward model $\mathbf{F}$, which translates $\mathbf{x}$ to a simulated measurement $\hat{\mathbf{y}}$ by

$$\hat{\mathbf{y}} = \mathbf{F}(\mathbf{x}) \,. \tag{4.1}$$

Both forward model and measurement introduce an error, leading to differences in measured and simulated spectrum.

$$\mathbf{y} = \mathbf{F}(\mathbf{x}) + \varepsilon_F + \varepsilon_\mathbf{y} \tag{4.2}$$

The forward model error $\varepsilon_\mathbf{F}$ arises either from the incomplete representation of the physical processes or errors in the model parameters. Typical model errors result from errors in the spectroscopic parameters, the absorption cross section parameterization, simplifications in the atmospheric state model (e.g. plane-parallel approximation), aerosol representation, the radiative transfer model (e.g. neglect of scattering) or from uncertainty in the a priori information (e.g. meteorological data and solar spectrum). This type of error can not be treated within the inversion itself, but has to be investigated through the comparison to more sophisticated models or independent data. The measurement error $\varepsilon_\mathbf{y}$ represents the

uncertainty inherent to any real measurement $\mathbf{y}$. Ideally, it is of statistical nature. Assuming it is, we can describe it by the error covariance matrix $\mathbf{S_y}$ and propagate it with the forward model to estimate the error it causes in the retrieval.

While the forward problem concerns accurately simulating the measurement, the goal of the inverse problem is to extract information of the underlying state from an observation. We want to estimate the state vector $\hat{\mathbf{x}}$ that best matches the observation $\mathbf{y}$. The most simple approach is the least-squares method, in which we minimize the difference between measurement and forward model.

$$\hat{\mathbf{x}} = \arg\min_{\mathbf{x}} \left(\|\mathbf{F}(\mathbf{x}) - \mathbf{y}\|^2 \right) \tag{4.3}$$

In case of a linear forward model, $\mathbf{F}$ can be represented by a matrix $\mathbf{K}$. In this case, we can directly solve the problem by using normal equations.

$$\hat{\mathbf{x}} = (\mathbf{K}^T\mathbf{K})^{-1}\mathbf{K}^T\mathbf{y} \tag{4.4}$$

However, the radiative transfer described here has a non-linear forward model. To still be able to solve the inverse problem, we linearize the forward model around a given state $\mathbf{x}_0$ and determine the best estimate iteratively. The linearization is given by

$$\mathbf{F}(\mathbf{x}) = \mathbf{F}(\mathbf{x}_0) + \mathbf{K}(\mathbf{x} - \mathbf{x}_0) + \mathscr{O}(\mathbf{x}^2)\,, \tag{4.5}$$

where the weighting function matrix $\mathbf{K}$, also known as the Jacobian, contains the partial derivatives of the forward model elements with respect to the state vector elements.

$$K_{ij} = \frac{\partial \mathbf{F}_i}{\partial x_j} \tag{4.6}$$

We can find $\mathbf{K}$ either analytically or numerically by evaluating finite differences in the forward model when perturbing individual state vector elements. With the linearized forward model, we find the best matching state (e.g. with a least-squares method) and subsequently linearize again around the solution. We iterate this procedure to find the final best estimate state.

The inverse problem discussed within this thesis is ill-posed. Not enough information is contained in the measurement to determine all state vector elements independently. Instead, we use a priori knowledge to regularize the problem and reduce the degrees of freedom. The Tikhonov-Phillips regularization modifies the minimization term (cost function) to achieve this. An additional term extends the cost function based on the difference between the state vector and the a priori.

$$\hat{\mathbf{x}} = \arg\min_{\mathbf{x}} \left(\left\| \mathbf{S_y}^{-\frac{1}{2}} (\mathbf{F}(\mathbf{x}) - \mathbf{y}) \right\|^2 + \gamma \|\mathbf{L}(\mathbf{x} - \mathbf{x_a})\|^2 \right) \tag{4.7}$$

Here, we added $\mathbf{S_y}$ to the least-squares term to normalize the deviation between simulated and measured spectrum by the measurement error. The regularization parameter γ determines the strength of the regularization by scaling the penalty term. The regularization matrix $\mathbf{L}$ determines on what property of the difference to the a priori we regularize. The two most simple choices for $\mathbf{L}$ are the unity matrix and the first order difference operator.

Using the unity matrix results in regularizing to the absolute difference to the a priori. If we use the first order difference operator, we penalize deviations in the first derivative of the difference, but not the absolute value. For absorber profiles this regularizes the profile shape, freely allowing a flat scaling of the full profile. In practice, we can use combinations of regularizations by constructing the regularization matrix from different submatrices. This additionally allows us to use different regularization parameters for parts of the state vector. For the linearized forward model, Equation (4.7) is minimized by

$$\hat{\mathbf{x}} = \mathbf{x}_\mathrm{a} + (\mathbf{K}^T {\mathbf{S}_\mathbf{y}}^{-1} \mathbf{K} + \gamma \mathbf{L}^T \mathbf{L})^{-1} \mathbf{K}^T {\mathbf{S}_\mathbf{y}}^{-1} (\mathbf{y} - \mathbf{F}(\mathbf{x}_\mathrm{a}))\,. \tag{4.8}$$

From this, we define the gain matrix $\mathbf{G} = (\mathbf{K}^T {\mathbf{S}_\mathbf{y}}^{-1} \mathbf{K} + \gamma \mathbf{L}^T \mathbf{L})^{-1} \mathbf{K}^T {\mathbf{S}_\mathbf{y}}^{-1}$ as the link between the model mismatch and the state vector update. We can interpret $\mathbf{G}$ as the generalized inverse of $\mathbf{K}$.

$$\hat{\mathbf{x}} = \mathbf{x}_\mathrm{a} + \mathbf{G}(\mathbf{y} - \mathbf{F}(\mathbf{x}_\mathrm{a})) \tag{4.9}$$

Since the best estimate state vector is iteratively determined, we are interested in computing the state vector update from the i-th iteration. This is given by

$$\mathbf{x}_{i+1} = \mathbf{A}\mathbf{x}_i + (1 - \mathbf{A})\mathbf{x}_\mathrm{a} + \mathbf{G}(\mathbf{y} - \mathbf{F}(\mathbf{x}_i))\,, \tag{4.10}$$

where we defined the averaging kernel matrix $\mathbf{A} = \mathbf{G}\mathbf{K}$. With this, the best estimate $\hat{\mathbf{x}}$ can be found with an appropriate iteration scheme and convergence criterion. The averaging kernel describes the sensitivity of the retrieval to the true state $\mathbf{x}_\mathrm{t}$. Accounting for the model and measurement error, we can express the dependency of the retrieval on a priori and true state as

$$\hat{\mathbf{x}} = \mathbf{A}\mathbf{x}_\mathrm{t} + (1 - \mathbf{A})\mathbf{x}_\mathrm{a} + \mathbf{G}\varepsilon_\mathbf{F} + \mathbf{G}\varepsilon_\mathbf{y}\,. \tag{4.11}$$

This shows that the retrieval not only depends on the measurement, but also on the a priori, since the regularization imposes boundaries to the estimation. The degrees of freedom for signal (DFS) are given by the trace of $\mathbf{A}$. The residual, which is the mismatch between model and measurement, is important for the analysis of the retrieval. As a simpler measure of retrieval quality, we evaluate the reduced χ^2. It is defined as the mean of the square residual, normalized to measurement error, accounting for the DFS.

$$\chi^2 = \frac{1}{(N - \mathrm{DFS} - 1)} \sum_{i=1}^{N} \left(\frac{y_i - F_i(\hat{\mathbf{x}})}{\sigma_i} \right)^2 \tag{4.12}$$

Here, σ_i is the i-th diagonal element of $\mathbf{S}_\mathbf{y}$ and N the number of spectral datapoints.

4.2 Observation Geometry

The EM27/SCA measures absorption spectra of ground-scattered sunlight in the *reflected-sunlight* measurement geometry. Depending on the surface topography, this is generally possible in either *downward* or *upward* viewing geometry. Here, only the downward viewing geometry is relevant, where the instrument is positioned at an elevated location (natural

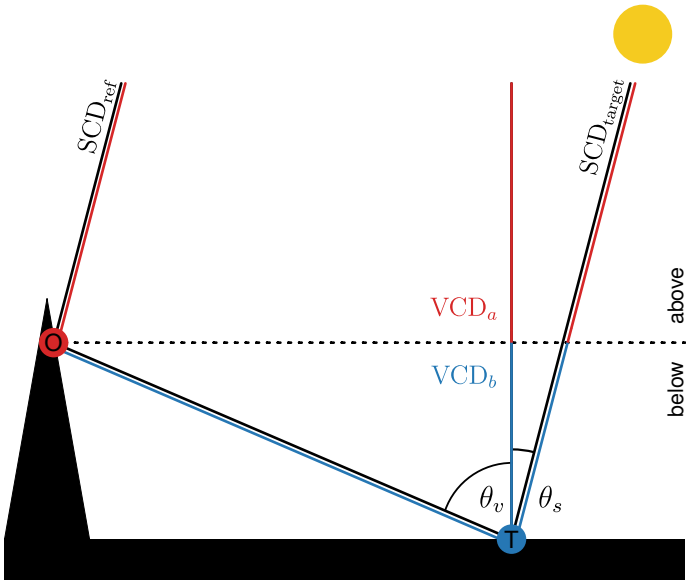

Figure 4.1: Observational geometry of the EM27/SCA. Panel (a) shows the downward viewing geometry with the observer (O) in an elevated location pointing down towards a target (T). Panel (b) shows the upward viewing geometry with the observer on the ground pointing up towards an elevated target.

elevation or high building), observing ground targets at lower altitude. The upward viewing geometry is outlined in Appendix A.5.

Figure 4.1 displays the downward viewing geometry. Overall, the observational geometry is determined by the position of the sun and the viewing direction of the instrument. They are represented by SZA θ_s and solar azimuth angle (SAA) ϕ_s, as well as viewing zenith angle (VZA) θ_v and viewing azimuth angle (VAA) ϕ_v. Neglecting atmospheric scattering, the geometric light path from the sun to the observer consists of a *vertical* component from the top of the atmosphere to the ground and a *horizontal* component from the ground through the planetary boundary layer to the instrument. Note that despite being termed that way, the light path components are not strictly vertical or horizontal. The vertical path is slanted due to the SZA, and the horizontal path is slanted due the VZA.

The target distance as well as the viewing angles θ_v and ϕ_v are calculated from the Global Positioning System (GPS) coordinates of observer O and target T. Given their latitude (lat), longitude (lon) and altitude (alt) the slant target distance d is given by

$$d = \sqrt{(d_\mathrm{hrz})^2 + (\mathrm{alt_O} - \mathrm{alt_T})^2}, \tag{4.13}$$

where the horizontal distance d_hrz is calculated via the haversine formula

$$d_\mathrm{hrz} = 2R_\mathrm{E} \arcsin\left(\sqrt{\left(\sin\frac{\mathrm{lat_T} - \mathrm{lat_O}}{2}\right)^2 + \cos(\mathrm{lat_T})\cos(\mathrm{lat_O})\left(\sin\frac{\mathrm{lon_T} - \mathrm{lon_O}}{2}\right)^2}\right), \tag{4.14}$$

with the Earth's radius R_E. The viewing angles are computed with

$$\theta_\mathrm{v} = \pi - \arctan\left(\frac{\mathrm{alt_O} - \mathrm{alt_T}}{d}\right), \tag{4.15}$$

$$\phi_\mathrm{v} = \frac{3\pi}{2} - \arccos\left(\frac{\mathrm{lat_O} - \mathrm{lat_T}}{(\mathrm{lon_O} - \mathrm{lon_T})\cos(\mathrm{lat_O})}\right), \tag{4.16}$$

where the $\cos(\mathrm{lat_O})$ term accounts for the distance covered by the same longitude angle being different with latitude.

It is inherent to the reflected-sun viewing geometry that not all atmospheric layers contribute equally to the absorption signal. The light path traverses the layer below the observer twice. Additionally, the second pass occurs under a shallow viewing angle. This leads to an enhanced light path in the atmospheric layer below the observer. Therefore, the measurement is more strongly influenced by the concentration in this layer. It is generally desirable to retrieve the vertical column density (VCD) from solar absorption spectra, since this quantity has no explicit dependency on the SZA. Both satellite-based and ground-based solar absorption measurements typically report total VCDs. However, the enhanced sensitivity below the observer level complicates the interpretation of the VCD in our case considerably. For the performance analysis within this thesis the slant column densitys (SCDs) is used, because they are directly related to the optical thickness measured in the spectrum. SCDs are defined as

$$\mathrm{SCD} = \mathrm{VCD} \cdot \mathrm{AMF}, \tag{4.17}$$

where the air mass factor (AMF) is the ratio between the geometric light path through the atmospheric layer and the layer's height. It is prescribed by the SZA for the vertical (AMF_v) and by the VZA for the horizontal path component (AMF_h).

$$\mathrm{AMF}_v = \frac{1}{\cos(\theta_\mathrm{s})}, \mathrm{AMF}_h = \frac{1}{\cos(\theta_\mathrm{v})} \tag{4.18}$$

Despite their usefulness for performance analysis, SCDs are not suitable for direct interpretation, because the largest variability is the change in the SZA with time. Therefore, I focus on partial VCDs for layers with mostly horizontal and mostly vertical light path. This is the case for the layer between target and observer level ($\mathrm{VCD_b}$), as well as the remaining atmosphere above that ($\mathrm{VCD_a}$). $\mathrm{VCD_a}$ and $\mathrm{VCD_b}$ are deduced from the combination of the target measurement with and the reflector measurement without a horizontal path component. In the downward viewing geometry, the AMF is given by the vertical AMF above and the sum of vertical and horizontal AMF for below observer level.

$$\mathrm{AMF}_a = \frac{1}{\cos(\theta_\mathrm{s})}, \mathrm{AMF}_b = \frac{1}{\cos(\theta_\mathrm{s})} + \frac{1}{\cos(\theta_\mathrm{v})} \tag{4.19}$$

The partial $\mathrm{VCD_a}$ above instrument level is directly given by the SCD of the reflector measurement. The partial $\mathrm{VCD_b}$ below instrument level is given by the difference between target and reflector measurement, accounting for the AMF_b.

$$\mathrm{VCD}_a = \mathrm{VCD}_{\mathrm{ref}} \tag{4.20}$$

$$\mathrm{VCD}_b = \frac{\mathrm{SCD}_{\mathrm{target}} - \mathrm{SCD}_{\mathrm{ref}}}{\frac{1}{\cos(\theta_{\mathrm{v}})} + \frac{1}{\cos(\theta_{\mathrm{s}})}} \tag{4.21}$$

4.3 Retrieval Setup

The retrieval infers the absorber VCDs from the measured spectra. I use a modified version of the RemoTeC radiative transfer and retrieval algorithm (Butz et al. 2012; Butz et al. 2011; Butz et al. 2010; Butz et al. 2009). It was developed for trace gas retrievals from NIR satellite measurements, but was previously adapted for direct-sun viewing ground-based observers. The forward model simulates the measurement from the state vector, which contains the absorber profiles in terms of partial VCDs. RemoTeC uses a Gauss-Newton scheme with reduced step size (Butz et al. 2012) to iteratively find the state vector for which the forward model best matches the measurement.

The forward model is adapted to accurately represent the observational geometry of the ground-scattered sunlight measurements. Two forward models are used for the downward viewing geometry. The first one neglects scattering by particles in the atmosphere, effectively corresponding to Beer-Lambert's law including a Lambertian surface reflection (Equation (2.25)). The bulk of the performance assessments of the EM27/SCA is performed with this forward model. However, Section 5.6 shows that aerosol scattering is the most important error source in this configuration. Therefore, I employ a second forward model which includes aerosol scattering in the atmospheric layer between instrument and target. Both forward models are described in more detail in Sections 4.3.1 and 4.3.2.

The forward model computes the radiative transfer in a plane-parallel model atmosphere, simulating the transmission spectrum from the state vector. The state vector contains the partial VCDs of the target absorbers in six layers. For reflector retrievals, the layers are equally sized in pressure. For target measurements, I construct the model atmosphere so that one layer lies between the instrument and the target. The other five layers are distributed equally in pressure above. In each layer, the radiative transfer is calculated in six sublayers (36 in total), which are again split in two for the calculation of the absorption cross sections from spectroscopic parameters at the appropriate pressure and temperature (72 layers in total).

The spectra do not contain enough information to retrieve profile information for the target absorbers. Therefore the retrieval is regularized such that there is only one degree of freedom for each absorber (see Sections 4.3.1 and 4.3.2). Two different approaches for regularization are used. First, the *profile scaling* regularization, where the absorber profile is scaled equally in all layers from the a priori profile. This is achieved by strongly regularizing the first derivative of the difference to the a priori profile. This effectively constrains the retrieval to uniform scaling of the a priori profile, such that the VCD is retrieved while preserving the shape of the a priori profile. This regularization is used in other retrieval algorithms for ground-based direct-sun measurements, i.e. GFIT and PROFFAST for Total Carbon Column Observing Network (TCCON) and COCCON. Profile scaling regularization is used for all reflector measurements and for the target measurements in scattering

retrievals. The second regularization approach is the *overhead* regularization. For this approach, the absorber profile is forced to the a priori profile above the instrument level, leaving one degree of freedom for the lowest layer. This means that while the layers above the instrument are fixed to the prior, the lowest layer is not regularized at all. I employ this approach for the non-scattering retrieval of target measurements. For these retrievals, the neglect of aerosol scattering below instrument level is expected to be the largest error. Therefore, the overhead regularization approach is used here in order to avoid propagating this error to the layers above instrument level. Otherwise, part of the error would be attributed to layers with lower pressure. There, the pressure broadening is lower and the line saturates faster, causing an additional error in the retrieved column density.

The measurement vector consists of parts of the measured spectrum, called the retrieval windows, where the absorption features of interest are located. The state vector contains, most importantly, the partial VCDs of the absorbers of interest. However, typically absorption features from other molecules spectrally overlap with the target absorber signature. These interfering absorbers are modeled simultaneously with the target absorbers. Therefore, the state vector additionally contains their total VCDs. Further, it includes information about the spectral retrieval windows, namely the coefficients of the albedo polynomials as well as spectral shift parameters. For scattering retrievals, the state vector additionally includes parameters for aerosol load, size and height distribution.

4.3.1 Non-Scattering Forward Model

In the non-scattering retrieval, the forward model is given by Beer-Lambert's law (Equation (2.11)) accounting for the surface reflection. Evaluating Beer-Lambert's law for each layer with the input radiance from the previous layer corresponds to adding the optical thickness of each layer l. Including the surface reflection modeled as a Lambertian reflection, the forward model calculates the measured radiance to

$$I_{\text{obs}} = r\frac{\mu_{\text{s}} F_{\text{s}}}{\pi} e^{-\Sigma_l \hat{\tau}_l}\,, \tag{4.22}$$

where F_{s} is the solar irradiance, μ_{s} is the cosine of the SZA, r is the surface albedo and $\hat{\tau}_l$ is the absorption optical path in each layer l. This corresponds to Equation (2.25). I_{obs} is calculated for each wavenumber in the specified retrieval windows. The optical thickness for each layer is calculated from the partial VCD, the AMF and the average absorption cross section σ_a in the layer

$$\hat{\tau}_l = \langle \sigma_a \rangle_l \cdot \text{VCD}_l \cdot \text{AMF}_l\,, \tag{4.23}$$

where the AMF is different for layers above (AMF_a) and below instrument level (AMF_b). The AMF is calculated from the SZA θ_{s} and the VZA θ_{v} according to Equation (4.19). The albedo is retrieved in each window individually, accounting for its broadband wavelength dependency by approximating it with a low-order polynomial.

4.3.2 Scattering Forward Model

The scattering forward model calculates the radiative transfer, explicitly including the scattering by particles in the atmosphere below instrument level. Here, the LINTRAN radiative transfer model (RTM) (Schepers et al. 2014) is used, which applies forward adjoint perturbation theory. The model was developed specifically for simulating radiance observations by satellites. To employ forward adjoint perturbation theory, it relies on the interchangeability of source and observer. In the viewing geometry here, the source is at the top of the atmosphere but the observer is within the atmosphere. Therefore, LINTRAN can not be used immediately. However, the geometry below instrument level resembles the satellite geometry at very shallow viewing angle. Therefore, the downward radiance at instrument level is calculated without scattering by using Beer-Lambert's law for all layers above the instrument level obs

$$I^{\downarrow}_{\text{obs}} = I_s \, e^{-\Sigma_{l>\text{obs}} \tau_l} \tag{4.24}$$

and use this as input for the LINTRAN RTM. Any photons scattered above instrument level would have to undergo a second scattering event below instrument level or be reflected off the ground to reach the detector. Assuming a low to moderate scattering optical depth in the free troposphere above the instrument, the contribution of these photons is expected to be lower than directly scattered photons. Despite the model error introduced by neglecting overhead scattering, I expect the overall model error to be much lower than for the non-scattering retrieval.

The optical properties of the aerosols are computed from microphysical quantities. They are computed through Mie theory from the aerosol size distribution and the complex refractive index. The size distribution is parameterized as a log-normal distribution with an effective radius and a width parameter. The given number of aerosols is vertically distributed across the layers according to a Gaussian distribution. I refer to the mean of the Gaussian distribution as the aerosol layer height (ALH). The Gaussian distribution is cut off at instrument and ground level, but the additional particles are redistributed accordingly. The RTM then calculates the backscattered radiance for the given solar and viewing direction.

There is not enough information in the measurements to determine all parameters related to aerosol scattering. The refractive index ($n = 1.4 + 0.001i$) as well as the widths of the size (0.5 µm) and the height distribution (500 m) are fixed a priori. The state vector elements describing the aerosol particles are the column density of scattering particles, the effective radius r_{eff} of their size distribution and the ALH. Additionally, the aerosol state vector elements need to be regularized for the retrieval to successfully converge. r_{eff} and the ALH are regularized but not the column density. Depending on the measurement, this results in 1 to 3 degrees of freedom for scattering signal (DFSS). As mentioned above, the profile scaling approach is used to regularize the absorber profile, since scattering is explicitly accounted for.

4.4 A Priori Information

This section summarizes the auxiliary data used in the retrieval. I present the data sources underlying the a priori gas profiles (Section 4.4.1), the top of the atmosphere solar spectrum (Section 4.4.2) and the spectroscopic database from which the absorption cross sections are computed (Section 4.4.3).

4.4.1 A Priori Absorber Profiles and Meteorological Information

A priori profiles for the different absorbers are derived from several models. For meteorological data, I use the NCEP FNL Operational Model Global Tropospheric Analyses (NCEP 2000). I obtain the surface pressure for target measurements by interpolating the pressure to the target location and measurement time. I use in situ measured pressure averaged over a 10 min interval centered on the time of measurement for the instrument pressure level. For reflector measurements, this simultaneously constitutes the surface pressure.

The a priori profiles for the absorbers are derived from CarbonTracker CT2019B (Jacobson et al. 2020) for CO_2 and from TM4 (Meirink et al. 2006) for CH_4 and CO. The profiles are interpolated to the measurement location and time. The O_2 and H_2O profiles are derived from the NCEP data.

4.4.2 Solar Spectrum

As input solar spectrum, the TSIS-1 Hybrid Solar Reference Spectrum (HSRS) is used (Coddington et al. 2021). It combines datasets with high spectral resolution from various sources with radiometrically calibrated but low resolution measurements of the Spectral Solar Irradiance Sensor-1 Spectral Irradiance Monitor (TSIS-1 SIM, Richard et al. (2020)) and Compact Spectral Irradiance Monitor (CSIM, Richard et al. (2019)). They measure top of the atmosphere spectra from the International Space Station (ISS) and from a sun-synchronous 575 km orbit, respectively. The high resolution dataset in the spectral range used here is a pseudo transmission spectrum generated with a disk-integrated solar line list (Toon 2015). The spectrum is generated by iteratively removing telluric absorption lines from spectra measured with different instruments. Mainly high resolution spectra recorded on Kitt Peak National Observatory are used, but spectra from the Atmospheric Trace Molecule Spectroscopy (ATMOS) experiment during ATLAS shuttle flights and MkIV balloon spectra are incorporated as well (Toon 2010, private comm.). Note that TSIS-1 HSRS is also used for the non-scattering retrieval, where the radiometric calibration of the solar spectrum is not requried. Using the solar line list directly results in differences in the CH_4 retrieval results (see Appendix A.6).

4.4.3 Spectroscopic Database

The forward model computes the radiative transfer in a plane-parallel model atmosphere, where each layer is associated with a pressure and a temperature. For each layer, Voigt lineshape absorption cross sections are calculated based on spectroscopic parameters provided by the HITRAN version 2020 database (Gordon et al. 2022). For the O_2 CIA pseudo

Table 4.1: Spectral range and absorbers in the different retrieval windows.

ID	spectral range		width	absorber		AP*
	exact [cm^{-1}]	rounded [µm]	[cm^{-1}]	target	interfering	
W1	7765 – 8005	1.25–1.29	240	O_2	H_2O, O_2 CIA	5
W2	6180 – 6260	1.60–1.62	80	CO_2	H_2O	4
W3	6297 – 6382	1.57–1.59	85	CO_2	H_2O	4
W4	5880 – 5996	1.67–1.70	116	CH_4	H_2O	4
W5	6007 – 6145	1.63–1.66	138	CH_4	H_2O, CO_2	4
W6	4208.7 – 4257.3	2.35–2.38	48.6	CO	H_2O, HDO, CH_4	4
W7	4262.0 – 4318.8	2.32–2.35	56.8	CO	H_2O, HDO, CH_4	4
W8	4762 – 4898	2.04–2.10	136	CO_2	H_2O	4

* order of the spectral albedo polynomial

absorber, I use data from the HITRAN revision (Karman et al. 2019). For the CO_2 absorption cross sections in the CO_2 retrieval window around 2.0 µm (W8), line mixing is relevant (see Section 4.5.3). There, a line mixing correction is applied on top of the HITRAN cross sections. The correction is given by the difference between lineshape calculations including line mixing and simple Voigt lineshape calculations (Hartmann et al. 2009; Lamouroux et al. 2010). This difference is then added to HITRAN 2020 Voigt cross sections.

4.5 Retrieval Windows

This section describes the spectral regions constituting the measurement vector, called retrieval windows. First, Section 4.5.1 discusses the extent of the retrieval windows and the absorbers considered in each window. The relative scaling of the CO_2 absorption cross sections between windows in the scattering retrieval is discussed in Section 4.5.2. Section 4.5.3 considers the use of line mixing cross sections for CO_2. Section 4.5.4 specifies where HDO is fitted independently of the general water isotope mix. Finally, Section 4.5.5 describes the spectral albedo polynomials.

4.5.1 Retrieval Window Extent

Deciding on the retrieval windows is a crucial step in setting up the retrieval, since it determines the measurement vector. I aim at capturing the main absorption features of one species within one window, while ensuring that some portion of the window is transparent to determine the albedo background polynomial. Depending on the absorption features, the transparent portion may lie in between individual absorption lines or, for closely spaced absorption bands, at the side of the window. Each retrieval window is defined specifically for one target absorber species. Table 4.1 lists all windows and the absorbing gases retrieved from it. O_2 is retrieved from W1, CO_2 from W2, W3 (around 1.6 µm) and W8 (around 2.0 µm), CH_4 from W4 and W5, as well as CO from W6 and W7. Each spectral window contains more than one absorber. The additional absorbing gases are included as interfering species. All windows are contaminated with H_2O absorption lines. In W1, a pseudo

absorber representing the collision induced absorption contribution from O_2 (O_2 CIA) is added. CO_2 is included in W5 and CH_4 in W6 and W7. The columns for the latter are retrieved independently from the target CO_2 and CH_4.

Figure 4.2 shows the retrieval windows for an example spectrum. Note that the underlying high resolution spectrum is calculated up to 30 cm^{-1} beyond the specified window limits to circumvent boundary effects in the modeled measurement caused by the ILS convolution. However, only the specified range is used within the retrieval for comparing measured and modeled spectrum. The retrieval window extent generally conforms to the standard TCCON retrieval windows specified by Wunch et al. (2015). Only for the longwave CO_2 window, a broader window is chosen which includes one of the strong CO_2 absorption branches and the weaker band next to it. I do not use the second strong branch, since it is significantly contaminated by water absorption. A smaller version of W8 is tested, which does not include the weaker CO_2 branch, with the non-scattering retrieval. In this case, the retrievals of reflector measurements show small differences of 2-3 permil in form of random scattering with no discernable bias. For target measurements, SCDs retrieved with the smaller window SCDs are 1 % to 3 % lower compared to the wider window. The difference shows a SZA dependence with higher differences at noon and lower differences in the morning and afternoon. While the SZA dependence is similar between days, the strength of the bias varies between days, pointing towards systematic errors due to the neglect of atmospheric scattering. The difference in precision is compared between retrievals with both window extents. The method for this is described in Section 5.4. The precision is 15 % better in retrievals with the wider window. This is not surprising, since more spectral information is contained in the wider window. Additionally, a wider range of absorption line strengths are contained in the window. The wider window also allows for including additional wavelength without absorption.

Initially, the CH_4 Q-branch around 6000 cm^{-1} was included in the CH_4 retrieval window. However, comparing reflector measurements to EM27/SUN direct-sun observations reveals a systematic and time dependent deviation with a magnitude of up to 1 % in the CH_4 VCDs. This deviation is not present when excluding the Q-branch from the retrieval window. Therefore, CH_4 is retrieved from W4 and W5, cutting out the Q-branch.

Figure 4.3 shows high resolution spectra modeled in the final retrieval iteration, providing the best estimate of the true spectrum for the respective measurement. A spectrum from the reflector and the Baldwin Park (BP) target are displayed together with absorption cross sections of the absorber retrieved from the respective windows. As previously specified, the radiative transfer is calculated based on a horizontally homogeneous model atmosphere. The absorption cross sections shown in Figure 4.3 are calculated under standard conditions for illustrative purposes. They do not originate from the retrieval, however they allow the identification of spectral signatures in the modeled spectrum. A qualitative examination of the modeled spectra illustrate the distinct fingerprint each absorber has on the spectrum. For O_2, CO_2 and CH_4 and H_2O the absorption feature can easily be recognized in the modeled spectrum. In W6 and W7, the interfering absorbers dominate the CO signal. The absorption lines are overall deeper in the target spectrum, due to the longer light path. Additionally, the water absorption features are much more pronounced, due to disproportionately high water content in the planetary boundary layer. While some water absorption lines overlap with

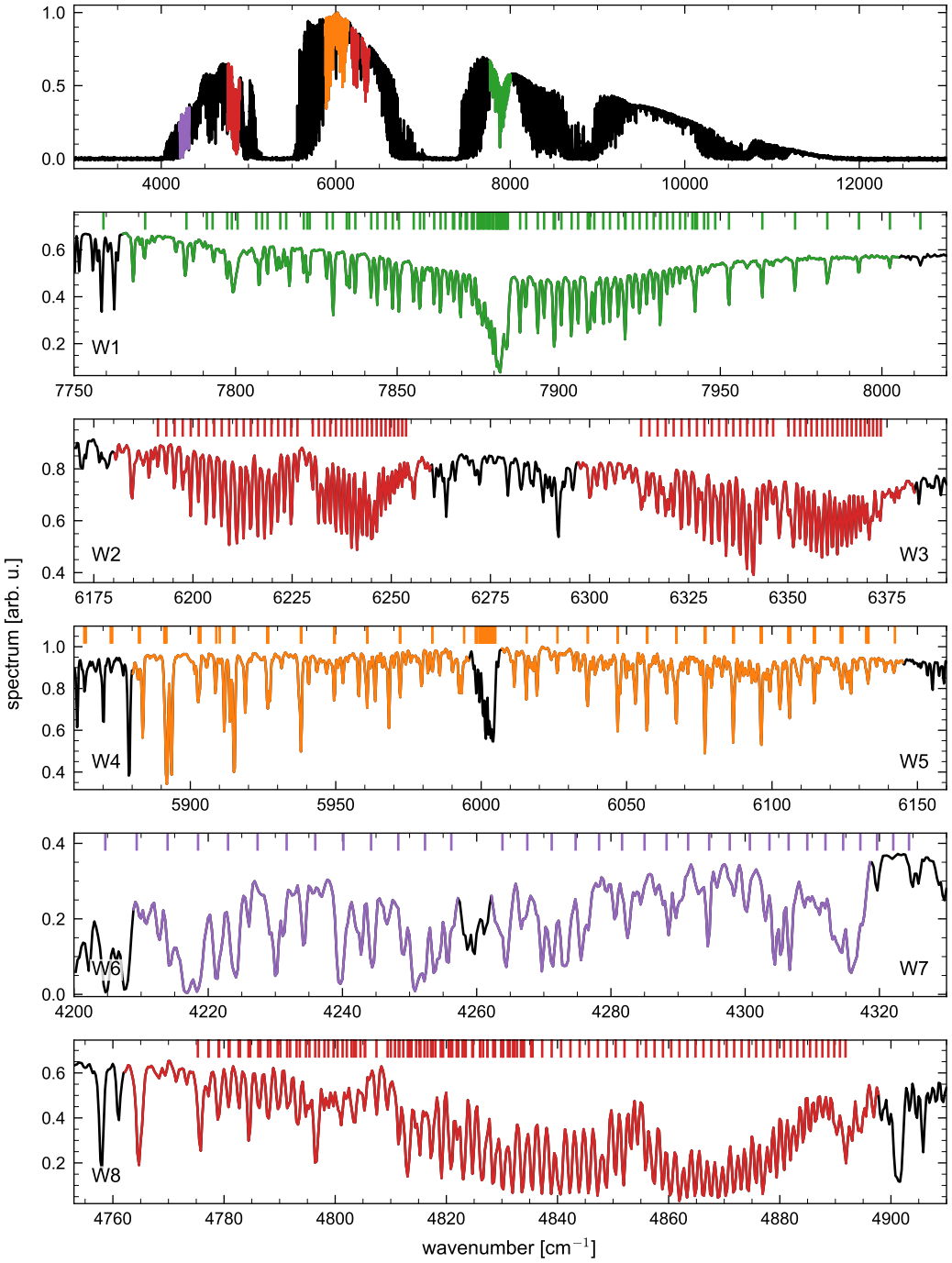

Figure 4.2: Spectral retrieval windows for absorber retrievals as specified in Table 4.1. The windows are marked in color in a spectrum of the Baldwin Park target (black, 24 April 2022, SZA = 46.58°). The top panel shows the full spectrum, the panels below show the sections with all windows. The target absorption line positions are indicated by colored bars above the spectrum (O_2 in green, CO_2 in red, CH_4 in orange and CO in purple). Note that W2–W3, W4–W5 and W6–W7 are shown together in one panel.

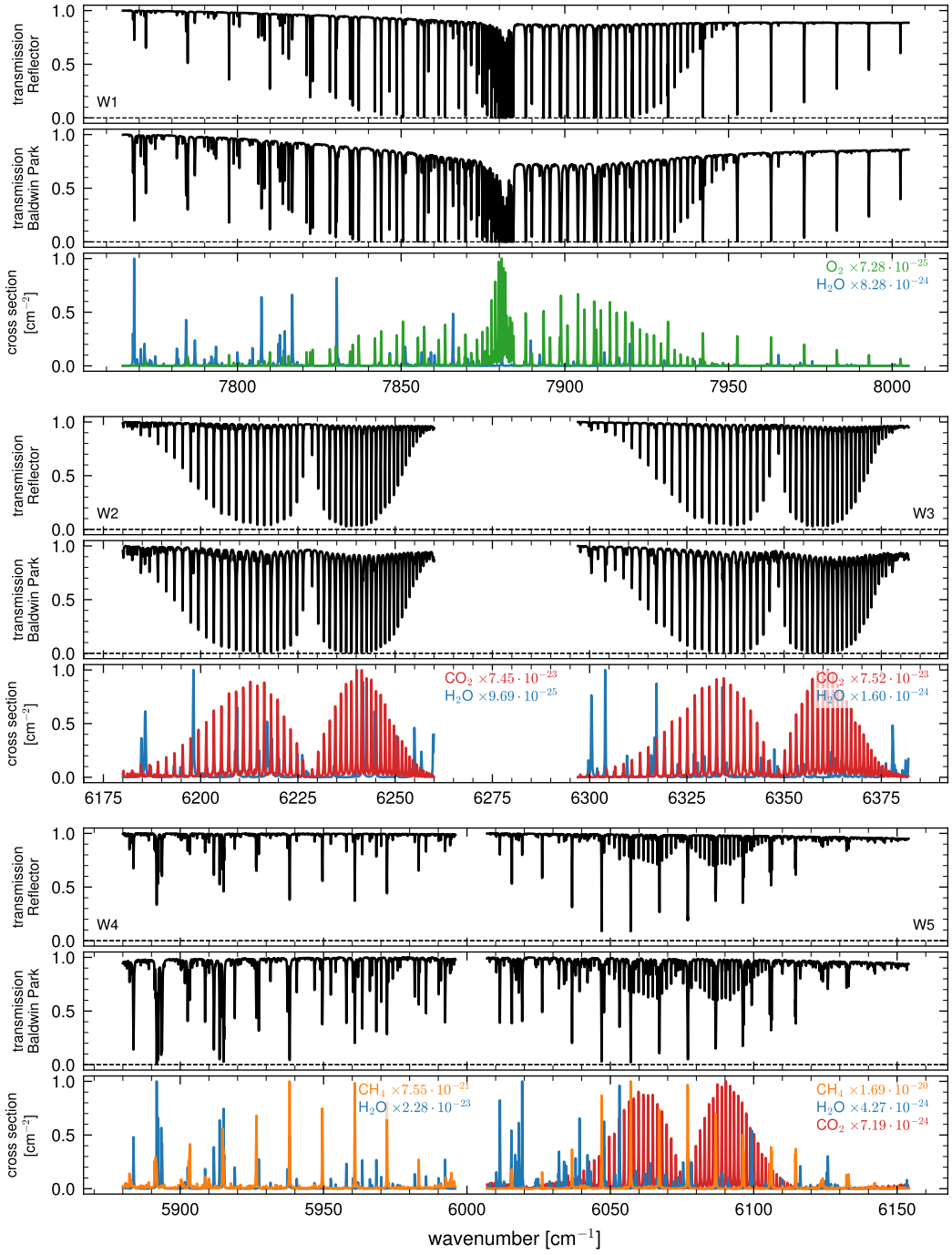

Figure 4.3: The high resolution modeled spectrum for each retrieval window. A reflector (top) and a target spectrum (middle) are shown per panel, the lowest subpanel shows the HITRAN 2020 absorption cross sections calculated with a Voigt lineshape for standard atmospheric conditions.

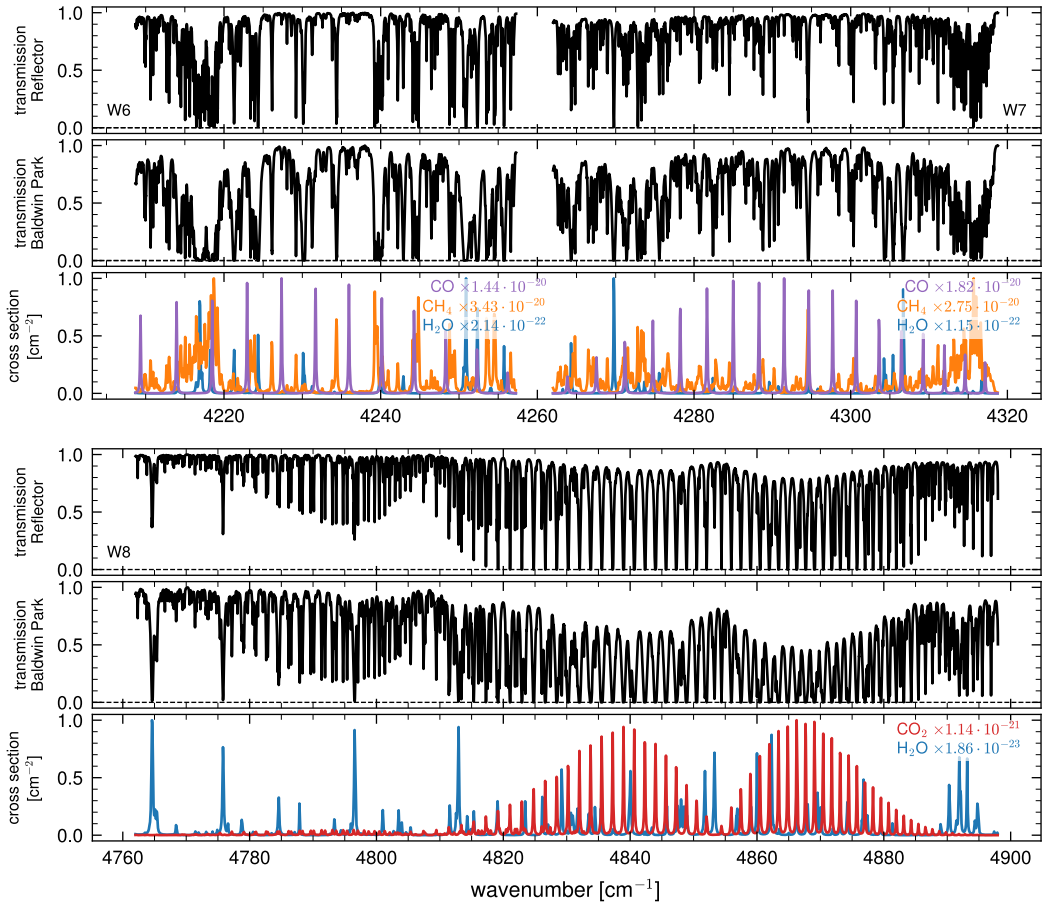

Figure 4.3: (continued) The cross sections for each species are normalized to a maximum value of one within each window. The normalization factor is noted in the legend. The modeled spectra additionally take into account the solar spectrum and in W1 the O_2 CIA pseudo-absorber. Note that cross sections are shown for a single pressure and temperature, while the modeled spectra are calculated over multiple atmospheric layers with different pressures and temperatures.

those of the target absorber, in every window there are distinct absorption features allowing to disentangle water vapor and the target absorber.

Despite the fact that many absorption lines are saturated in the high resolution spectrum, the absorption features in the EM27/SCA spectra do not extend down to zero. This is due to the instrument lineshape dominating the absorption line width, leading to a washing out of the saturated features. Regardless of not being intuitively apparent from the EM27/SCA spectrum, the underlying absorption lines are largely saturated, especially for the target observations. Still, every window contains at least some non-saturated lines. Note that absorption features caused by saturated lines still deepen with an increasing SCD. This can be seen for instance from the base of the O_2 absorption features in the target spectra. This results from additional photons being absorbed in the wings of the absorption lines, especially at high pressure in the lower atmosphere. This means that also saturated lines provide some information on the absorber abundance.

4.5.2 Relative Line Strength between Windows

Each absorber is retrieved from different windows independently in the non-scattering retrieval. Subsequently, the best estimate VCDs for each absorber are averaged a posteriori between windows. Therefore, all windows are fundamentally independent in the non-scattering retrieval. For scattering retrievals this is not the case, as the same microphysical aerosol properties are used in every window. It is known that inconsistencies in spectroscopic line strength parameters between windows can lead to relative disagreement in retrieved CO_2 between windows (Karlovets et al. 2021). To prevent errors caused by this, a scaling factor is determined from the same period used for the precision analysis (Section 5.4). I calculate the average ratio between SCDs retrieved from different windows in reflector spectra. The scaling factors relative to W2 are 1.0089 (W3) and 1.0093 (W8). In all scattering retrievals, the absorption cross sections in the respective windows are multiplied by this factor.

4.5.3 CO_2 Line Mixing Cross Sections

Collisional line mixing occurs when the initial and final states of transitions with similar energy exhibit efficient collisional coupling. In this case, they can no longer be described as independent two-state systems, which leads to additional absorption pathways. This changes the absorption cross sections and subsequently leads to errors in the retrieved column densities. Hartmann et al. (2009) showed that the systematic errors caused by neglecting line mixing in CO_2 retrievals in the spectral range covered by W8 amount to 0.6 % to 1.1 %. In the spectral range of W2 and W3, they show that the errors are substantially lower, but also that the error depends on the airmass. Total airmasses are in the range of 1 to 3 for reflector measurements and 2 to 6 for the targets, depending on SZA and target distance. In this range, the error due to the neglect of line mixing is expected to be below 0.2 %, which I consider negligible. For W8 however, this is in fact relevant. Comparing retrievals using the Voigt lineshape to retrievals using the line mixing correction, the χ^2 is 20 % to 30 % lower when using the line mixing corrected cross sections. The SCD is 0.6 % to 1.8 % higher for retrievals neglecting line mixing, with a clear airmass dependence. For reflector mea-

surements the 1/cos(SZA) dependency is obvious. Target measurements show consistently higher biases, scaling with target distance. Consequently, I use the line mixing correction to the HITRAN 2020 CO_2 absorption cross sections for all retrievals from W8.

4.5.4 Separate HDO Cross Sections

HITRAN absorption cross sections for one absorber generally include cross sections from many isotopes (Gordon et al. 2022). The cross sections are weighted with their typical atmospheric abundances. While this is a good approximation in most cases, the isotopic ratio is variable for H_2O and HDO has relevant absorption features in some of the retrieval windows used here. Fu et al. (2014) retrieve HDO separately from CLARS-FTS spectra in the spectral ranges corresponding to W2-W8. Due to the lower spectral resolution, the sensitivity of the retrieval to HDO may be different. Therefore, the sensitivity to HDO variability is tested by retrieving one day of measurements once with cross sections based on the standard isotopic composition and once with H_2O and HDO as distinct absorbers. Only in W3, W6 and W7, the retrieved HDO values deviate from zero, within their scatter. Furthermore, the inclusion of HDO change the systematic residuals only in these windows. Examining the changes in the SCDs of the target absorbers only reveals relevant changes in the CO SCDs retrieved in W6 and W7. The change is largest for reflector retrievals with a decrease of up to 10 % when including HDO. Differences for target retrievals are lower. The CO_2 SCD retrieved from W3 changes only by around 1 permil. Since this is a minor effect in the context of the measurement precision, going forward I use the standard isotopic composition in this windows. HDO is included in W6 and W7 as distinct absorbers, along side the main isotope.

4.5.5 Albedo Polynomial

Within the forward model, the surface albedo is approximated by a polynomial for each window. The coefficients for the polynomial are included in the state vector. The order of the polynomial has to be chosen a priori. To find the best order, I run a retrieval with quadratic polynomials and fit a polynomial to the systematic residual (cf. Section 5.3). The result shows clear thresholds beyond which the fitted polynomial is stable. While in some cases stability is already reached with a third order polynomial, for fourth order polynomial it is consistently the case. The only exception is W1, where a fifth order polynomial is necessary. Therefore, albedo polynomials of of degree four (W2–W8) and five (W1) are used hereafter.

The albedo polynomial can also compensates for other broadband variability of the spectral continuum within each window. In the non-scattering retrieval where uncalibrated spectra are used, the albedo polynomial accounts for broadband instrument characteristics, e.g., the detector sensitivity and the spectral variability of the optical throughput. Therefore, the numerical value of the polynomial can not directly be interpreted as the physical albedo there, but as product of albedo and the radiometric calibration factor.

Investigating the albedo polynomial over the course of one day, their shape is largely consistent, with variations on the order of 1 %. This, together with the fact that the systematic residuals do not show broadband variation in any window (cf. Section 5.3), indicates that the choice of polynomial provides a good approximation of the spectral continuum. In

Table 4.2: Thresholds for data filters.

Filter	Criteria	
Large SZA	SZA	$< 70°$
Sensor saturation	IFG maximum	< 4.8
Cloud	DC_{var}	< 0.03
Low SNR	SNR	< 100 (W1–W5) < 50 (W6–W8)
Fit quality	χ^2	< 3 (non-scattering) < 5 (scattering)
Cloud	$\frac{\text{retrieved } O_2 \text{ SCD}}{\text{geometric } O_2 \text{ SCD}}$	1.03 (non-scattering) 1.075 (scattering: reflector)

terms of absolute magnitude, the albedo polynomials retrieved from reflector measurements show a continuous 20 % increase over the course of one day. This increase has no clear dependency on the SZA, i.e. the albedo increases further with the decreasing SZA after local noon. Note that this result can not be interpreted as a directionally dependent albedo of the reflector plate. Other effects may influence the continuum level. For example, variations in overhead aerosol loading directly impact the spectral continuum level. Contrary to the reflector spectra, the assumption of the Lambertian surface reflection is not as good for the target spectra. There, a clear SZA dependency is visible in the albedo polynomials. This is discussed in Section 5.2.

4.6 Data Filtering

To interpret the retrieval results correctly and get an accurate analysis of the instrument performance, irregular and unsuitable measurements are excluded. Besides cases where the retrieval does not fully converge, measurements at a high SZA, contaminated by clouds and with poor fit quality are removed. The latter two are judged based on properties of the interferogram, χ^2 and, in case of non-scattering retrievals, the deviation between retrieved and a priori O_2 SCD. The following section describes the filters in detail and assess their impact on the data yield during the deployment at Mt. Wilson (cf. Section 5.1). Figure 4.4 summarizes the filters and the corresponding thresholds. Figure 4.4 shows the filtering variables for which an empirical threshold was defined.

Only measurements at SZA $< 70°$ are analyzed to limit spectroscopic uncertainties. It is possible to analyze spectra with higher SZA, however within the scope of this thesis and especially for the performance evaluation I chose a conservative value, which can be extended in future studies.

The next two filters are based on interferogram properties. I filter measurements which could be subject to detector nonlinearity. Based on the analysis in Section 3.5, measurements with a maximum interferogram value above 4.8 are removed. However, this did not occur during the deployment at Mt. Wilson. Additionally, measurements are removed

where the interferogram DC component shows increased variability. This removes measurements subject to cloud contamination. Partial obstruction of the sun causes temporal variability during the recording of a single interferogram. This causes variability of the DC component. The DC variability (DC_{var}) is the fraction of the maximum (DC_{max}) to the minimum value (DC_{min}). One is subtracted so that a DC_{var} of zero corresponds to no variability.

$$DC_{var} = \frac{DC_{max}}{DC_{min}} - 1 \tag{4.25}$$

Since the DC components of all interferograms are curved (cf. Figure 3.10), even consistently illuminated interferograms do not have a DC_{var} of zero. This smile effect limits the effectiveness of this filter. However, interferograms recorded under partial cloud cover show significantly enhanced DC_{var}. I determine the threshold from reflector measurements during the cloud free days 13 April, 24 April, 29 April and 4 May 2022, which are verified with the help of the context camera. Interferograms with $DC_{var} > 0.03$ are classified as cloud contaminated and excluded from the analysis. Note that this threshold changes when the instrument optics are modified, i.e. during alignment, as this may change the curvature of the DC baseline. This filter excludes 7.5 % of the LA measurements. However, this ratio is dominated by a few rather cloudy days, i.e. 20 April and 26 April 2022. Removing particularly cloudy days drops the filtering ratio significantly. This cloud filter has limitations for weak contrasting cloud events, since averaging multiple scans smoothens the variations in the DC baseline. In some cases, this may reduce DC_{var} below the smile-limited threshold. This is acceptable, since the DC correction compensates for minor illumination variations (Keppel-Aleks et al. 2007). To some extend, this is additionally compensated by the second cloud filter described below. Nevertheless, it is still possible that this produces outlier data and adds to the overall measurement uncertainty.

The DC variation filter removes only measurements subject to partial cloud cover. Measurements under full cloud cover are identified by the overall low signal and subsequently unusually low SNR. Additionally to cloud detection, also low SNR measurements are filtered because the retrieval uncertainty would be high. Spectra with SNR below 100 in W1–W5 are excluded. Due to limited throughput towards the cutoff wavelength, most target measurements have SNR below this 100 in W6–W8 (cf. Section 5.2). Therefore, the threshold is lowered to 50 for those windows. This filter removes 0.2 % (W1–W5), 0.9 % (W8) and 4.9 % (W6–W7) of the LA measurements.

Despite these filters, some retrievals fail to converge. Retrievals classified as non-nominal are removed, e.g., due to non-convergence after 30 iterations or a failing matrix inversion due to singular values. For non-scattering retrievals with W1–W5, this is 1 %, for scattering retrievals, this is 8 % of the measurements. For non-scattering CO retrievals (W6–W7), this is 16 % of the remaining measurements, even though retrievals reaching the maximum number of iterations are accepted for CO. I accept the filtering and convergence failure rate for CO retrievals, as enough data remains to assess the instrument performance for CO and the analysis of CO is not continued further due to low precision. All successful retrievals are additionally filtered for poor fit quality based on the χ^2 representing the residuals. Since the residuals are systematic, the χ^2 is consistently greater than one and the filtering threshold

depends on the spectral windows used in the retrieval. The maximum χ^2 is set to 3 for non-scattering, and to 5 for scattering retrievals.

To remove remaining cloud contaminated measurements, I construct a filter based on the ratio between the O_2 SCDs retrieved from the measurement and the one calculated from the geometric light path and a priori information on the atmospheric state (geometric O_2 SCDs). This method is also employed by CLARS-FTS (e.g. Wong et al. (2015)). For scattering retrievals of target measurements, this is not possible, since no O_2 is retrieved in favor of the aerosol parameters. For non-scattering retrievals, measurements are discarded where the ratio is above 1.03, meaning the retrieved O_2 is higher than the geometric O_2 SCD. The threshold is empirically determined and is applied before the instrument specific O_2 calibration factor (Section 5.5.1). Because of this, the threshold changes when a different ILS is used. When using the empirical ILS correction in W1 (cf. Section 5.3.2), the threshold is adjusted to 1.075. 2 % of the remaining LA campaign measurements are removed by this filter, most of them being reflector measurements. For reflector measurements, this filter removes measurements where clouds increase the effective light path. Atmospheric scattering generally reduces the O_2 SCD of target measurements, as into-beam scattering dominates, reducing the effective light path. This renders the O_2 based filter ineffective as a cloud filter, because the light path shortening effect of the aerosols typically dominates. A lower boundary can be used to filter aerosol contaminated measurements as was done in multiple CLARS-FTS studies (He et al. 2019; Wong et al. 2015; Zeng et al. 2020a). In this thesis, I do not filter based on a lower threshold, since I want to address the aerosol scattering influence by including it explicitly in the retrieval.

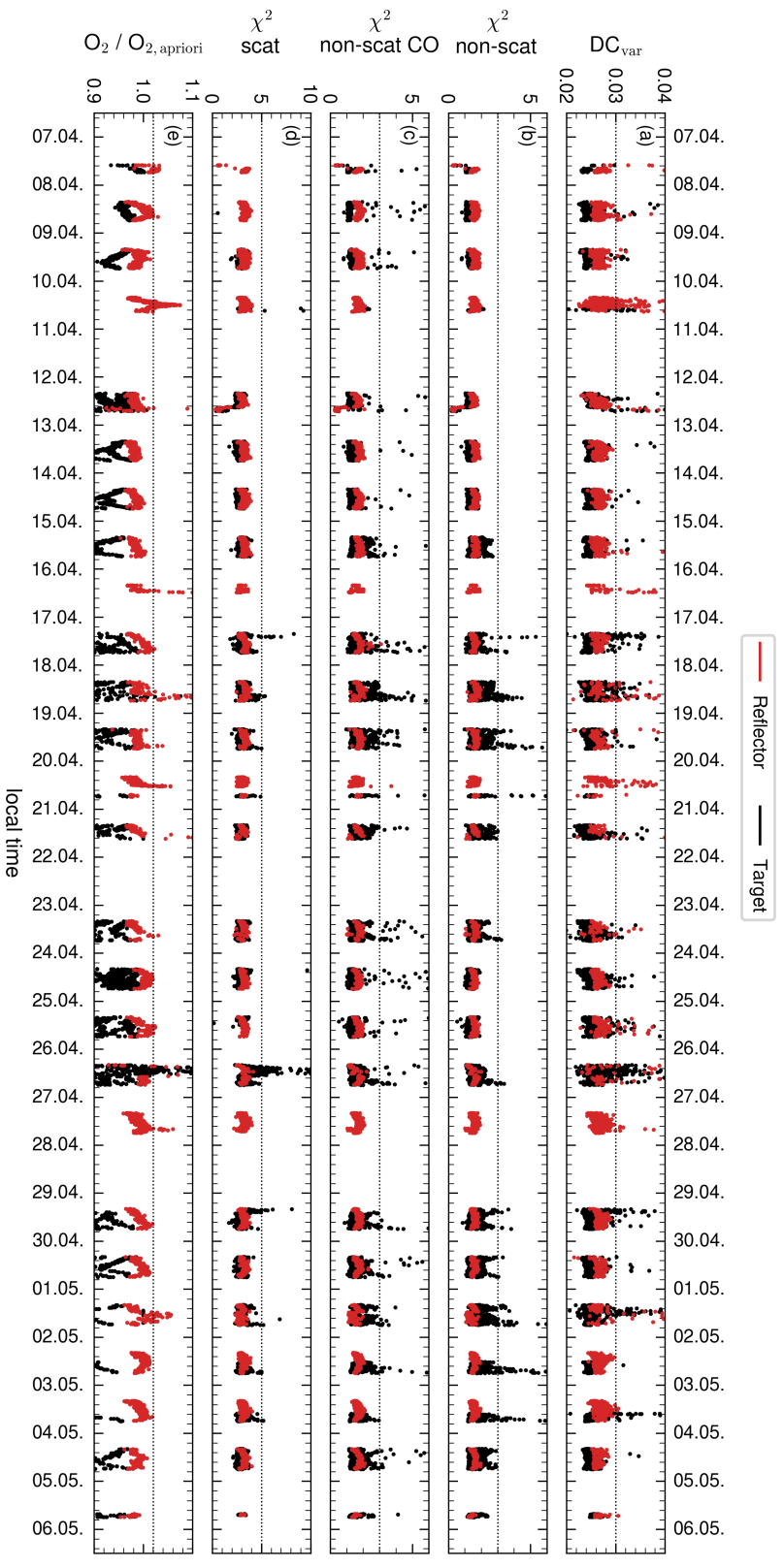

Figure 4.4: Filtering variables for which the threshold was defined empirically. Panel (a) shows DC$_{var}$ and (b-d) show χ^2 respectively for non-scattering (W1–W5 (b) and W1–W7 (c)) and scattering (d) retrievals. Panel (e) shows the ratio of retrieved and geometric O_2 SCD. Note that the y-axes are cut off to increase visibility of the thresholds.

5 Performance Demonstration for the Los Angeles Basin

This chapter evaluates the performance of the EM27/SCA instrument and the retrieval algorithm based on atmospheric measurements of the northern LA basin. The SNR (Section 5.2), retrieval performance through the analysis of the fitting residuals (Section 5.3) and the measurement precision (Section 5.4) are evaluated from those measurements. Section 5.5 compares the EM27/SCA measurements from the northern LA basin to simultaneous CLARS-FTS measurements. Section 5.6 discusses the error introduced by aerosol scattering. Section 5.7 presents the scattering retrieval which corrects the aerosol scattering-induced bias. Finally, Section 5.8 discusses the detectability of urban emission patterns by EM27/SCA measurements.

5.1 Deployment on Mt. Wilson

We deployed the EM27/SCA for one month (7 April to 5 May 2022) next to the CLARS to evaluate the instrument performance in terms of precision and accuracy and to assess its ability to capture urban emission patterns. The observatory is located on top of Mt. Wilson at 1673 m a.s.l. with a direct line of sight into most of the LA basin. CLARS houses the CLARS-FTS, which routinely observes the LA basin in the reflected sunlight geometry since 2010.

The CLARS-FTS is placed in an air conditioned 23 m^2 shipping container. Its pointing system resides in a telescope dome on top of the container. CLARS-FTS routinely records spectra with a maximum OPD of 5 cm, corresponding to a spectral resolution of 0.2 cm^{-1}, with two detectors (InGaAs and silicon (Si)) in the NIR and visible (VIS) spectral range. Its FOV amounts to 4.97 mrad which is slightly larger than the EM27/SCA FOV. The ILS of the CLARS-FTS is close to nominal and therefore can be represented by a theoretical ILS for the retrieval of CLARS-FTS spectra. The ILS is calculated from maximum OPD and FOV, accounting for finite resolution and self apodization. Fu et al. (2014) describes the CLARS-FTS in great detail.

We set up the EM27/SCA on a small viewing terrace in direct proximity to the CLARS. From there, the EM27/SCA has approximately the same largely unobstructed view into the LA basin as the CLARS-FTS. This setup conforms well to the downward viewing geometry presented in Section 4.2. With 1670 m altitude compared to the 100 m to 300 m altitude throughout the basin, the location is elevated above the planetary boundary layer (Fu et al. 2014). On 26 days between 7 April and 5 May 2022 the EM27/SCA observed up to nine targets in the northern LA basin. Despite CLARS-FTS usually observing 33 targets throughout the whole LA basin, we focused with both instruments on targets with up

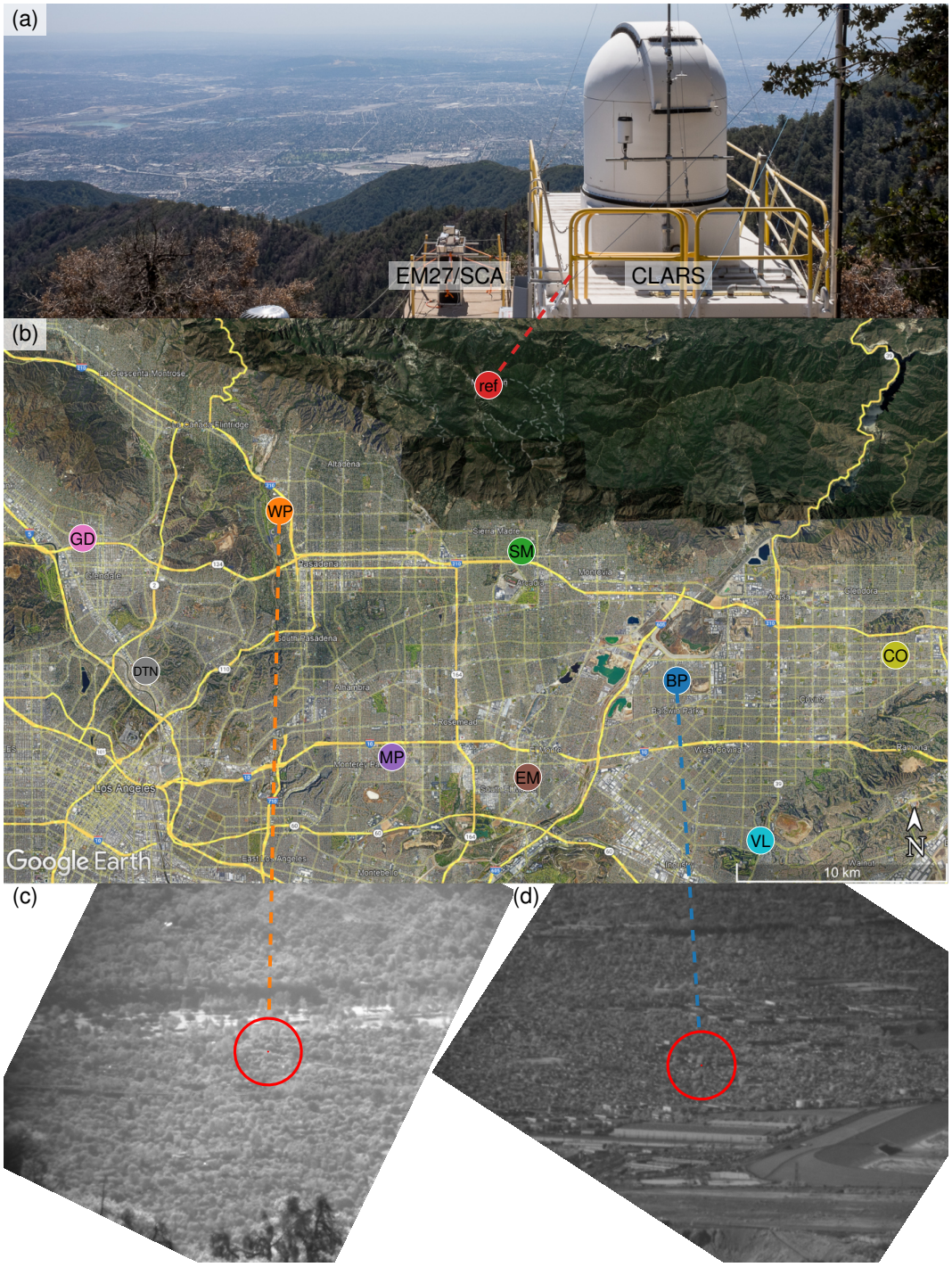

Figure 5.1: Panel (a) shows the deployment of the EM27/SCA on Mt. Wilson side-by-side with the CLARS-FTS. All targets and the CLARS site (ref) are indicated on the map in panel (b). The FOV is indicated with a circle in the pictures from the imaging camera of the targets WP (c) and BP (d). Pictures from the imaging camera for all targets are shown in Figure A.2.

Table 5.1: List of the ground-scattering targets across the northern Los Angeles basin.

	Target	Short	Latitude [°]	Longitude [°]	Slant distance from FTS [km]
C	Reflector	ref	34.221	-118.057	0.00
1	Sierra Madre	SM	34.153	-118.040	7.86
2	West Pasadena	WP	34.170	-118.165	11.46
3	Baldwin Park	BP	34.098	-117.960	16.38
4	Monterey Park	MP	34.066	-118.107	17.94
5	El Monte	EM	34.057	-118.037	18.39
6	Glendale	GD	34.159	-118.266	20.49
7	Downtown (near)	DTN	34.102	-118.234	20.99
8	Charter Oak	CO	34.109	-117.848	22.98
9	Valinda	VL	34.030	-117.917	24.88

to 25 km slant distance. We chose the lower number of rather close targets to have higher revisiting rates for each target and restrict the error due to atmospheric scattering for this performance evaluation. Figure 5.1 shows and Table 5.1 lists the targets and their coordinates. We used targets in the proximity of the original CLARS-FTS targets, but shifted them to ensure an as homogeneous FOV as possible for each target. We selected the targets using the CLARS-FTS pointing system and its imaging camera. We subsequently matched the pointing of the EM27/SCA via its imaging camera to the pictures from the CLARS-FTS imaging camera. We verified the correct pointing at the beginning of each measurement day. The GPS coordinates of the targets are available through the calibrated CLARS-FTS pointing system (Fu et al. 2014).

The sampling of the ground scattering targets alternated with reflector observations. We started with a reflector observation, then iterated with increasing VAA through the targets in the northern LA basin. To avoid large gaps in between reflector measurements, we recorded an additional reflector observation between the fifth (El Monte (EM)) and sixth (Monterey Park (MP)) target. In the early period of the campaign we sampled only a subset of the nine targets with low slant distances. For three days, until 11 April 2022, we alternated between Sierra Madre (SM) target and the reflector. From 12 April to 17 April 2022, we observed the targets SM, West Pasadena (WP) and Baldwin Park (BP) with one reflector measurement in each cycle. From 17 April to 5 May 2022, we observed all nine targets. With a measurement duration of 1 min plus some measurement and pointing overhead, the duration for one cycle was 2 min for one target, 5 min for three targets and 12 min for all nine targets. From 23 April 2022 onward we recorded three consecutive spectra for each target, increasing the cycle duration to 36 min. The CLARS-FTS records one spectrum over 3 min and has more pointing overhead due to a slower rotation speed of the telescope dome. The cycles between both instruments are therefore not synchronized. Figure 5.2 shows an overview of the operation mode and number of measurements per hour throughout the campaign. On some days no measurements were possible due to cloud cover. In cases where the marine layer covered the LA basin with clouds, we only recorded reflector measurements.

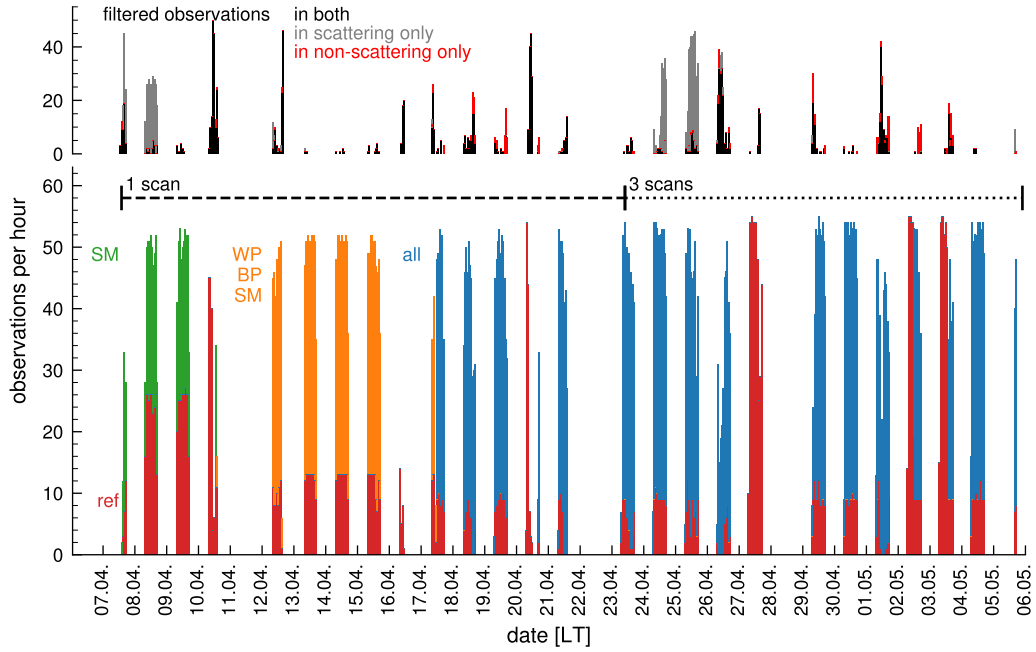

Figure 5.2: Overview of the measurements at Mt. Wilson between 7 April and 5 May 2022. The lower panel shows the number of valid observations in each hour. Reflector measurements are marked in red, target measurements are colored according to the number of targets included in the cycle. The top panel shows the number of filtered measurements in each hour (cf. Section 4.6). Measurements with SZA $> 70°$ are excluded.

To assess the aerosol loading of the atmosphere, aerosol optical depth (AOD) measurements from the AERONET are used (AERONET 2024). The AERONET measures the AOD globally with a standardization of instruments, calibration, processing and distribution (Giles et al. 2019). Using Cimel sun photometers, it delivers AOD at different wavelengths together with Ångström coefficients. The AOD measurements are available from the sites on Mt. Wilson and at the California Institute of Technology (Caltech). The Mt. Wilson site is located 350 m north of CLARS. The Caltech site is located 5 km south-east of the WP target. The AOD at 1270 nm (corresponding to the $O_2\Delta$ band) serves as reference AOD in this work. However, only data on the AOD at 1020 nm is available for both sites. Therefore, the measurements are scaled to 1270 nm according to Equation (2.17) using the closest available Ångström coefficient provided from the same measurement, which is specified for the range from 440 nm to 870 nm. Figure 5.3 shows an overview of the AERONET data from both stations during the deployment period. Mt. Wilson measurements are generally lower, due to the elevated position outside the planetary boundary layer (PBL).

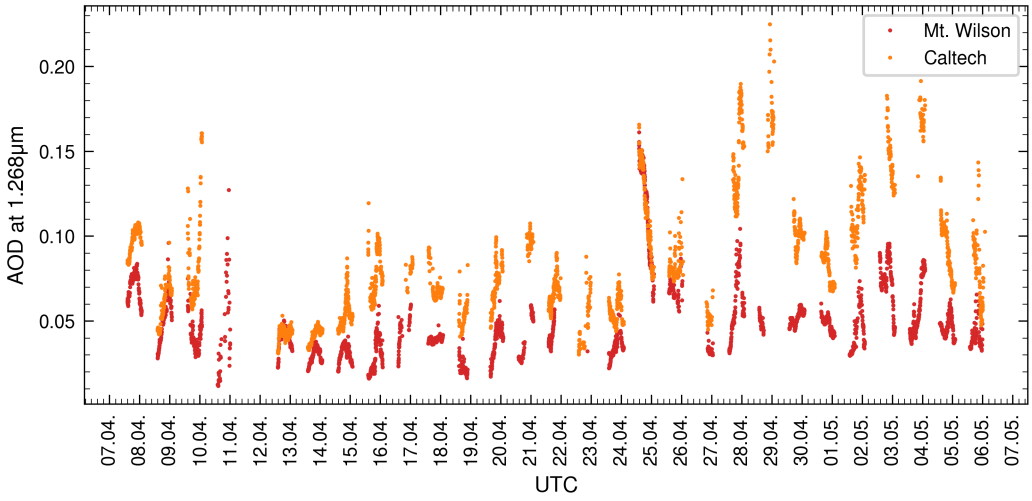

Figure 5.3: Aerosol Robotic Network (AERONET) data from the Mt. Wilson (red) and Caltech (orange) site during the deployment of the EM27/SCA on Mt. Wilson.

5.2 Signal to Noise Ratio

The signal-to-noise ratio (SNR) is the ratio between maximum signal in the spectral range of interest and the spectral noise. The maximum signal varies considerably with wavenumber. Therefore, the SNR is determined for each retrieval window individually. The standard deviation in the interval from 2500 cm^{-1} to 3056 cm^{-1} quantifies the spectral noise. This region lies beyond the detector cut off, where no signal is recorded. The spectral noise is assumed to be uniform throughout the full spectral range.

The measurement period on Mt. Wilson provides an overview of the SNR under typical conditions. Figure 5.4 shows the SNR for all retrieval windows (cf. Section 4.5) for measurements of the reflector and the two targets WP and BP. The SNR varies between targets, but also between retrieval windows. The SNR differences between targets are generally caused by differences in surface albedo. In contrast, the SNR differences between the retrieval windows are caused by the spectral variations in detector sensitivity and optical throughput, as well as by broad spectral variability in the albedo. The latter is a minor contribution for reflector measurements, because the reflector albedo is close to spectrally uniform. For reflector measurements, the SNR is generally higher due to its higher albedo. Typical SNR values for the CO_2 and CH_4 windows (W2–W5) range from 400 to 600 for reflector and 200 to 400 for target measurements. The remaining windows (W1, W6-W8) exhibit lower SNR. In W1, the reflector SNR is reduced to the range of 200 to 400. For target measurements, the higher albedo in W1 partially compensates for the reduced detector sensitivity, resulting in only minor SNR reductions compared to W2–W5. For the windows at longer wavelength (W6–W8), reductions in target albedos compared to W2–W5 widen the gap between the reflector and target SNRs. While the reflector SNR drops to 200 to 400, the target SNRs typically has values in the range 50 to 200. Generally, the SNRs for

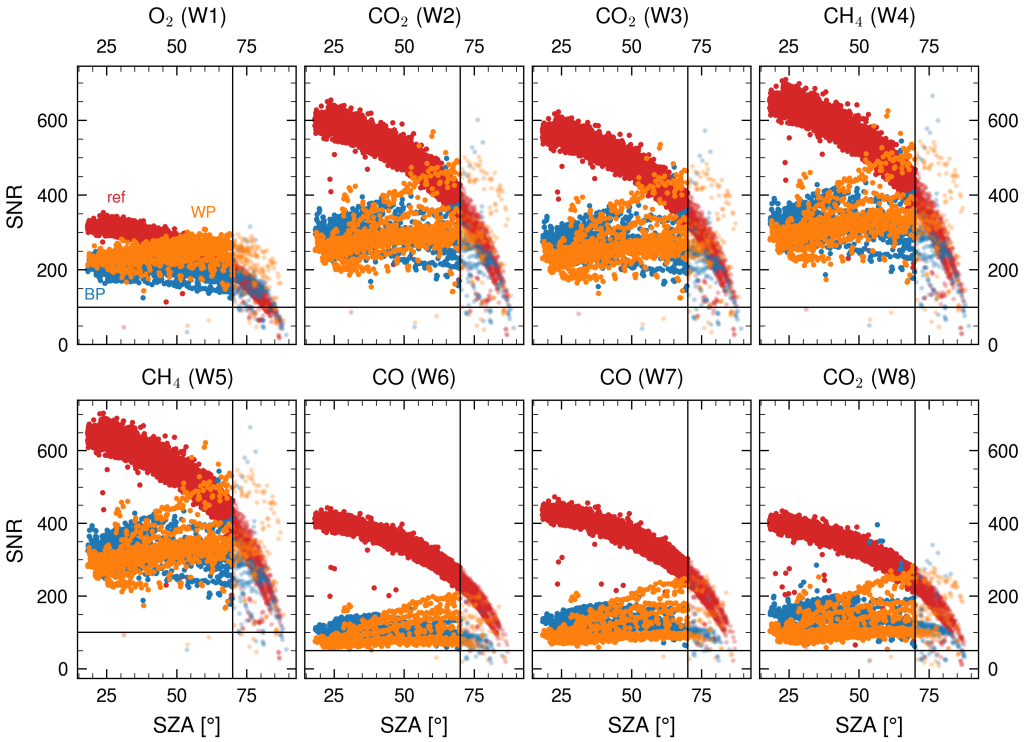

Figure 5.4: SNR over the course of the LA campaign, shown for all retrieval windows (W1-W8) and selected targets (reflector red, WP orange and BP blue).

all targets fall in the same range. The only exception is the SM target, which consistently shows lower SNR in all windows, other than W1.

Figure 5.4 shows that the SNRs of the reflector and target measurements exhibit distinctly different SZA dependencies. While the SNR for reflector measurements follows a clear but curved SZA dependency, the target SNR is generally more flat and exhibits considerably more scatter. The reflector pattern originates from the flatness of the Lambertian reflector surface. Consequently, the incoming solar irradiance and reflected radiance are proportional to the cosine of the SZA. Some low SNR outliers are due to cloud contaminated observations leading to sudden reductions in signal. Such measurements need to be excluded from further processing. The ground targets show a weaker dependency on SZA. While the pattern is overall more flat, the relationship between SNR and SZA is also less compact.

Figure 5.5 shows the SNR of W2 for all targets, with the time of day color coded. The figure reveals the SZA dependency of the SNR to be more uniform than Figure 5.4 suggests. For some targets, this is true throughout the day, but for all at least either in the morning or in the afternoon. The weaker SZA dependency and especially the absence of a clear cosine SZA dependency can by understood by considering that the surfaces of the ground targets are less uniform. The instrument FOV covers a mixture of different surface orientations, canceling the clear SZA dependency. On the other hand, many targets show upward branches with variable magnitude towards high SZA, either in the morning or in the

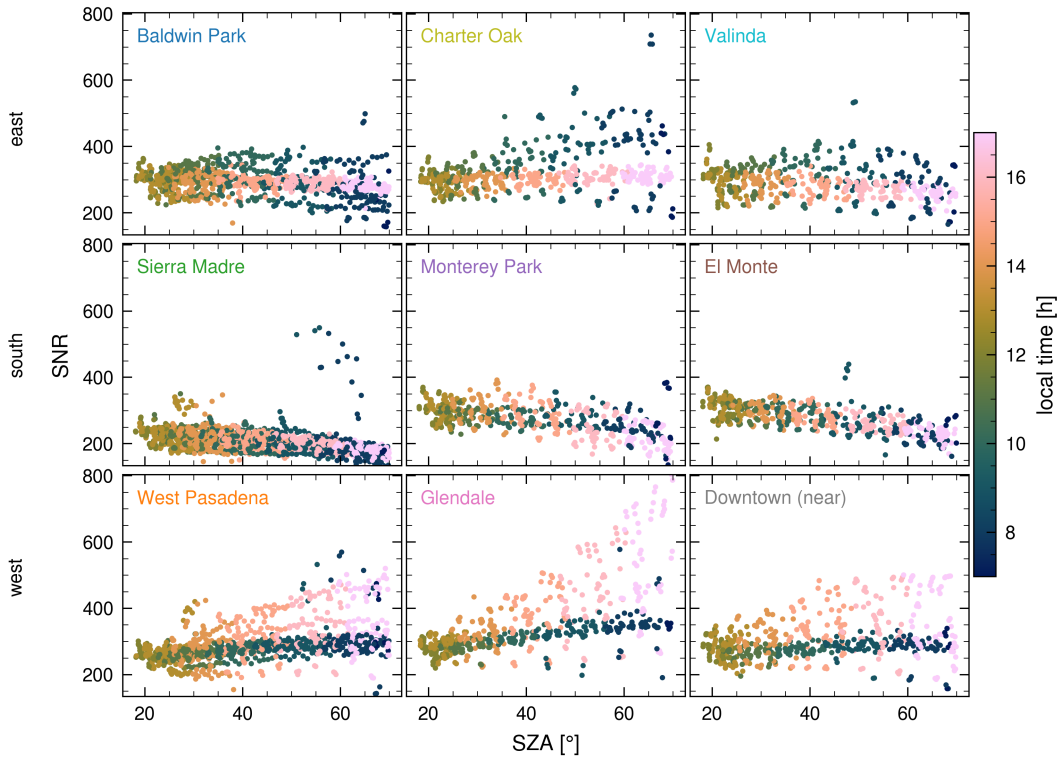

Figure 5.5: SNR of W2 over the course of the LA campaign, shown for all targets. The color corresponds to the local time of day. The top and bottom row correspond to targets located towards the east and west, favoring scattering during morning and evening hours respectively. The middle row shows the remaining targets with uniform SNR distribution over the course of the day.

evening. This effect is caused by an increase in signal through atmospheric scattering, leading to an increased SNR. The dominant effect is particle scattering of direct sunlight into the horizontal path component towards the instrument. Since the solar radiance is much larger than the surface reflected radiance, into-beam scattering exceeds extinction. Due to the strong forward peak in the Mie scattering phase function, scattering occurs predominantly at low scattering angles. For the eastward targets (Charter Oak (CO), Valinda (VL) and BP), forward scattering conditions are given in the morning. For the westward targets (WP, Glendale (GD) and Downtown (near) (DTN)), the same is true in the evening. The effect is strongest for the eastmost and westmost targets (CO and GD) with large horizontal path components and at high SZA. This shows that in some situations atmospheric scattering contributes significantly to the overall signal, raising the SNR. The amount of scattered radiance additionally depends on the atmospheric conditions, leading to distinct SNR branches for individual days (e.g. for WP). For the westward targets (WP, GD, DTN), the SNR is compact in the morning and exhibits upward branches in the evening, increasing with SZA. For the eastmost target (CO), the opposite is the case. The SNR is compact in the evening and increased SNR is visible in the morning. The targets SM, MP and EM do not

show such branches. MP and EM are located in the south of Mt. Wilson, where the sun is at high elevation when the solar azimuth matches the viewing direction. For SM, additionally the viewing zenith angle is steeper and the horizontal path is rather short compared to other targets. This leads to comparatively weak SZA dependency of the SNR. In conclusion, the observed pattern in SNR results from atmospheric scattering, rather than from surface reflectivity, which would not change from day to day.

Overall, the EM27/SCA measurements have a SNR exceeding 100 in W1–W5 for all targets and much higher SNR for reflector measurements. For W6–W8, the SNR is worse, only exceeding a SNR of 50 in many cases. The reflector SNR has a distinct cosine SZA dependency, whereas the target measurements have a rather flat SNR. Additionally, atmospheric scattering contributes significantly to the overall signal under forwards scattering conditions.

5.3 Systematic Residuals

The spectral retrieval yields the state vector best matching the measurement. The best estimate is found by iteratively minimizing the difference of the measured spectrum to the spectrum modeled from the state vector via the forward model. Comparing the measurement to the spectrum modeled from the final state vector (i.e. the best estimate) yields insights into the performance of instrument and retrievals, as well as into systematic errors. Looking at individual residuals, they are largely dominated by instrument noise. The residuals are averaged over a full day to investigate the systematic errors. To avoid distortions due to diurnally variable signal levels, the relative residuals are averaged. For this purpose, the residuum of each window is first divided by the respective maximum of the spectrum. As the uncorrelated noise averages out, the systematic contributions to the residuals remain.

Based on context camera images and AERONET data, the 13 April 2022 is identified as cloud-free day with low aerosol loading and thus well suited for the evaluation of the retrieval performance. Figure 5.6 shows single and systematic residuals from non-scattering retrievals. The systematic residuals are the average residuals of 124 (reflector) and 117 (BP) measurements, respectively, over the course of 13 April 2022. The spectra shown for reference and their individual residuals are recorded at SZA of approximately 45° in the afternoon of that day.

The root mean square (RMS) of the systematic residuals for the CO_2 and CH_4 retrieval windows (W2–W5) is below 0.13 % for reflector and below 0.2 % for the target measurements, with individual spikes up to 0.5 %. The systematic residuals in the CO windows (W6–W7) are larger with RMS of 0.3 and 0.6 % for reflector and target measurements respectively and several spikes exceeding 1 %. This is in part related to the absorption lines in those windows being significantly deeper, with strong water absorption lines and CH_4 Q-branches at 4215 cm^{-1} to 4220 cm^{-1} and 4312 cm^{-1} to 4317 cm^{-1}.

The O_2 window (W1) has notably higher systematic residuals compared to the CO_2 and CH_4 windows with a RMS of 0.3 % and 0.4 % for reflector and target observations respectively. Additionally, the residuals show distinct spikes around the central Q-branch as well as around isolated absorption lines towards the edges of the window. Those features are in detail discussed in Section 5.3.2. The other windows do not show this consistent pattern in

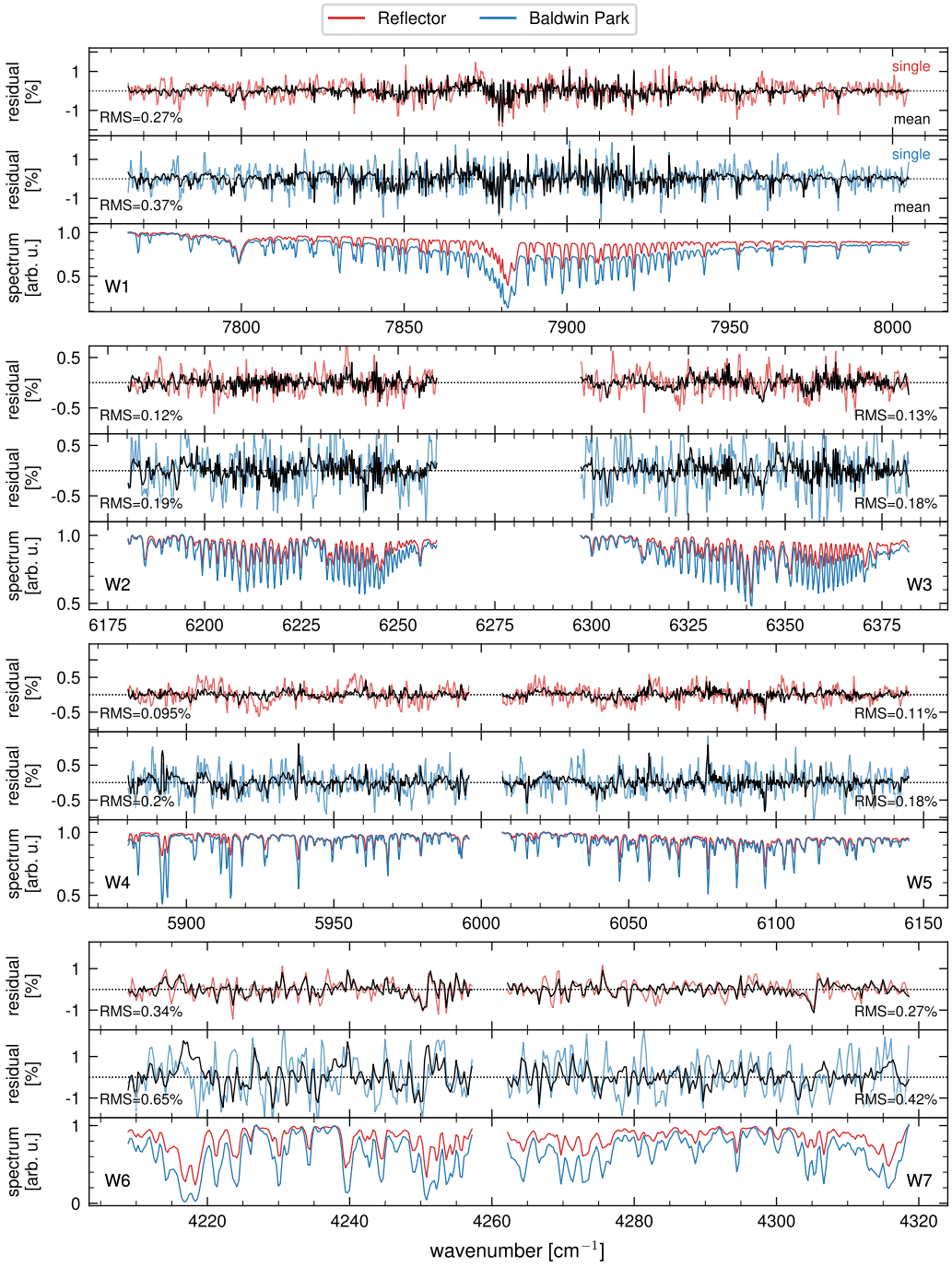

Figure 5.6: Systematic residual (black) of non-scattering retrievals, averaged over measurements from 13 April 2022. The panels show (top to bottom) retrieval windows for O_2 (W1), CO_2 (W2,3), CH_4 (W4,5) and CO (W6,7). The subpanels show the systematic residuals (black) for reflector (top) and the BP target (center). The bottom subpanel shows spectra recorded at SZA of approximately 45° in the afternoon. The individual residual corresponding to this spectrum are shown in color in the background of the systematic residuals.

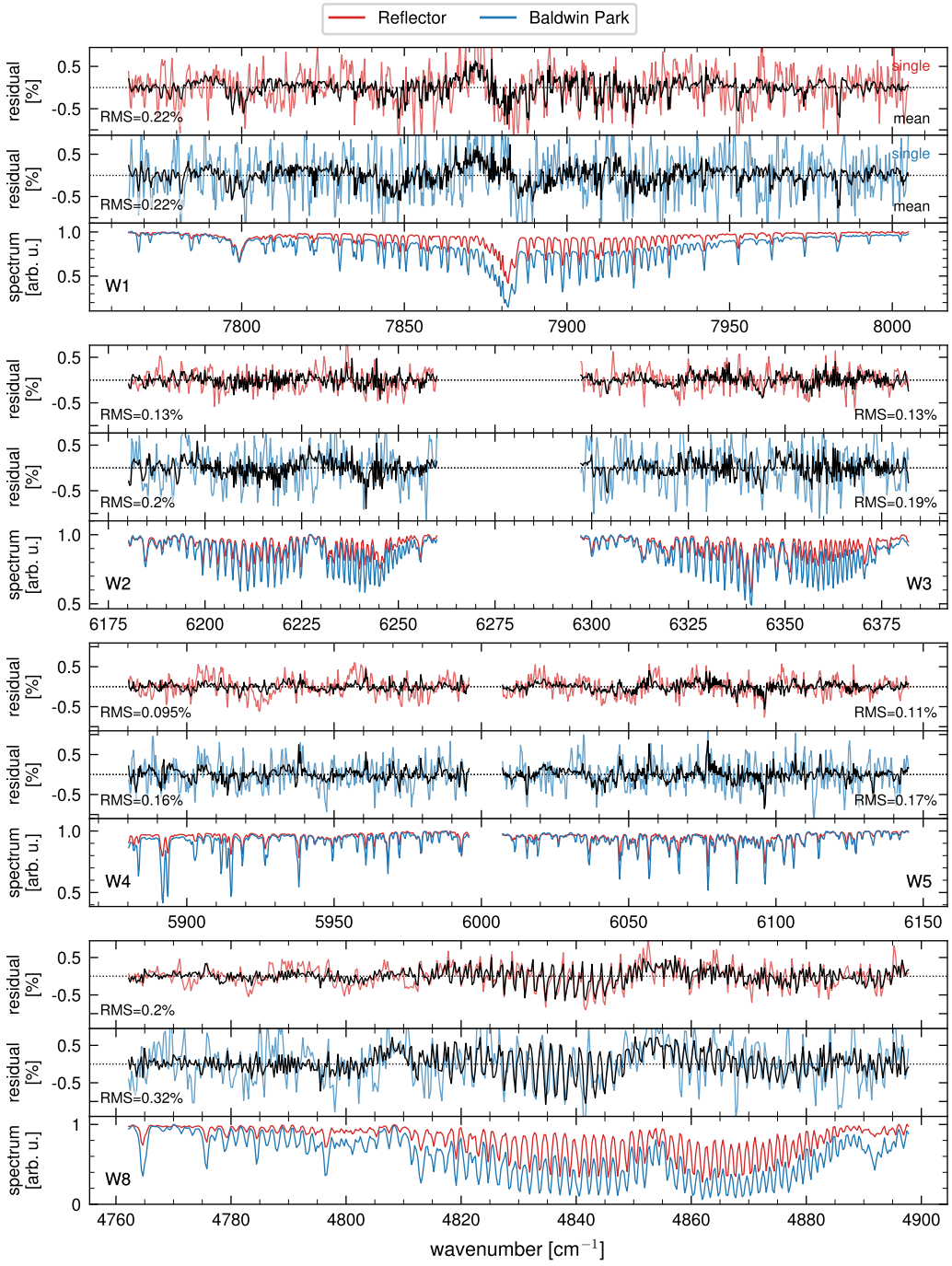

Figure 5.7: Same as Figure 5.6, but for the scattering retrieval. The W6 and W7 are not retrieved, instead W8 is shown in the lowest panel.

the residuals. However, especially in the CH_4 windows (W4–W5) there are some distinct spikes in the systematic residuals of target measurements. Although some are also present in the CO_2 windows (W2–W3), the systematic residuals there are more uniform. Inspecting the spectral positions of the spikes, some of them are related to H_2O absorption lines. The spikes at 5892 cm^{-1} (W4), 6015.5 cm^{-1} (W5), 6240 cm^{-1} (W2) and 6305 cm^{-1} (W3) are caused by H_2O absorption lines, while the spike at 6344 cm^{-1} (W3) is caused by a line in the solar spectrum. Nevertheless, some spikes are also related to CH_4 absorption lines overlapping with water absorption lines. The residual spikes at 5938 cm^{-1} (W4), 6077 cm^{-1} (W5) and 6096 cm^{-1} are such cases. These individual spikes in the systematic residuals are most likely linked to either errors in the spectroscopic database or the atmospheric model, but not to the instrument line shape, as the residuals are differently shaped (compare e.g. residuals at 6077 cm^{-1} and 6096 cm^{-1}). For CO_2, no patten in the residual can be attributed to a single absorption line, since the absorption lines are too densely spaced. The systematic residuals in the CO_2 windows W2 and W3 are overall lower than the spikes discussed before.

Systematic residuals corresponding to telluric absorption lines are higher for target than reflector measurements. This is expected, since errors in the absorption cross sections originating from incorrect spectroscopic parameters or errors in the atmospheric model, scale with the SCD. Similarly, errors in the ILS lead to stronger residuals for deeper absorption lines. Thus, the longer optical path leads to larger residuals. For residuals caused by water absorption lines, the effect is even stronger as the higher water content in the lower atmosphere leads to disproportionately higher SCDs compared to the geometric light path enlargement. In contrast, the residuals caused by solar absorption lines, whose strength is independent of the telluric light path length, are equal for target and reflector measurements. This can be seen for the residual spike at 6344 cm^{-1} (W3), which is equally deep for reflector and target measurements.

Figure 5.7 displays the systematic residual for the scattering retrieval. The shape of the systematic residuals in W2–W5 is nearly identical to the non-scattering retrieval. The same spikes are present, with only minor changes in magnitude. The RMS is approximately equal for W2, W3 and W5, slightly dropped from 0.2 % to 0.16 % for W4. The systematic residual in W1 is significantly reduced, but this is a result of the empirically determined ILS used in this window (cf. Section 5.3.2). The scattering retrieval includes W8. Here, the residual is not entirely dominated by noise but dominated by a systematic mismatch of model and measurement in the range from 4820 cm^{-1} to 4850 cm^{-1}, which was also observed by Hartmann et al. (2009). Therefore, this is most likely not an instrument effect but rather caused by spectroscopic errors and assumptions on the atmospheric state. In conjunction with the reasonably low RMS of the systematic residuals, with 0.2 % and 0.36 % for reflector and target respectively, this is acceptable.

In conclusion, systematic effects are present in the residuals of the spectral retrievals in all windows. However, except for W1, they are limited to a reasonable level, which is expected in context of errors in the spectroscopic database and assumptions on the atmospheric state.

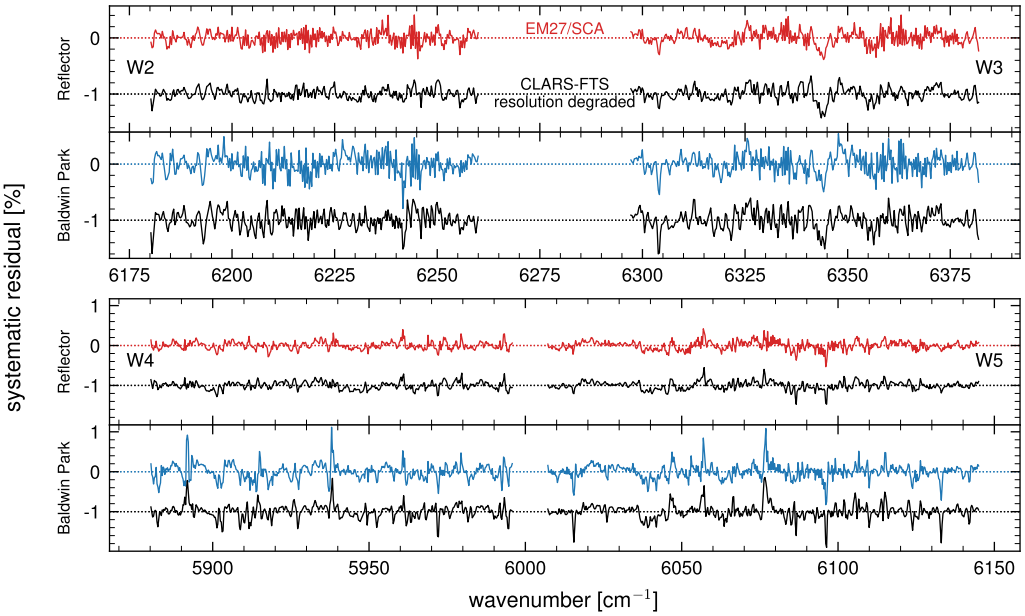

Figure 5.8: Systematic residuals of retrievals from EM27/SCA (colored) and CLARS-FTS (black) spectra. The resolution of the latter was degraded to EM27/SCA resolution prior to the retrieval. The CO_2 (W2–W3) and CH_4 (W4–W5) windows are displayed in the top and bottom panel respectively. For each window systematic residuals of reflector (red) and BP (blue) measurements are shown. The CLARS-FTS residuals (black) are shifted down by 1 % for better visibility.

5.3.1 Comparison to CLARS-FTS Systematic Residuals

To verify that the systematic residuals are in fact not related to instrument effects, I compare those of the EM27/SCA to the CLARS-FTS. For this comparison, the resolution of the CLARS-FTS spectra is artificially degraded by convolving them with the ILS of the EM27/SCA. Since the CLARS-FTS ILS is much more narrow in comparison, this suffices to make both spectra have the same resolution. After the convolution, the spectra are resampled onto the coarser EM27/SCA spectral grid. Figure 5.8 shows the systematic residuals of W2–W5 of equivalent retrievals from degraded CLARS-FTS and EM27/SCA spectra. Both instruments share the same systematic residual pattern and distinct spikes. In some parts of W2 and W3, the EM27/SUN residuals are higher and show narrowly spaced spikes pointing to minor instrument effects. However, the overall close similarity between both systematic residuals shows that the systematic errors are dominated by model errors such as forward model approximations and errors in the spectroscopic parameters for telluric or solar absorption lines.

5.3.2 ILS in the O_2 Window

The previous section showed that the systematic residuals in the O_2 window (W1) are particularly high and consistently show a distinct pattern around individual absorption lines. This is not a systematic error in the spectroscopic data or the retrieval, as retrievals of CLARS-

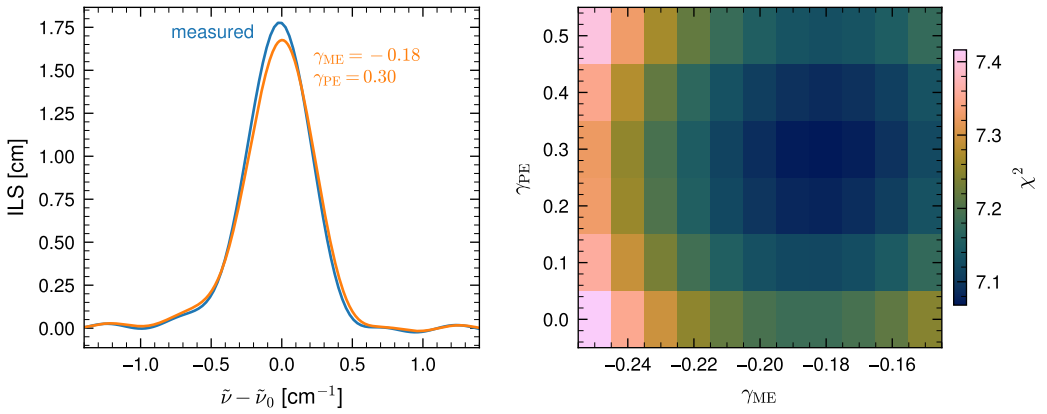

Figure 5.9: Empirical estimation of the ILS in W1. The right panel shows the average χ^2 of one day of W1 reflector retrievals with various ILS. The ILS are generated from ME and PE according to Equations (5.1) and (5.2). The left panel shows the comparison between measured and best estimate ILS.

FTS spectra, neither original nor degraded to the spectral resolution of the EM27/SCA, show these residual patterns. Testing different spectroscopic parameters and retrieval settings, did not result in significant reductions of the systematic residuals. Consequently, the ILS remains as the only possible explanation. Most likely, the measured ILS incorrectly represents the ILS in this particular window. For the other windows, the measured ILS is representative, because similarly deep isolated absorption lines there do not produce such large and consistent systematic patterns. The cause for the ILS only differing in this window is unclear. For the non-scattering retrievals, where the retrievals of the different species are independent, this systematic error is accepted. It leads to a larger calibration factor for O_2 in Section 5.5.1, but otherwise, the systematic deviations are not larger than for the other species. For scattering retrievals, where the aerosol parameters effectively couple the windows, an empirical ILS correction correction is needed.

To this end, an ensemble of ILS is generated and used to retrieve one day of reflector spectra. From the result, the best estimate for the ILS in W1 is determined as the one which yields the lowest mean χ^2. A similar approach as in the scene heterogeneity analysis in Section 3.9.2 is used to generate the ensemble. The modulation efficiency (ME) and phase error (PE) parameters underlying the measured ILS are scaled (cf. Section 3.1.2). The ME and PE of the measured ILS depend on the OPD. They are scaled based on a factor γ_{ME} and γ_{PE} according to

$$\mathrm{ME}_\gamma = \left(1 + \gamma_{ME} \frac{\mathrm{OPD}}{\mathrm{OPD}_{max}}\right) \cdot \mathrm{ME}, \tag{5.1}$$

$$\mathrm{PE}_\gamma = (1 + \gamma_{PE}) \cdot \mathrm{PE}, \tag{5.2}$$

where γ_{ME} and γ_{PE} describe the deviation from the measured ILS. Note, that the generated ME and PE correspond to the measured ones, when γ_{ME} and γ_{PE} are 0. Different ILS are generated from combinations of γ_{ME} and γ_{PE} parameters. With each, W1 of the reflector

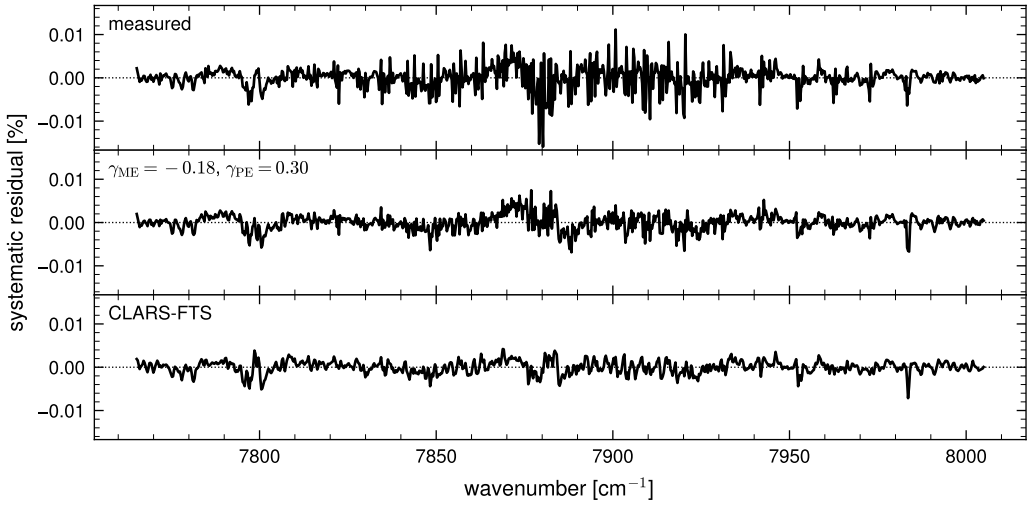

Figure 5.10: Systematic residuals (W1) of reflector measurements averaged over the 13 April 2022, shown for a retrieval using the measured ILS (top) and for a retrieval using the best estimate ILS correction (center). The bottom panel shows the systematic residuals of CLARS-FTS reflector measurements from the same day.

spectra from the 13 April 2022 are retrieved. Figure 5.9 shows the average χ^2 from the reflector retrievals with each γ_{ME}, γ_{PE} pair. A clear minimum exists, where the ME is substantially reduced compared to the original measured ILS. Increasing or decreasing ME and PE further than the range shown here, raises the χ^2 even more. The combination of $\gamma_{ME} = -0.18$ and $\gamma_{PE} = 0.3$ yields the lowest average χ^2. The corresponding best estimate ILS is shown in the left panel of Figure 5.9, constituting the empirical correction for the ILS in W1. While the increase in average χ^2 is only a few permil in the immediate vicinity, the average χ^2 using the best estimate ILS is 20 % lower compared to using the original ILS. Using this ILS in the other retrieval windows significantly increases the residuals there, even for an individual reflector spectrum. Figure 5.10 displays the improvement in the systematic residual in W1 for the best estimate ILS. The characteristic spikes around the O_2 absorption lines are substantially reduced. The systematic residual is now similar to the one of the resolution degraded CLARS-FTS spectra.

The retrieved O_2 SCDs are around 5 % higher than the ones retrieved with the original ILS. For reflector measurements, the difference shows a clear and consistent 1/cos(SZA) dependence with a minimum difference of 5 % at minimum SZA and values reaching 6 % at SZA of 70°. While the reductions in χ^2 in W1 are similar in target spectra, the difference in O_2 SCD shows an inverse behavior with maximum difference of 4.5 % to 4.8 % around noon and lower differences (down to 4 % for WP) at high SZA. However, the SZA dependency is less strong and reflects the O_2 SCD reduction pattern due to atmospheric scattering. Overall, the O_2 SCDs exhibits a consistent but not constant increase, when using the empirical ILS correction.

In conclusion, the empirical ILS correction represents the ILS in W1 better than the original ILS. It is used (in W1 only) for all scattering retrievals, where the retrieval windows are coupled through aerosol information being simultaneously retrieved from all windows.

5.4 Precision

The observational error can be decomposed into accuracy and precision. While the accuracy quantifies the possible bias, the precision quantifies the repeatability of the measurements, i.e. its scatter assuming constant atmospheric conditions. Due to the lack of ground truth, assessing the accuracy is difficult here. Section 5.5 approaches it through comparisons to independent measurements. This section focuses on the precision of the retrieved SCDs.

In general, the precision mainly depends on the measurement SNR, but also on spectral resolution and the absorption signal of the particular gas. The measurement noise propagates directly to the retrieval error. Therefore, the measurement SNR directly influences the precision of retrieved SCDs. Additionally, the spectral absorption features differ in shape and strength between absorbers and windows. Consequently, the precision is distinct for each absorber. Additionally, systematic errors like spectroscopic and ILS errors influence the precision. They typically do not change over time, but the sensitivity of the retrieval to particular parameters may change with atmospheric state, e.g. as the atmospheric water content changes. This necessitates an empirical assessment of the precision.

5.4.1 SCD Precision

Here, the deviation of individual measurements from their temporal rolling average provides an empirically estimate of the measurement precision. For this purpose, measurements from the period 12 April to 15 April 2022 during the LA campaign are evaluated, where we cycled between only three targets. This analysis focuses on the retrieved SCD because the SCD is directly related to the optical thickness. Therefore, it is the quantity most closely related to the measured spectrum. Here, the relative precision of the SCDs is analyzed and subsequently propagated to the precision of the below instrument VCD (cf. Section 4.2), the quantity of interest for emission measurements.

The relative precision $\frac{\Delta\mathrm{SCD}}{\mathrm{SCD}}$ is the standard deviation σ of the ratio between individual measurements SCD_i and an average $\langle\mathrm{SCD}\rangle_t$ over a time window of width t centered around the measurement i.

$$\frac{\Delta\mathrm{SCD}}{\mathrm{SCD}} = \sigma\left(\frac{\mathrm{SCD}_i}{\langle\mathrm{SCD}\rangle_t}\right) \tag{5.3}$$

To avoid errors in the rolling average due to non-linear changes in AMF with SZA, the VCDs are averaged. Subsequently, the averaged VCD are converted to the SCD using the SZA at the time of measurement i.

$$\langle\mathrm{SCD}\rangle_t = \sum_{l=1}^{L}\left(\frac{1}{N}\sum_{j=1}^{N}\mathrm{VCD}_{l,j}\right)\mathrm{AMF}_{l,i} \tag{5.4}$$

Table 5.2: Relative precision of the SCDs retrieved from EM27/SCA measurements. The precision is estimated from the deviation of individual measurements from their 30 min average. Numbers in parenthesis display maximum last digit changes when using 20 and 40 min averaging intervals.

	window	Reflector N=346	Sierra Madre N=367	West Pasadena N=414	Baldwin Park N=368
O_2	W1	0.49(1)%	0.39(3)%	0.40(3)%	0.51(5)%
CO_2	W2, W3	0.37(2)%	0.58(3)%	0.41(3)%	0.39(3)%
CH_4	W4, W5	0.51(2)%	0.77(4)%	0.54(5)%	0.49(4)%
CO*	W6, W7	7.1(3)%	19.5(1.1)%	13.4(6)%	8.1(3)%

* N is lower for CO retrievals: 266 (ref), 183 (SM), 200 (WP), 264 (BP)

The partial VCDs of the N measurements within the interval of size t around the measurement i are averaged. Subsequently, the average partial VCDs are multiplied by the AMF and summed over the L model atmosphere layers. The AMF is different for the layers above and below instrument layer and depends on the SZA.

The fundamental challenge in estimating precision from atmospheric measurements using temporal variability is that the atmospheric state is inherently variable. Using the rolling average as the best estimate for the true state constitutes the averaging time as the key variable. It has to be large enough to render the impact of the precision on the average negligible, but short enough to ensure that the natural atmospheric variability is small in the interval, so that the average is actually representative of the true state. As a trade-off between both, an averaging interval of 30 min is used. This corresponds to 7 measurement cycles. Repeating the analysis with averaging intervals of 20 min (5 cycles) and 40 min (9 cycles) shows differences in the resulting precision estimates of 5 % to 10 % (cf. Table 5.2).

The relative precision of the non-scattering retrieved SCDs is calculated for each absorber. Figure 5.11 displays the relative deviations of the SCDs from the rolling average and its distribution. Table 5.2 lists the corresponding precision estimates. The results are based on the non-scattering retrieval including W1–W7. No distinct SZA dependency of the scatter is visible in the relative deviation. This is the case even though the total SCD increases substantially with SZA. Instead, the total deviations increase with SZA. This is most prominent for reflector measurements but also visible for target measurements, where the relative increase in SCD with SZA is not as large. This supports the assumption that relative deviations of the SCD from the rolling average are a good measure of measurement precision.

For CO_2, CH_4 and O_2, the relative SCD precisions range from 0.37 % to 0.77 %. Reflector measurements have a comparable precision to target measurements, despite the notably higher SNR. This is likely due to the absorption features being shallower for reflector measurements (cf. Figure 3.12). Measurements in Heidelberg, where the light path difference between reflector and target measurements is less substantial, previously showed that the higher SNR of reflector measurements translates to a noticeably higher precision (Hemmer 2019). Comparing targets, the particularly low SNR for the SM target (cf. Section 5.2), propagates to low precision in CO_2 and CH_4. This highlights the importance of target se-

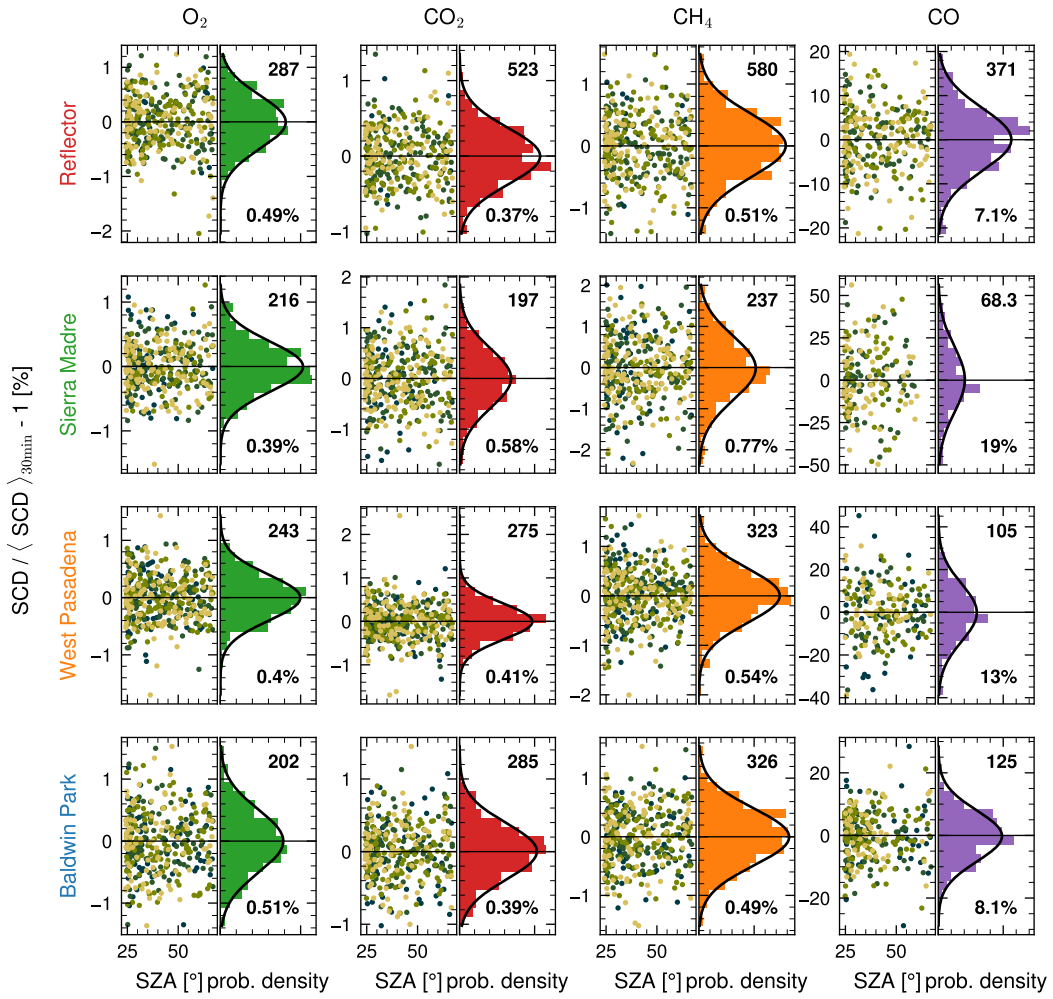

Figure 5.11: Precision of the EM27/SCA derived from the relative differences between the SCDs and their 30 min rolling average. The rows show the different targets, the columns show the different absorbers. Each panel shows the relative difference against SZA on the left and as histogram on the right. Histograms are complemented with a normal distribution with corresponding mean and standard deviation (black line). The mean SNR and the standard deviation are shown in upper and lower right of each panel respectively.

lection, as dark scenes can reduce measurement precision. However, the WP and BP targets are more representative of all other targets. There, the precision range is narrower with 0.37 % to 0.54 % of relative SCD precision.

Across all targets, the CH_4 precision is generally worse compared to CO_2, despite the higher SNR. This points to a consequence of systematic errors, which is consistent with larger spikes in the systematic residuals of CH_4 seen in Section 5.3. With 7.1 % for reflector and 8.1 % to 19.5 % for target measurements, the precision for CO is considerably lower. In part, this is because the SNR of the target measurements in the CO windows (W6, W7) is lower compared to all other windows. Additionally, due to the weak CO absorption features, the precision is also low for the reflector measurements, where this is not the case. In particular, the absorption features are much weaker than the CH_4 and water absorption features in these windows. Especially in target measurements, high amounts of interfering water impacts CO precision.

So far, CO_2 precision is only estimated from W2 and W3. When including W8 in the retrieval and averaging all resulting SCDs, the precision increases. For reflector measurements, CO_2 precision increases from 0.37 % to 0.26 %. For target measurements, the improvement is less pronounced from 0.41 % to 0.37 % for WP and from 0.39 % to 0.34 % for BP. The additional spectral information available through W8 clearly improves the precision. For target measurements, the benefit of the additional spectral information seems to be low. One explanation is that the low SNR in W8 leads to lower precision of the CO_2 SCD retrieved from this window. Since all SCDs are averaged without weighting, this might deteriorate the combined precision. Additionally, wavelength dependent scattering impacting W8 differently than W2 and W3 possibly negates the benefit of the additional information. Coupling the absorbers between windows in the non-scattering retrieval improves the CO_2 and CH_4 precision slightly for reflector measurements. For target measurements, CH_4 precision improves, but for the non-scattering CO_2 retrieval including W8, the precision worsens. This shows that both effects play a role. For reflector measurement, the precision improves because the retrieval now internally weighs the information from the different windows according to their SNR. For the target measurement, this beneficial effect is compensated by the increased mismatch between the spectrally distant windows under the influence of aerosol scattering.

The precision for CO_2 and CH_4 is considerably lower when switching to the scattering retrieval. This is not surprising since more parameters are determined from the same spectral information. Additionally, the retrieval windows are effectively coupled through the simultaneous retrieval of aerosol parameters from all windows. This implies that measurement noise from the O_2 window contributes to the GHG retrieval. Thus, a more appropriate comparison is between the precisions in the ratio of the GHG to O_2 (discussed in Section 5.6.3). In that case, the precision of the non-scattering retrievals is worse than the one presented here, due to the contribution of the O_2 measurement precision. Nevertheless, the precision of the scattering retrieval is still lower. However, the main advantage of the scattering retrieval is the mitigation of systematic errors caused by aerosol scattering, which are not represented in the precision estimates. The scattering induced systematic errors in the non-scattering retrieval and their treatment through the scattering retrieval are discussed in Sections 5.6 and 5.7. In conclusion, combining the results there with the precision consideration here shows that the scattering retrieval sacrifices precision for improved accuracy.

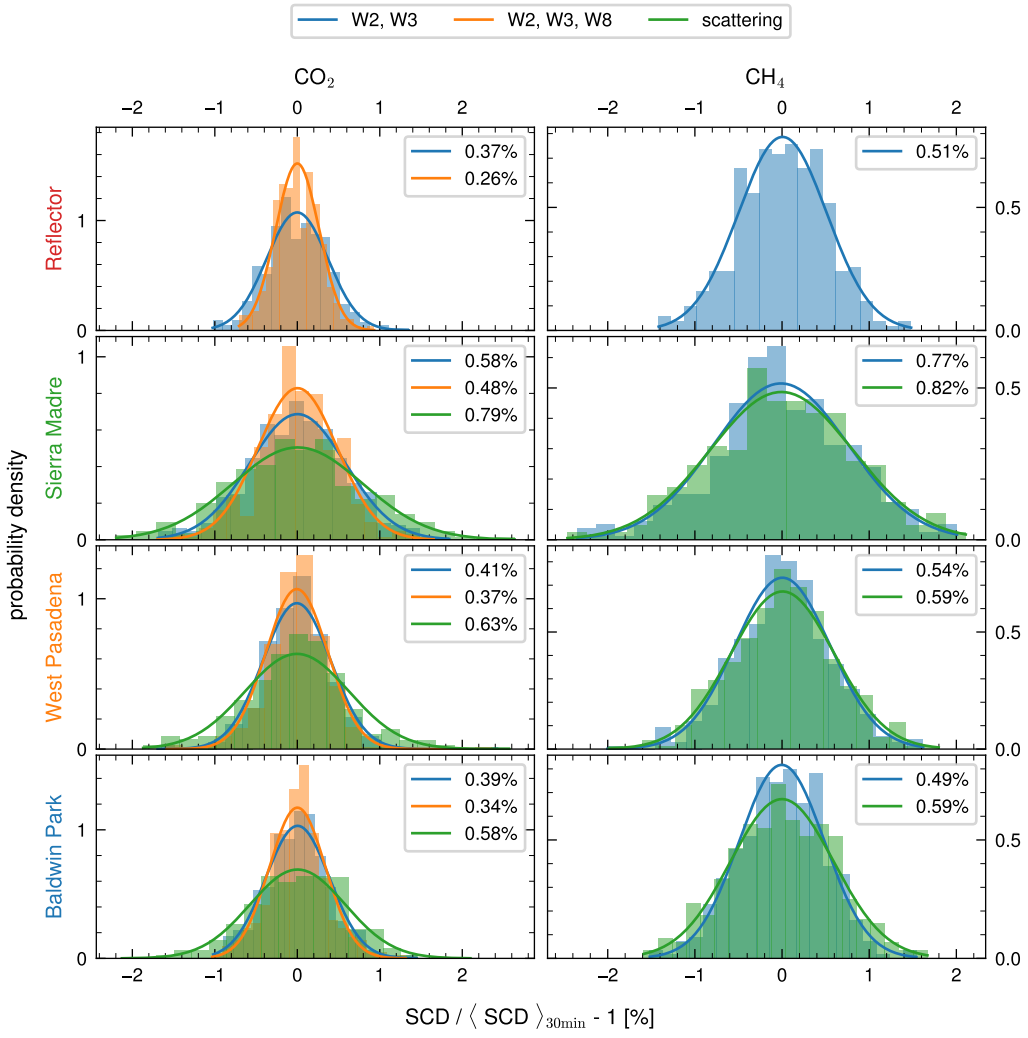

Figure 5.12: Relative SCD precision for CO_2 (left) and CH_4 (right) determined for different retrieval configurations. The non-scattering retrievals are performed in standard configuration (blue) and including the W8 (orange). The scattering retrieval is shown in green.

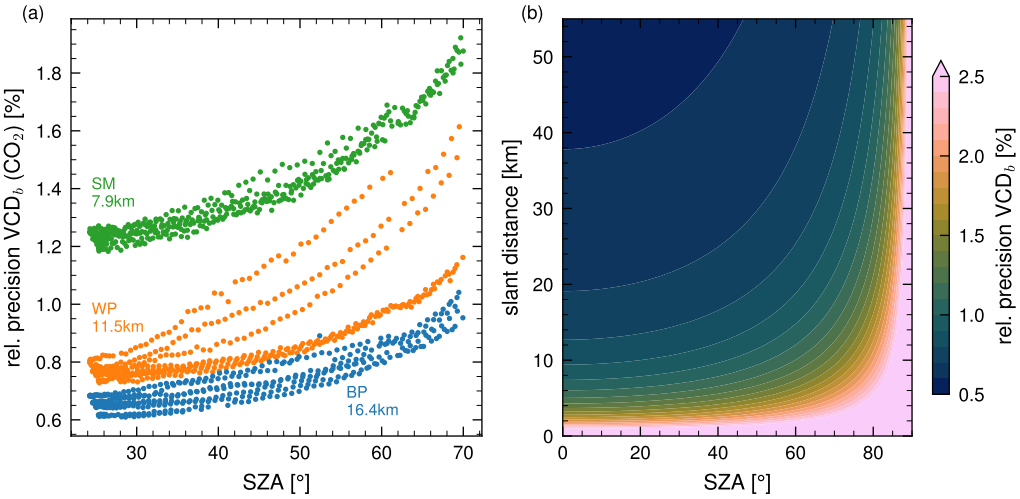

Figure 5.13: Precision of the below instrument level VCD_b in dependence on SZA and slant target distance. The right panel shows the propagation of 0.5 % relative SCD precision to VCD_b precision, assuming a isothermal ideal gas atmosphere with scale height of 8000 m and an altitude difference of 1500 m between instrument and target. The left panel shows the VCD_b precision propagated via Equation (5.6) from the values in Table 5.2 using reflector and target SCD retrieved from measurements during 12 April to 15 April 2022.

Table 5.3: Relative precision of VCD_b propagated from the relative SCD precisions listed in Table 5.2 via Equation (5.6). The value ranges result from evaluation of measurements from 12 April to 15 April 2022.

	Sierra Madre	West Pasadena	Baldwin Park
O_2	0.85 % to 1.5 %	0.75 % to 1.7 %	0.8 % to 1.4 %
CO_2	1.2 % to 1.9 %	0.7 % to 1.6 %	0.6 % to 1.0 %
CH_4	1.5 % to 2.5 %	0.9 % to 2.0 %	0.75 % to 1.3 %

5.4.2 Partial VCD Precision

The precision values presented above quantify the immediate retrieval precision. However, the ultimate quantity of interest lies in the partial VCD below instrument level (VCD_b), which combines target and reflector measurements (cf. Section 4.2). The precision of below instrument SCD, ΔSCD_b, depends on both target and reflector precision, as well as on the observational geometry itself through the solar and viewing zenith angles. For the precision estimation, the errors in target and reflector measurements are assumed to be random and independent (i.e. not correlated).

$$\Delta SCD_b = \sqrt{\Delta SCD^2_{\text{target}} + \Delta SCD^2_{\text{ref}}} \tag{5.5}$$

$\Delta\mathrm{SCD}_b$ depends on the absolute precision of both SCDs. However, the relative precision is constant rather than the absolute precision. Therefore, the absolute precision depends on the actual value of the SCDs, which incorporates information on atmospheric state, target distance and viewing geometry. The relative precision in the $\mathrm{VCD_b}$ in the downward viewing geometry is related to the relative SCD precisions by

$$\frac{\Delta\mathrm{VCD_b}}{\mathrm{VCD_b}} = \sqrt{\left(\left(1+\frac{\mathrm{SCD_a}}{\mathrm{SCD}_b}\right)\frac{\Delta\mathrm{SCD_{target}}}{\mathrm{SCD_{target}}}\right)^2 + \left(\frac{\mathrm{SCD_a}}{\mathrm{SCD}_b}\frac{\Delta\mathrm{SCD_{ref}}}{\mathrm{SCD_{ref}}}\right)^2}, \tag{5.6}$$

where the relative size of $\mathrm{SCD_b}$ and $\mathrm{SCD_a}$ include the aforementioned dependencies. The most important influences are the slant target distance and the SZA. To look at the underlying dependency, a relative SCD precision of 0.5 % for reflector and target measurement is propagated to relative $\mathrm{VCD_b}$ precision assuming an isothermal ideal-gas atmosphere with a scale height H of 8000 m. Additionally, an altitude difference h between instrument and target of 1500 m is assumed, which is representative for measurements of the LA basin from Mt. Wilson. With these assumptions, the ratio between $\mathrm{SCD_a}$ and $\mathrm{SCD_b}$ can be calculated from the SZA θ_s and the target distance d.

$$\left.\frac{\mathrm{SCD_a}}{\mathrm{SCD_b}}\right|_{\text{ideal atm}} = \frac{\frac{1}{\cos\theta_\mathrm{s}}e^{-\frac{h}{H}}}{\left(\frac{1}{\cos\theta_\mathrm{s}}+\frac{d}{h}\right)\left(1-e^{-\frac{h}{H}}\right)} \tag{5.7}$$

Figure 5.13 shows the resulting relative precision of $\mathrm{VCD_b}$. For large slant target distances, the $\mathrm{SCD_b}$ is much larger than $\mathrm{SCD_{ref}}$ and the below instrument precision approaches the target precision. Contrary, for small target distance $\mathrm{SCD_b}$ becomes small and the precision deteriorates. The SZA has a similar effect, influencing $\mathrm{SCD_a}$ much more than $\mathrm{SCD_b}$. An increase in SZA increases the ratio the $\mathrm{SCD_{ref}}/\mathrm{SCD_b}$ as the offset from the target distance becomes negligible, leading to a worse in relative $\mathrm{VCD_b}$ precision. Both dependencies are non-linear, so that the relative $\mathrm{VCD_b}$ precision deteriorates rapidly for short distances and high SZA.

Figure 5.13 also shows the propagation of the empirically determined relative precision of CO_2 SCDs from Table 5.2 to the relative $\mathrm{VCD_b}$ precision. The values are computed with Equation (5.6) from the measured target and reflector SCDs during the period from 12 April to 15 April 2022. Figure 5.13 confirms the general relationships between relative $\mathrm{VCD_b}$ precision and target distance as well as SZA. The relative $\mathrm{VCD_b}$ precision deteriorates with SZA and improves with target distance. The relative SCD precisions in the range of 0.4 % to 0.5 % propagate to relative $\mathrm{VCD_b}$ precisions of 0.6 % to 1.0 % under decent conditions. In this context decent conditions mean a moderately long target distance and no strong scattering influence. This is the case for the BP target as well as the WP target when excluding afternoon measurements. For the very close SM target, this is not given. The combination of comparatively low SCD precision due to low SNR and the short target distance lead to worse relative $\mathrm{VCD_b}$ precision. Also during strongly scattering-impacted measurements, the $\mathrm{VCD_b}$ precisions decreases. This is the case for WP afternoon measurements, visible as three distinct upward branches. Due to the scattering induced light path shortening the difference between $\mathrm{SCD_a}$ and $\mathrm{SCD_b}$ becomes small, which deteriorates the relative $\mathrm{VCD_b}$ precision. In those cases, the relative $\mathrm{VCD_b}$ precision amounts to up to 2 %

(SM) and 1.6 % (WP). Table 5.3 summarizes the ranges for the relative VCD_b precision of all absorbers.

Since the scattering retrieval explicitly accounts for aerosol scattering, the VCD_b will not be underestimated. When applying the precision estimation presented here, the increase in the relative VCD_b precision would apparently be mitigated. However, the light path shortening is a real radiative transfer effect. Subsequently, the sensitivity to the layer below instrument level is in fact reduced. It is a priori not clear how the scattering conditions impact the measurement precision in the scattering retrieval. This requires a detailed analysis and is beyond the scope of this thesis. Overall this evaluation suggests that longer target distances improve the precision of below instrument VCDs. However, one has to consider the trade-off that longer distances increase the impact of atmospheric scattering and with it the systematic errors in the retrieval. This is especially true since the precision improvement with target distance becomes marginal at high distance. Recommendations for favorable target distances depend on the assessment of scattering induced biases and on the effectiveness in mitigating them through the scattering retrieval.

5.5 Comparison to CLARS-FTS

This section compares the EM27/SCA measurements to independent reflected-sun measurements. To this end, I analyze measurements acquired on Mt. Wilson, as described in Section 5.1, where the EM27/SCA was co-located with the CLARS-FTS. Both instruments use the same measurement principle and observed the same targets. Therefore, a direct comparison of their simultaneous measurements is possible.[1]

To circumvent discrepancies caused by spectroscopic parameters, a priori values and the retrieval method, the CLARS-FTS spectra are processed by the RemoTeC retrieval rather than by their operational retrieval[2]. The non-scattering retrieval is used with equivalent retrieval settings for EM27/SCA and CLARS-FTS. Using an albedo polynomial of order 4 in W2, as well as W6–W7, leads to non-converging retrievals, but a third order polynomial represents the continuum of the CLARS-FTS spectra well in W2. For W6–W7 even a quadratic polynomial is enough. Equivalent filter thresholds are applied for the SNR, the χ^2 and the ratio of the retrieved to the geometric O_2 SCD (cf. Section 4.6). Since interferogram properties are not available, the corresponding data filters are omitted. The CLARS-FTS ILS is accurately represented by the theoretical ILS, accounting for the finite resolution caused by the maximum OPD of 5 cm and the self apodization resulting from the finite FOV semi-angle of 4.97 mrad.

The only remaining impediment for a quantitative comparison is that we did not synchronize the target cycling, due to differing measurement duration. Comparing CLARS-FTS and EM27/SCA, the former has a better precision (Fu et al. 2014). Consequently, their partial VCDs are interpolated linearly to the EM27/SCA measurement times. Subsequently, the SCDs are calculated with the AMFs given in Equation (4.18). Instead of the VCDs, the SCDs is interpolated to avoid artifacts due to the non-linear time dependency on SZA which otherwise leads to a systematic overestimation of the interpolated SCDs at large SZA. Only

[1] The CLARS-FTS team kindly provided their raw spectra for this analysis.
[2] modified GFIT, described by Fu et al. (2014)

Table 5.4: Scale factors between EM27/SCA and CLARS-FTS measurements, as determined from reflector spectra.

Gas	Scale Factor non-scattering	scattering
O_2	1.0469	0.9936
CO_2	1.0088	1.0115
CH_4	1.0184	1.0190
CO*	0.9964	

* CO is not retrieved in the scattering retrieval.

measurements are taken into account, where corresponding CLARS-FTS measurements before and after the EM27/SCA measurement are available within one CLARS-FTS cycle after filtering. This leaves 7291 measurements (4033 for CO) available for analysis.

5.5.1 SCD Comparison

Comparing the SCDs retrieved from CLARS-FTS and EM27/SCA spectra, they differ by a scaling factor. Previous studies found absorber specific VCD scaling factors between FTS with different spectral resolution. This is neither specific to a single instrument nor to a retrieval algorithm. Petri et al. (2012) found resolution dependent scaling factors for CO_2, CH_4 and O_2 VCDs by comparing GFIT retrievals of Bruker IFS 66 and IFS 125 HR spectra. Similarly, Frey et al. (2019) found VCD scaling factors when comparing PROFFIT retrievals of EM27/SUN and IFS 125 HR spectra. Additionally, they found similar factors when retrieving IFS 125 HR spectra at EM27/SUN resolution. They traced the cause to differences in spectral resolution by truncating the interferograms accordingly.

The comparison of SCDs retrieved from EM27/SCA and CLARS-FTS reflector measurements yields the scaling factors. The average scaling factors over the whole measurement period for each absorber are listed in Table 5.4. Despite the fact that no aerosol is included in either retrieval for the reflector measurements, the scaling factors are different for retrievals with and without scattering configuration. The relevant differences are the additional retrieval window for CO_2 (W8) and the use of calibrated spectra in the scattering retrieval configuration. Additionally, differences in data filtering may induce small numerical changes in the scale factors. Besides the resolution difference of both instruments, there might be other influences impacting the scaling factors, most prominently errors in the ILS. This is most likely the case for O_2, where the scaling factor is the largest by a considerable margin in the non-scattering retrievals. However, for the scattering retrieval the scaling factor is close to 1. When determining the scaling factor from non-scattering retrievals using the corrected ILS (cf. Section 5.3.2), the O_2 SCDs of EM27/SCA and CLARS-FTS match considerably better, with a scaling factor of 0.994. The EM27/SCA SCDs are multiplied with the scale factors tabulated in Table 5.4 for all following analysis.

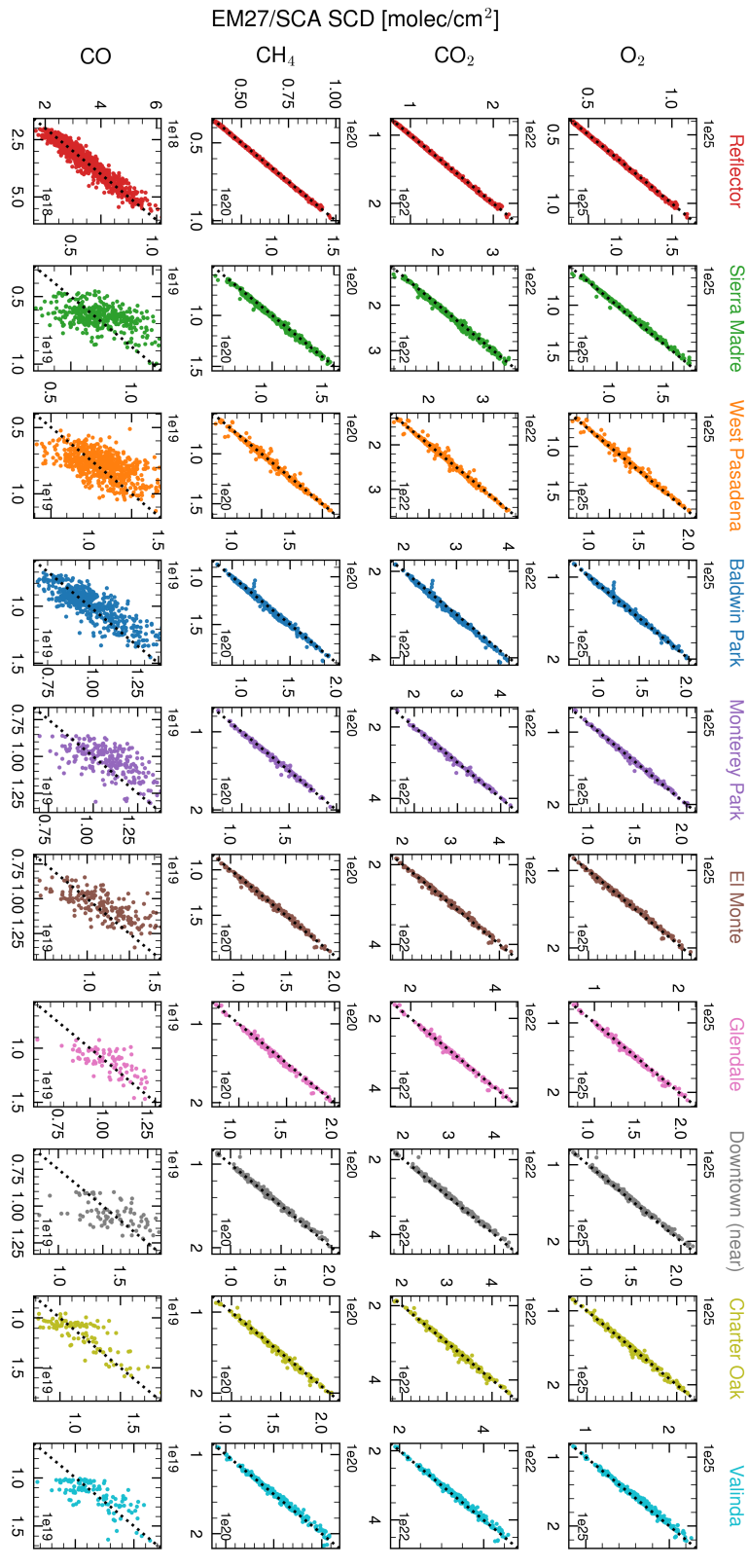

Figure 5.14: Correlation between simultaneous EM27/SCA and CLARS-FTS measurements of the reflector and all targets. The spectra from both instruments are retrieved with the same algorithm, spectroscopic parameters, a priori values and equivalent settings. CLARS-FTS measurements are linearly interpolated to the time of the EM27/SCA measurements.

Figure 5.14 shows the correlation between EM27/SCA and CLARS-FTS SCDs for all target and reflector measurements. They show a good correlation for CO_2, CH_4 and O_2 with correlation coefficients in the range of 0.994 to 0.998 for the target and 1 for the reflector measurements. A few outliers scatter comparatively far away from the 1:1 line for target measurements (i.e. for WP). Without the retrieved/geometric O_2 ratio filter, the reflector measurements show similar outliers. Therefore, outliers in the scatterplots for target measurements are most likely due to cloud influence not captured by the DC variation filter. For some species of individual targets, slight deviations from the 1:1 line are present. No general pattern in the deviations for any absorber is evident, as both upward and downward deviations occur for a given absorber. However, the slopes of the linear regression are consistently above or below one for each target across CO_2, CH_4 and O_2, hinting towards systematic errors, i.e. pointing mismatches between both instruments or influences of minor EM27/SCA FOV heterogeneities. Differences between target measurements will be further discussed in Section 5.5.2.

For the CO SCDs the correlation is generally impacted by the low precision due to low SNR, interfering water absorption and the overall weakness of the CO absorption signal. Despite larger scatter, the correlation between reflector measurements is decent (correlation coefficient of 0.96), however for target measurements, depending on SCD amplitude, the correlation is blurred. This is in part because the SNR in the CO windows is significantly lower for target measurements compared to reflector measurements. Additionally, interference from water absorption is also considerably higher in the target spectra because of the long light path in the planetary boundary layer. The correlation coefficients range between 0.47 (SM) for targets with low SCD amplitude to 0.83 (BP) for targets with high SCD amplitude.

5.5.2 Partial VCD Comparison

The previous section discussed the agreement between EM27/SCA and CLARS-FTS in terms of SCD. However, the partial VCDs (cf. Section 4.2) are much more useful for interpretation. Firstly, they remove the apparent variability due to the change in light path with SZA. Secondly, GHG emissions mostly influence the partial VCD below instrument level. Therefore, this section compares the partial VCDs above (VCD_a) and below instrument level (VCD_b) retrieved from EM27/SCA and CLARS-FTS spectra.

The partial VCDs are determined independently for both instruments. The VCD_a is immediately given by the reflector measurement. To obtain VCD_b, reflector and target measurements are combined. The VCD of adjacent reflector measurements are linearly interpolated to the time of the target measurements. Interpolated values and values computed from them are hereafter marked with ‡. Using the AMF above instrument level, the partial SCD above instrument level are calculated and subtracted from the total SCD retrieved from the target measurement. From this partial SCD, the VCD_b is calculated via the AMF_b by

$$VCD_b = \frac{SCD_{target} - SCD_{ref}^{‡}}{AMF_b}. \tag{5.8}$$

Figure 5.15 shows the partial VCDs above and below instrument level for three illustrative days of the retrieved gases (CO_2, CH_4, O_2 and CO). The first two days stem from the

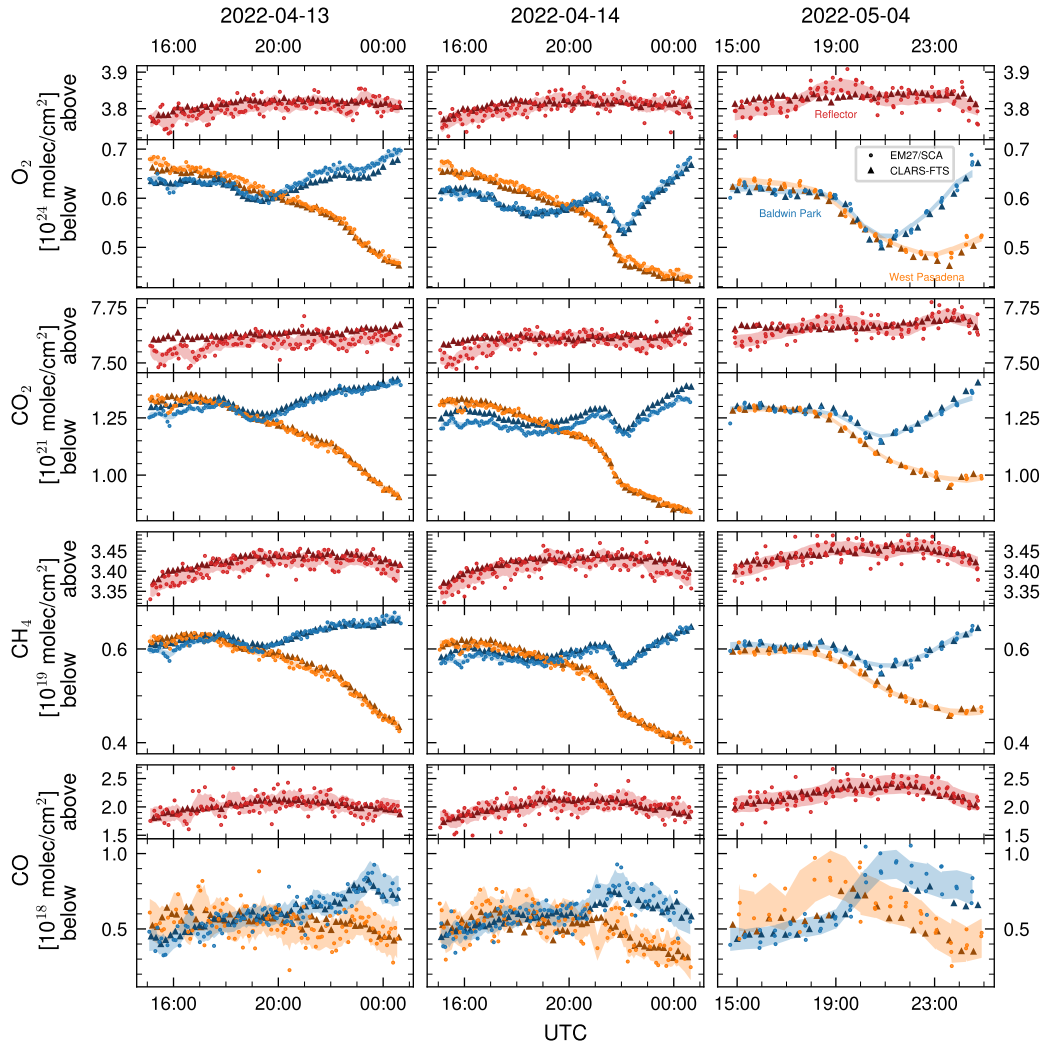

Figure 5.15: Partial VCD retrieved from EM27/SCA and CLARS-FTS spectra on three illustrative days (columns) for O_2, CO_2, CH_4 and CO (top to bottom row). In each tile the partial VCD above instrument level (VCD_a) is shown in red in the upper subplot, the partial VCD below instrument level (VCD_b) is shown in the lower subplot for WP (orange) and BP (blue) target.

campaign period where we cycled only three targets and thus show higher measurement density. Note that besides better precision, the integration time of one CLARS-FTS measurement is three times longer than for one EM27/SCA measurement. This reduces the number of measurements shown as well as the scatter. The one-sigma measurement precision of the EM27/SCA is indicated as a shaded band around the 1-hour rolling average. For above instrument partial VCDs the precision corresponds to the reflector precision. For the below instrument partial VCDs, the relative precision is calculated from the SCD precisions using Gaussian error propagation.

$$\frac{\Delta \mathrm{VCD_b}}{\mathrm{VCD_b}} = \sqrt{\left(\mathrm{SCD_{tar}} \left.\frac{\Delta \mathrm{SCD}}{\mathrm{SCD}}\right|_{\mathrm{tar}}\right)^2 + \left(\mathrm{SCD^{\ddagger}_{ref}} \left.\frac{\Delta \mathrm{SCD}}{\mathrm{SCD}}\right|_{\mathrm{ref}}\right)^2} \tag{5.9}$$

The partial VCDs above instrument level show no substantial diurnal cycle. The most notable deviation is the slight reduction for CH_4 with increasing SZA. The VCD_a agree well between EM27/SCA and CLARS-FTS within the limits of the measurement precision. At some times, there are systematic deviations between both instruments, such as for O_2 at 19:00 UTC and for CO_2 at the start of all three days. Comparison measurements with a direct-sun EM27/SUN (described in Appendix A.8) show similar systematic deviations of up to 0.6 %. In both cases, the systematic deviations show a slow time dependency on time scales of hours. Similar to there, deviations of VCD_b in Figure 5.15 are mostly common to the retrieved CO_2 and O_2 and only weakly present in the CH_4. This is most likely caused by effects of the non-ideal ILS and its uncertainty or possibly small instabilities in the ILS.

The partial VCDs below instrument level show a distinct diurnal variability in O_2, CO_2 and CH_4, with a clear target specific systematic pattern. For CO, the large scatter due to low precision masks most of the variability. The overall variation in VCD_b is equally captured by both instruments and will be discussed below. First, I focus on the comparison of EM27/SCA and CLARS-FTS.

Despite the general agreement, there are systematic differences between EM27/SCA and CLARS-FTS. The differences are more pronounced for the BP target than the WP target. Particular strong examples are the O_2 in the afternoon of 2022-04-13 and the CO_2 throughout the the full day 2022-04-14.

To analyze the statistics of the partial VCD differences between both instruments, the VCD_a and VCD_b are calculated from the interpolated CLARS-FTS SCDs for the full campaign period. The histograms of the relative deviations of both instruments partial VCDs are shown in Figure 5.16. Overall, the differences follow a Gaussian distribution. The relative difference for VCD_a has a mean of 0, as per the scaling factors. The standard deviation is 0.7 % to 0.8 %, which exceeds the EM27/SCA precision of 0.4 % to 0.5 %. In part, this can be explained by contributions of CLARS-FTS precision. However, also systematic deviations visible in Figure 5.15 contribute to the increased standard deviation.

For VCD_b, the standard deviations is in the range of 1.6 % to 1.8 %. This exceeds the EM27/SCA VCD_b precision of 0.6 % to 1.2 % (cf. Figure 5.13) even more than for the reflector measurements. Since the systematic deviations, as visible in Figure 5.15, are not constant throughout the measurement period, they contribute to the standard deviation. However, they also shift the mean of the distribution, if the occurring values are predominantly higher or lower. For O_2, the mean of the relative difference is significantly reduced for most targets. This is related to the ILS issue addressed in Section 5.3.2. When the O_2 VCD_b for the BP target is calculated using the empirically corrected ILS, the mean reduces to -0.2 %. For all targets, the mean deviation of CO_2 and CH_4 has the same sign. However, the magnitude is consistently larger for CO_2. Additionally, Pointing errors can cause a bias in the VCD_b. Because the target SCD used to calculate VCD_b directly depends on the pointing, pointing errors of both instruments cause relative differences in their VCD_b. This is most likely the case to a small extent, as a small drift in the EM27/SCA pointing was observed throughout a measurement day. However, pointing errors would impact all species equally.

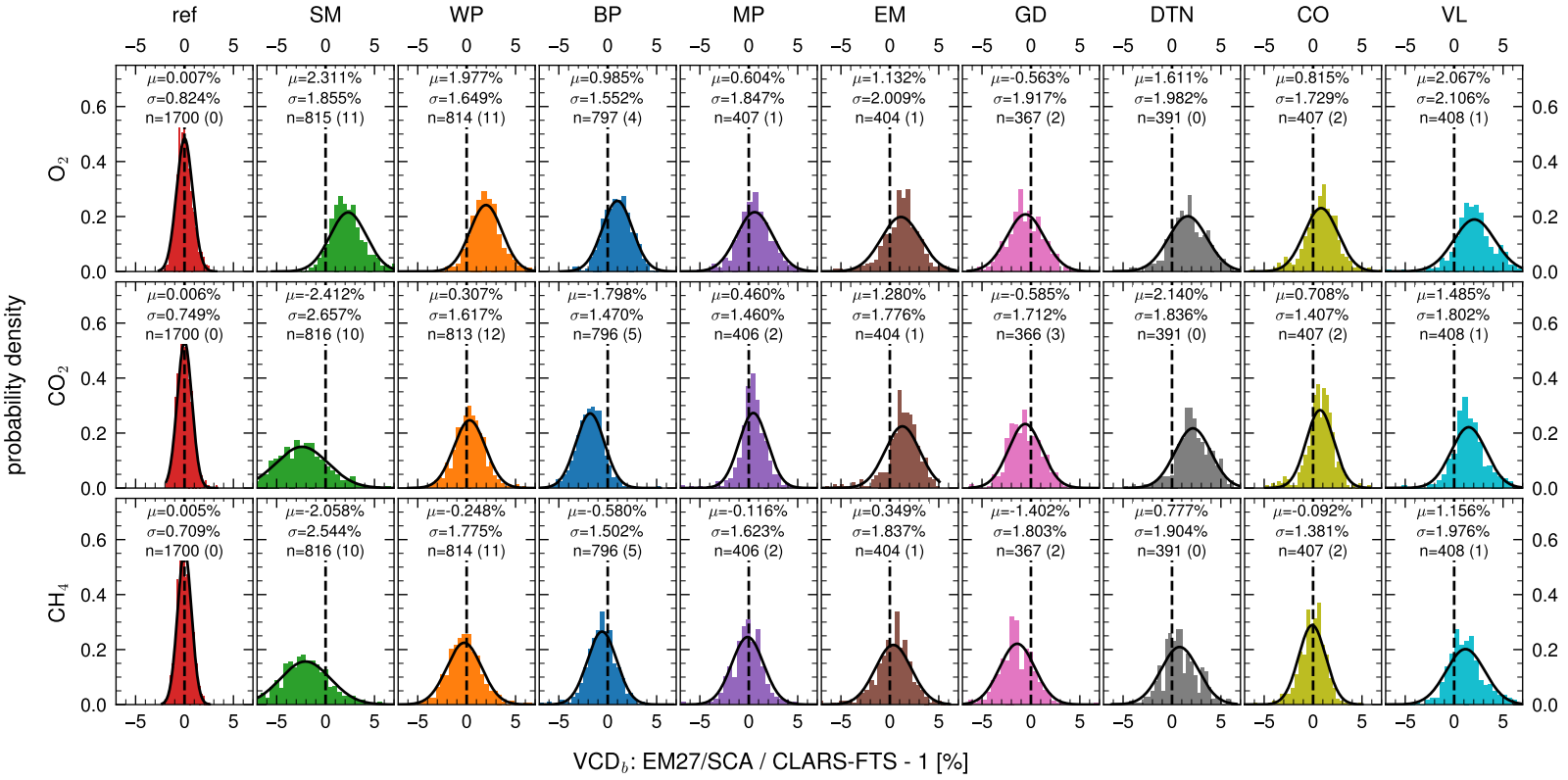

Figure 5.16: Histograms of the relative differences between EM27/SCA and CLARS-FTS partial VCDs. Differences are shown for O_2, CO_2 and CH_4 (top to bottom) and for all targets (columns). The VCD_a is shown for the reflector, the VCD_b is shown for all targets. In each subpanel, the mean μ and standard deviation σ of the relative differences is shown together with the number of measurements N and the number of removed outliers in parenthesis. Outliers are measurements, where absolute relative difference exceeds 10 %.

Therefore, the discrepancy in the difference for the different species makes it unlikely that this is the dominating effect. Checking the correlation of the difference with SZA or SNR shows no clear pattern. However, a weak dependency is visible when correlating the difference with time of day. The shape of the dependency is different for each target. This points towards either differences in the influence of atmospheric scattering on both instruments, or towards mild scene heterogeneity. Despite carefully selecting targets with as homogeneous surface reflectivity across the instrument FOV as possible, perfect homogeneity in an urban setting is not achievable[3]. Differences in the scene homogeneity with time of day are plausible due to differences in illumination of the ground scene through changes in solar azimuth and zenith angle. As discussed in Section 3.9, heterogeneous scenes alter the ILS for the particular measurement, which does not match the recorded ILS. Since the effect strongly depends on the susceptibility to the illumination pattern, which could differ between instruments, this could cause the differences in VCD_b. The CLARS-FTS is expected to be much less impacted by scene heterogeneity due to its near ideal ILS and higher spectral resolution, which reduces the overall impact of the ILS. Most likely, the EM27/SCA is more prone to scene heterogeneity, possibly causing the systematic VCD_b differences between both instruments. This would also explain the disparity in the differences between targets. Tu 2019 showed that for retrievals of EM27/SUN spectra, CO_2 is about twice as sensitive to errors in the ILS as CH_4. Despite the plausibility, this hypothesis can not be ultimately confirmed since an analysis similar to Section 3.9.2 is not possible. Contrary to the strong scene heterogeneity there, the differences in the residuals in this mild case are smaller than the instrument noise. Changes in the scene homogeneity over time due to changing illumination conditions also prevent the evaluation of average residuals.

The differences between instruments discussed here are systematic. However, they are second order effects in the context of the overall VCD_b variability. As pointed out before, the variability in VCD_b is dominated by a target-specific pattern that both instruments capture. For the WP target, the VCD_b decreases by roughly 30 % for all three days shown. The BP target shows a smaller and more complicated pattern, which increases VCD_b in the afternoon but is otherwise different between the days. The pattern is consistent between species, including O_2. The only real temporal variability in O_2 is due to the surface pressure that is much smaller than the magnitude visible in Figure 5.15. Therefore, the variation can be attributed to light path shortening through aerosol scattering, which are discussed in Section 5.6.2. Note that the differences between instruments do not show a correlation with the overall VCD_b pattern. Therefore, they are likely caused by systematic effects, similar to the ones discussed earlier for VCD_a, rather than differences in retrieval errors related to atmospheric scattering.

5.6 Impact of Aerosol Scattering

This section discusses the impact of aerosol scattering on the EM27/SCA measurements retrieved with the non-scattering retrieval. Since Rayleigh scattering by molecules is very small in the NIR spectral range and only observations during cloud-free conditions are analyzed, the dominating scattering effect is Mie scattering caused by aerosols. In general,

[3] Figure A.2 shows pictures from the imaging camera for all targets.

light scattering by aerosols modifies the path of the photons through the atmosphere. Consequently, the absorption signal measured by the instrument changes accordingly. The O_2 measurement allows for quantification of the impact of scattering, since sources and sinks are negligible for O_2 compared to its amount. Therefore, deviations from the geometric O_2 SCD are caused by radiative transfer effects. Using the geometric O_2 SCD inferred from pressure data, the *O_2 ratio* quantifies the impact of aerosol scattering.

$$\mathrm{O_2\,ratio} = \frac{\text{retrieved}\,\mathrm{O_2\,SCD}}{\text{geometric}\,\mathrm{O_2\,SCD}} \tag{5.10}$$

Section 5.6.1 discusses the scattering impact on the reflector measurements. Section 5.6.2 follows, discussing the impact on the target measurements. Subsequently, two possibilities are explored to correct the model error of neglecting scattering. First, Section 5.6.3 discusses the proxy method. This method is also routinely employed in ground based direct-sun observations to correct for other errors common to the species. Second, Section 5.7 discusses the scattering retrieval, which explicitly includes aerosol scattering in the forward model.

5.6.1 Aerosol Impact on Reflector Measurements

Figure 5.17 shows the AERONET aerosol optical depth (AOD) measurements for 24 April 2022, together with O_2 ratio, XCO_2 and XCH_4 retrieved from EM27/SCA and CLARS-FTS reflector measurements. On that day, the AERONET measurements on Mt. Wilson show exceptionally high aerosol levels with a clear decline over the course of the day. The AOD at 1268 nm ($O_2\Delta$ band) declines from 0.15 to 0.07 throughout the day. The EM27/SCA measurements do not show a matching trend in the O_2 ratio. However, the more precise CLARS-FTS measurements show a 1 % decrease from 17:00 on, matching the pattern of the AOD. This trend can be understood by considering that aerosol scattering provides an additional contribution to the irradiance which is reflected by the Lambertian reflector plate. The scattered light experienced a longer path through the atmosphere than direct sunlight. Therefore, the sky-scattered light enhances the effective light path, such that the absorption signal in the spectra increases, leading to an overestimation of the VCD. A similar trend is present for CO_2 and CH_4. Since the light path enhancing effects are to first order common to all species, they cancel in the XCO_2 and XCH_4 of reflector measurements, as shown in Figure 5.17. The O_2 ratio quantifies the impact of a change in overhead aerosol loading by $\Delta\tau_s = 0.08$ to about 1 % in the VCD retrieved from reflector measurements. The effect cancels below levels detectable in the XGHGs.

The larger precision scatter and systematic deviations in the EM27/SCA data mask the aerosol scattering effect on the EM27/SCA reflector retrieval. Since the measurement geometry is the same for both instruments, the findings on aerosol impact on the CLARS-FTS reflector measurements also apply the EM27/SCA.

5.6.2 Aerosol Impact on Target Measurements

In general, atmospheric light scattering alters the light path from the sun to the instrument during target measurements. The non-scattering forward model assumes the direct path

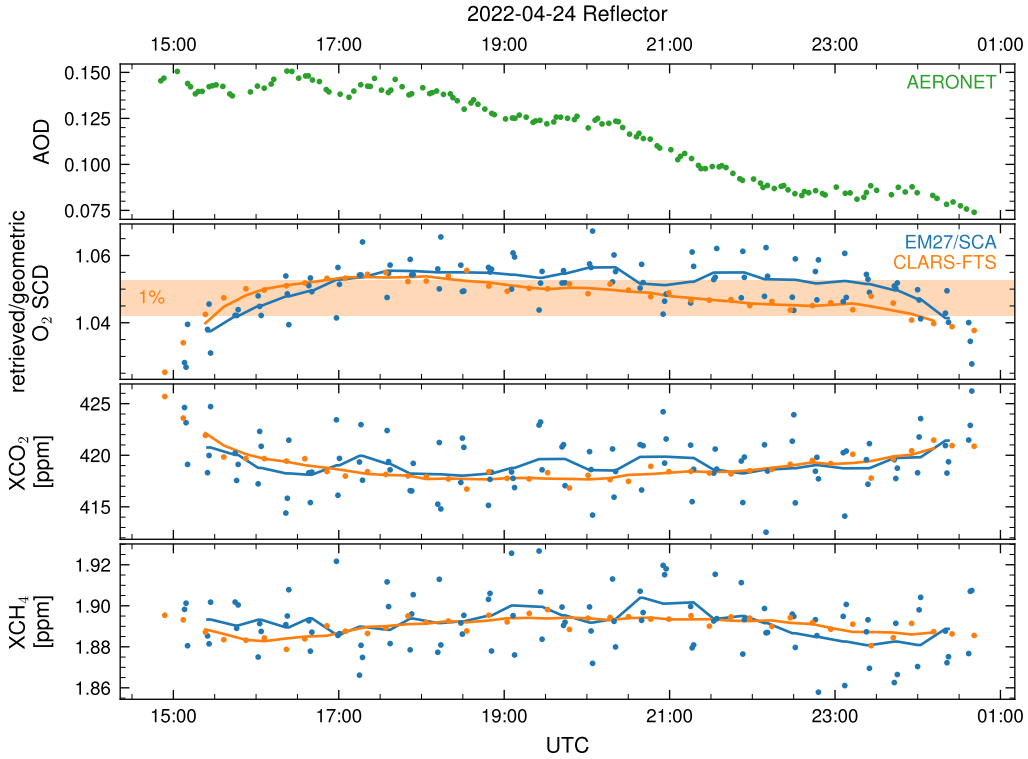

Figure 5.17: Reflector measurements during one day (2022-04-24) with extreme aerosol loading above Mt. Wilson. The first panel shows AOD measurements of the Mt. Wilson AERONET station. The second panel shows the O_2 VCD retrieved from EM27/SCA (blue) and CLARS-FTS (orange) measurements. The shaded area visualizes a 1 % band around the CLARS-FTS daily average. The lower two panels similarly show XCO_2 and XCH_4.

from the sun to the surface to the instrument. However, there are additional paths possible, which include either one or more scattering events in the atmosphere. Generally, light paths with multiple scattering events at aerosol and/or the surface can potentially increase the effective light path. However, this is not the case here. As Section 5.6.3 will show, the dominating aersosol scattering effect is light path shortening.

Light path shortening occurs, when direct sunlight is scattered by aerosol particles into the line of sight between target and instrument. The aerosol-scattered light experienced a shorter path through the atmosphere compared to the ground-scattered light. Since the radiance reflected by the surface is significantly lower than the solar radiance, into-beam scattered direct sunlight can make up a significant portion of the radiance that reaches the detector. A large horizontal light path facilitates this effect. The importance of aerosol scattering depends on (1) the amount of aerosol and (2) the scattering angle. Regarding the former, a higher amount of aerosol in the line of sight leads to a higher fraction of aerosol-scattered radiance in the measurement. For the latter, the scattering angle determines the value of the scattering phase function. Since aerosol scattering can be described

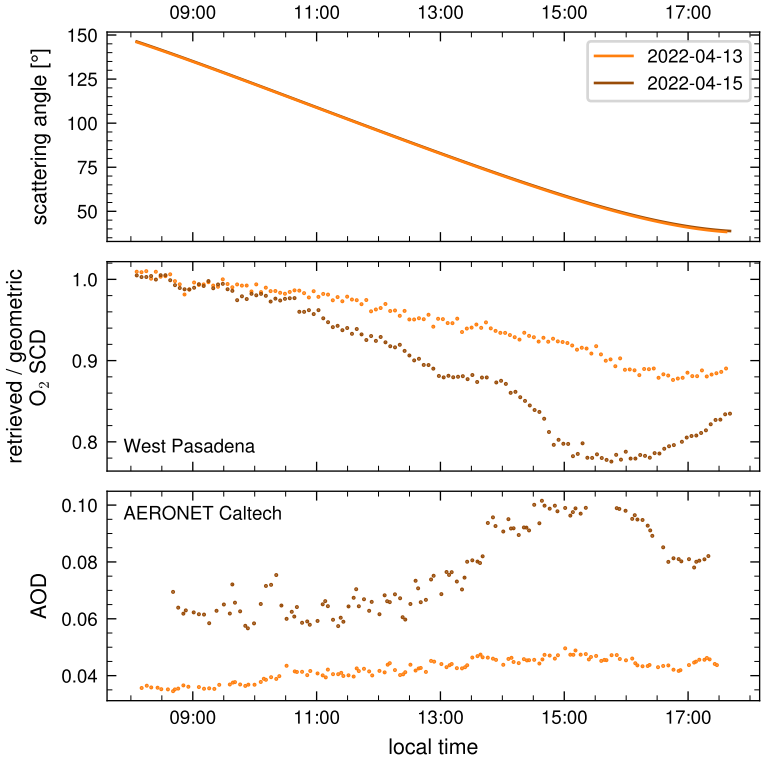

Figure 5.18: Impact of scattering on EM27/SCA measurements. The figure shows data from two days, one with low (13 April 2022, in light shading) and one with high aerosol loading (15 April 2022, in dark shade). The top panel shows the scattering calculated from sun position and viewing direction. The center panel shows the ratio between retrieved and geometric O_2 SCD for the WP target. The bottom panel shows the AOD measured at the Caltech AERONET site, 5 km south-east of the WP target.

by Mie scattering, the scattering phase function is peaked in forward direction. Therefore, a lower scattering angle increases the probability of into-beam scattering and consequently the portion of aerosol-scattered radiance in the measurement.

Figure 5.18 shows the effective light path shortening in EM27/SCA measurements decomposed into aerosol loading and scattering angle contributions. The figure shows the O_2 ratio for the WP target for two days with different aerosol loading, as quantified by the AERONET AOD measurement at the Caltech site. On the 13 April 2022 aerosol levels are low and fairly constant throughout the day. On the 15 April 2022, aerosol levels are overall higher and show a peak around 14:00–16:00 local time. During the first day, variability in the O_2 ratio is mainly driven by the change in scattering angle. Its shape follows the scattering angle. On the second day, the changes in aerosol loading are superimposed on the scattering angle effect. Since the differences in scattering angle are low between both days, both days can be directly compared. The generally higher aerosol loading of the second day results in an overall stronger scattering and thus stronger light path shortening. This effect is reflected in the gradually steeper decline of the O_2 ratio during the day. Furthermore, the

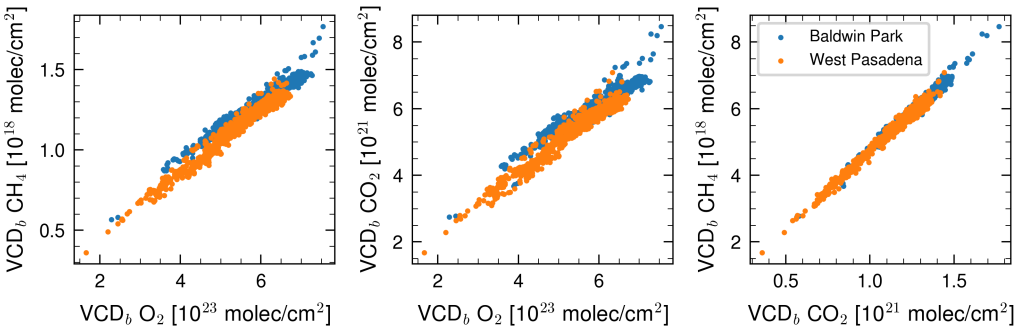

Figure 5.19: Correlation between combinations of the VCD_b of CO_2, CH_4 and O_2, shown for the two targets WP (orange) and BP (blue).

peak in AOD in the afternoon results in a clearly visible timely correlated drop of the O_2 ratio.

The processes presented above also explain the VCD_b reduction pattern visible in Figure 5.15. The WP target is located towards west-southwest direction (VAA=240°). Due to the pointing direction towards the WP target, scattering angles are small in the evening, when SAA and VAA match and at the same time also the SZA is high. This matches the decrease in VCD_b visible during the afternoon, when geometric conditions gradually increasingly facilitate effective into-beam scattering. The BP target is located towards the south-southeast direction (VAA=147°). Thus, the smallest scattering angle is given in the late morning. At that time, the SZA is already high, leading to a larger minimum scattering angle than for the WP target. Additionally, the slant path distance is larger than for WP. The variation for BP is consequently dominated by the variability in aerosol loading, leading to a more complex pattern.

To summarize, this section confirms the hypothesis that the large variability in VCD_b observed in Figure 5.15 is caused aerosol scattering. It demonstrates the model error introduced by neglecting scattering in the retrieval. It shows that even with moderate horizontal paths, the scattering impact is substantial in the reflected-sun measurement geometry.

5.6.3 Proxy Method

The previous section showed that the pattern in the VCD_b, visible in Figure 5.15, is caused by aerosol scattering, which changes the radiative transfer and with it the effective light path. The resulting pattern is similar between all species in Figure 5.15. Figure 5.19 confirms this consistency throughout the whole dataset by showing the correlation of the VCD_b between species. Other effects, e.g., changes in ground pressure and systematic errors, contribute to the correlation, but only cause changes with a lower magnitude than the one shown here. Scattering dominates the variability in VCD_b and, to a first order approximation, the light path alteration impacts the absorption features of all species similarly. The strong correlation suggests the possibility to correct the light path alteration by evaluating the ratio between to different absorbers. There, the error could effectively cancel.

One common option is to calculate the column-averaged dry-air mole fraction (DMF) of the GHG (XGHG) by using the ratio between retrieved GHG and O_2 and multiplying by the known and constant DMF of O_2 of 0.2095.

$$\mathrm{XGHG} = \frac{\mathrm{GHG\,SCD}}{\mathrm{O_2\,SCD}} \cdot 0.2095 \tag{5.11}$$

Here, this method is referred to as *proxy method*, since the well known O_2 is used as proxy for the scattering-induced error, which is assumed to be similar between the species. Calculating the XGHG is commonly used in ground-based direct-sun observations to correct for other systematic errors common to the species (Frey et al. 2019; Fu et al. 2014; Washenfelder et al. 2006; Wunch et al. 2010; Wunch et al. 2011). These other benefits apply here too, but the primary goal is the potential to correct for the scattering error.

Figure 5.20 shows the correlation of the XGHG with aerosol scattering, with the O_2 ratio as measure for the scattering impact on the particular measurement. First of all, the figure shows that light path shortening is the dominating effect, since the O_2 ratio is for all targets mostly below one. Secondly, the figure shows that the light path reduction partially cancels. While the O_2 ratio reduces, down to half in some cases, the XGHG increases. Additionally, the relative increase in XGHG is lower than the relative O_2 ratio reduction. However, a clear residual correlation of the XGHG with the O_2 ratio is visible in Figure 5.20.

The representation in Figure 5.20 also reflects the measurement uncertainty and natural variability with a possible true correlation between aerosol loading and XGHG enhancements. However, since the correlation of XGHG to scattering impact is consistent across all targets and thus independent of target direction, natural variability can be excluded. Consider for example the CO target towards the east and the GD target towards the west. For both targets, forward scattering conditions are present during different times of day and thus high influence of aerosol scattering is also expected at different times. Yet, both targets show similar XGHG enhancements at low O_2 ratio. Assuming no major systematic differences in the local enhancement patterns, this demonstrates that the correlation is not caused by a true enhancement of XGHG, but rather by an overestimation of XCO_2 and XCH_4 induced by the aerosol scattering. Additionally, the ILS error in W1 does not cause the correlation. The overestimation persists when repeating the analysis using the empirically corrected ILS in W1.

Instead, the wavenumber dependency of the ground and aerosol scattering properties causes the bias in XGHG. It introduce differences in the radiative transfer between the different spectral retrieval windows. Since the retrieval window of O_2 is spectrally distant from the CO_2 and CH_4 windows, the errors do not fully cancel in the XGHG. Light path shortening impacting O_2 stronger than CO_2 and CH_4, leads to an overestimation of the XGHG. Zhang et al. (2015) showed this for CLARS-FTS measurements. They found a 10 % XCO_2 overestimation at an O_2 ratio of 0.7[4].

However, for the ratio between CO_2 and CH_4 this is not the case. The retrieval windows of both species are spectrally close, leading to similar radiative transfer for both. Thus, the scattering induced errors are expected to cancel in the ratio of CO_2 and CH_4. The bottom panel of Figure 5.20 shows that the CH_4/CO_2 ratio has no significant dependency

[4]Read off Figure 6b in Zhang et al. (2015), where $b_{O_2} = 30\%$ corresponds to an O_2 ratio of 0.7.

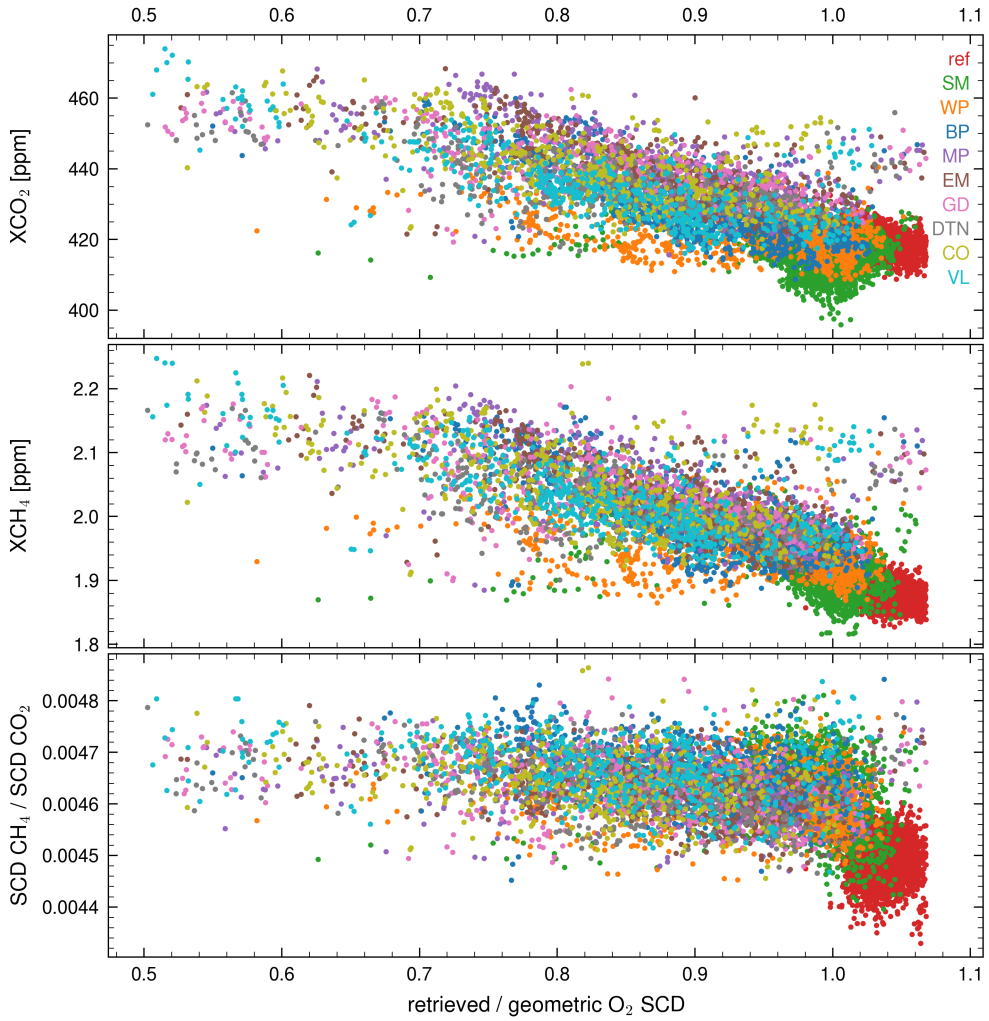

Figure 5.20: Correlation of XCO_2, XCH_4 and the CH_4/CO_2 ratio with the O_2 ratio, demonstrating the bias caused by aerosol scattering. Data is shown from all targets (colors), including the reflector measurements (red), during the full deployment period on Mt. Wilson.

on the O_2 ratio. This confirms that the ratio between CH_4 and CO_2 provides a good way to correct for the radiative transfer errors. However, to obtain the CH_4 DMF with this correction a reliable estimate of the CO_2 DMF is needed. He et al. (2019) and Zeng et al. (2023) successfully used this method to estimate the CH_4 emission from the LA basin. They average the CLARS-FTS measurements to obtain monthly ratios between excess CH_4 and CO_2 in the LA basin above the background, determined from reflector measurements. After applying additional corrections to account for biogenic CO_2 fluxes and systematic bias in CLARS-FTS measurements, they infer the LA basin CH_4 emissions based on the inventory data for CO_2 emissions.

Despite CH_4/CO_2 ratio the method being successful in this application, it requires both accurate a priori information and long averaging times to yield accurate results. For the

campaign based measurement scheme envisioned for the portable EM27/SCA, this is a major limitation. The remaining option is to explicitly account for aerosol scattering in the radiative transfer calculations of the retrieval, which is discussed in the following section.

5.7 Scattering Retrievals

This section provides a possibility to compensate for the effects of aerosol scattering by explicitly accounting for it in the RTM of the retrieval. The forward model described in Section 4.3.2 is used to simulate the measured radiance in an atmosphere, which is aerosol loaded below instrument level.

The state vector in the retrieval includes parameters for aerosol column (n_s), aerosol layer height (ALH) and aerosol size (r_{eff}). While the aerosol column is retrieved freely from the measurement, the ALH and aerosol size are regularized (cf. Section 4.3) to its a priori values of 1000 m and 1.2 µm respectively. These a priori values are physically reasonable, but they are not based on auxiliary data. In a first step, retrievals of individual spectra are performed, using the scattering forward model in the otherwise unmodified setup of the non-scattering retrieval. In this setup, the initial aerosol parameters are fixed. The resulting SCDs increases with increasing imposed aerosol column. This is expected from the apparent reduction in SCD for the non-scattering retrievals. In the range of AODs between 0.0 to 0.2, there are only minor changes in the fitting residuals. The changes in χ^2 are below 1 %. This suggests that there is not enough information content in the spectra, to retrieve aerosol loading and the O_2 column density simultaneously. Retrievals where both quantities are retrieved do not converge. However, when adding the CO_2 retrieval window at 2 µm (W8) to this setup, the CO_2 column yields significantly different values for the columns retrieved from W2/W3 and W8. Additionally, the difference changes with imposed AOD. This means, that the relative difference between the spectrally distant CO_2 windows carries information on the aerosol. When the CO_2 is coupled between both windows, this information can be used in the retrieval to determine aerosol parameters. Based on this, the retrieval setup is modified in two ways. First, the O_2 column is fixed to its a priori and second a single CO_2 column is retrieved from W2, W3 and W8. This allows to reliably retrieve CO_2 and CH_4 columns and aerosol parameters simultaneously. The DFS for the aerosol parameters, the DFSS, range from 1 to 3 somewhat depending on the aerosol information contained in the particular measurement.

The three aerosol parameters (n_s, ALH and r_{eff}) are used in the retrieval algorithm to calculate the AOD. Despite not being a state vector element, it is useful to monitor the AOD found by the retrieval, as it is directly related to the radiative transfer. To this end, AERONET measurements are compared to the retrieved AOD over the WP target, which is closest to the AERONET site inside the LA basin at Caltech. Figure 5.21 shows the AOD data measured at the AERONET sites on Mt. Wilson and at Caltech. The scattering retrieval accounts only for aerosols below instrument level, but the AERONET measurements consider the total column AOD. Therefore, the retrieved AOD are compared to the difference between the measurements in the basin (Caltech) and above instrument level (Mt. Wilson), effectively yielding a measure for the partial AOD below instrument level. This direct comparison has some limitations. Aerosols are highly spatially variable but the AERONET

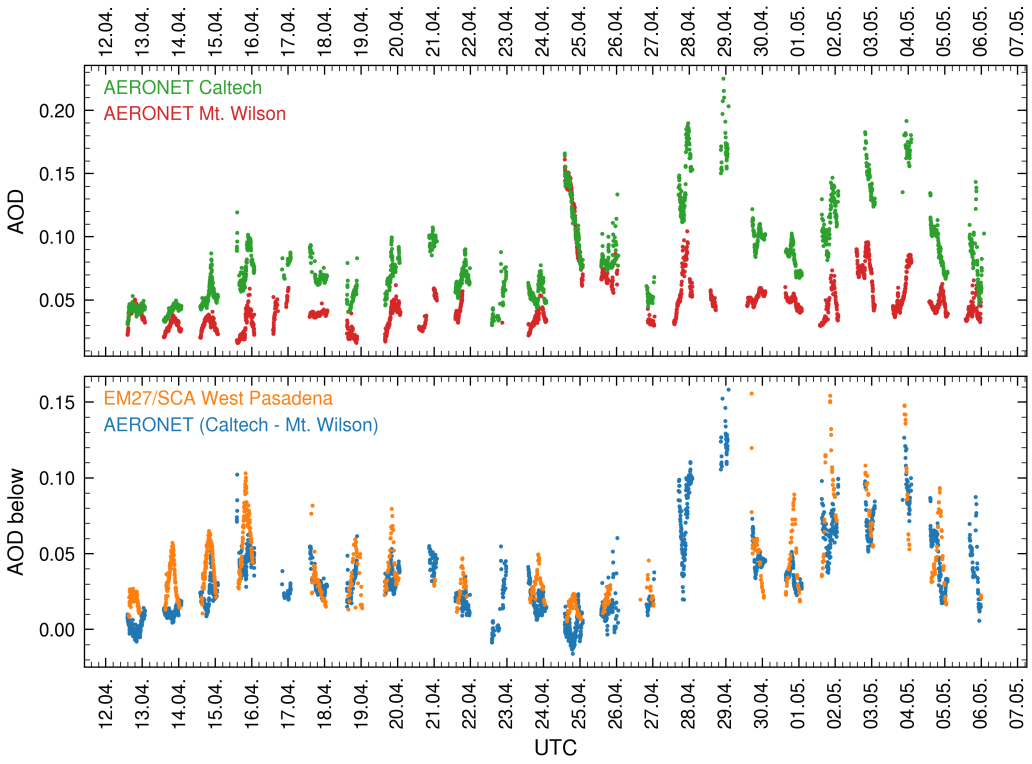

Figure 5.21: Comparison of AOD retrieved from EM27/SCA measurements of the WP target to AOD measurements from AERONET. The upper panel shows measurements from the AERONET sites at Caltech and Mt. Wilson. The lower panel compares the values found by the scattering retrieval to the difference between AERONET measurements on both sites, which gives an estimate of the partial AOD below instrument level. For better visibility, EM27/SCA retrieved AODs exceeding 0.16 are omitted on 18 April 2022 and 2 May 2022 (13 in total).

measurement sites are 12 km apart. Furthermore, the steep topography at the northern edge of the LA basin limits the assumption that the aerosol loading above instrument level over the basin is accurately represented the Mt. Wilson measurement. Some of the aerosol above Mt. Wilson may be below instrument level in the basin. While this limits the quantitative evaluation of the partial AODs, the comparison allows for qualitative plausibility check of the retrieval results. More importantly however, there is some ambiguity with the vertical aerosol distribution. The same effective light path reduction can be a result of an aerosol layer with high AOD at low ALH and at low AOD at high ALH.

In Figure 5.21, the retrieved AODs are overall compatible with the partial AOD inferred from AERONET measurements. Especially the relative day-to-day variability of both agree well. The retrieval finds low AOD values for days where low aerosol loading is expected from AERONET measurement (e.g. 12 April, 25 April) and vice versa (e.g. 16 April, 1 June to 3 June). On the 24 April, where Mt. Wilson and Caltech both show high values but the difference is low, the retrieval finds low AODs. Overall the retrieval seems to overestimate

the AOD and shows larger diurnal variability. The overestimation could in part be caused by the Mt. Wilson AOD measurements systematically overestimating the above instrument level AOD in the basin, due to the topography.

Figure 5.22 shows the retrieval results for the WP and BP target on three days where they were densely sampled. The comparison the VCD_b inferred from the scattering retrieval to the non-scattering retrieval shows that the strong variability due to scattering is effectively mitigated. The retrieved AOD shows a strong diurnal pattern with considerably higher values at low SZA. Focusing on the aerosol parameters directly included in the state vector, a corresponding similar pattern is visible in the ALH showing low values at low SZA. This illustrates the ambiguity between AOD and ALH mentioned above. Contrary to the retrieved AOD, the aerosol column captures the diurnal pattern in the AERONET AOD measurements quite well. However, it follows the measurements inside the basin more closely than the difference between both AERONET stations. The ALH is consistently higher than the a priori value exhibiting a clear diurnal pattern. The size parameter r_{eff} is retrieved with values above and below the a priori, to which it is regularized. The diurnal cycle of r_{eff} correlates with the scattering impact visible form the VCD_b variation in the non-scattering retrieval. For high scattering impact the retrieval finds low r_{eff}. The pattern in the DFSS also corresponds closely to the pattern in the non-scattering VCD_b. This clearly shows that the information content used for aerosols by the retrieval increases when the scattering impact on the measurements is large. Further detailed investigations are necessary to evaluate individual measurements or the diurnal patterns in AOD or the physical aerosol parameters. It is likely that more a priori knowledge on aerosol properties and vertical distribution is required. Nevertheless, the scattering retrieval overall yields stable and plausible results. It mitigates the apparent reduction in VCD_b caused by aerosol scattering in the non-scattering retrieval, providing a reliable scattering correction for the target measurements in the reflected-sun geometry.

The following analysis assesses the performance in correcting for the scattering induced bias in the EM27/SCA measurements. To this end, the analysis performed for the proxy method in Section 5.6.3 is repeated for the scattering retrieval results. Here, the XGHG is computed with the a priori O_2 SCD, since no retrieved value is available. Similar to Figure 5.20, the retrieved XGHG values are compared against the O_2 ratio as proxy for the scattering influence on the particular measurement. For each measurement, the O_2 ratio is determined from the same spectrum in the non-scattering retrieval.

Figure 5.23 shows the distribution of the XGHG values in relation to the O_2 ratio. Besides the XGHG inferred from the scattering retrieval, the figure show the XGHG from the non-scattering retrievals in black. The comparison between both shows a systematic offset. For measurements with low scattering impact (O_2 ratio ≈ 1) and for the reflector measurements, the XGHG calculated from the non-scattering retrieval is lower than that from the scattering retrieval. This offset is not introduced by the differences in the forward model, since it is also present in the reflector measurements where the forward models are the same. Instead, it results from the different treatment of the O_2 SCD and the additional retrieval window for CO_2. For the non-scattering retrieval, an overestimation in the O_2 SCD leads to a underestimation of the XGHG. It is known from TCCON and EM27/SUN calibration efforts that errors in the spectroscopic parameters of O_2 induce a constant high bias of the retrieved O_2 columns compared to O_2 columns calculated from pressure data, leading

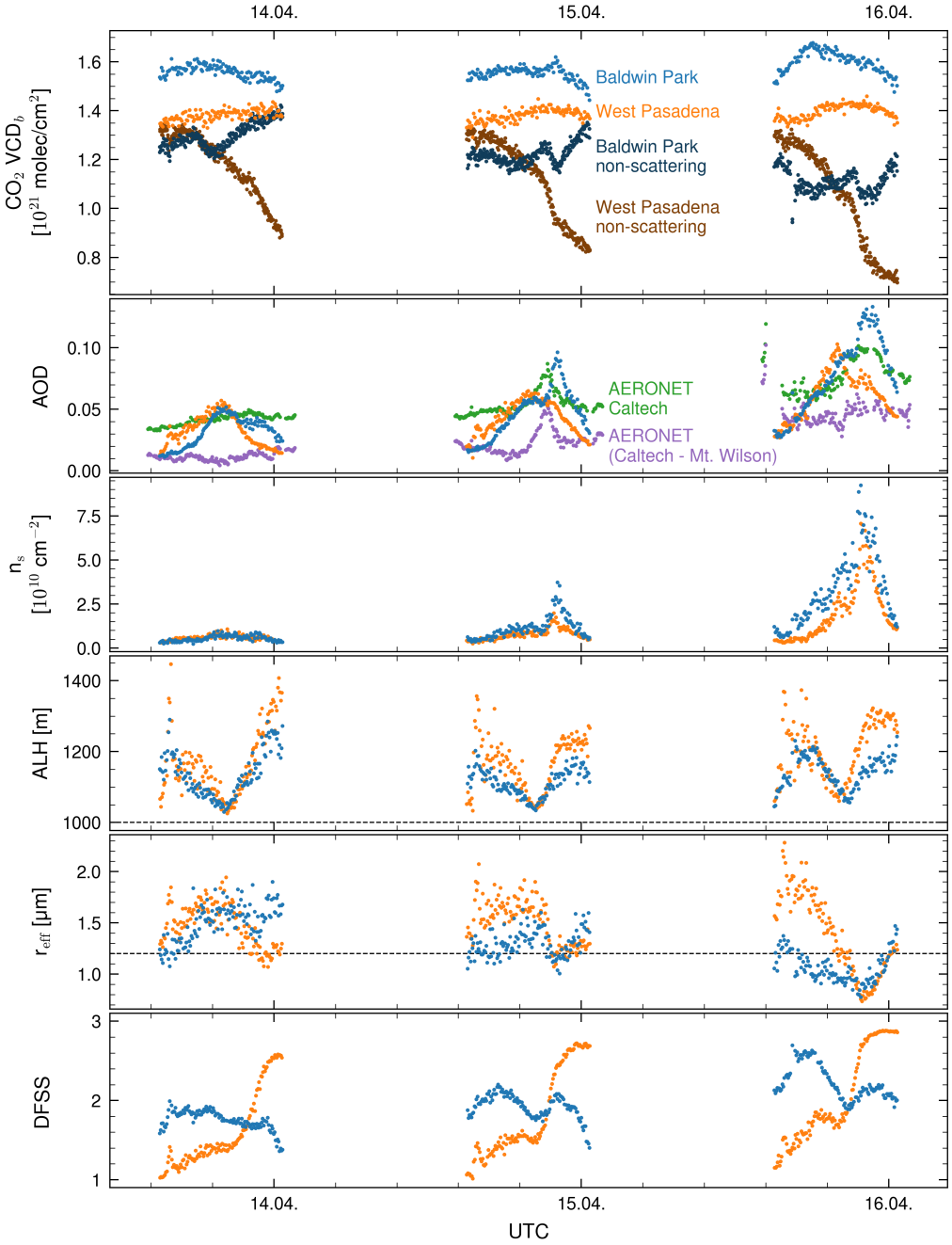

Figure 5.22: Retrieval results of the scattering retrieval for the dense sampling period of the WP and BP targets. The top panel compares the CO_2 VCD_b determined from the scattering retrieval (light shade) to the non-scattering retrieval (dark shade). The second panel compares the retrieved AOD to the AOD measurements at the Caltech AERONET site and to partial AOD, which is the difference between AERONET measurements at Caltech and Mt. Wilson. The panels 3 to 5 show the aerosol properties which are state vector elements in the retrieval. The dashed line indicates the a priori values for ALH and r_{eff}. The lowermost panel shows the DFS for the aerosol properties.

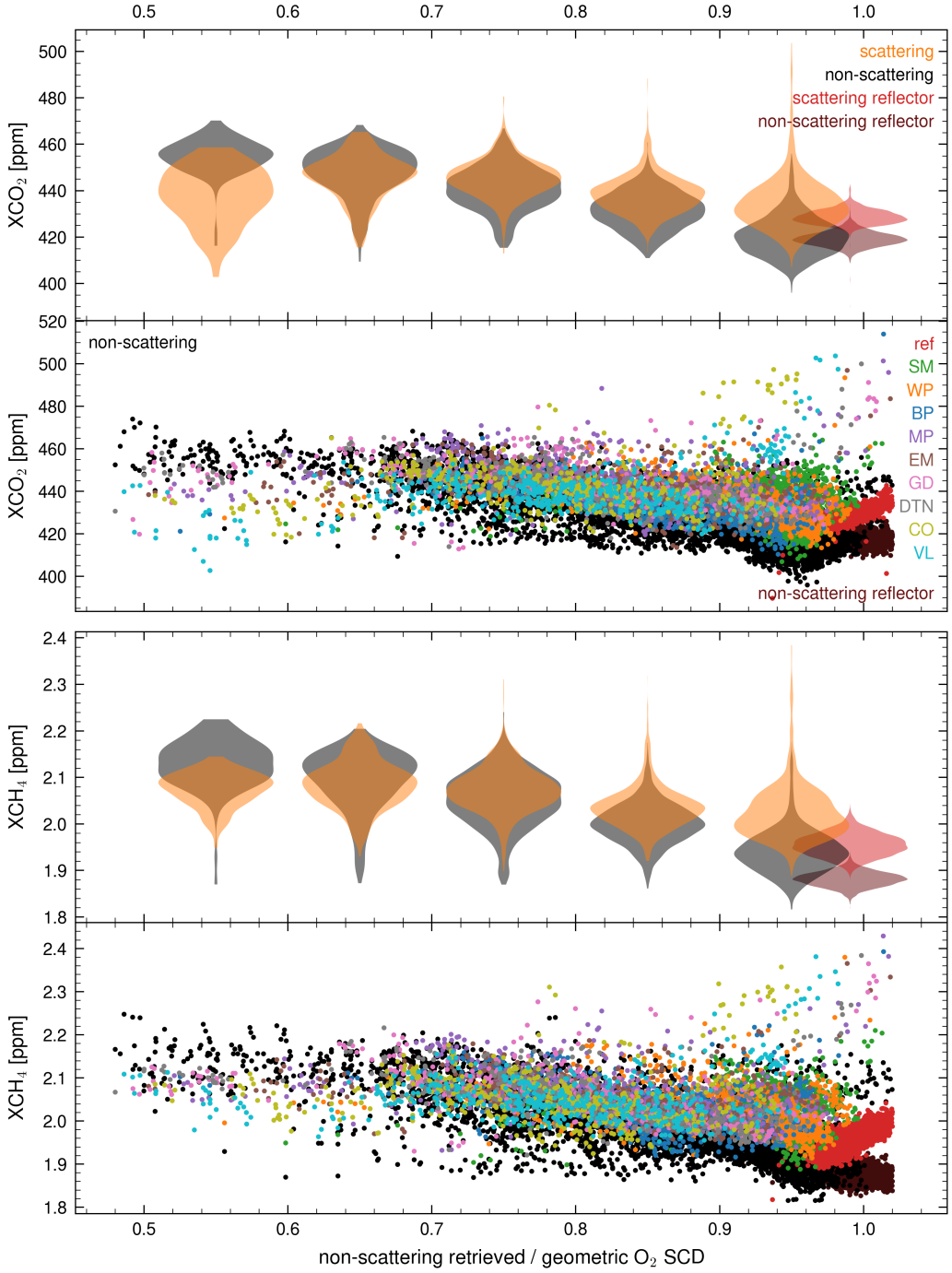

Figure 5.23: Correlation of XCO_2 (top) and XCH_4 (bottom) with the O_2 ratio, retrieved with scattering (colored) and non-scattering retrieval (black). For each GHG, the lower subpanel shows the XGHG values retrieved from all targets over the full campaign period on Mt. Wilson. The upper subpanel shows the distribution in 0.1 O_2 ratio intervals from 0.5 to 1.0. For reflector measurements the distribution is computed over all measurements.

to a low bias in the XGHG (Frey et al. 2015; Washenfelder et al. 2006; Wunch et al. 2010). This low bias is not present for the XGHG from the scattering retrieval, since there the O_2 SCD is calculated with O_2 from pressure data. For the XCO_2 values, an additional offset between both retrievals is introduced by the usage of W8 for the CO_2 retrieval through differences in systematic spectroscopic errors. The target retrievals show some outlier at high O_2 ratio and abnormally high XGHG. Most of these exhibit larger then normal fitting χ^2 and can most likely be excluded by stricter filtering criteria.

Focusing on the scattering dependency of the XGHG values from the scattering retrieval, the distribution exhibits a much flatter dependency on O_2 ratio than the non-scattering retrieval. This shows that the scattering retrieval largely corrects for the scattering influences. The large high bias at low O_2 ratio, which the XGHG computed with the proxy method from non-scattering retrievals exhibits, is significantly reduced. This means that the aerosol properties and distribution are sufficiently accurately represented to describe the wavenumber-dependent radiative transfer in the retrieval. The simultaneous retrieval of the aerosol properties across all windows is able to accommodate the wavenumber dependency of the aerosol optical properties. Thus, the influence of aerosol scattering is explicitly included in the forward model and the absorber columns can be retrieved without the scattering induced bias.

Besides the forward model also the regularization differs between scattering and non-scattering retrieval (cf. Section 4.3). To investigate the influence of the regularization difference, the analysis is repeated only switching the regularization of the respective retrieval. The bias is not negated by the scattering retrieval when using the overhead regularization. When applying the profile scaling regularization to the non-scattering retrieval, the bias significantly increases further. This shows that the profile scaling regularization does not cause the mitigation of the scattering induced bias. At the same time it is required for the mitigation.

The retrieval of aerosol information requires abandoning the retrieval of the O_2 SCD. This has implications for the XGHG results, since the method relies on the geometric O_2 SCD inferred from pressure data. The reflector values show a clear upward trend with increasing O_2 ratio, confirming the influence of aerosol scattering on reflector measurements analyzed in Section 5.6.1. Since scattering effects are disregarded above instrument level, the reflector measurements currently do not use information from the O_2 absorption features in the scattering retrieval. When accounting for the bias introduced by spectroscopic O_2 errors, it is therefore possible to use the proxy method for the reflector measurements, since scattering effects are limited there.

By reducing the main error to the target retrievals, other sources of uncertainty become relevant. The scattering retrieval uses the spectral information of the O_2 window to retrieve aerosol properties. Thus, errors in the O_2 a priori, i.e. surface pressure, propagate to errors in the retrieved aerosol parameters. Similarly, errors in the pointing relate to errors in the assumed geometric O_2 column. This influences the XGHG calculated from the geometric O_2 directly, but also influences the aerosol retrieval under assumption of the fixed O_2. In principle, error sources common to all spectral windows also affect the aerosol retrieval. Thus, retrieval errors in pressure or pointing could be compensated by errors in the radiative transfer. It is however unclear how these kind of errors propagate and it is doubtful that they cancel fully in the retrieval. Calculating the XGHG from geometric rather than

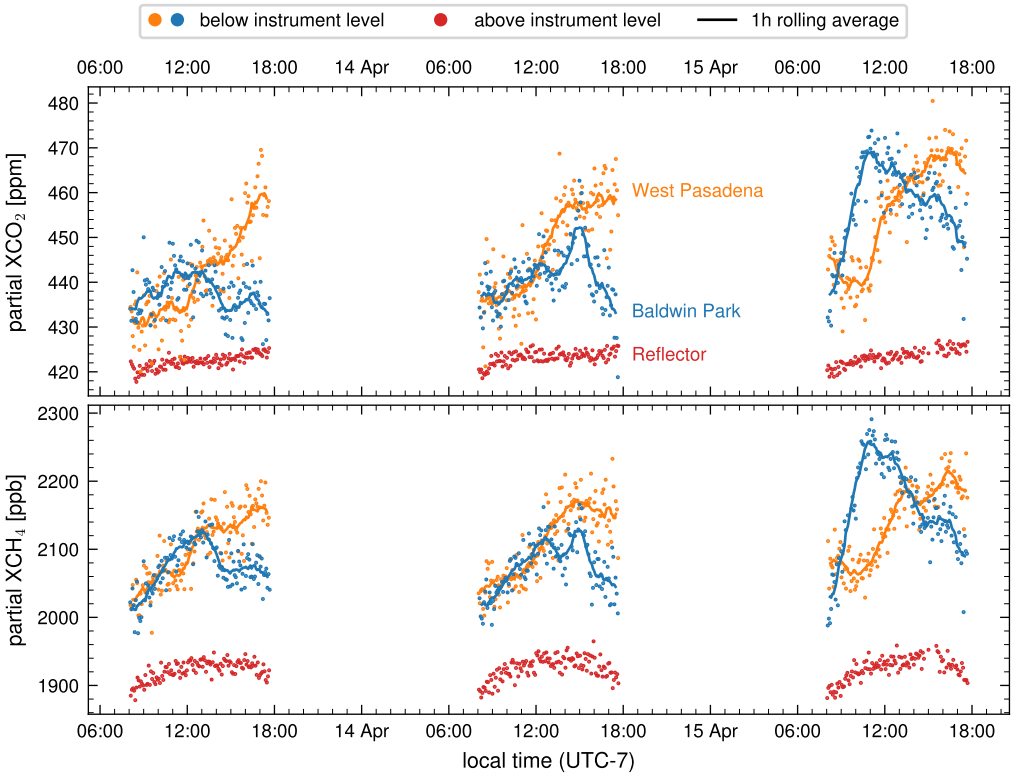

Figure 5.24: XCO_2 (top) and XCH_4 (bottom) calculated from the partial VCDs above (red) and below (orange, blue) instrument level for three consecutive days (13 to 15 April 2022). XGHGs below instrument level show enhancements compared to the XGHG above instrument level computed from the reflector measurements. The diurnal enhancement patterns differ between the WP (orange) and the BP (blue) target. The solid line shows the 1-hour rolling average for the XGHGs below.

spectroscopic O_2 additionally annuls the benefits of canceling other error sources common to GHG and O_2 (Washenfelder et al. 2006; Wunch et al. 2011). Additionally, the aerosol parameters are regularized in the retrieval. This leads to an influence of the specific a priori values chosen for the regularized aerosol parameters (ALH, r_{eff}). Moreover, some of the aerosol parameters are fixed to plausible values, but without prior knowledge.

Despite the additional error sources addressed here, the analysis of Figure 5.23 clearly shows that the scattering retrieval successfully reduces the main error source of the non-scattering retrieval. It is able to significantly reduces the scattering induced bias in the GHG retrievals by explicitly including aerosol scattering in the retrieval.

5.8 Patterns of Urban Emissions

Urban emissions increase the GHG concentrations above the urban region. Therefore, measurements of the GHG enhancements and their spatiotemporal patterns yield information on the urban emissions. To assess the value of the EM27/SCA measurements for this pur-

pose, I analyze the enhancements in XGHG computed from the retrieved partial VCDs. Figure 5.24 shows time series of partial XCO_2 and XCH_4 of the WP and BP target and the reflector on three consecutive days. The partial XGHG is calculated from the partial VCD with Equation (5.11). The geometric O_2 column is used for the ratio, since no O_2 columns are retrieved. The target measurements in Figure 5.24 show the partial XGHG below instrument level, calculated from VCD_b. Additionally, the 1-hour rolling average is show, which averages 13 measurements. Complementary, the reflector measurements show the XGHG above instrument level calculated from the VCD_a. The difference between target and reflector XGHG therefore represents the urban enhancement averaged across the atmospheric layer below instrument level.

Overall, the reflector XGHGs show low diurnal variability. At a low magnitude, the reflector XCO_2 shows a small upward trend over the course of the day. This trend is caused by aerosol scattering influencing the non-scattering retrieved reflector measurements as discussed in Section 5.6.1. This is confirmed by the abscence of the trend when the XGHG is calculated with the retrieved O_2 column. However, the retrieved O_2 column does not provide a straight forward correction since a bias of around 2 % is introduced due to errors in the O_2 absorption cross sections (e.g. Wunch et al. 2011). The morning values, which show low influence of aerosol scattering, agree well with the values measured at Mauna Loa observatory during that time of 420.5 ppm (Thoning et al. 2024a). Therefore, they accurately represent the free tropospheric background. For XCH_4, the reflector measurements show a spurious SZA dependency which is also known from other studies (e.g. Knapp et al. 2021; Wunch et al. 2011). The SZA dependency dominates the linear trend due to aerosol influence. Also here, the CH_4 concentration of 1935 ppb measured at Mauna Loa (Thoning et al. 2024b) is reasonably represented by the measurements during low SZA. For accurate XGHG enhancements, both effects need to be corrected. However, in comparison to the variability below instrument level, these effects are comparatively small.

The XGHGs below instrument level show much larger diurnal variability then the reflector measurements. The variability is on the order of 30 ppm in CO_2 and 200 ppb in CH_4. Additionally, the partial XGHGs below show a minimum enhancement of approximately 10 ppm in CO_2 and 100 ppb in CH_4. Wunch et al. (2009) show that the urban emissions cause a diurnal variability in total column XGHG with a magnitude of 2 ppm to 4 ppm for CO_2 and 30 ppb to 40 ppb for CH_4. Hedelius et al. (2018) quantifies typical enhancements measured by the TCCON station at Caltech, Pasadena, relative to a background station to 0 ppm to 6 ppm CO_2 and -10 ppb to 30 ppb CH_4. They find similar urban enhancements in OCO-2 XCO_2 data. The enhancement measured in total column XGHG measurements is significantly lower than the enhancement expected in the partial XGHG shown in Figure 5.24. Assuming the enhancements are confined to the lowest 1.5 km of a 8 km total column, partial XGHG below instrument level would be 5 times as high. An total column XCO_2 enhancement of 4 ppm then corresponds to around 20 ppm CO_2 and a total column XCH_4 enhancement of 30 ppb corresponds to a 150 ppb CH_4 enhancement in the partial XGHG below instrument level. This is between the mean and the 84th percentile of mid-afternoon mean values Verhulst et al. (2017) report for their in situ measurements. In this context, the enhancements shown in Figure 5.24 are rather high but not impossible. These unlikely high enhancements could be caused by a residual scattering-induced high bias in the retrievals. Indicators for this in the observed enhancements may be the correlation between species and

the enhancement following the light-path reduction pattern shown in Figure 5.22. However, both indications are inconclusive. Firstly, the correlation in the enhancement patterns are also strong in direct-sun observations (Wunch et al. 2009). Secondly, there are indications that the correlation between light path shortening and the enhancements are not causal. For the BP target, the enhancement pattern only partially matches the light path shortening pattern (cf. Figure 5.22). While the small peak in XCO_2 coincides with the observed light path shortening, the much larger peak on 15 April does not. Here, the light path shortening shows a double dip, while the enhancement shows a single peak followed by a gradual decline. While some portion of the signal might still be related to residual scattering impacts, this shows that the measurements are able to capture real variability. For the WP target, the enhancements consistently increase in the afternoon, where also scattering becomes more important. However, the expected pattern caused by urban emissions also has that shape. Hedelius et al. (2018) and Wunch et al. (2009) find a similar pattern in direct-sun total column measurements. Both studies were conducted in proximity ($\leq 5\,\mathrm{km}$) to the target location. The peak in the enhancements measured by Wunch et al. (2009) at the NASA Jet Propulsion Laboratory in the west of Pasadena consistently occured in the afternoon. Hedelius et al. (2018) show enhancements peaking in the early afternoon in the TCCON measurements at Caltech, Pasadena. They argue that these are "from morning rush hour emissions being transported from downtown Los Angeles (southwest) to Caltech, and from mixed-layer dynamics" (Hedelius et al. 2018). Following their argument, the EM27/SCA measurements are able to capture this transported emission signal. The BP target shows a distinctly different pattern with lower enhancements during the first two days, but a stronger enhancement during 15 April. The enhancement peak occurs significantly earlier than for the WP target. For 13 and 14 April, the enhancements match between both targets in the morning but differ in the late afternoon. This highlights the value of measurements from multiple targets, allowing for spatial information and enabling more consistent capturing of the emission signal.

In conclusion, the EM27/SCA is able to measure urban enhancements in XCO_2 and XCH_4. The very large enhancements indicate the need to verify the accuracy of the scattering-retrieval. Nevertheless, the presented data show enhancement patterns exceeding the measurement uncertainty. This shows that the measurements detect spatiotemporal enhancement patterns requried for estimating urban emissions.

6 Conclusion

This work presents the EM27/SCA, a portable ground-based FTS capable of recording ground-scattered sunlight spectra to retrieve atmospheric CO_2 and CH_4 column densities. It is the first portable FTS measuring in the reflected-sun geometry. It serves as a promising prototype for a versatile and transportable instrument for mapping CO_2 and CH_4 area sources. In reflected-sun measurements, the light traverses the lower atmosphere quasi-horizontally after being reflected at the observed ground target. Comparing target observations to at-instrument reflector observations yields partial vertical column densities in the atmospheric layer between the instrument and the target. Therefore, the measurements exhibit higher sensitivity to near-ground concentrations than total column measurements. At the same time, they inherently average horizontally, making them representative of the source area. Hence, reflected-sun measurements are suitable for determining emissions through atmospheric inversions. The continuous scanning through the source area enables the detection of spatial and temporal patterns.

In this work, the EM27/SCA and its components are documented and characterized based on laboratory measurements. Its performance is assessed based on measurements of the northern LA basin. A retrieval that explicitly accounts for aerosol scattering successfully mitigates the scattering-induced bias, which otherwise dominates the variability of CO_2 and CH_4 column densities retrieved from the LA measurements. The resulting time series of XCO2 and XCH4 show that the EM27/SCA can measure urban emission signatures.

The instrument performance is assessed based on a 1-month deployment alongside CLARS-FTS observing nine targets in the northern LA basin. The spectral SNR ranges from 200 to 400 for typical ground targets and up to 600 for reflector measurements in the O_2, CO_2 and CH_4 retrieval windows. These values are comparable to typical values for CLARS-FTS (Fu et al. 2014) and the TANSO-FTS instrument onboard GOSAT (Yoshida et al. 2011), although they operate at higher spectral sampling.

The measurement precision is empirically determined based on non-scattering retrievals of measurements during three densely sampled days. Evaluating the deviations of individual measurements from their 30 min average, the relative precision lies in the range of 0.4 % to 0.5 % for the O_2, CO_2 and CH_4 SCDs retrieved from measurements of the reflector and of typical targets. For CO, the low SNR below 2 µm (50 to 200) and the weak absorption features in the available retrieval window lead to a precision of 7 % to 14 %. The EM27/SCA typically records 1-minute measurements. Co-adding three measurements arrives at a similar temporal resolution to CLARS-FTS. Assuming the co-addition improves the precision by a factor of $\sqrt{3}$, the precision of the CLARS-FTS is roughly a factor two to three better than the portable EM27/SCA. The difference is most likely due to the higher spectral resolution of CLARS-FTS.

The SCD precision propagates to the relative precision in the partial VCD below instrument level (VCD_b). Depending on slant target distance and SZA, the VCD_b precisions lie in the range of 0.6 % to 1 % under moderate scattering conditions. Expected urban enhancements in the boundary layer of around 20 ppm in CO_2 and 150 ppb in CH_4 are well above the precisions found under typical conditions. Strong scattering impact reduces the effective light path below instrument level. For those cases and for short target distances, the precision of VCD_b deteriorates in the non-scattering retrieval.

The instrument lineshape (ILS) is characterized in laboratory open-path reflector measurements of H_2O absorption lines. The ILS deviates significantly from the theoretical ILS and a multi-parameter ILS model is needed to describe it accurately. While the uncertainty in the individual ILSs under parameter variation is low (1 ‰), back-to-back repeated ILS measurements deviate by below 1 % and the long term repeatability of the ILS is around 2 %. Despite this significant uncertainty, the day-averaged systematic residuals of the reflector and target measurements closely match the spectrally degraded CLARS-FTS systematic residuals in magnitude and shape, confirming good instrument performance. The only exception is the O_2 retrieval window, where the residuals match only after an empirical correction to the ILS.

The accuracy of the EM27/SCA measurements is assessed by comparing them to simultaneous CLARS-FTS reflected-sun observations on Mt. Wilson. The retrieved columns generally show good agreement with the independent measurements after correcting for a constant offset, which is expected for spectroscopic retrievals from different instruments. However, systematic deviations on the order of the measurement precision are visible in the VCDs of reflector measurements and even larger deviations in the VCD_b of target measurements. Scene heterogeneity likely contributes to the target measurement accuracy as laboratory measurements showed scene heterogeneity impacting the ILS and extreme-case field observations confirmed it. Deviations in reflector measurements show no correlation to other variables. This indicates that instrument instabilities are causing limited but slowly time-dependent systematic errors. Both effects need to be addressed in a next-generation instrument. Scene heterogeneity can be addressed, e.g., through a fiber-based homogenizer. Instrument stability can be addressed by improved detector optics, e.g., through a longer focal length OAP, increasing the alignment quality and robustness.

Due to the large horizontal paths and shallow viewing angle through the lower atmosphere, aerosol scattering causes the dominant error in the non-scattering retrieval, reducing the effective light path by up to 50 %. The scattering impact is quantified by the ratio between the retrieved and the geometrically calculated O_2 SCD. Changes in scattering angle and aerosol loading are the dominant cause for the VCD_b variability in the non-scattering retrieval. While the pattern of this effect is similar in all species, rationing CO_2 and CH_4 by O_2 does not cancel the scattering effects entirely. Due to a wavelength dependency of the radiative transfer, a significant bias remains in the XGHG values calculated from the non-scattering retrievals. A retrieval is implemented, which explicitly accounts for aerosol scattering below instrument level. By retrieving effective aerosol parameters simultaneously with CO_2 and CH_4, it is possible to mitigate most of the scattering-induced bias in the retrieval.

In previous studies, measurements of CLARS-FTS were used to investigate CH_4 emissions from the ratio between CH_4 and CO_2. Given the agreement between both instruments,

similar studies are possible with the EM27/SCA, although most likely with higher uncertainty. Accurately modeling the radiative transfer, including scattering, opens the opportunity to also address CO_2 emissions. At the same time, CH_4 emission estimates which do not rely on CO_2 emission inventories become possible. Additionally, urban emission estimates on shorter timescales may become feasible.

The time series of partial XCO_2 and XCH_4 below and above instrument level show that the EM27/SCA can measure urban enhancements. Further investigation is needed on the unrealistic high magnitude of the enhancements. Additionally, the remaining systematic instability and scene heterogeneity need to be addressed. Nevertheless, spatiotemporal urban enhancement patterns are detectable from the measurements. Future efforts will focus on analyzing urban enhancement patterns based on the scattering retrieval. Ultimately, combining the EM27/SCA measurements with a transport model in an atmospheric inversion can yield valuable insights into urban CO_2 and CH_4 emissions. The portable EM27/SCA provides the opportunity to extend such observations from the LA basin to other urban areas around the globe.

A Appendix

A.1 Single Scattering Approximation with Observer Inside the Atmosphere

We solve Equation (2.22) in the single scattering approximation for the radiance $I(\tau_2)$ at optical thicknesses τ_2, given the initial radiance $I(\tau_1)$ at τ_1.

$$\mu \frac{dI}{d\tau} = -I + \frac{\tilde{\omega}}{4\pi} \int_{4\pi} p(\hat{\Omega}', \hat{\Omega}) I(\hat{\Omega}') \, d\Omega' \tag{A.1}$$

$$\frac{dI}{d\tau} + \frac{1}{\mu} I = \frac{F_s \tilde{\omega}}{4\pi} p(\Theta) e^{-\frac{\tau}{\mu_s}} \tag{A.2}$$

$$\frac{dI}{d\tau} e^{\frac{\tau}{\mu}} + \frac{1}{\mu} I e^{\frac{\tau}{\mu}} = \frac{F_s \tilde{\omega}}{4\pi} p(\Theta) e^{-\frac{\tau}{\mu_s}} e^{\frac{\tau}{\mu}} \tag{A.3}$$

$$\frac{d}{d\tau} \left[I e^{\frac{\tau}{\mu}} \right] = \frac{F_s \tilde{\omega}}{4\pi} p(\Theta) e^{-\tau \left(\frac{1}{\mu_s} - \frac{1}{\mu} \right)} \tag{A.4}$$

$$\int_{\tau_1}^{\tau_2} \frac{d}{d\tau} \left[I e^{\frac{\tau}{\mu}} \right] d\tau = \frac{F_s \tilde{\omega}}{4\pi} p(\Theta) \int_{\tau_1}^{\tau_2} e^{\tau \left(\frac{1}{\mu} - \frac{1}{\mu_s} \right)} \, d\tau \tag{A.5}$$

$$I(\tau_2) e^{\frac{\tau_2}{\mu}} - I(\tau_1) e^{\frac{\tau_1}{\mu}} = \frac{F_s \tilde{\omega}}{4\pi} p(\Theta) \frac{1}{\left(\frac{1}{\mu} - \frac{1}{\mu_s} \right)} \left[e^{\tau_2 \left(\frac{1}{\mu} - \frac{1}{\mu_s} \right)} - e^{\tau_1 \left(\frac{1}{\mu} - \frac{1}{\mu_s} \right)} \right] \tag{A.6}$$

$$I(\tau_2) e^{\frac{\tau_2}{\mu}} = I(\tau_1) e^{\frac{\tau_1}{\mu}} + \frac{F_s \tilde{\omega}}{4\pi} p(\Theta) \frac{1}{\left(\frac{1}{\mu} - \frac{1}{\mu_s} \right)} \left[e^{\tau_2 \left(\frac{1}{\mu} - \frac{1}{\mu_s} \right)} - e^{\tau_1 \left(\frac{1}{\mu} - \frac{1}{\mu_s} \right)} \right] \tag{A.7}$$

$$I(\tau_2) = I(\tau_1) e^{\frac{\tau_1}{\mu}} e^{-\frac{\tau_2}{\mu}} + \frac{F_s \tilde{\omega}}{4\pi} p(\Theta) \frac{1}{\left(\frac{1}{\mu} - \frac{1}{\mu_s} \right)} \left[e^{\tau_2 \left(\frac{1}{\mu} - \frac{1}{\mu_s} \right)} - e^{\tau_1 \left(\frac{1}{\mu} - 1 \right)} \right] e^{-\frac{\tau_2}{\mu}} \tag{A.8}$$

$$I(\tau_2) = I(\tau_1) e^{\frac{\tau_1 - \tau_2}{\mu}} + \frac{F_s \tilde{\omega}}{4\pi} p(\Theta) \frac{1}{\left(\frac{1}{\mu} - 1 \right)} \left[e^{-\frac{\tau_2}{}} - e^{\left(\frac{\tau_1 - \tau_2}{\mu} - \tau_1 \right)} \right] \tag{A.9}$$

A.2 Single Scattering Ground Reflection Linearized

We make the linear approximation $e^x = 1 + x$ for $x \ll 1$ in Equation (2.29). This will be invalid in nearly all cases, but it is useful to illustrate the effect of scattering. We split Equation (2.29) in a direct and a scattering term and examine the scattering term with this approximation.

$$I_{\text{sca}}(\tau_{\text{obs}}) = \frac{F_{\text{s}}\tilde{\omega}}{4\pi\mu} p(\Theta) \frac{1}{\left(\frac{1}{\mu} - \frac{1}{}\right)} \left(e^{-\frac{\tau_{\text{obs}}}{}} - e^{-\frac{\tau_{\text{g}}}{} - \frac{\tau_{\text{obs}} - \tau_{\text{g}}}{\mu}} \right) \tag{A.10}$$

$$I_{\text{sca}}(\tau_{\text{obs}}) = \frac{F_{\text{s}}\tilde{\omega}}{4\pi} p(\Theta) \frac{}{-\mu} \left(1 - \frac{\tau_{\text{obs}}}{} - 1 + \frac{\tau_{\text{g}}}{} + \frac{\tau_{\text{obs}} - \tau_{\text{g}}}{\mu} \right) \tag{A.11}$$

$$I_{\text{sca}}(\tau_{\text{obs}}) = \frac{F_{\text{s}}\tilde{\omega}}{4\pi} p(\Theta) \frac{}{-\mu} \left(\frac{\tau_{\text{g}} - \tau_{\text{obs}}}{} - \frac{\tau_{\text{g}} - \tau_{\text{obs}}}{\mu} \right) \tag{A.12}$$

$$I_{\text{sca}}(\tau_{\text{obs}}) = \frac{F_{\text{s}}\tilde{\omega}}{4\pi} p(\Theta) \frac{}{-\mu} \left((\tau_{\text{g}} - \tau_{\text{obs}}) \frac{\mu -}{\mu} \right) \tag{A.13}$$

$$I_{\text{sca}}(\tau_{\text{obs}}) = \frac{F_{\text{s}}}{4\pi} \tilde{\omega}\, p(\Theta) \frac{\tau_{\text{obs}} - \tau_{\text{g}}}{\mu} \tag{A.14}$$

We combine this with the linearized direct term

$$I_{\text{dir}}(\tau_{\text{obs}}) = r \frac{F_{\text{s}}}{\pi} \left(1 - \frac{\tau_{\text{g}}}{} - \frac{\tau_{\text{obs}} - \tau_{\text{g}}}{\mu} \right) \tag{A.15}$$

to we find the total radiance given by

$$I(\tau_{\text{obs}}) = r \frac{F_{\text{s}}}{\pi} \left(1 - \frac{\tau_{\text{g}}}{} - \frac{\tau_{\text{obs}} - \tau_{\text{g}}}{\mu} \right) + \frac{F_{\text{s}}}{4\pi} \tilde{\omega}\, p(\Theta) \frac{\tau_{\text{obs}} - \tau_{\text{g}}}{\mu} \tag{A.16}$$

$$I(\tau_{\text{obs}}) = r \frac{F_{\text{s}}}{\pi} \left(1 - \frac{\tau_{\text{g}}}{} \right) - \left(r \frac{F_{\text{s}}}{\pi} - \frac{F_{\text{s}}}{4\pi} \tilde{\omega}\, p(\Theta) \right) \frac{\tau_{\text{obs}} - \tau_{\text{g}}}{\mu} \tag{A.17}$$

$$I(\tau_{\text{obs}}) = r \frac{F_{\text{s}}}{\pi} \left(1 - \frac{\tau_{\text{g}}}{} - \left(1 - \frac{\tilde{\omega}\, p(\Theta)}{4r} \right) \frac{\tau_{\text{obs}} - \tau_{\text{g}}}{\mu} \right) \tag{A.18}$$

A.3 EM27/SCA Sensitivity Enhancement

The lower radiance of ground-scattered sunlight are compensated by two approaches. First, the instruments etendue is increased by increasing the FOV from 4.72 mrad to 9.09 mrad and the beam diameter from 0.6 cm to 2.6 cm. This increases the number of photons reaching the detector by a factor 70. Secondly, the custom detector element exhibits a higher gain. I determine the increase in gain by comparing the center burst amplitude of simultaneous EM27/SCA and EM27/SUN measurements.

I estimate the power reaching the detector from the radiance I to be

$$P = \Omega A \int_{\lambda_{\min}}^{\lambda_{\max}} I \, d\lambda \,, \tag{A.19}$$

accounting for the FOV solid angle Ω and the thoughput area A of the respective instrument, as well as the respective spectral bandwidth (0.9 µm to 2.5 µm for EM27/SCA and 0.85 µm to 1.8 µm for EM27/SUN). For this estimation, I assume the solar spectral radiance to be given by Planck's law at a solar temperature of 5700 K. I calculate the ground-scattered radiance from this using Equation (3.18). I infer the instrument signal from the interferogram peak height of simultaneous reflector and direct-sun measurements (at SZA $= 57.8°$). I calculate the gain as the ratio of signal to input power P. Thus, the EM27/SCA has a 1100 times higher gain, bringing the overall sensitivity enhancement to a factor $\approx 10^5$.

Note that the increased gain of the custom detector electronics also increase the noise. The SNR of the modified setup is therefore significantly lower (cf. Section 5.2) than for direct-sun measurements by a standard EM27/SUN.

A.4 EM27/SCA Standard OPUS Settings

Table A.1: Default EM27/SCA operation parameters, as set in the OPUS experiment file *EM27SUN_sca.xpm*. The parameters for the Fourier transformation only apply to the OPUS spectra preview, since I perform the conversion to spectra with a separate software.

	Parameter	Value
Advanced	Resolution	0.5 cm^{-1}
	Sample scan time	10 scans
	Save data	100 cm^{-1} to 15 797 cm^{-1}
Optic	Detector Setting	RT-InGaAs DC [Internal]
	Scanner Velocity	10 kHz
	Sample signal gain	x1
	Sample preamp. gain	irrelevant, not available on custom preamplifier
Acquisition	Wanted high frequency limit	15 797 cm^{-1}
	Laser wavenumber	15 798.02 cm^{-1}
	High pass filter	Open
	Low pass filter	10 kHz
	Acquisition mode	Double sided, Forward-Backward
FT	Phase resolution	4
	Phase correction mode	Mertz
	Apodization function	Norton-Beer, Medium
	Zerofilling factor	8

A.5 Upward Viewing Geometry

Besides the downward viewing geometry used within the main text, reflected-sun measurements are also possible in an upward viewing geometry displayed in Figure A.1. There, the viewing direction is raised towards elevated targets, e.g. against a mountainside. In this case, the VCD_a and VCD_b refer to the partial VCDs above and below the target level, instead of above and below the observer level. Here, the partial VCD_b is again given by the difference between target and reflector measurement. However, the relevant AMF is the difference between horizontal and vertical AMF. Because the target is located at higher altitude than the instrument, the light traverses also the layer of interest in reflector measurements. Therefore, the partial VCD_a is not directly given by the reflector measurement. To calculate the VCD_a, the VCD_b is subtracted from the total VCD, which in turn is determined in the reflector observation.

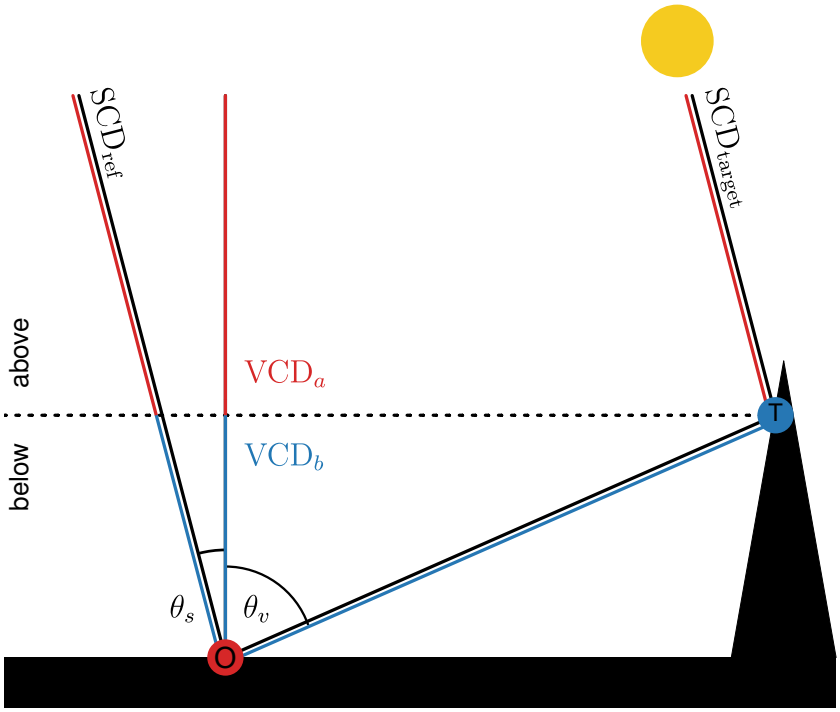

Figure A.1: Observational geometry in the upward viewing case with the observer (O) on the ground pointing up towards an elevated target (T).

$$\mathrm{VCD}_a = \cos(\theta_s)\mathrm{SCD}_{\mathrm{ref}} - \mathrm{VCD}_b \tag{A.20}$$

$$\mathrm{VCD}_b = \frac{\mathrm{SCD}_{\mathrm{target}} - \mathrm{SCD}_{\mathrm{ref}}}{\frac{1}{\cos(\theta_v)} - \frac{1}{\cos(\theta_s)}} \tag{A.21}$$

A.6 Retrieval Differences Due to the Solar Spectrum

The version of RemoTeC, which was adapted for ground-based measurements, uses the solar line list by Toon (2015) directly to calculate the solar spectrum within the retrieval. This is necessarry to calculate an accurate solar spectrum for direct-sun observations where the FOV only partially covers the solid angle of the sun. I compare two retrievals only differing in the solar spectrum input, where one uses the solar line list and the other uses the TSIS-1 HSRS. The CH_4 VCDs is on the order of 0.5 % to 1 % lower for reflector measurements when using the TSIS-1 HSRS. A small change in CO_2 VCDs is also detectable. However, the difference there is less than 1 permil. The systematic residuals (cf. Section 5.3) of one day of measurements show that they are overall lower in the CH_4 and CO_2 retrieval windows at around 1.6 µm (W2–W5) for the TSIS-1 HSRS. Individual large spikes are reduced. Most notably, the largest spike in W5 at 6108 cm^{-1} disappears. This is surprising since TSIS-1 HSRS is also based on the same solar line list. For consistency, the TSIS-1 HSRS is used for all retrievals, as it is radiometrically calibrated and shows lower systematic residuals.

A.7 Targets in the Northern Los Angeles Basin

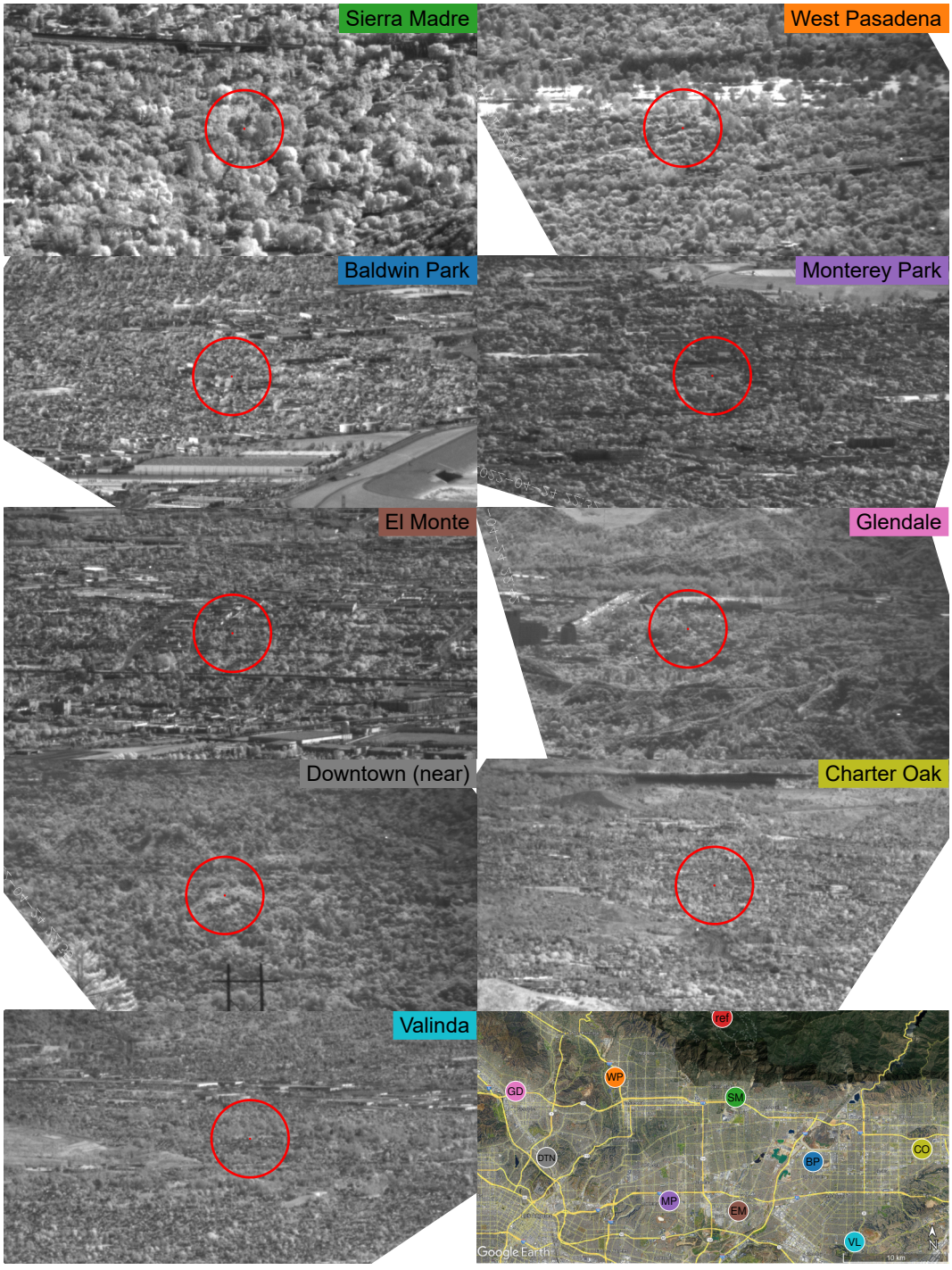

Figure A.2: Pictures of the observed targets captured with the imaging camera during measurements. All targets in the northern LA basin observed during the deployment on Mt. Wilson (ref) during 7 April to 5 May 2022 are shown. The EM27/SCA nominal FOV is marked in each target picture with a circle.

A.8 Comparison to Direct-Sun EM27/SUN

During field measurements the Lambertian reflector plate directly adjacent to the instrument is observed in order to constrain the overhead VCD in target measurements. Since the reflector measurements do not have a horizontal path component, they closely resemble direct-sun measurements. Therefore, I compare reflector measurements of the EM27/SCA to direct-sun measurements collected with a standard EM27/SUN. We set up the EM27/SCA together with an EM27/SUN on the roof of the IUP and measure simultaneously with both instruments. During the measurements presented in this section, we additionally pointed to four targets along the Odenwald hillside. Here, only the reflector measurements are compared to direct-sun observations. Due to the additional targets, the sampling is more sparse for the EM27/SCA observations.

Enders (2021) analyzes multiple days of these measurements in depth for the agreement between the EM27/SCA reflector measurements and direct-sun measurements with a standard EM27/SUN (SN132). He finds that the EM27/SCA overestimates the CO_2 (4 %) and CH_4 VCDs (3 %) but not the O_2 VCDs. Day-to-day variations of the bias are slightly higher than the single day standard deviation of the differences. The bias for XCO_2 and XCH_4[1] is more consistent between measurements, indicating common influences on the VCD biases of the different species. Especially sky-scattered sunlight contributions to the reflector illumination can potentially increase the effective light path. This leads to an increase of the VCD of reflector measurements relative to the direct-sun measurements. Apart from the wavelength dependency of the atmospheric scattering properties, to first order, this contribution would be common between all species. During the measurement days, no impact of a light path enhancing effect of aerosol scattering could be observed within the measurement uncertainty and with the limited information on aerosols available. A light path enhancing effect is however visible in reflector measurements during an isolated cloud event, where a thin cloud passes. This increases the VCDs of all species in the reflector measurements but not in the direct-sun measurements. Enders (2021) found that such events effectively cancel in the XGHG, where no effect of the cloud could be observed. Thus, the impact of clouds on reflector measurements can be detected by analyzing the O_2 VCD and mitigated by ratioing by O_2. He additionally observes sub-diurnal trends not present in direct-sun measurements, which do not match between species and have no explanation.

The retrieval setup used by Enders (2021) is similar to the one employed here, with some differences in spectroscopic absorption cross section data, the solar spectrum and some modification to the CH_4 retrieval window. I repeat the retrieval for one day with the settings specified in Chapter 4. Figure A.3 shows the comparison of the VCDs from both instruments on 2021-06-01. I interpolate the denser sampled and higher precision EM27/SUN measurements to the EM27/SCA measurement times to calculate the mean μ and standard deviation σ of the relative difference between both. The relative difference is defined as

$$\frac{\Delta\mathrm{VCD}}{\mathrm{VCD}} = \frac{\mathrm{VCD}_{\mathrm{sca}}}{\mathrm{VCD}_{\mathrm{dir}}} - 1\,, \tag{A.22}$$

where $\mathrm{VCD}_{\mathrm{sca}}$ and $\mathrm{VCD}_{\mathrm{dir}}$ are the VCDs retrieved from the EM27/SCA and EM27/SUN measurements respectively. Due to the much higher precision of the EM27/SUN, its scatter

[1] XGHG introduced in Equation (5.11)

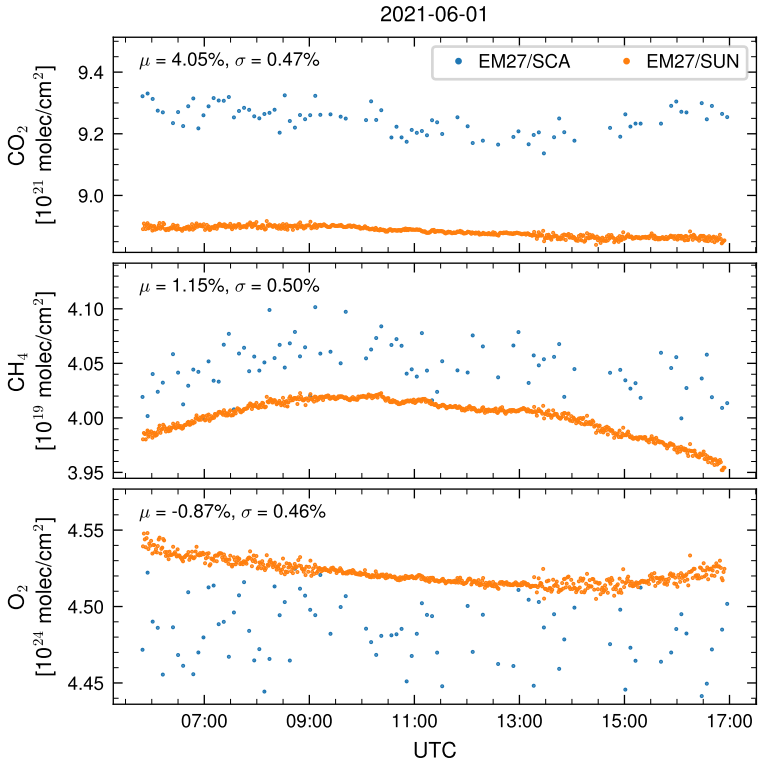

Figure A.3: VCDs of CO_2, CH_4 and O_2 (top to bottom) retrieved from EM27/SCA reflector measurements (blue) and EM27/SUN direct-sun measurements (orange). For each species the mean μ and standard deviation σ of the relative difference between both instruments is specified. The relative difference is calculated with Equation (A.22).

has a negligible effect on the relative difference. For O_2 and CH_4 the standard deviation matches the expectation from the EM27/SCA precision. For CO_2, a small diurnal pattern, which is not present in direct-sun measurements, increases the standard deviation of the relative differences to 0.46 % above the expected precision of 0.37 %. More prominently, the reflector measurements have a systematic offset to the direct-sun measurements. The offset is most pronounced for CO_2, where the EM27/SCA measurements exceed the direct-sun VCDs by 4 %. Offsets are also present for CH_4 (1.2 %) and O_2 (-0.8 %). Differences to the offsets reported by Enders (2021) are expected, since spectroscopic data from HITRAN 2020,instead of the HITRAN 2016, is used here. However, the change in offset for CH_4 is particularly large. Besides the different absorption cross section data, this is caused by the differences in the employed solar spectrum and the exclusion of the Q-branch from the CH_4 retrieval window. When switching to the TSIS-1 HSRS solar spectrum, systematic residuals improved while the retrieved CH_4 VCDs reduced by up to 1 % (cf. Section 4.4.2).

Generally biases, although usually with smaller magnitude, are common when comparing measurements of different FTS. Even the EM27/SUNs within the COCCON need a small XGHG calibration, even after consistently calibrating the ILS of all instruments and applying the same retrieval. Here however, the comparison is not only between different FTS,

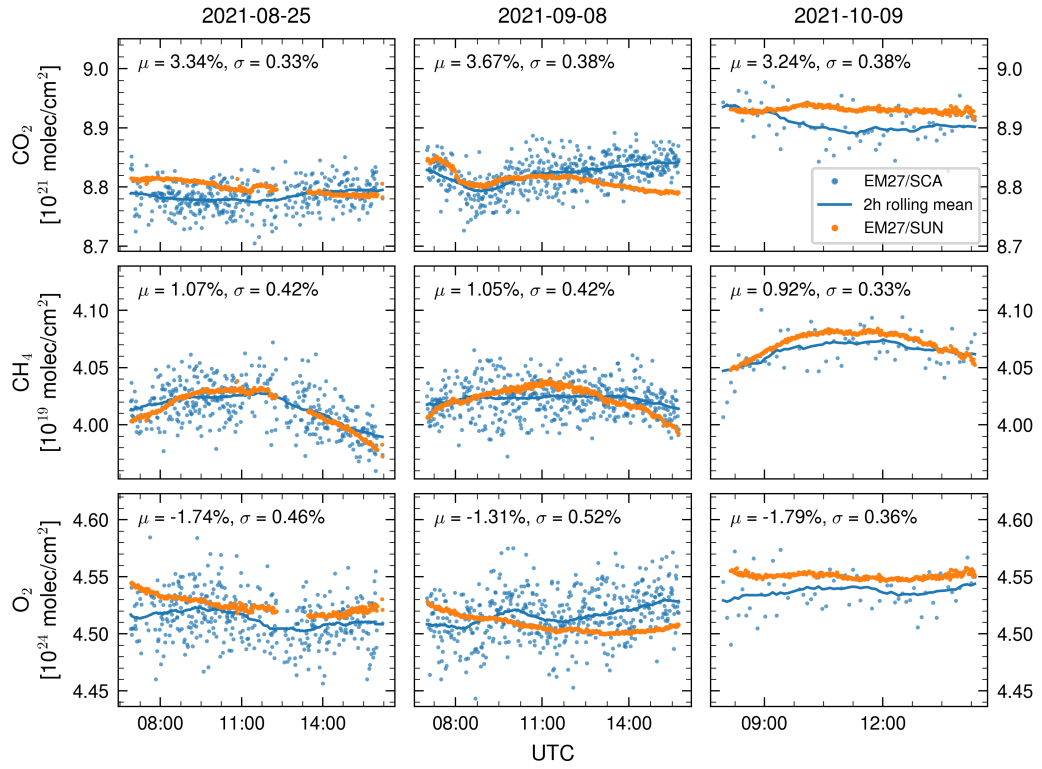

Figure A.4: VCD of CO_2, CH_4 and O_2 (top to bottom) retrieved from EM27/SCA reflector measurements (blue) and EM27/SUN direct-sun measurements (orange). The 2 h rolling average of the EM27/SCA measurements is shown with a solid blue line. During the first two measurement days (2021-08-25 and 2021-09-08) the EM27/SCA reflector was placed under a sun-tracker, excluding sky-scattered sunlight. During the third measurement day (2021-10-09) the EM27/SCA was side-by-side with a standard EM27/SUN. I divided the VCDs from EM27/SCA measurements by the average difference to the EM27/SUN measurements over the two days, where it was placed under the sun-tracker. The mean μ and standard deviation σ of the relative difference specified in each panel is calculated before this bias correction.

but also between different types of observations. While the EM27/SUN points directly at the sun, the Lambertian reflector plate also reflects sky-scattered sunlight. Using the single scattering approximation with a Harvey Greenstein scattering function, assuming an asymmetry parameter of 0.8 and an aerosol optical depth of 0.05, Müller (2019) estimated that despite the much higher radiance of sunlight, sky-scattered light contributes around 5 % to the radiance hitting the reflector. In principle, this could cause an enhancement of the effective light path. However, it should be noted that the majority of the additional signal comes from solid angles close to the sun, since forward scattering is strongly favored in Mie scattering.

I investigate whether sky-scattered sunlight has a relevant influence on the reflector measurements by comparing usual side-by-side measurements (20221-10-09) with measurements where we excluded the influence of sky-scattered sunlight on two days (2021-08-25

and 2021-09-08). For the first measurement, we placed the EM27/SCA together with a standard EM27/SUN (SN119) on the IUP roof. For the second experiment, we placed the EM27/SCA inside the IUP roof laboratory under a permanently installed sun-tracker with a large optical throughput. In the following, I refer to the second experiment as *tracker experiment*. We positioned the instrument such, that the sun-tracker illuminates the reflector plate and closed the shades of the laboratory. This excludes nearly all of the sky-scattered sunlight. From the distance between tracker and reflector of 4 m and the diameter of the tracker mirror of 15 cm, I calculate that the incident light comes from a solid angle with a radius of 1°. Only radiation from this solid angle contributes to the reflector measurement. We simultaneously measured with a standard EM27/SUN (SN132) on the roof platform just above the laboratory.

Figure A.4 shows the comparison of VCDs for both experiments after the bias correction described below. Focussing on the mean difference first, the daily mean μ of the relative difference between the both instruments is specified in each panel. Note that the retrieval here uses a different ILS (measured on 2021-08-13) than the retrieval previously presented (measured on 2021-04-23). This is necessary, because the ILS changed after the replacement of the metrology laser at the end of July 2021 (cf. Figure 3.16). Therefore, the offsets are not directly comparable. Except for the ILS, all retrieval settings are identical. Overall, the mean differences in both experiments are similar. In particular, the difference in bias between both *tracker experiment* days is larger than the difference in bias between the first *tracker experiment* day and the standard measurement day. I conclude that the differences between the EM27/SCA and EM27/SUN measurements are not driven by sky-scattered light, but rather by systematic differences between the instruments, e.g. the effect of the non-perfect ILS and its uncertainty. Since the bias is largely consistent over many measurements, to first order, this can be corrected by an empiric bias correction.

Turning to the diurnal pattern in the differences between both instruments, the reflector measurements shown in Figure A.4 are divided by the average ratio of the instruments over both *tracker experiment* days. The figure shows that after the removal of the bias, a residual diurnal pattern remains. The systematic deviation between both reflector and direct-sun measurement is variable on the order of the EM27/SCA's precision. This pattern is not consistent over multiple days, but varies generally rather slowly on a time scale of a few hours. Therefore, it does not interfere with the precision estimation, which is based on a rolling average over a shorter time. The data do not show any matching pattern of the deviation to pressure, temperature, SNR or retrieved water content. Since the EM27/SUN is a long term stable instrument (Alberti et al. 2022; Frey et al. 2015; Frey et al. 2019), I conclude that this is most likely caused by effects of the non-ideal ILS and its uncertainty or possibly small instabilities in the ILS.

A rolling average allows to quantify the systematic errors by reducing the measurement scatter. I calculate the difference of a two hour rolling average of the EM27/SCA VCDs to linearly interpolated EM27/SUN VCDs. After the bias correction, the maximum difference is approximately 0.6 %. I conclude that systematic errors of 0.6 % add to the overall uncertainty of the EM27/SCA VCD measurements.

A typical approach to limit systematic errors in total column GHG measurements is to ratio them by the O_2 VCD retrieved from the same spectrum (Frey et al. 2019; Fu et al. 2014; Washenfelder et al. 2006; Wunch et al. 2011). Since the DMF of O_2 has very low variability,

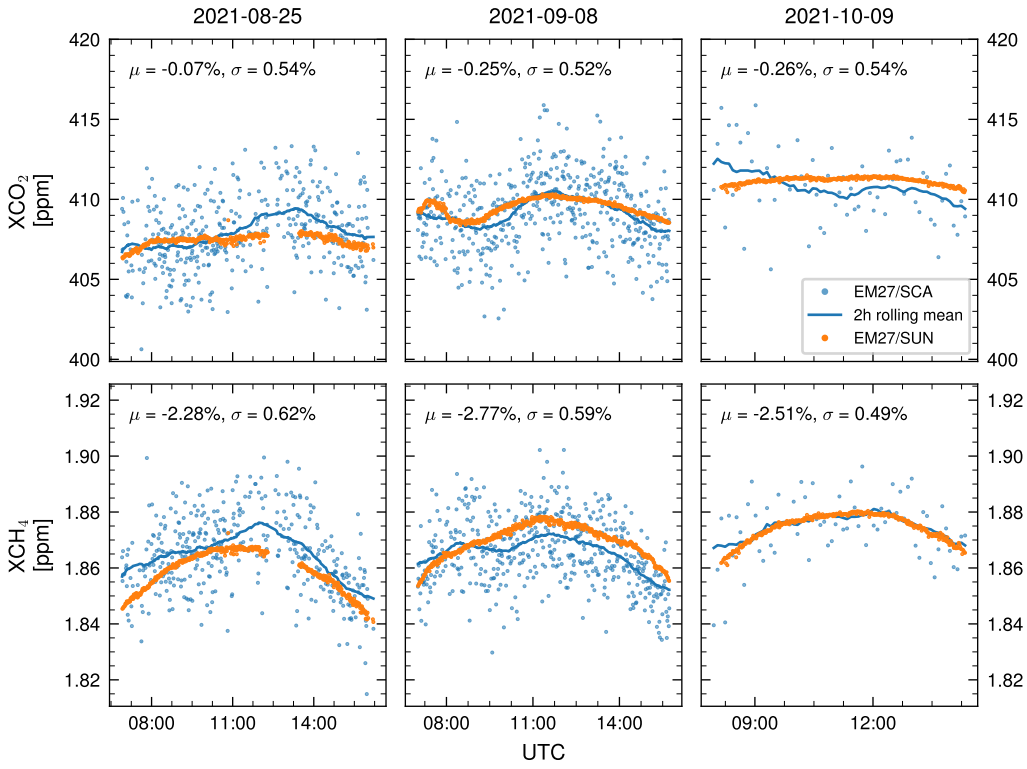

Figure A.5: Same as Figure A.4 but for XCO_2 and XCH_4 calculated from EM27/SCA reflector measurements (blue) and EM27/SUN direct-sun measurements (orange). The blue line indicates the two hour rolling average of the EM27/SCA measurements. Here, the EM27/SCA retrieval uses an empirically corrected ILS in the O_2 window (cf. Section 5.3.2).

the column-averaged DMF for the GHG (XGHG) can be inferred from the ratio of their column densities (cf. Equation (5.11)). The O_2 DMF is typically assumed to be 0.2095. The systematic errors common to both absorbers, cancel when ratioing by O_2. A major contribution to the bias in the XGHG is introduced by the ILS error in the O_2 retrieval window. Figure A.5 shows the same comparison as Figure A.4 for XCO_2 and XCH_4, using the empirically corrected ILS (cf. Section 5.3.2) in W1 for retrieving O_2. Compared to the VCD, the bias is reduced for XCO_2 but increased for XCH_4. For CO_2, ratioing by O_2 cancels the bias largely, whereas for CH_4 a bias of about $-2.5\,\%$ remains. Generally, the XCH_4 bias is expected to be larger than the XCO_2 bias. Despite CH_4 being less prone to ILS errors, the ILS errors cancel better in XCO_2 (Alberti et al. 2022; Tu 2019). As for the VCDs, a residual systematic pattern remains for the XGHGs after correcting for the bias. The maximum difference of the two hour rolling average to the interpolated EM27/SUN measurements is $0.4\,\%$ for XCO_2 and $0.7\,\%$ for XCH_4.

In this section, I presented a comparison between the EM27/SCA reflector measurements and standard EM27/SUN direct-sun observations. A general offset between both measurements which depends on the specific retrieval settings makes a bias correction necessary.

Here, no influence of sky-scattered sunlight on the reflector measurements was detectable through comparing standard reflector measurement to measurement which exclude sky-scattered sunlight by using a sun-tracker for EM27/SCA reflector measurements. However, in Section 5.6.1 such an influence can be detected during a day with high aerosol loading. Enders (2021) detected the influence of passing thin clouds in the retrieved VCD and could show that the effect cancels in the XGHG. I filter such cases by comparing the retrieved to the geometric O_2 SCD. Finally, I investigated the variability in the difference between reflector and direct-sun measurements and conclude that they could not be related to environmental influences. They constitute a systematic error of 0.6 % in the VCD measurements, translating to an error of up to 0.4 % in XCO_2 and 0.7 % in XCH_4.

Acronyms

ADC	Analog-to-digital converter
AERONET	Aerosol Robotic Network
ALH	Aerosol layer height
AMF	Air mass factor
AOD	Aerosol optical depth
BDRF	Bidirectional reflectance distribution function
BP	Baldwin Park target
Caltech	California Institute of Technology
CB	Center-burst
CH_4	Methane
CLARS	California Laboratory for Atmospheric Remote Sensing
CLARS-FTS	California Laboratory for Atmospheric Remote Sensing – Fourier-transform spectrometer (Fu et al. 2014)
CO	Charter Oak target
CO	Carbon monoxide
CO_2	Carbon dioxide
COCCON	COllaborative Carbon Column Observing Network
DC	Direct current
DFS	Degrees of freedom for signal
DFSS	Degrees of freedom for scattering signal
DMF	Dry-air mole fraction
DTN	Downtown (near) target
EM	El Monte target
EM	Electromagnetic
EM27/SCA	Portable FTS, subject of this work
EM27/SUN	Portable FTS for direct-sun total column measurements (Gisi et al. 2012)
FOV	Field of view
FTS	Fourier-transform spectrometer
GD	Glendale target
GHG	Greenhouse gas
GPS	Global Positioning System
H_2O	Water
HeNe	Helium neon laser
ILS	Instrument lineshape
InGaAs	Indium gallium arsenide detector
IPCC	Intergovernmental Panel on Climate Change

IUP	Institute of Environmental Physics, Heidelberg University
LA	Los Angeles
ME	Modulation efficiency
MP	Monterey Park target
NBM	Norton-Beer medium apodization
NG	Natural gas
NIR	Near infrared spectral range
O_2	Oxygen
OAP	Off-axis parabolic mirror
OPD	Optical path difference
PBL	Planetary boundary layer
PE	Phase error
RMS	Root mean square
RTE	Radiative transfer equation
RTM	Radiative transfer model
SAA	Solar azimuth angle
SCD	Slant column density
Si	Silicon detector
SM	Sierra Madre target
SNR	Signal-to-noise ratio
SZA	Solar zenith angle
TCCON	Total Carbon Column Observing Network
UNFCCC	United Nations Framework Convention on Climate Change
VAA	Viewing azimuth angle
VCD	Vertical column density
VIS	Visible spectral range
VL	Valinda target
VZA	Viewing zenith angle
WP	West Pasadena target
XGHG	Column-averaged dry-air mole fraction of a greenhouse gas (cf. Equation (5.11))

List of Figures

List of Tables

Bibliography

Aerosol Robotic Network (2024). *Aerosol Robotic Network (AERONET) Homepage*. URL: https://aeronet.gsfc.nasa.gov/ (visited on 2024-03-01).

Alberti, C., F. Hase, M. Frey, D. Dubravica, T. Blumenstock, A. Dehn, P. Castracane, G. Surawicz, R. Harig, B. C. Baier, C. Bès, J. Bi, H. Boesch, A. Butz, Z. Cai, J. Chen, S. M. Crowell, N. M. Deutscher, D. Ene, J. E. Franklin, O. García, D. Griffith, B. Grouiez, M. Grutter, A. Hamdouni, S. Houweling, N. Humpage, N. Jacobs, S. Jeong, L. Joly, N. B. Jones, D. Jouglet, R. Kivi, R. Kleinschek, M. Lopez, D. J. Medeiros, I. Morino, N. Mostafavipak, A. Müller, H. Ohyama, P. I. Palmer, M. Pathakoti, D. F. Pollard, U. Raffalski, M. Ramonet, R. Ramsay, M. K. Sha, K. Shiomi, W. Simpson, W. Stremme, Y. Sun, H. Tanimoto, Y. Té, G. M. Tsidu, V. A. Velazco, F. Vogel, M. Watanabe, C. Wei, D. Wunch, M. Yamasoe, L. Zhang, and J. Orphal (2022). "Improved Calibration Procedures for the EM27/SUN Spectrometers of the COllaborative Carbon Column Observing Network (COCCON)". *Atmos. Meas. Tech.* 15:8, pp. 2433–2463. DOI: 10.5194/amt-15-2433-2022.

Aster, R. C., B. Borchers, and C. H. Thurber (2013). *Parameter Estimation and Inverse Problems*. 2nd ed. Elsevier AP, Amsterdam ; Heidelberg [u.a.], X, 360 S.

Baldridge, A. M., S. J. Hook, C. I. Grove, and G. Rivera (2009). "The ASTER Spectral Library Version 2.0". *Remote Sens. Environ.* 113:4, pp. 711–715. DOI: 10.1016/j.rse.2008.11.007.

Bransden, B. H. and C. J. Joachain (2003). *Physics of Atoms and Molecules*. 2. ed. Prentice Hall, Harlow ; Munich [u.a.] XIV, 1114 S.

Brioude, J., W. M. Angevine, R. Ahmadov, S.-W. Kim, S. Evan, S. A. McKeen, E.-Y. Hsie, G. J. Frost, J. A. Neuman, I. B. Pollack, J. Peischl, T. B. Ryerson, J. Holloway, S. S. Brown, J. B. Nowak, J. M. Roberts, S. C. Wofsy, G. W. Santoni, T. Oda, and M. Trainer (2013). "Top-down Estimate of Surface Flux in the Los Angeles Basin Using a Mesoscale Inverse Modeling Technique: Assessing Anthropogenic Emissions of CO, NO_x and CO_2 and Their Impacts". *Atmos. Chem. Phys.* 13:7, pp. 3661–3677. DOI: 10.5194/acp-13-3661-2013.

Butz, A., A. Galli, O. Hasekamp, J. Landgraf, P. Tol, and I. Aben (2012). "TROPOMI Aboard Sentinel-5 Precursor: Prospective Performance of CH4 Retrievals for Aerosol and Cirrus Loaded Atmospheres". *Remote Sens. Environ.* 120, pp. 267–276. DOI: 10.1016/J.RSE.2011.05.030.

Butz, A., S. Guerlet, O. Hasekamp, D. Schepers, A. Galli, I. Aben, C. Frankenberg, J.-M. Hartmann, H. Tran, A. Kuze, G. Keppel-Aleks, G. Toon, D. Wunch, P. Wennberg, N. Deutscher, D. Griffith, R. Macatangay, J. Messerschmidt, J. Notholt, and T. Warneke (2011). "Toward Accurate CO_2 and CH_4 Observations from GOSAT". *Geophys. Res. Lett.* 38:14. DOI: 10.1029/2011GL047888.

Butz, A., O. P. Hasekamp, C. Frankenberg, J. Vidot, and I. Aben (2010). "CH 4 Retrievals from Space-Based Solar Backscatter Measurements: Performance Evaluation against Simulated Aerosol and Cirrus Loaded Scenes". *J. Geophys. Res. Atmos.* 115:D24. DOI: 10.1029/2010JD014514.

Butz, A., A. S. Dinger, N. Bobrowski, J. Kostinek, L. Fieber, C. Fischerkeller, G. B. Giuffrida, F. Hase, F. Klappenbach, J. Kuhn, P. Lübcke, L. Tirpitz, and Q. Tu (2017). "Remote Sensing of Volcanic CO2, HF, HCl, SO2 and BrO in the Downwind Plume of Mt. Etna". *Atmos. Meas. Tech.* 10, pp. 1–14. DOI: 10.5194/amt-10-1-2017.

Butz, A., O. P. Hasekamp, C. Frankenberg, and I. Aben (2009). "Retrievals of Atmospheric CO_2 from Simulated Space-Borne Measurements of Backscattered near-Infrared Sunlight: Accounting for Aerosol Effects". *Appl. Optics* 48:18, p. 3322. DOI: 10.1364/AO.48.003322.

C40 (2024). *C40 Cities - A Global Network of Mayors Taking Urgent Climate Action*. URL: https://www.c40.org/ (visited on 2024-03-18).

Carranza, V., T. Rafiq, I. Frausto-Vicencio, F. M. Hopkins, K. R. Verhulst, P. Rao, R. M. Duren, and C. E. Miller (2018). "Vista-LA: Mapping Methane-Emitting Infrastructure in the Los Angeles Megacity". *Earth. Syst. Sci. Dat* 10:1, pp. 653–676. DOI: 10.5194/essd-10-653-2018.

Christen, A. (2014). "Atmospheric Measurement Techniques to Quantify Greenhouse Gas Emissions from Cities". *Urban Climate*. ICUC8: The 8th International Conference on Urban Climate and the 10th Symposium on the Urban Environment 10, pp. 241–260. DOI: 10.1016/j.uclim.2014.04.006.

Coddington, O. M., E. C. Richard, D. Harber, P. Pilewskie, T. N. Woods, K. Chance, X. Liu, and K. Sun (2021). "The TSIS-1 Hybrid Solar Reference Spectrum". *Geophys. Res. Lett.* 48:12, e2020GL091709. DOI: 10.1029/2020GL091709.

Cui, Y. Y., J. Brioude, S. A. McKeen, W. M. Angevine, S.-W. Kim, G. J. Frost, R. Ahmadov, J. Peischl, N. Bousserez, Z. Liu, T. B. Ryerson, S. C. Wofsy, G. W. Santoni, E. A. Kort, M. L. Fischer, and M. Trainer (2015). "Top-down Estimate of Methane Emissions in California Using a Mesoscale Inverse Modeling Technique: The South Coast Air Basin". *J. Geophys. Res. Atmos.* 120:13, pp. 6698–6711. DOI: 10.1002/2014JD023002.

Davis, K. J., A. Deng, T. Lauvaux, N. L. Miles, S. J. Richardson, D. P. Sarmiento, K. R. Gurney, R. M. Hardesty, T. A. Bonin, W. A. Brewer, B. K. Lamb, P. B. Shepson, R. M. Harvey, M. O. Cambaliza, C. Sweeney, J. C. Turnbull, J. Whetstone, and A. Karion (2017). "The Indianapolis Flux Experiment (INFLUX): A Test-Bed for Developing Urban Greenhouse Gas Emission Measurements". *Elem. Sci. Anth.* 5:0, p. 21. DOI: 10.1525/elementa.188.

Dietrich, F., J. Chen, B. Voggenreiter, P. Aigner, N. Nachtigall, and B. Reger (2021). "MUCCnet: Munich Urban Carbon Column Network". *Atmos. Meas. Tech.* 14:2, pp. 1111–1126. DOI: 10.5194/amt-14-1111-2021.

Eldering, A., C. W. O'Dell, P. O. Wennberg, D. Crisp, M. R. Gunson, C. Viatte, C. Avis, A. Braverman, R. Castano, A. Chang, L. Chapsky, C. Cheng, B. Connor, L. Dang, G. Doran, B. Fisher, C. Frankenberg, D. Fu, R. Granat, J. Hobbs, R. A. M. Lee, L. Mandrake, J. McDuffie, C. E. Miller, V. Myers, V. Natraj, D. O'Brien, G. B. Osterman, F. Oyafuso, V. H. Payne, H. R. Pollock, I. Polonsky, C. M. Roehl, R. Rosenberg, F. Schwandner, M. Smyth, V. Tang, T. E. Taylor, C. To, D. Wunch, and J. Yoshimizu (2017). "The Orbiting

Carbon Observatory-2: First 18 Months of Science Data Products". *Atmos. Meas. Tech.* 10:2, pp. 549–563. DOI: 10.5194/amt-10-549-2017.

Enders, V. (2021). "Characterizing a New Spectrometer Measuring Sunlight Scattered at a Reflector Plate". BA thesis. University of Heidelberg.

Flörke, M., C. Schneider, and R. I. McDonald (2018). "Water Competition between Cities and Agriculture Driven by Climate Change and Urban Growth". *Nat. Sustain.* 1:1, pp. 51–58. DOI: 10.1038/s41893-017-0006-8.

Forster, P., T. Storelvmo, K. Armour, W. Collins, J.-L. Dufresne, D. Frame, D. J. Lunt, T. Mauritsen, M. Palmer, M. Watanabe, M. Wild, and H. Zhang (2021). "The Earth's Energy Budget, Climate Feedbacks, and Climate Sensitivity". In: *Climate Change 2021: The Physical Science Basis. Contribution of Working Group I to the Sixth Assessment Report of the Intergovernmental Panel on Climate Change [Masson-Delmotte, V., P. Zhai, A. Pirani, S.L. Connors, C. Péan, S. Berger, N. Caud, Y. Chen, L. Goldfarb, M.I. Gomis, M. Huang, K. Leitzell, E. Lonnoy, J.B.R. Matthews, T.K. Maycock, T. Waterfield, O. Yelekçi, R. Yu, and B. Zhou (Eds.)]* Cambridge University Press, Cambridge, United Kingdom and New York, NY, USA, pp. 923–1054. DOI: 10.1017/9781009157896.009.

Forstmaier, A., J. Chen, F. Dietrich, J. Bettinelli, H. Maazallahi, C. Schneider, D. Winkler, X. Zhao, T. Jones, C. van der Veen, N. Wildmann, M. Makowski, A. Uzun, F. Klappenbach, H. Denier van der Gon, S. Schwietzke, and T. Röckmann (2023). "Quantification of Methane Emissions in Hamburg Using a Network of FTIR Spectrometers and an Inverse Modeling Approach". *Atmos. Chem. Phys.* 23:12, pp. 6897–6922. DOI: 10.5194/acp-23-6897-2023.

Foy, B. de, J. J. Schauer, A. Lorente, and T. Borsdorff (2023). "Investigating High Methane Emissions from Urban Areas Detected by TROPOMI and Their Association with Untreated Wastewater". *Environ. Res. Lett.* 18:4, p. 044004. DOI: 10.1088/1748-9326/acc118.

Frey, M., F. Hase, T. Blumenstock, J. Groß, M. Kiel, G. Mengistu Tsidu, K. Schäfer, M. K. Sha, and J. Orphal (2015). "Calibration and Instrumental Line Shape Characterization of a Set of Portable FTIR Spectrometers for Detecting Greenhouse Gas Emissions". *Atmos. Meas. Tech.* 8:7, pp. 3047–3057. DOI: 10.5194/amt-8-3047-2015.

Frey, M., M. K. Sha, F. Hase, M. Kiel, T. Blumenstock, R. Harig, G. Surawicz, N. M. Deutscher, K. Shiomi, J. E. Franklin, H. Bösch, J. Chen, M. Grutter, H. Ohyama, Y. Sun, A. Butz, G. Mengistu Tsidu, D. Ene, D. Wunch, Z. Cao, O. Garcia, M. Ramonet, F. Vogel, and J. Orphal (2019). "Building the COllaborative Carbon Column Observing Network (COCCON): Long-Term Stability and Ensemble Performance of the EM27/SUN Fourier Transform Spectrometer". *Atmos. Meas. Tech.* 12:3, pp. 1513–1530. DOI: 10.5194/amt-12-1513-2019.

Friedlingstein, P., M. O'Sullivan, M. W. Jones, R. M. Andrew, D. C. E. Bakker, J. Hauck, P. Landschützer, C. Le Quéré, I. T. Luijkx, G. P. Peters, W. Peters, J. Pongratz, C. Schwingshackl, S. Sitch, J. G. Canadell, P. Ciais, R. B. Jackson, S. R. Alin, P. Anthoni, L. Barbero, N. R. Bates, M. Becker, N. Bellouin, B. Decharme, L. Bopp, I. B. M. Brasika, P. Cadule, M. A. Chamberlain, N. Chandra, T.-T.-T. Chau, F. Chevallier, L. P. Chini, M. Cronin, X. Dou, K. Enyo, W. Evans, S. Falk, R. A. Feely, L. Feng, D. J. Ford, T. Gasser, J. Ghattas, T. Gkritzalis, G. Grassi, L. Gregor, N. Gruber, Ö. Gürses, I. Harris, M. Hefner, J. Heinke, R. A. Houghton, G. C. Hurtt, Y. Iida, T. Ilyina, A. R. Jacobson, A. Jain, T. Jarníková, A.

Jersild, F. Jiang, Z. Jin, F. Joos, E. Kato, R. F. Keeling, D. Kennedy, K. Klein Goldewijk, J. Knauer, J. I. Korsbakken, A. Körtzinger, X. Lan, N. Lefèvre, H. Li, J. Liu, Z. Liu, L. Ma, G. Marland, N. Mayot, P. C. McGuire, G. A. McKinley, G. Meyer, E. J. Morgan, D. R. Munro, S.-I. Nakaoka, Y. Niwa, K. M. O'Brien, A. Olsen, A. M. Omar, T. Ono, M. Paulsen, D. Pierrot, K. Pocock, B. Poulter, C. M. Powis, G. Rehder, L. Resplandy, E. Robertson, C. Rödenbeck, T. M. Rosan, J. Schwinger, R. Séférian, T. L. Smallman, S. M. Smith, R. Sospedra-Alfonso, Q. Sun, A. J. Sutton, C. Sweeney, S. Takao, P. P. Tans, H. Tian, B. Tilbrook, H. Tsujino, F. Tubiello, G. R. van der Werf, E. van Ooijen, R. Wanninkhof, M. Watanabe, C. Wimart-Rousseau, D. Yang, X. Yang, W. Yuan, X. Yue, S. Zaehle, J. Zeng, and B. Zheng (2023). "Global Carbon Budget 2023". *Earth. Syst. Sci. Data* 15:12, pp. 5301–5369. DOI: 10.5194/essd-15-5301-2023.

Fu, D., T. J. Pongetti, J. F. Blavier, T. J. Crawford, K. S. Manatt, G. C. Toon, K. W. Wong, and S. P. Sander (2014). "Near-Infrared Remote Sensing of Los Angeles Trace Gas Distributions from a Mountaintop Site". *Atmos. Meas. Tech.* 7:3, pp. 713–729. DOI: 10.5194/amt-7-713-2014.

Giles, D. M., A. Sinyuk, M. G. Sorokin, J. S. Schafer, A. Smirnov, I. Slutsker, T. F. Eck, B. N. Holben, J. R. Lewis, J. R. Campbell, E. J. Welton, S. V. Korkin, and A. I. Lyapustin (2019). "Advancements in the Aerosol Robotic Network (AERONET) Version 3 Database – Automated near-Real-Time Quality Control Algorithm with Improved Cloud Screening for Sun Photometer Aerosol Optical Depth (AOD) Measurements". *Atmos. Meas. Tech.* 12:1, pp. 169–209. DOI: 10.5194/amt-12-169-2019.

Gisi, M., F. Hase, S. Dohe, T. Blumenstock, A. Simon, and A. Keens (2012). "XCO_2-Measurements with a Tabletop FTS Using Solar Absorption Spectroscopy". *Atmos. Meas. Tech.* 5:11, pp. 2969–2980. DOI: 10.5194/amt-5-2969-2012.

Global Covenant of Mayors (2024). *Global Covenant of Mayors for Climate & Energy*. URL: https://www.globalcovenantofmayors.org/ (visited on 2024-03-18).

Gordon, I. E., L. S. Rothman, R. J. Hargreaves, R. Hashemi, E. V. Karlovets, F. M. Skinner, E. K. Conway, C. Hill, R. V. Kochanov, Y. Tan, P. Wcisło, A. A. Finenko, K. Nelson, P. F. Bernath, M. Birk, V. Boudon, A. Campargue, K. V. Chance, A. Coustenis, B. J. Drouin, J. .-. Flaud, R. R. Gamache, J. T. Hodges, D. Jacquemart, E. J. Mlawer, A. V. Nikitin, V. I. Perevalov, M. Rotger, J. Tennyson, G. C. Toon, H. Tran, V. G. Tyuterev, E. M. Adkins, A. Baker, A. Barbe, E. Canè, A. G. Császár, A. Dudaryonok, O. Egorov, A. J. Fleisher, H. Fleurbaey, A. Foltynowicz, T. Furtenbacher, J. J. Harrison, J. .-. Hartmann, V. .-. Horneman, X. Huang, T. Karman, J. Karns, S. Kassi, I. Kleiner, V. Kofman, F. Kwabia–Tchana, N. N. Lavrentieva, T. J. Lee, D. A. Long, A. A. Lukashevskaya, O. M. Lyulin, V. Yu. Makhnev, W. Matt, S. T. Massie, M. Melosso, S. N. Mikhailenko, D. Mondelain, H. S. P. Müller, O. V. Naumenko, A. Perrin, O. L. Polyansky, E. Raddaoui, P. L. Raston, Z. D. Reed, M. Rey, C. Richard, R. Tóbiás, I. Sadiek, D. W. Schwenke, E. Starikova, K. Sung, F. Tamassia, S. A. Tashkun, J. Vander Auwera, I. A. Vasilenko, A. A. Vigasin, G. L. Villanueva, B. Vispoel, G. Wagner, A. Yachmenev, and S. N. Yurchenko (2022). "The HITRAN2020 Molecular Spectroscopic Database". *J. Quant. Spectrosc. Ra.* 277, p. 107949. DOI: 10.1016/j.jqsrt.2021.107949.

Griffiths, P. R. and J. A. de Haseth (2007). *Fourier Transform Infrared Spectrometry*. 2. ed. Wiley-Interscience. 704 pp. DOI: 10.1002/047010631X.

Gulev, S., P. Thorne, J. Ahn, F. Dentener, C. Domingues, S. Gerland, D. Gong, D. Kaufman, H. Nnamchi, J. Quaas, J. Rivera, S. Sathyendranath, S. Smith, B. Trewin, K. von Schuckmann, and R. Vose (2021). "Changing State of the Climate System". In: *Climate Change 2021: The Physical Science Basis. Contribution of Working Group I to the Sixth Assessment Report of the Intergovernmental Panel on Climate Change[Masson-Delmotte, V., P. Zhai, A. Pirani, S.L. Connors, C. Péan, S. Berger, N. Caud, Y. Chen, L. Goldfarb, M.I. Gomis, M. Huang, K. Leitzell, E. Lonnoy, J.B.R. Matthews, T.K. Maycock, T. Waterfield, O. Yelekçi, R. Yu, and B. Zhou (Eds.)]* Cambridge University Press, Cambridge, United Kingdom and New York, NY, USA, pp. 287–422. DOI: 10.1017/9781009157896.004.

Gurney, K. R., J. Liang, R. Patarasuk, Y. Song, J. Huang, and G. Roest (2020). "The Vulcan Version 3.0 High-Resolution Fossil Fuel CO_2 Emissions for the United States". *J. Geophys. Res. Atmos.* 125:19, e2020JD032974. DOI: 10.1029/2020JD032974.

Gurney, K. R., R. Patarasuk, J. Liang, Y. Song, D. O'Keeffe, P. Rao, J. R. Whetstone, R. M. Duren, A. Eldering, and C. Miller (2019). "The Hestia Fossil Fuel CO_2 Emissions Data Product for the Los Angeles Megacity (Hestia-LA)". *Earth. Syst. Sci. Data* 11:3, pp. 1309–1335. DOI: 10.5194/essd-11-1309-2019.

Gurney, K. R., I. Razlivanov, Y. Song, Y. Zhou, B. Benes, and M. Abdul-Massih (2012). "Quantification of Fossil Fuel CO_2 Emissions on the Building/Street Scale for a Large U.S. City". *Environ. Sci. Technol.* 46:21, pp. 12194–12202. DOI: 10.1021/es3011282.

Hansen, J. E. and L. D. Travis (1974). "Light Scattering in Planetary Atmospheres". *Space Sci Rev* 16:4, pp. 527–610. DOI: 10.1007/BF00168069.

Hartmann, J.-M., H. Tran, and G. C. Toon (2009). "Influence of Line Mixing on the Retrievals of Atmospheric CO_2 from Spectra in the 1.6 and 2.1µm Regions". *Atmos. Chem. Phys.* 9:19, pp. 7303–7312. DOI: 10.5194/acp-9-7303-2009.

Hartmann, J.-M., C. Boulet, and D. Robert (2008). *Collisional Effects on Molecular Spectra: Laboratory Experiments and Models, Consequences for Applications*. Elsevier.

Hase, F., M. Frey, T. Blumenstock, J. Groß, M. Kiel, R. Kohlhepp, G. Mengistu Tsidu, K. Schäfer, M. K. Sha, and J. Orphal (2015). "Application of Portable FTIR Spectrometers for Detecting Greenhouse Gas Emissions of the Major City Berlin". *Atmos. Meas. Tech.* 8:7, pp. 3059–3068. DOI: 10.5194/amt-8-3059-2015.

Hase, F. (2000). "Inversion von Spurengasprofilen Aus Hochaufgelösten Bodengebundenen FTIR-Messungen in Absorption". Forschungszentrum Karlsruhe. 149 pp. URL: http://swbplus.bsz-bw.de/bsz086717057abs.htm.

Hase, F., T. Blumenstock, and C. Paton-Walsh (1999). "Analysis of the Instrumental Line Shape of High-Resolution Fourier Transform IR Spectrometers with Gas Cell Measurements and New Retrieval Software". *Appl. Optics* 38:15, pp. 3417–22. DOI: 10.1364/AO.38.003417.

Hase, F., M. Frey, M. Kiel, T. Blumenstock, R. Harig, A. Keens, and J. Orphal (2016). "Addition of a Channel for XCO Observations to a Portable FTIR Spectrometer for Greenhouse Gas Measurements". *Atmos. Meas. Tech.* 9:5, pp. 2303–2313. DOI: 10.5194/amt-9-2303-2016.

Hazan, L., J. Tarniewicz, M. Ramonet, O. Laurent, and A. Abbaris (2016). "Automatic Processing of Atmospheric CO_2 and CH_4 Mole Fractions at the ICOS Atmosphere Thematic Centre". *Atmos. Meas. Tech.* 9:9, pp. 4719–4736. DOI: 10.5194/amt-9-4719-2016.

He, L., Z.-C. Zeng, T. J. Pongetti, C. Wong, J. Liang, K. R. Gurney, S. Newman, V. Yadav, K. Verhulst, C. E. Miller, R. Duren, C. Frankenberg, P. O. Wennberg, R.-L. Shia, Y. L. Yung, and S. P. Sander (2019). "Atmospheric Methane Emissions Correlate With Natural Gas Consumption From Residential and Commercial Sectors in Los Angeles". *Geophys. Res. Lett.* 46:14, pp. 8563–8571. DOI: 10.1029/2019GL083400.

Hedelius, J. K., J. Liu, T. Oda, S. Maksyutov, C. M. Roehl, L. T. Iraci, J. R. Podolske, P. W. Hillyard, J. Liang, K. R. Gurney, D. Wunch, and P. O. Wennberg (2018). "Southern California Megacity CO_2, CH_4, and CO Flux Estimates Using Ground- and Space-Based Remote Sensing and a Lagrangian Model". *Atmos. Chem. Phys.* 18:22, pp. 16271–16291. DOI: 10.5194/acp-18-16271-2018.

Hemmer, B. (2019). "Toward Ground-Scattered Sunlight Measurements of Carbon Dioxide and Methane". MA thesis. University of Heidelberg.

Hopkins, F. M., E. A. Kort, S. E. Bush, J. R. Ehleringer, C.-T. Lai, D. R. Blake, and J. T. Randerson (2016). "Spatial Patterns and Source Attribution of Urban Methane in the Los Angeles Basin". *J. Geophys. Res. Atmos.* 121:5, pp. 2490–2507. DOI: 10.1002/2015JD024429.

Hsu, Y.-K., T. VanCuren, S. Park, C. Jakober, J. Herner, M. FitzGibbon, D. R. Blake, and D. D. Parrish (2010). "Methane Emissions Inventory Verification in Southern California". *Atmospheric Environment* 44:1, pp. 1–7. DOI: 10.1016/j.atmosenv.2009.10.002.

Hu, H., J. Landgraf, R. Detmers, T. Borsdorff, J. Aan de Brugh, I. Aben, A. Butz, and O. Hasekamp (2018). "Toward Global Mapping of Methane With TROPOMI: First Results and Intersatellite Comparison to GOSAT". *Geophys. Res. Lett.* 45:8, pp. 3682–3689. DOI: 10.1002/2018GL077259.

International Energy Agency (2008). *World Energy Outlook 2008*. International Energy Agency, Paris, France. URL: https://www.iea.org/reports/world-energy-outlook-2008.

Jacobson, A. R., K. N. Schuldt, J. B. Miller, T. Oda, P. Tans, Arlyn Andrews, J. Mund, L. Ott, G. J. Collatz, T. Aalto, S. Afshar, K. Aikin, S. Aoki, F. Apadula, B. Baier, P. Bergamaschi, A. Beyersdorf, S. C. Biraud, A. Bollenbacher, D. Bowling, G. Brailsford, J. B. Abshire, G. Chen, Huilin Chen, Lukasz Chmura, Sites Climadat, A. Colomb, S. Conil, A. Cox, P. Cristofanelli, E. Cuevas, R. Curcoll, C. D. Sloop, K. Davis, S. D. Wekker, M. Delmotte, J. P. DiGangi, E. Dlugokencky, J. Ehleringer, J. W. Elkins, L. Emmenegger, M. L. Fischer, G. Forster, A. Frumau, M. Galkowski, L. V. Gatti, E. Gloor, T. Griffis, S. Hammer, L. Haszpra, J. Hatakka, M. Heliasz, A. Hensen, O. Hermanssen, E. Hintsa, J. Holst, D. Jaffe, A. Karion, S. R. Kawa, R. Keeling, P. Keronen, P. Kolari, K. Kominkova, E. Kort, P. Krummel, D. Kubistin, C. Labuschagne, R. Langenfelds, O. Laurent, T. Laurila, T. Lauvaux, B. Law, J. Lee, I. Lehner, M. Leuenberger, I. Levin, J. Levula, J. Lin, M. Lindauer, Z. Loh, M. Lopez, I. T. Luijkx, C. L. Myhre, T. Machida, I. Mammarella, G. Manca, A. Manning, A. Manning, M. V. Marek, P. Marklund, M. Y. Martin, H. Matsueda, K. McKain, H. Meijer, F. Meinhardt, N. Miles, C. E. Miller, M. Mölder, S. Montzka, F. Moore, Josep-Anton Morgui, S. Morimoto, B. Munger, Jaroslaw Necki, S. Newman, S. Nichol, Y. Niwa, S. O'Doherty, Mikaell Ottosson-Löfvenius, B. Paplawsky, J. Peischl, O. Peltola, Jean-Marc Pichon, S. Piper, C. Plass-Dölmer, M. Ramonet, E. Reyes-Sanchez, S. Richardson, H. Riris, T. Ryerson, K. Saito, M. Sargent, M. Sasakawa, Y. Sawa, D. Say, B. Scheeren, M. Schmidt, A. Schmidt, M. Schumacher, P. Shepson, M. Shook, K.

Stanley, M. Steinbacher, B. Stephens, C. Sweeney, K. Thoning, M. Torn, J. Turnbull, K. Tørseth, P. V. D. Bulk, D. V. Dinther, A. Vermeulen, B. Viner, G. Vitkova, S. Walker, D. Weyrauch, S. Wofsy, D. Worthy, Dickon Young, and Miroslaw Zimnoch (2020). *CarbonTracker CT2019B*. NOAA Global Monitoring Laboratory. DOI: 10.25925/20201008.

Jägermeyr, J., C. Müller, A. C. Ruane, J. Elliott, J. Balkovic, O. Castillo, B. Faye, I. Foster, C. Folberth, J. A. Franke, K. Fuchs, J. R. Guarin, J. Heinke, G. Hoogenboom, T. Iizumi, A. K. Jain, D. Kelly, N. Khabarov, S. Lange, T.-S. Lin, W. Liu, O. Mialyk, S. Minoli, E. J. Moyer, M. Okada, M. Phillips, C. Porter, S. S. Rabin, C. Scheer, J. M. Schneider, J. F. Schyns, R. Skalsky, A. Smerald, T. Stella, H. Stephens, H. Webber, F. Zabel, and C. Rosenzweig (2021). "Climate Impacts on Global Agriculture Emerge Earlier in New Generation of Climate and Crop Models". *Nat. Food* 2:11, pp. 873–885. DOI: 10.1038/s43016-021-00400-y.

Jeong, S., S. Newman, J. Zhang, A. E. Andrews, L. Bianco, J. Bagley, X. Cui, H. Graven, J. Kim, P. Salameh, B. W. LaFranchi, C. Priest, M. Campos-Pineda, E. Novakovskaia, C. D. Sloop, H. A. Michelsen, R. P. Bambha, R. F. Weiss, R. Keeling, and M. L. Fischer (2016). "Estimating Methane Emissions in California's Urban and Rural Regions Using Multitower Observations". *J. Geophys. Res. Atmos.* 121:21, pp. 13, 031–13, 049. DOI: 10.1002/2016JD025404.

Johnson, M. R., B. M. Conrad, and D. R. Tyner (2023). "Creating Measurement-Based Oil and Gas Sector Methane Inventories Using Source-Resolved Aerial Surveys". *Commun. Earth Environ.* 4:1, 1, pp. 1–9. DOI: 10.1038/s43247-023-00769-7.

Jungmann, M., S. N. Vardag, F. Kutzner, F. Keppler, M. Schmidt, N. Aeschbach, U. Gerhard, A. Zipf, S. Lautenbach, A. Siegmund, T. Goeschl, and A. Butz (2022). "Zooming-in for Climate Action—Hyperlocal Greenhouse Gas Data for Mitigation Action?" *Clim. Action* 1:1, p. 8. DOI: 10.1007/s44168-022-00007-4.

Karlovets, E. V., I. E. Gordon, L. S. Rothman, R. Hashemi, R. J. Hargreaves, G. C. Toon, A. Campargue, V. I. Perevalov, P. Čermák, M. Birk, G. Wagner, J. T. Hodges, J. Tennyson, and S. N. Yurchenko (2021). "The Update of the Line Positions and Intensities in the Line List of Carbon Dioxide for the HITRAN2020 Spectroscopic Database". *J. Quant. Spectrosc. Ra.* 276, p. 107896. DOI: 10.1016/j.jqsrt.2021.107896.

Karman, T., I. E. Gordon, A. van der Avoird, Y. I. Baranov, C. Boulet, B. J. Drouin, G. C. Groenenboom, M. Gustafsson, J.-M. Hartmann, R. L. Kurucz, L. S. Rothman, K. Sun, K. Sung, R. Thalman, H. Tran, E. H. Wishnow, R. Wordsworth, A. A. Vigasin, R. Volkamer, and W. J. van der Zande (2019). "Update of the HITRAN Collision-Induced Absorption Section". *Icarus* 328, pp. 160–175. DOI: 10.1016/j.icarus.2019.02.034.

Keppel-Aleks, G., G. C. Toon, P. O. Wennberg, and N. M. Deutscher (2007). "Reducing the Impact of Source Brightness Fluctuations on Spectra Obtained by Fourier-transform Spectrometry." *Appl. Optics* 46:21, pp. 4774–4779. DOI: 10.1364/AO.46.004774.

Kiel, M., A. Eldering, D. D. Roten, J. C. Lin, S. Feng, R. Lei, T. Lauvaux, T. Oda, C. M. Roehl, J.-F. Blavier, and L. T. Iraci (2021). "Urban-Focused Satellite CO_2 Observations from the Orbiting Carbon Observatory-3: A First Look at the Los Angeles Megacity". *Remote Sens. Environ.* 258, p. 112314. DOI: 10.1016/j.rse.2021.112314.

Kim, J., A. A. Shusterman, K. J. Lieschke, C. Newman, and R. C. Cohen (2018). "The BErkeley Atmospheric CO_2 Observation Network: Field Calibration and Evaluation of

Low-Cost Air Quality Sensors". *Atmos. Meas. Tech.* 11:4, pp. 1937–1946. DOI: 10.5194/amt-11-1937-2018.

KIT IMK-ASF (2024). *COCCON Data Processing (PROFFAST)*. URL: https://www.imk-asf.kit.edu/english/3225.php (visited on 2024-03-25).

Klappenbach, F., M. Bertleff, J. Kostinek, F. Hase, T. Blumenstock, A. Agusti-Panareda, M. Razinger, and A. Butz (2015). "Accurate Mobile Remote Sensing of XCO_2 and XCH_4 Latitudinal Transects from Aboard a Research Vessel". *Atmos. Meas. Tech.* 8:12, pp. 5023–5038. DOI: 10.5194/amt-8-5023-2015.

Knapp, M., R. Kleinschek, F. Hase, A. Agustí-Panareda, A. Inness, J. Barré, J. Landgraf, T. Borsdorff, S. Kinne, and A. Butz (2021). "Shipborne Measurements of XCO_2, XCH_4, and XCO above the Pacific Ocean and Comparison to CAMS Atmospheric Analyses and S5P/TROPOMI". *Earth. Syst. Sci. Data* 13:1, pp. 199–211. DOI: 10.5194/essd-13-199-2021.

Kochanov, R. V., I. E. Gordon, L. S. Rothman, P. Wcisło, C. Hill, and J. S. Wilzewski (2016). "HITRAN Application Programming Interface (HAPI): A Comprehensive Approach to Working with Spectroscopic Data". *Journal of Quantitative Spectroscopy and Radiative Transfer*. XVIIIth Symposium on High Resolution Molecular Spectroscopy (HighRus-2015), Tomsk, Russia 177, pp. 15–30. DOI: 10.1016/j.jqsrt.2016.03.005.

Kort, E. A., C. Frankenberg, C. E. Miller, and T. Oda (2012). "Space-Based Observations of Megacity Carbon Dioxide". *Geophys. Res. Lett.* 39:17. DOI: 10.1029/2012GL052738.

Kostinek, J. (2015). "Enhancing Optical Throughput and Detector Sensitivity of the EM / FTS IR Spectrometer". MA thesis. Karlsruhe Institute of Technology.

Kuenen, J., S. Dellaert, A. Visschedijk, J.-P. Jalkanen, I. Super, and H. Denier van der Gon (2022). "CAMS-REG-v4: A State-of-the-Art High-Resolution European Emission Inventory for Air Quality Modelling". *Earth. Syst. Sci. Data* 14:2, pp. 491–515. DOI: 10.5194/essd-14-491-2022.

Kulp, S. A. and B. H. Strauss (2019). "New Elevation Data Triple Estimates of Global Vulnerability to Sea-Level Rise and Coastal Flooding". *Nat. Commun.* 10:1, p. 4844. DOI: 10.1038/s41467-019-12808-z.

Kuze, A., H. Suto, M. Nakajima, and T. Hamazaki (2009). "Thermal and near Infrared Sensor for Carbon Observation Fourier-transform Spectrometer on the Greenhouse Gases Observing Satellite for Greenhouse Gases Monitoring". *Appl. Optics* 48:35, pp. 6716–6733. DOI: 10.1364/AO.48.006716.

Lamouroux, J., H. Tran, A. L. Laraia, R. R. Gamache, L. S. Rothman, I. E. Gordon, and J. .-. Hartmann (2010). "Updated Database plus Software for Line-Mixing in CO_2 Infrared Spectra and Their Test Using Laboratory Spectra in the 1.5–2.3μm Region". *Journal of Quantitative Spectroscopy and Radiative Transfer*. XVIth Symposium on High Resolution Molecular Spectroscopy (HighRus-2009) 111:15, pp. 2321–2331. DOI: 10.1016/j.jqsrt.2010.03.006.

Lian, J., T. Lauvaux, H. Utard, F.-M. Bréon, G. Broquet, M. Ramonet, O. Laurent, I. Albarus, K. Cucchi, and P. Ciais (2022). "Assessing the Effectiveness of an Urban CO_2 Monitoring Network over the Paris Region through the COVID-19 Lockdown Natural Experiment". *Environ. Sci. Technol.* 56:4, pp. 2153–2162. DOI: 10.1021/acs.est.1c04973.

Liou, K.-N. (2002). *An Introduction to Atmospheric Radiation*. Academic Press. 583 pp.

Löw, B. A., R. Kleinschek, V. Enders, S. P. Sander, T. J. Pongetti, T. D. Schmitt, F. Hase, J. Kostinek, and A. Butz (2023). "A Portable Reflected-Sunlight Spectrometer for CO_2 and CH_4". *Atmos. Meas. Tech.* 16:21, pp. 5125–5144. DOI: 10.5194/amt-16-5125-2023.

Luqman, M., P. J. Rayner, and K. R. Gurney (2023). "On the Impact of Urbanisation on CO_2 Emissions". *npj Urban Sustain* 3:1, pp. 1–8. DOI: 10.1038/s42949-023-00084-2.

Luther, A., R. Kleinschek, L. Scheidweiler, S. Defratyka, M. Stanisavljevic, A. Forstmaier, A. Dandocsi, S. Wolff, D. Dubravica, N. Wildmann, J. Kostinek, P. Jöckel, A.-L. Nickl, T. Klausner, F. Hase, M. Frey, J. Chen, F. Dietrich, J. Nęcki, J. Swolkień, A. Fix, A. Roiger, and A. Butz (2019). "Quantifying CH_4 Emissions from Hard Coal Mines Using Mobile Sun-Viewing Fourier Transform Spectrometry". *Atmos. Meas. Tech.* 12:10, pp. 5217–5230. DOI: 10.5194/amt-12-5217-2019.

Luther, A., J. Kostinek, R. Kleinschek, S. Defratyka, M. Stanisavljević, A. Forstmaier, A. Dandocsi, L. Scheidweiler, D. Dubravica, N. Wildmann, F. Hase, M. M. Frey, J. Chen, F. Dietrich, J. Nęcki, J. Swolkień, C. Knote, S. N. Vardag, A. Roiger, and A. Butz (2022). "Observational Constraints on Methane Emissions from Polish Coal Mines Using a Ground-Based Remote Sensing Network". *Atmos. Chem. Phys.* 22:9, pp. 5859–5876. DOI: 10.5194/acp-22-5859-2022.

Lwasa, S., K. Seto, X. Bai, H. Blanco, K. Gurney, Ş. Kilkiş, O. Lucon, J. Murakami, J. Pan, A. Sharifi, and Y. Yamagata (2022). "Urban Systems and Other Settlements". In: *IPCC, 2022: Climate Change 2022: Mitigation of Climate Change. Contribution of Working Group III to the Sixth Assessment Report of the Intergovernmental Panel on Climate Change [P.R. Shukla, J. Skea, R. Slade, A. Al Khourdajie, R. van Diemen, D. McCollum, M. Pathak, S. Some, P. Vyas, R. Fradera, M. Belkacemi, A. Hasija, G. Lisboa, S. Luz, J. Malley, (Eds.)]* Cambridge University Press, Cambridge, UK and New York, NY, USA. DOI: 10.1017/9781009157926.010.

Maasakkers, J. D., D. J. Varon, A. Elfarsdóttir, J. McKeever, D. Jervis, G. Mahapatra, S. Pandey, A. Lorente, T. Borsdorff, L. R. Foorthuis, B. J. Schuit, P. Tol, T. A. van Kempen, R. van Hees, and I. Aben (2022). "Using Satellites to Uncover Large Methane Emissions from Landfills". *Science Advances* 8:32, eabn9683. DOI: 10.1126/sciadv.abn9683.

Marcotullio, P. J., A. Sarzynski, J. Albrecht, N. Schulz, and J. Garcia (2013). "The Geography of Global Urban Greenhouse Gas Emissions: An Exploratory Analysis". *Climatic Change* 121:4, pp. 621–634. DOI: 10.1007/s10584-013-0977-z.

Masson, V., A. Lemonsu, J. Hidalgo, and J. Voogt (2020). "Urban Climates and Climate Change". *Annual Review of Environment and Resources* 45:1, pp. 411–444. DOI: 10.1146/annurev-environ-012320-083623.

Matthews, B. and H. Schume (2022). "Tall Tower Eddy Covariance Measurements of CO_2 Fluxes in Vienna, Austria". *Atmospheric Environment* 274, p. 118941. DOI: 10.1016/j.atmosenv.2022.118941.

McKain, K., A. Down, S. M. Raciti, J. Budney, L. R. Hutyra, C. Floerchinger, S. C. Herndon, T. Nehrkorn, M. S. Zahniser, R. B. Jackson, N. Phillips, and S. C. Wofsy (2015). "Methane Emissions from Natural Gas Infrastructure and Use in the Urban Region of Boston, Massachusetts". *Proc. Natl. Acad. Sci. USA* 112:7, pp. 1941–1946. DOI: 10.1073/pnas.1416261112.

McKain, K., S. C. Wofsy, T. Nehrkorn, J. Eluszkiewicz, J. R. Ehleringer, and B. B. Stephens (2012). "Assessment of Ground-Based Atmospheric Observations for Verification of Green-

house Gas Emissions from an Urban Region". *Proc. Natl. Acad. Sci. USA* 109:22, pp. 8423–8428. DOI: 10.1073/pnas.1116645109.

Meerdink, S. K., S. J. Hook, D. A. Roberts, and E. A. Abbott (2019). "The ECOSTRESS Spectral Library Version 1.0". *Remote Sens. Environ.* 230, p. 111196. DOI: 10.1016/J.RSE.2019.05.015.

Meirink, J. F., H. J. Eskes, and A. P. H. Goede (2006). "Sensitivity Analysis of Methane Emissions Derived from SCIAMACHY Observations through Inverse Modelling". *Atmos. Chem. Phys.* 6:5, pp. 1275–1292. DOI: 10.5194/acp-6-1275-2006.

Mertz, L. (1967). "Auxiliary Computation for Fourier Spectrometry". *Infrared Physics* 7:1, pp. 17–23. DOI: 10.1016/0020-0891(67)90026-7.

Miller, J. B., S. J. Lehman, K. R. Verhulst, C. E. Miller, R. M. Duren, V. Yadav, S. Newman, and C. D. Sloop (2020). "Large and Seasonally Varying Biospheric CO2 Fluxes in the Los Angeles Megacity Revealed by Atmospheric Radiocarbon". *Proc. Natl. Acad. Sci. USA*. DOI: 10.1073/pnas.2005253117. pmid: 33046637.

Mitchell, L. E., J. C. Lin, L. R. Hutyra, D. R. Bowling, R. C. Cohen, K. J. Davis, E. DiGangi, R. M. Duren, J. R. Ehleringer, C. Fain, M. Falk, A. Guha, A. Karion, R. F. Keeling, J. Kim, N. L. Miles, C. E. Miller, S. Newman, D. E. Pataki, S. Prinzivalli, X. Ren, A. Rice, S. J. Richardson, M. Sargent, B. B. Stephens, J. C. Turnbull, K. R. Verhulst, F. Vogel, R. F. Weiss, J. Whetstone, and S. C. Wofsy (2022). "A Multi-City Urban Atmospheric Greenhouse Gas Measurement Data Synthesis". *Sci. Data* 9:1, 1, p. 361. DOI: 10.1038/s41597-022-01467-3.

Moore, D. P., N. P. Li, L. P. Wendt, S. R. Castañeda, M. M. Falinski, J.-J. Zhu, C. Song, Z. J. Ren, and M. A. Zondlo (2023). "Underestimation of Sector-Wide Methane Emissions from United States Wastewater Treatment". *Environ. Sci. Technol.* 57:10, pp. 4082–4090. DOI: 10.1021/acs.est.2c05373.

Moran, D., K. Kanemoto, M. Jiborn, R. Wood, J. Többen, and K. C. Seto (2018). "Carbon Footprints of 13 000 Cities". *Environ. Res. Lett.* 13:6, p. 064041. DOI: 10.1088/1748-9326/aac72a.

Mueller, K. L., T. Lauvaux, K. R. Gurney, G. Roest, S. Ghosh, S. M. Gourdji, A. Karion, P. DeCola, and J. Whetstone (2021). "An Emerging GHG Estimation Approach Can Help Cities Achieve Their Climate and Sustainability Goals". *Environ. Res. Lett.* 16:8, p. 084003. DOI: 10.1088/1748-9326/ac0f25.

Müller, R. (2019). "Modifying the EM-27 Spectroscope for Indirect Sunlight Calibration". Project Report. University of Heidelberg.

National Centers for Environmental Prediction, National Weather Service, NOAA, and U.S. Department of Commerce (2000). *NCEP FNL Operational Model Global Tropospheric Analyses, Continuing from July 1999*. Boulder CO, Research Data Archive at the National Center for Atmospheric Research, Computational and Information Systems Laboratory. DOI: 10.5065/D6M043C6.

Newman, S., S. Jeong, M. L. Fischer, X. Xu, C. L. Haman, B. Lefer, S. Alvarez, B. Rappenglueck, E. A. Kort, A. E. Andrews, J. Peischl, K. R. Gurney, C. E. Miller, and Y. L. Yung (2013). "Diurnal Tracking of Anthropogenic CO_2 Emissions in the Los Angeles Basin Megacity during Spring 2010". *Atmos. Chem. Phys.* 13:8, pp. 4359–4372. DOI: 10.5194/acp-13-4359-2013.

Norton, R. H. and R. Beer (1977). "Errata: New Apodizing Functions For Fourier Spectrometry". *Journal of the Optical Society of America* 67:3, p. 419. DOI: 10.1364/JOSA.67.000419.

Oda, T. (2015). *ODIAC Fossil Fuel CO_2 Emissions Dataset*. In collab. with S. Maksyutov. GeoTIFF,NetCDF. Version ODIAC2022. Center for Global Environmental Research, National Institute for Environmental Studies, Center for Global Environmental Research, National Institute for Environmental Studies. DOI: 10.17595/20170411.001.

Ohyama, H., M. M. Frey, I. Morino, K. Shiomi, M. Nishihashi, T. Miyauchi, H. Yamada, M. Saito, M. Wakasa, T. Blumenstock, and F. Hase (2023). "Anthropogenic CO_2 Emission Estimates in the Tokyo Metropolitan Area from Ground-Based CO_2 Column Observations". *Atmos. Chem. Phys.* 23:23, pp. 15097–15119. DOI: 10.5194/acp-23-15097-2023.

Petrescu, A. M. R., C. Qiu, M. J. McGrath, P. Peylin, G. P. Peters, P. Ciais, R. L. Thompson, A. Tsuruta, D. Brunner, M. Kuhnert, B. Matthews, P. I. Palmer, O. Tarasova, P. Regnier, R. Lauerwald, D. Bastviken, L. Höglund-Isaksson, W. Winiwarter, G. Etiope, T. Aalto, G. Balsamo, V. Bastrikov, A. Berchet, P. Brockmann, G. Ciotoli, G. Conchedda, M. Crippa, F. Dentener, C. D. Groot Zwaaftink, D. Guizzardi, D. Günther, J.-M. Haussaire, S. Houweling, G. Janssens-Maenhout, M. Kouyate, A. Leip, A. Leppänen, E. Lugato, M. Maisonnier, A. J. Manning, T. Markkanen, J. McNorton, M. Muntean, G. D. Oreggioni, P. K. Patra, L. Perugini, I. Pison, M. T. Raivonen, M. Saunois, A. J. Segers, P. Smith, E. Solazzo, H. Tian, F. N. Tubiello, T. Vesala, G. R. van der Werf, C. Wilson, and S. Zaehle (2023). "The Consolidated European Synthesis of CH_4 and N_2O Emissions for the European Union and United Kingdom: 1990–2019". *Earth. Syst. Sci. Data* 15:3, pp. 1197–1268. DOI: 10.5194/essd-15-1197-2023.

Petri, C., T. Warneke, N. Jones, T. Ridder, J. Messerschmidt, T. Weinzierl, M. Geibel, and J. Notholt (2012). "Remote Sensing of CO_2 and CH_4 Using Solar Absorption Spectrometry with a Low Resolution Spectrometer". *Atmos. Meas. Tech.* 5:7, pp. 1627–1635. DOI: 10.5194/amt-5-1627-2012.

Petty, G. W. (2006). *A First Course in Atmospheric Radiation*. 2. ed. Sundog Publ., Madison. XII, 459 S.

Prahl, S. (2023). *Miepython: Pure Python Implementation of Mie Scattering*. Version v2.5.3. Zenodo. DOI: 10.5281/zenodo.8218010.

Rebmann, C., M. Aubinet, H. Schmid, N. Arriga, M. Aurela, G. Burba, R. Clement, A. De Ligne, G. Fratini, B. Gielen, J. Grace, A. Graf, P. Gross, S. Haapanala, M. Herbst, L. Hörtnagl, A. Ibrom, L. Joly, N. Kljun, O. Kolle, A. Kowalski, A. Lindroth, D. Loustau, I. Mammarella, M. Mauder, L. Merbold, S. Metzger, M. Mölder, L. Montagnani, D. Papale, M. Pavelka, M. Peichl, M. Roland, P. Serrano-Ortiz, L. Siebicke, R. Steinbrecher, J.-P. Tuovinen, T. Vesala, G. Wohlfahrt, and D. Franz (2018). "ICOS Eddy Covariance FluxStation Site Setup: A Review". *International Agrophysics* 32:4, pp. 471–494. DOI: 10.1515/intag-2017-0044.

Riahi, K., R. Schaeffer, J. Arango, K. Calvin, C. Guivarch, T. Hasegawa, K. Jiang, E. Kriegler, R. Matthews, G. Peters, A. Rao, S. Robertson, A. Sebbit, J. Steinberger, M. Tavoni, and D. van Vuuren (2022). "Mitigation Pathways Compatible with Long-Term Goals". In: *In IPCC, 2022: Climate Change 2022: Mitigation of Climate Change. Contribution of Working Group III to the Sixth Assessment Report of the Intergovernmen-*

tal Panel on Climate Change [P.R. Shukla, J. Skea, R. Slade, A. Al Khourdajie, R. van Diemen, D. McCollum, M. Pathak, S. Some, P. Vyas, R. Fradera, M. Belkacemi, A. Hasija, G. Lisboa, S. Luz, J. Malley, (Eds.)] Cambridge University Press, Cambridge, UK and New York, NY, USA. DOI: 10.1017/9781009157926.005.

Richard, E., D. Harber, O. Coddington, G. Drake, J. Rutkowski, M. Triplett, P. Pilewskie, and T. Woods (2020). "SI-traceable Spectral Irradiance Radiometric Characterization and Absolute Calibration of the TSIS-1 Spectral Irradiance Monitor (SIM)". *Remote Sensing* 12:11, 11, p. 1818. DOI: 10.3390/rs12111818.

Richard, E., D. Harber, G. Drake, J. Rutkowsi, Z. Castleman, M. Smith, J. Sprunck, W. Zheng, P. Smith, M. Fisher, A. Sims, B. Cervelli, M. Fowle, M. Miller, M. Chambliss, T. Woods, P. Pilewskie, C. Yung, M. Stephens, N. Tomlin, M. White, and J. Lehman (2019). "Compact Spectral Irradiance Monitor Flight Demonstration Mission". In: *CubeSats and SmallSats for Remote Sensing III*. CubeSats and SmallSats for Remote Sensing III. Vol. 11131. SPIE, pp. 15–34. DOI: 10.1117/12.2531268.

Rodgers, C. D. (2000). *Inverse Methods for Atmospheric Sounding*. World Scientific, Singapore [u.a.] XVI, 238 S.

Roedel, W. and T. Wagner (2017). *Physik Unserer Umwelt: Die Atmosphäre*. 5. Aufl. 2. Springer Spektrum, Berlin, Heidelberg. DOI: 10.1007/978-3-662-54258-3.

Sargent, M., Y. Barrera, T. Nehrkorn, L. R. Hutyra, C. K. Gately, T. Jones, K. McKain, C. Sweeney, J. Hegarty, B. Hardiman, J. A. Wang, and S. C. Wofsy (2018). "Anthropogenic and Biogenic CO_2 Fluxes in the Boston Urban Region". *Proc. Natl. Acad. Sci. USA* 115:29, pp. 7491–7496. DOI: 10.1073/pnas.1803715115.

Sargent, M. R., C. Floerchinger, K. McKain, J. Budney, E. W. Gottlieb, L. R. Hutyra, J. Rudek, and S. C. Wofsy (2021). "Majority of US Urban Natural Gas Emissions Unaccounted for in Inventories". *Proc. Natl. Acad. Sci. USA* 118:44, e2105804118. DOI: 10.1073/pnas.2105804118.

Saunois, M., A. R. Stavert, B. Poulter, P. Bousquet, J. G. Canadell, R. B. Jackson, P. A. Raymond, E. J. Dlugokencky, S. Houweling, P. K. Patra, P. Ciais, V. K. Arora, D. Bastviken, P. Bergamaschi, D. R. Blake, G. Brailsford, L. Bruhwiler, K. M. Carlson, M. Carrol, S. Castaldi, N. Chandra, C. Crevoisier, P. M. Crill, K. Covey, C. L. Curry, G. Etiope, C. Frankenberg, N. Gedney, M. I. Hegglin, L. Höglund-Isaksson, G. Hugelius, M. Ishizawa, A. Ito, G. Janssens-Maenhout, K. M. Jensen, F. Joos, T. Kleinen, P. B. Krummel, R. L. Langenfelds, G. G. Laruelle, L. Liu, T. Machida, S. Maksyutov, K. C. McDonald, J. McNorton, P. A. Miller, J. R. Melton, I. Morino, J. Müller, F. Murguia-Flores, V. Naik, Y. Niwa, S. Noce, S. O'Doherty, R. J. Parker, C. Peng, S. Peng, G. P. Peters, C. Prigent, R. Prinn, M. Ramonet, P. Regnier, W. J. Riley, J. A. Rosentreter, A. Segers, I. J. Simpson, H. Shi, S. J. Smith, L. P. Steele, B. F. Thornton, H. Tian, Y. Tohjima, F. N. Tubiello, A. Tsuruta, N. Viovy, A. Voulgarakis, T. S. Weber, M. van Weele, G. R. van der Werf, R. F. Weiss, D. Worthy, D. Wunch, Y. Yin, Y. Yoshida, W. Zhang, Z. Zhang, Y. Zhao, B. Zheng, Q. Zhu, Q. Zhu, and Q. Zhuang (2020). "The Global Methane Budget 2000–2017". *Earth. Syst. Sci. Data* 12:3, pp. 1561–1623. DOI: 10.5194/essd-12-1561-2020.

Schepers, D., J. M. J. aan de Brugh, Ph. Hahne, A. Butz, O. P. Hasekamp, and J. Landgraf (2014). "LINTRAN v2.0: A Linearised Vector Radiative Transfer Model for Efficient Simulation of Satellite-Born Nadir-Viewing Reflection Measurements of Cloudy Atmo-

spheres". *Journal of Quantitative Spectroscopy and Radiative Transfer* 149, pp. 347–359. DOI: 10.1016/j.jqsrt.2014.08.019.

Schewe, J., J. Heinke, D. Gerten, I. Haddeland, N. W. Arnell, D. B. Clark, R. Dankers, S. Eisner, B. M. Fekete, F. J. Colón-González, S. N. Gosling, H. Kim, X. Liu, Y. Masaki, F. T. Portmann, Y. Satoh, T. Stacke, Q. Tang, Y. Wada, D. Wisser, T. Albrecht, K. Frieler, F. Piontek, L. Warszawski, and P. Kabat (2014). "Multimodel Assessment of Water Scarcity under Climate Change". *Proc. Natl. Acad. Sci. USA* 111:9, pp. 3245–3250. DOI: 10.1073/pnas.1222460110.

Schmitt, T. D. (2024). "An Open-Path Observatory for Greenhouse Gases Based on High Resolution Fourier Transform Spectroscopy". PhD thesis. Heidelberg University. DOI: 10.11588/heidok.00034470.

Shusterman, A. A., V. E. Teige, A. J. Turner, C. Newman, J. Kim, and R. C. Cohen (2016). "The BErkeley Atmospheric CO_2 Observation Network: Initial Evaluation". *Atmos. Chem. Phys.* 16:21, pp. 13449–13463. DOI: 10.5194/acp-16-13449-2016.

Stagakis, S., C. Feigenwinter, R. Vogt, D. Brunner, and M. Kalberer (2023). "A High-Resolution Monitoring Approach of Urban CO_2 Fluxes. Part 2 – Surface Flux Optimisation Using Eddy Covariance Observations". *Science of The Total Environment* 903, p. 166035. DOI: 10.1016/j.scitotenv.2023.166035.

Stamnes, K. H., G. E. Thomas, and J. J. Stamnes (2017). *Radiative Transfer in the Atmosphere and Ocean*. Second edition. Cambridge University Press, Cambridge, United Kingdom, xvii, 512 Seiten.

Thoning, K. W., A. M. Crotwell, and J. W. Mund (2024a). *Atmospheric Carbon Dioxide Dry Air Mole Fractions from Continuous Measurements at Mauna Loa, Hawaii, Barrow, Alaska, American Samoa and South Pole, 1973-2023*. Version 2024-02-12. National Oceanic and Atmospheric Administration (NOAA), Global Monitoring Laboratory (GML), Boulder, Colorado, USA. DOI: 10.15138/yaf1-bk21.

Thoning, K. W., X. Lan, A. M. Crotwell, and J. W. Mund (2024b). *Atmospheric Methane from Quasi-Continuous Measurements at Barrow, Alaska and Mauna Loa, Hawaii, 1986-2023*. Version 2024-02-12. National Oceanic and Atmospheric Administration (NOAA), Global Monitoring Laboratory (GML), Boulder, Colorado, USA. DOI: 10.15138/ve0c-be70.

Toon, G. C. (2015). *Solar Line List for the TCCON 2014 Data Release (GGG2014.R0) [Data Set]*. CaltechDATA. DOI: 10.14291/TCCON.GGG2014.SOLAR.R0/1221658.

Tu, Q. (2019). "Observation of Atmospheric Greenhouse Gas Abundances on Regional Scales in Boreal Areas Using Portable FTIR Spectrometers". PhD thesis. Karlsruher Institut für Technologie (KIT). DOI: 10.5445/IR/1000095901.

Turnbull, J. C., A. Karion, K. J. Davis, T. Lauvaux, N. L. Miles, S. J. Richardson, C. Sweeney, K. McKain, S. J. Lehman, K. R. Gurney, R. Patarasuk, J. Liang, P. B. Shepson, A. Heimburger, R. Harvey, and J. Whetstone (2019). "Synthesis of Urban CO_2 Emission Estimates from Multiple Methods from the Indianapolis Flux Project (INFLUX)". *Environ. Sci. Technol.* 53:1, pp. 287–295. DOI: 10.1021/acs.est.8b05552.

United Nations Framework Convention on Climate Change (UNFCCC) (2015). "Paris Agreement". In: *UNFCCC, COP Report No. 21, Addenum, at 21, U.N. Doc. FCCC/CP/2015/10/Add.1 (Jan. 29, 2016)*.

Verhulst, K. R., A. Karion, J. Kim, P. K. Salameh, R. F. Keeling, S. Newman, J. Miller, C. Sloop, T. Pongetti, P. Rao, C. Wong, F. M. Hopkins, V. Yadav, R. F. Weiss, R. M. Duren, and C. E. Miller (2017). "Carbon Dioxide and Methane Measurements from the Los Angeles Megacity Carbon Project – Part 1: Calibration, Urban Enhancements, and Uncertainty Estimates". *Atmos. Chem. Phys.* 17:13, pp. 8313–8341. DOI: 10.5194/acp-17-8313-2017.

Vogel, F. R., M. Frey, J. Staufer, F. Hase, G. Broquet, I. Xueref-Remy, F. Chevallier, P. Ciais, M. K. Sha, P. Chelin, P. Jeseck, C. Janssen, Y. Té, J. Groß, T. Blumenstock, Q. Tu, and J. Orphal (2019). "XCO_2 in an Emission Hot-Spot Region: The COCCON Paris Campaign 2015". *Atmos. Chem. Phys.* 19:5, pp. 3271–3285. DOI: 10.5194/acp-19-3271-2019.

Wang, Y., M. Fang, Z. Lou, H. He, Y. Guo, X. Pi, Y. Wang, K. Yin, and X. Fei (2024). "Methane Emissions from Landfills Differentially Underestimated Worldwide". *Nat. Sustain.*, pp. 1–12. DOI: 10.1038/s41893-024-01307-9.

Warren, R., J. Price, E. Graham, N. Forstenhaeusler, and J. VanDerWal (2018). "The Projected Effect on Insects, Vertebrates, and Plants of Limiting Global Warming to 1.5°C Rather than 2°C". *Science* 360:6390, pp. 791–795. DOI: 10.1126/science.aar3646.

Washenfelder, R. A., G. C. Toon, J.-F. Blavier, Z. Yang, N. T. Allen, P. O. Wennberg, S. A. Vay, D. M. Matross, and B. C. Daube (2006). "Carbon Dioxide Column Abundances at the Wisconsin Tall Tower Site". *J. Geophys. Res.* 111:D22, p. D22305. DOI: 10.1029/2006JD007154.

Watts, N., M. Amann, N. Arnell, S. Ayeb-Karlsson, K. Belesova, H. Berry, T. Bouley, M. Boykoff, P. Byass, W. Cai, D. Campbell-Lendrum, J. Chambers, M. Daly, N. Dasandi, M. Davies, A. Depoux, P. Dominguez-Salas, P. Drummond, K. L. Ebi, P. Ekins, L. F. Montoya, H. Fischer, L. Georgeson, D. Grace, H. Graham, I. Hamilton, S. Hartinger, J. Hess, I. Kelman, G. Kiesewetter, T. Kjellstrom, D. Kniveton, B. Lemke, L. Liang, M. Lott, R. Lowe, M. O. Sewe, J. Martinez-Urtaza, M. Maslin, L. McAllister, S. J. Mikhaylov, J. Milner, M. Moradi-Lakeh, K. Morrissey, K. Murray, M. Nilsson, T. Neville, T. Oreszczyn, F. Owfi, O. Pearman, D. Pencheon, S. Pye, M. Rabbaniha, E. Robinson, J. Rocklöv, O. Saxer, S. Schütte, J. C. Semenza, J. Shumake-Guillemot, R. Steinbach, M. Tabatabaei, J. Tomei, J. Trinanes, N. Wheeler, P. Wilkinson, P. Gong, H. Montgomery, and A. Costello (2018). "The 2018 Report of the Lancet Countdown on Health and Climate Change: Shaping the Health of Nations for Centuries to Come". *The Lancet* 392:10163, pp. 2479–2514. DOI: 10.1016/S0140-6736(18)32594-7.

Wecht, K. J., D. J. Jacob, M. P. Sulprizio, G. W. Santoni, S. C. Wofsy, R. Parker, H. Bösch, and J. Worden (2014). "Spatially Resolving Methane Emissions in California: Constraints from the CalNex Aircraft Campaign and from Present (GOSAT, TES) and Future (TROPOMI, Geostationary) Satellite Observations". *Atmos. Chem. Phys.* 14:15, pp. 8173–8184. DOI: 10.5194/acp-14-8173-2014.

Wei, T., J. Wu, and S. Chen (2021). "Keeping Track of Greenhouse Gas Emission Reduction Progress and Targets in 167 Cities Worldwide". *Front. Sustain. Cities* 3, p. 696381. DOI: 10.3389/frsc.2021.696381.

Wendisch, M. and P. Yang (2012). *Theory of Atmospheric Radiative Transfer*. Wiley-VCH, Weinheim. XIII, 321 S.

Wheeler, T. and J. von Braun (2013). "Climate Change Impacts on Global Food Security". *Science* 341:6145, pp. 508–513. DOI: 10.1126/science.1239402.

Wong, C. K., T. J. Pongetti, T. Oda, P. Rao, K. R. Gurney, S. Newman, R. M. Duren, C. E. Miller, Y. L. Yung, and S. P. Sander (2016). "Monthly Trends of Methane Emissions in Los Angeles from 2011 to 2015 Inferred by CLARS-FTS Observations". *Atmos. Chem. Phys.* 16:20, pp. 13121–13130. DOI: 10.5194/acp-16-13121-2016.

Wong, K. W., D. Fu, T. J. Pongetti, S. Newman, E. A. Kort, R. Duren, Y. K. Hsu, C. E. Miller, Y. L. Yung, and S. P. Sander (2015). "Mapping CH_4 : CO_2 Ratios in Los Angeles with CLARS-FTS from Mount Wilson, California". *Atmos. Chem. Phys.* 15:1, pp. 241–252. DOI: 10.5194/acp-15-241-2015.

Wu, K., K. J. Davis, N. L. Miles, S. J. Richardson, T. Lauvaux, D. P. Sarmiento, N. V. Balashov, K. Keller, J. Turnbull, K. R. Gurney, J. Liang, and G. Roest (2022). "Source Decomposition of Eddy-Covariance CO_2 Flux Measurements for Evaluating a High-Resolution Urban CO_2 Emissions Inventory". *Environ. Res. Lett.* 17:7, p. 074035. DOI: 10.1088/1748-9326/ac7c29.

Wunch, D., G. C. Toon, P. O. Wennberg, S. C. Wofsy, B. B. Stephens, M. L. Fischer, O. Uchino, J. B. Abshire, P. Bernath, S. C. Biraud, J.-F. L. Blavier, C. Boone, K. P. Bowman, E. V. Browell, T. Campos, B. J. Connor, B. C. Daube, N. M. Deutscher, M. Diao, J. W. Elkins, C. Gerbig, E. Gottlieb, D. W. T. Griffith, D. F. Hurst, R. Jiménez, G. Keppel-Aleks, E. A. Kort, R. Macatangay, T. Machida, H. Matsueda, F. Moore, I. Morino, S. Park, J. Robinson, C. M. Roehl, Y. Sawa, V. Sherlock, C. Sweeney, T. Tanaka, and M. A. Zondlo (2010). "Calibration of the Total Carbon Column Observing Network Using Aircraft Profile Data". *Atmos. Meas. Tech.* 3:5, pp. 1351–1362. DOI: 10.5194/amt-3-1351-2010.

Wunch, D., P. O. Wennberg, G. C. Toon, G. Keppel-Aleks, and Y. G. Yavin (2009). "Emissions of Greenhouse Gases from a North American Megacity". *Geophys. Res. Lett.* 36:15. DOI: 10.1029/2009GL039825.

Wunch, D., G. C. Toon, V. Sherlock, N. M. Deutscher, C. Liu, D. G. Feist, and P. O. Wennberg (2015). "Documentation for the 2014 TCCON Data Release". Version GGG2014.R0. In collab. with D. Wunch, P. O. Wennberg, and TCCON. DOI: 10.14291/TCCON.GGG2014.DOCUMENTATION.R0/1221662.

Wunch, D., G. C. Toon, J.-F. L. Blavier, R. A. Washenfelder, J. Notholt, B. J. Connor, D. W. T. Griffith, V. Sherlock, and P. O. Wennberg (2011). "The Total Carbon Column Observing Network". *Philos. T. R. Soc. A* 369:1943, pp. 2087–2112. DOI: 10.1098/rsta.2010.0240.

Wunch, D., G. C. Toon, J. K. Hedelius, N. Vizenor, C. M. Roehl, K. M. Saad, J.-F. L. Blavier, D. R. Blake, and P. O. Wennberg (2016). "Quantifying the Loss of Processed Natural Gas within California's South Coast Air Basin Using Long-Term Measurements of Ethane and Methane". *Atmos. Chem. Phys.* 16:22, pp. 14091–14105. DOI: 10.5194/acp-16-14091-2016.

Yadav, V., R. Duren, K. Mueller, K. R. Verhulst, T. Nehrkorn, J. Kim, R. F. Weiss, R. Keeling, S. Sander, M. L. Fischer, S. Newman, M. Falk, T. Kuwayama, F. Hopkins, T. Rafiq, J. Whetstone, and C. Miller (2019). "Spatio-Temporally Resolved Methane Fluxes From the Los Angeles Megacity". *J. Geophys. Res. Atmos.* 124:9, pp. 5131–5148. DOI: 10.1029/2018JD030062.

Yadav, V., K. Verhulst, R. Duren, A. Thorpe, J. Kim, R. Keeling, R. Weiss, D. Cusworth, M. Mountain, C. Miller, and J. Whetstone (2023). "A Declining Trend of Methane Emis-

sions in the Los Angeles Basin from 2015 to 2020". *Environ. Res. Lett.* 18:3, p. 034004. DOI: 10.1088/1748-9326/acb6a9.

Yoshida, Y., Y. Ota, N. Eguchi, N. Kikuchi, K. Nobuta, H. Tran, I. Morino, and T. Yokota (2011). "Retrieval Algorithm for CO_2 and CH_4 Column Abundances from Short-Wavelength Infrared Spectral Observations by the Greenhouse Gases Observing Satellite". *Atmos. Meas. Tech.* 4:4, pp. 717–734. DOI: 10.5194/amt-4-717-2011.

Zeng, Z.-C., V. Natraj, F. Xu, S. Chen, F.-Y. Gong, T. Pongetti, K. Sung, G. Toon, S. Sander, and Y. Yung (2021). "GFIT3: A Full Physics Retrieval Algorithm for Remote Sensing of Greenhouse Gases in the Presence of Aerosols". *Atmos. Meas. Tech.* 14, pp. 6483–6507. DOI: 10.5194/amt-14-6483-2021.

Zeng, Z.-C., T. Pongetti, S. Newman, T. Oda, K. Gurney, P. I. Palmer, Y. L. Yung, and S. P. Sander (2023). "Decadal Decrease in Los Angeles Methane Emissions Is Much Smaller than Bottom-up Estimates". *Nat. Commun.* 14:1, 1, p. 5353. DOI: 10.1038/s41467-023-40964-w.

Zeng, Z.-C., Y. Wang, T. J. Pongetti, F.-Y. Gong, S. Newman, Y. Li, V. Natraj, R.-L. Shia, Y. L. Yung, and S. P. Sander (2020a). "Tracking the Atmospheric Pulse of a North American Megacity from a Mountaintop Remote Sensing Observatory". *Remote Sens. Environ.* 248, p. 112000. DOI: 10.1016/j.rse.2020.112000.

Zeng, Z.-C., F. Xu, V. Natraj, T. J. Pongetti, R.-L. Shia, Q. Zhang, S. P. Sander, and Y. L. Yung (2020b). "Remote Sensing of Angular Scattering Effect of Aerosols in a North American Megacity". *Remote Sens. Environ.* 242, p. 111760. DOI: 10.1016/j.rse.2020.111760.

Zeng, Z.-C., Q. Zhang, V. Natraj, J. S. Margolis, R.-L. Shia, S. Newman, D. Fu, T. J. Pongetti, K. W. Wong, S. P. Sander, P. O. Wennberg, and Y. L. Yung (2017). "Aerosol Scattering Effects on Water Vapor Retrievals over the Los Angeles Basin". *Atmos. Chem. Phys.* 17:4, pp. 2495–2508. DOI: 10.5194/acp-17-2495-2017.

Zeng, Z.-C., V. Natraj, F. Xu, T. J. Pongetti, R.-L. Shia, E. A. Kort, G. C. Toon, S. P. Sander, and Y. L. Yung (2018). "Constraining Aerosol Vertical Profile in the Boundary Layer Using Hyperspectral Measurements of Oxygen Absorption". *Geophys. Res. Lett.* 45:19, pp. 10, 772–10, 780. DOI: 10.1029/2018GL079286.

Zhang, Q., V. Natraj, K.-F. Li, R.-L. Shia, D. Fu, T. J. Pongetti, S. P. Sander, C. M. Roehl, and Y. L. Yung (2015). "Accounting for Aerosol Scattering in the CLARS Retrieval of Column Averaged CO_2 Mixing Ratios". *J. Geophys. Res. Atmos.* 120:14, pp. 7205–7218. DOI: 10.1002/2015JD023499.

Acknowledgements

At the end of this work, I would like to thank everyone who contributed to and/or supported me during this thesis. My gratitude goes to ...

... Prof. Dr. André Butz for supervising my thesis with an open ear at any time, and with valuable scientific guidance, advice and perspective on every aspect of it.

... Dr. Sanam Vardag for many discussions and advice, sometimes at very short notice.

... Dr. Frank Hase for sharing his FTS knowledge with me in helpful discussions.

... Ralph Kleinschek for his ideas, assistance and shared experience throughout all technical developments.

... Dr. Stanley Sander and Thomas Pongetti for the fuitful collaboration, for giving me the opportunity to measure on Mt. Wilson and for providing me their raw data for analysis.

... Ralph Kleinschek and Vincent Enders for creating a productive and memorable campaign experience on Mt. Wilson.

... Ralph Kleinschek, Tobias Schmitt, Lukas Weis, Vincent Enders, Robin Müller and Jonas Kuhn for hands-on building and/or theoretical considerations that led to an operational EM27/SCA and beyond.

... Ralph Pfeifer, Heribert Sommer, Alexandra Mertens and Sebastian Gehrig for their ready help and advice on all small and large projects.

... Angelika Gassama and Rebekka Benetatos for their guidance through the administrative jungle.

... Tobias Schmitt, Lukas Pilz and Marvin Knapp for the superb office atmosphere, the shared knowledge and ideas, and the right balance between productive focus and curious distraction.

... the Atmo group for many interesting and helpful scientific discussions, and also for the entertaining recreational phases.

... the members of the HCE College for the interdisciplinary insights and exchange.

... Tobias Schmitt, Clara Löw, Eva-Marie Metz, Karolin Voss, Leonie Scheidweiler, Lukas Pilz, Lukas Weis, Marvin Knapp, Maximilian May, Thomas Plewa and Tobias Heldt for their proofreading and constructive input during the writing process.

... all my friends who accompanied me along the way during hikes, at picnics, at campfires, during extensive board games, while bouldering or running and for sociable and relaxing lunch & coffee breaks. Thank you Anni, Freddy, Julia, Lukas, Lukas, Merlin, Mikko, Rabea, Simon, Tobias, Tobias and many more.

... my family for their continuous support and encouragement.

... Clara Löw for her pragmatic mindset, affection, occasionally needed distraction and unconditional support during the entire time.